SISSA
Scuola
Internazionale
Superiore di
Studi Avanzati

Physics Area - PhD course in
Astroparticle Physics

Complementary probes of the nature of dark matter

Candidate:
Jan Tristram Acuña

Advisor:
Piero Ullio, Ph. D.

Academic Year 2020-21

ABSTRACT

COMPLEMENTARY PROBES OF THE NATURE OF DARK MATTER

Jan Tristram Acuña **Adviser:**
Piero Ullio, Ph.D.

There is overwhelming evidence for the existence of a nonbaryonic dark matter (DM) component in the Universe's energy budget, coming from various astrophysical and cosmological probes, but its nature is very much unknown. A plethora of models have been proposed, mostly under the umbrella of the particle DM paradigm. The desired properties of DM indicates that it is only natural to expect that a viable DM candidate lies in extensions of the Standard Model (SM). In this work, we have considered minimal models that address the so-called DM puzzle, which are also motivated by theoretical issues and experimental anomalies in the SM. Firstly, motivated by the possibility that the nonbaryonic component could be described by a dark sector framework that is as complex as the SM, we consider a scenario in which DM resides in a multicomponent dark sector. The stable species are charged under an unbroken U(1) dark force, mediated by a massless dark photon, and they also interact with ordinary matter through scalar portals. We study its implications on cosmology, by studying its early Universe evolution through the numerical solution of a set of Boltzmann equations which track the relic densities and the temperatures of the dark and visible sectors. On the other hand, the reported discrepancy between the SM prediction and the recently announced experimental measurement of the muon magnetic dipole moment is addressed from the point of view of new physics. Here we introduced a minimal model, inspired by the MSSM, where the bino-like Majorana fermion is regarded as the DM candidate, while other species such as the sleptons are necessary to both alleviate the tension in the muon $g-2$, as well as to produce the correct relic density of DM. Meanwhile, the attempt to understand the nature of DM is not only limited to tracking its early Universe history nor to provide solutions to experimental anomalies, but also by probing it in relaxed structures, that have formed at late times, such as the halo in our own Milky Way (MW) galaxy. DM in the MW halo can be probed through direct detection searches, which rely on observing possible recoil signals induced by scatterings of DM with nuclei or with electrons. Deriving direct detection limits on DM requires the calculation of the theoretical recoil signal, which involves specifying the elementary interaction of DM with ordinary matter, as well as properly assessing the systematic uncertainties coming from nuclear physics, atomic physics, and astrophysics. Here we focus on quantifying the astrophysical uncertainty which enters in the assumption for the velocity distribution of DM in the MW. We advocate the implementation of equilibrium axisymmetric modeling to describe the DM phase space distribution function (PSDF). This has

the advantage of being self-consistent with the MW mass model, which is axisymmetric and is well-supported by latest kinematic data on tracers of the underlying MW gravitational potential. We assess the impact of the axisymmetric PSDF particularly on DM-electron scattering, which is an excellent probe of sub-GeV DM, and compare the resulting exclusion limits coming from the Standard Halo Model (SHM) that is often quoted in the literature.

PACS:

Acknowledgments

The completion of this thesis would not have been possible without the help of professors, colleagues, and friends.

Firstly, I thank SISSA for giving me the opportunity to pursue my PhD under a fellowship grant. Secondly, I would like to thank my adviser, Piero Ullio, for his guidance and patience in supervising me during the PhD. His invaluable comments and profound insights, have been quite useful, not just in the work I have carried out under his supervision, but also in making me realize that there are so many exciting things to learn about dark matter. Working under him has made me understand that the PhD journey may, at times, involve several iterations of doing and rechecking the same calculation, which is vastly different from simply completing a problem set.

I extend my gratitude to my collaborators, Marco Fabbrichesi, Patrick Stengel, and Mihael Petač, for the fruitful discussions about the respective projects we have worked on, for providing feedback on some of my preliminary results, and for addressing some of the questions I had when things became hazy.

I also would like to thank my professors, both at ICTP and SISSA, for providing me with the necessary background knowledge to tackle problems in my chosen research program.

Special thanks go to Ian Vega, for giving me career advice and for sharing his excitement about the future of astroparticle/particle/gravitational physics research in the Philippines; and to Flip Tanedo, for serving as a role model for young researchers, such as myself, in the field of dark matter physics.

I thank my friends for sticking with me, through thick and thin, during my stay here in Trieste, especially the ones I met during the ICTP diploma program: Adu, Vicharit, and D. Marfo. I also thank Philip, Noel, and all the Filipino students at ICTP that I have met throughout the years, for making me feel less homesick. To Pamela, thank you for cheering me up when I needed it most.

I thank my family for supporting my career choice, and for providing me with moral support. I also dedicate this thesis to my grandmother, Eligia, who once told me that she had wished she had gone to do a PhD after getting an MA.

To everyone who has helped me in one way or another, thank you very much.

Table of Contents

Chapter 1

Introduction

The observational successes of the Standard Big Bang cosmology has cemented its status as a scientific theory. It rests alongside the Standard Model (SM) of Particle Physics, which is the currently accepted framework for describing three of the four fundamental interactions — electromagnetic, weak, and strong — and for classifying the elementary particles known at present. The Standard Big Bang cosmology adequately explains the following observations, known as the "pillars of modern cosmology": the accelerated expansion of the Universe, the origin of the cosmic microwave background radiation (CMB), the primordial abundances of light elements, and the formation of galaxies and large-scale structure. Meanwhile, the concordance model of cosmology is a particular realization of the Big Bang theory that has been used to describe the matter and energy content of the Universe, and has been used to provide a mechanism for generating the initial seeds of perturbations through inflation, that allowed the growth of structure. It should be noted that under the concordance model, the Universe's energy budget is distributed among the following: (1) baryons, which, in this context, includes electrons apart from protons, neutrons, and nuclei; (2) dark matter (DM), which is postulated to be a collisionless, pressureless fluid that is nonbaryonic in nature; and (3) dark energy (DE), which comprises bulk of the energy budget, and is responsible for the accelerated expansion of the Universe. Assuming a spatially flat topology and by performing a six-parameter fit on the measurements from the Planck satellite, the relative contributions, taken at the present epoch, of nonbaryonic matter, baryonic matter, dark energy, and radiation, respectively, are [1]

$$\begin{aligned} \Omega_c h^2 = 0.11933 \pm 0.00091, \qquad \Omega_b &= 0.02242 \pm 0.00014, \quad \Omega_\Lambda = 0.6889 \pm 0.0056, \\ \Omega_r &= (1+z_{eq})^{-1}\Omega_m \approx 9.18 \times 10^{-5}. \end{aligned} \tag{1.1}$$

Such cosmological parameters are concordant with, *e.g.* measurements of the distances of supernova Ia (SNIa) standard candles. In what follows, we shall focus our attention on DM, dubbed as one of the "known unknowns" in cosmology, and the quest for understanding the nature of DM has been the subject of tremendous research activity for, at least, the past three decades.

1.1 Evidences for DM

There are overwhelming evidences, coming from independent observations that span a wide range of length and time scales, that point to the existence of DM. Such observations have revealed

that, at the very least, DM has gravitational interactions with ordinary matter, *i.e.* the form of matter whose elementary constituents are SM particles. The common denominator that relates these observations is the realization that there is the problem of "missing mass," and, in order to account for these observations, one must postulate the existence of an extra form of matter.

1.1.1 Dynamical evidence in the local Galaxy and in galaxy clusters

Although most of the credit for early investigations of DM is attributed to Fritz Zwicky, it has already been pointed out by Lord Kelvin as early as 1904 that there could be some form of matter within the Milky Way (MW) galaxy (from here on, we shall refer to the MW galaxy as "Galaxy") that is, perhaps, not entirely dark, but is too faint to be observed. The basis of his conclusion is the application of the virial theorem to the Galaxy, assuming that it is composed of a gas of non-interacting particles in dynamical equilibrium. From the virial theorem, one can establish a relationship between the velocity dispersion, and the virial mass and virial radius of the Galaxy. Meanwhile, Kapetyn [2] made an attempt to construct a model of the mass distribution in the Galaxy, by assuming that isodensity surfaces are coaxial ellipsoids of revolution with an axial ratio of 5.1. A necessary condition for the stability of this stellar system is the presence of rotation about the Galactic polar axis. Here, Kapetyn also made some remarks regarding the application of the kinetic theory of gases on the Galactic system, although the assumption that the peculiar velocities of stars are Maxwellian breaks down because of stellar streaming[1], *i.e.* the peculiar motions of stars in the Solar neighborhood are not random, but are biased in directions away and toward the Galactic center. In the same paper, Kapetyn provided a means to determine the local density of DM: the average effective mass of stars can obtained by determining the total mass within some volume, inferred from velocity measurements, divided by the number of luminous stars, inferred from some luminosity function which gives the number of luminous objects within a luminosity interval. Knowing the number of luminous stars within some volume of space, and the average mass of a luminous star, the local DM density can be estimated. Oort [3] improved upon Kapetyn's calculation of the local total matter density by considering a refined model of the Galaxy, and using the relationship between the derivative of the vertical acceleration and the local matter density. Oort finds $0.092\,M_\odot/\mathrm{pc}^3$, which differs from Kapetyn's estimate by just 7.6%. The local DM density is inferred by estimating the local density of visible stars, whose absolute magnitudes are below 13.5. Knowing the luminosity function — in this case, he had a table of values for the number objects within some bin of absolute magnitude, the average mass of objects within that bin, and the limiting distance of such objects — Oort obtained a value of $0.0378\,M_\odot/\mathrm{pc}^3$ for the local density of visible stars; this implies that the local DM density, to which he referred to as "nebulous" or "meteoric" matter, is less than $0.05\,M_\odot/\mathrm{pc}^3$; compare this with current estimates, *e.g.* [4] and [5] where they respectively give $0.0101 \pm 0.0007\,M_\odot/\mathrm{pc}^3$ and $0.016 \pm 0.010\,M_\odot/\mathrm{pc}^3$.

Of course, the contributions of Fritz Zwicky in establishing that there is DM in the cosmos cannot be brushed aside. We emphasize here that, although Zwicky used the same methodology of using the virial theorem to estimate the density of DM in a finite volume, he was the first to apply it for the case of galaxy clusters, particularly the Coma cluster [6][2]. The main motivation

[1] not to be confused with stellar streams caused by tidal stripping of globular clusters

[2] an English translation from the original German is available in [7]

for Zwicky to perform this analysis was the apparently large value of the velocity dispersion, where the corresponding RMS value is roughly in the order of 1000 km/s, of nebular components within the Coma cluster; the velocities of these nebulae were measured by Hubble and Humanson in 1931 by measuring the Doppler shift of the spectral lines coming from these nebulae. Assuming that the Coma cluster is in a state of dynamical equilibrium, where the virial theorem can be applied, one can show that the velocity dispersion $\langle v^2 \rangle$ can be related to the virial mass M and the virial radius R via

$$\langle v^2 \rangle = \frac{3G_N M}{5R} \tag{1.2}$$

$$= (82\,\mathrm{km/s})^2 \left(\frac{M}{800 \times 10^9 M_\odot} \right) \left(\frac{10^6\,\mathrm{ly}}{R} \right). \tag{1.3}$$

In Zwicky's analysis, he assumed that there are 800 nebulae each having a mass of $10^9 M_\odot$. Zwicky further argues that even if one relaxes the virial theorem, in such a way that the average kinetic energy is minus the average potential energy, this only increases the velocity dispersion by a factor of 2. In order for the virial theorem prediction to match the observed velocity dispersion, one must consider the possibility that the average density of the Coma cluster must be at least 300-400 times the density of luminous matter; this is the point where Zwicky concludes that dark matter exists in amounts much larger than luminous matter. In 1937, Zwicky advocated the use of the virial theorem to determine the masses of individual nebulae and of the whole cluster; he pointed out that the usual methods of estimating the masses of nebulae that are based on luminosities and internal rotations of nebulae only provide lower limits on these masses and are, thus, unreliable [8]. Applying the virial theorem to the Coma cluster, knowing the measured value of the velocity dispersion, and assuming that there are 1000 nebulae within the cluster, he found that the average mass of one nebula is at least $4.5 \times 10^{10}\,\mathrm{M}_\odot$. Furthermore, he pointed out that the average luminosity of a nebula is $8.5 \times 10^7\,\mathrm{L}_\odot$; at this point he effectively introduced the notion of the mass-to-light ratio, and he found that

$$\frac{M}{L} \approx 500 \frac{M_\odot}{L_\odot} \tag{1.4}$$

for the Coma cluster. This final result, however, depends on the velocity dispersion from redshift measurements and on the inferred size of the cluster, which can be obtained from the Hubble velocity-distance relation

$$v = H_0 r. \tag{1.5}$$

At that time, the Hubble parameter H_0 was measured to be 558 km/s/Mpc, which is around 8 times larger than the modern value, *e.g.* that is reported in [9], and thus the actual mass-to-light ratio should actually go down to 60. Even so, there is some evidence that there is DM within the Coma cluster.

So far in this discussion, the hint that there is a form of matter that is too faint to be seen ultimately rests on the assumption that the virial theorem can be used to estimate the total gravitational mass of the system, and the discrepancy between the virial mass and the amount of luminous matter is accounted for by DM. However, even Zwicky himself put this assumption into question, especially in the determination of the mass of the Virgo cluster using this method.

Nevertheless, the distribution of nebulae in the Coma cluster (see Fig. 3 of [8]) suggests that it is in dynamical equilibrium, the virial theorem holds, and the fact that there is a huge mass-to-light ratio warranted further investigation.

1.1.2 Galaxy rotation curves

In the 1939 paper of Babcock [10], he mentioned that internal motions of nebulae, such as circular velocities that can be obtained using redshift measurements, can be used to determine the total mass and infer the mass distributon within the orbital radius of a nebula. This can be easily seen by noting that the enclosed mass $M(r)$ within some distance r from the center of a galaxy is related to the local circular velocity $V_c(r)$ via

$$V_c^2(r) = \frac{G_N M(r)}{r}, \tag{1.6}$$

which simply follows from matching the local gravitational acceleration from Newton's law of gravitation with the centripetal acceleration required to sustain the circular motion. Babcock obtained the rotation curve of M31, also known as the Andromeda galaxy, up to 100 arc minutes; assuming that our distance from M31 is 744 kpc [11], this translates to a radial distance of around 21.6 kpc from the center of M31. In order to infer the mass distribution within M31, Babcock had to formulate a mass model of M31, consisting of a sphere surrounded by similar, concentric, coaxial spheroidal shells. The densities and geometrical properties of these mass components were chosen such that the gravitational acceleration matches the centripetal acceleration required to produce the observed circular velocities. Based on the mass model, he found that the mass-to-light ratio increases with increasing radial distance away from the center, along the major axis: this is the first indication that there is more matter in the outskirts of galaxies, but Babcock made a conservative statement that the large mass-to-light ratio could be due to absorption effects or some novel effect that modifies the dynamics in the outskirts. A year later, Oort [12] arrived at similar findings, but using measurements of the rotation curve of NGC 3115, a galaxy of type S0 without spiral arms. The mass distribution for this galaxy was modelled as concentric ellipsoidal shells with axial ratio 2/3; the mass density and the light density was tabulated in shells within the following intervals along the major axis of the galaxy: 0-10 arcminutes, 10-20 arcminutes, and 20-70 arcminutes. He found that in the outer regions of the galaxy, the mass-to-light ratio is 249, modulo a corrective factor by which the actual distance to the galaxy differs from the fiducial value of 1.5 Mpc. Oort mentions in this paper that the mass distribution of mass in NGC 3115 does not reflect the light distribution in the same galaxy, and that the large mass-to-light ratio that he inferred indicates "an extreme relative density of very faint dwarfs or interstellar material." There was also reason to conclude that the "luminous system appears to be embedded in a large and more or less a homogeneous mass of great density."

The detection of the 21 cm hydrogen line radiation in 1951 [13] allowed measurements of circular velocities, based on signals from the radio band, that are complementary with optical-based measurements. For instance, this enabled Roberts [14] to measure the rotation curve of M31 within 120 arcminutes. By performing a fit to the data points using the interpolating function

$$V_c(R) = \frac{AR}{(1 + B^n R^n)^{3/(2n)}}, \tag{1.7}$$

he found that the circular velocities on each side of the major axis of M31 are asymmetric, which had been previously noted by [15]. Using (1.6), one can determine the total mass of M31, and Roberts obtained a value $3.1 \pm 0.5 \times 10^{11}\,\mathrm{M}_{\odot}$. On the other hand, he notes that the assumption of a Keplerian motion, applied to the distant points in the rotation curve measurement, leads to lower mass estimates for the mass of M31; to Roberts, this was an indication that at the largest distances covered by his measurements, Keplerian motion was a poor assumption. Freeman [16] took advantage of the rotation curves of M33 and NGC 300 taken from 21 cm measurements, to make conclusions about the total mass and mass distribution of each of the two galaxies. He first assumed an exponential disk model for the luminous stellar component. For such a disk model, the surface mass density at a cylindrical radial distance R from the center is given by

$$\Sigma(R) = \Sigma_0 \exp(-R/R_d), \tag{1.8}$$

where R_d is the scale length and Σ_0 is a normalization parameter. Freeman used photometric data to determine the best fit values of Σ_0 and R_d, for each galaxy that he considered. He then compared the prediction for the circular velocity, under the assumption of an exponential disk, with the rotation curve from 21 cm measurements. He found indications that there must be additional matter, that is undetected in both the optical and 21 cm band, and for M33 and NGC 300, the mass resides mostly in this non-luminous component. Furthermore, the matter distribution for each of these galaxies is vastly different from the exponential disk model. On the other hand, the often-cited work of Ford and Rubin [17] featured the measurement of the rotation curve of M31, using measurements obtained with an image-tube spectrograph, up to 120 arcminutes corresponding to the extent of the emission region. They obtained a rotation curve, consistent with [14], that is flattening over the last 30% of the optical disk. This key observation of the flattening of the rotation curve is one motivation for Ford & Rubin paper to deviate from previous works on rotation curves regarding the mass model that one adopts for a galaxy. Prior to Ford & Rubin, there have been conscious efforts in choosing mass models that lead to fits of the rotation curve, beyond the last observed region in radial distance, with a Keplerian fall off. Rogstad and Shostak [18] also found flat rotation curves from neutral hydrogen studies of five Scd type galaxies, and concluded that, based on the inferred mass-to-light ratios of the galaxies under consideration, there must be low-luminosity material residing in the outskirts of these galaxies. From the rotation curves of M31, M101, and M81 extending to relatively larger distances (a little over 30 kpc), Roberts and Rots [19] arrived to the conclusion that the presence of a significant amount of matter in the outer regions of galaxies is required, and that the edge of a galaxy lies beyond what is observed from photometric measurements.

Most in the astronomical community in the late '70s were convinced that flat rotation curves are present in galaxies, save for issues regarding side lobe effects that contaminate the signal for the case of single dish telescopes (*e.g.* see the discussion in [21] and [22]). Rotation curve measurements imply that the enclosed mass increases roughly with distance from the galactic center, at distances where the rotation curve is flat, and that the outer regions of galaxies are dominated by some non-luminous form of matter. It cannot be denied that there is a mismatch between the mass inferred from rotation curves and the mass inferred from optical observations. However, the exact nature of the additional matter component required to account for this mass discrepancy was not firmly established: the possibility that this extra form of matter is made up of very faint compact objects like brown dwarfs and planets was favored over the case of

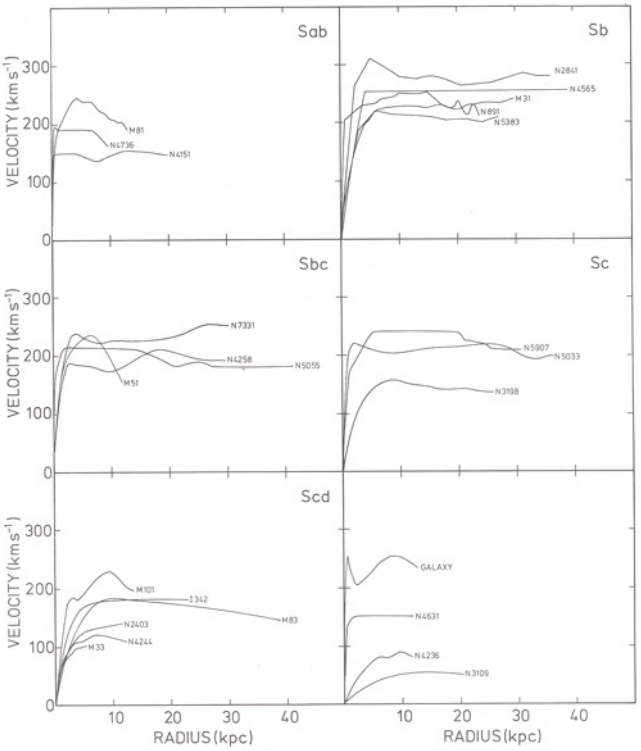

Figure 1.1: Rotation curves of 25 galaxies of different Hubble types; this catalog of galaxies exhibit flat rotation curves. Taken from [20].

nonbaryonic DM. Einasto, Kaasik, and Saar [23] advanced the possibility that the missing mass could be in some form of "hidden matter." Meanwhile, Ostriker and Peebles [24] demonstrated through numerical simulations that thin disks supported by rotation alone are unstable to barlike modes, while models with an additional spherical halo component were found to be more stable; this should ring a bell to the alert reader that the extra matter component could reside within a halo. By 1979, the review article by Faber and Gallagher [25] gave a definitive statement, that was shared by most astronomers and cosmologists, that the evidences based on current data at the time for mass-to-light ratios of galaxies, make a very strong case for the existence of invisible matter in the Universe. To add, Faber and Gallagher cite the Ostriker and Peebles paper on the stability analysis of purely galactic disks, mentioning that the findings of Ostriker and Peebles provide indirect evidence for DM in galaxies.

1.1.3 Structure formation

By the early 1970s, the view that galaxies are surrounded by DM halos, which had been the inferred configuration of galaxies based on the observed flat rotation curves, was accepted by the wider astrophysical community. Thus, the study of structure formation already included DM as one of the matter components on top of baryons. In 1974, Press and Schechter [26] carried out the first N-body simulations, which naturally incorporates nonlinear effects, of a cold gas of self-gravitating masses, and they found that structures form in a hierarchical fashion in this scenario, *i.e.* low mass objects aggregate to form larger structures. White and Rees [27] improved upon the earlier work of Press and Schechter by incorporating both the dissipationless clustering of

DM, and gas dynamics for the formation of galaxies and galaxy clusters. In particular, White and Rees argued that the potential wells provided by DM facilitated the condensation of gas components to form luminous structures through dissipative and radiative cooling. Subsequent N-body simulations were carried out by Aarseth, Goth, and Turner [28], and Efstathiou [29] to study the growth of structure in the Universe.

A key feature of investigations of the impact of DM in structure formation is the agnostic assumption regarding its interactions, either with baryons or with itself: DM is considered to have only gravitational interactions with matter. If DM were to have interactions with photons and baryons, these must be extremely weaker than baryon-photon interactions, in order to facilitate gravitational collapse at matter-radiation equality. Rather, structure formation mainly depends on the mass of the DM relic [30]. In particular, DM relics can be: hot DM (HDM), which are relativistic DM relics; cold DM (CDM), which are non-relativistic relics; and warm DM (WDM), whose typical velocities lie between the thermal velocities of HDM and CDM relics. The degree of clustering of these different types of relics can be characterized by the so-called free streaming scale, a concept that is related to the Jeans' scale at which instabilities can occur. In the case of Jeans' instability, gravitational collapse occurs because the internal pressure of the fluid is insufficient to balance out the compressional force of gravity; equivalently, the characteristic collapse time is shorter than the characteristic propagation time of sound waves within a finite volume. On the other hand, for the structure formation of pressure-less DM, sound waves do not propagate, but the individual DM particles do have characteristic velocities set by their thermal distribution. From requiring the similar criterion that the collapse time is less than the travel time of DM particles within the characteristic size of the collapsed structure, the cutoff scales in length and in mass are roughly given by

$$R \gtrsim \frac{v_{th}}{(G_N \rho)^{1/2}}, \quad M \gtrsim \frac{v_{th}^3}{(G_N^3 \rho)^{1/2}}. \tag{1.9}$$

Above these scales, virialized structures can form. Hence, for CDM with low thermal velocities, one initially forms smaller structures, which then cluster together to form larger structures — this is the bottom-up scenario of structure formation. On the other hand, the cutoff scale for HDM is at the scale of superclusters, *i.e.* around $10^{15} M_\odot$, and large structures form first before they disintegrate into fragments — this is the top-down scenario of structure formation. In the intermediate case of WDM, where the cutoff scale is usually below galaxy cluster scales, it inherits both scenarios of structure formation from HDM and CDM: top-down scenario for scales below the cutoff, and bottom-up scenario for scales above the cutoff. These different predictions on the manner in which structure formation proceeds allows us to discriminate between these models, which can be tested against galaxy surveys. Among the earliest galaxy surveys that have been carried out, data from the CfA redshift survey in the 1980s [31] established the presence of the cosmic web. Also, the amount of clustering that is revealed by the CfA survey is in stark disagreement with the large coherence length of matter distributions seen in N-body simulations of HDM [32]. On the other hand, N-body simulations carried out under the CDM hypothesis, which take into account nonlinear gravitational clustering, gave better agreement with the CfA survey, for $\Omega_m = 0.2$ and $\Omega_\Lambda = 0.8$ [33]; these findings secured the status of CDM as the leading paradigm for DM.

1.1.4 X-ray observations, gravitational lensing, and the Bullet Cluster

The X-ray emission due to hot gas in galaxy clusters provides a way to infer the mass of a galaxy cluster. The directly observable quantity is the surface brightness of the X-ray emission and the X-ray spectrum: from these quantities, the temperature of the gas T as well as its density distribution $\rho(\vec{r})$ can be inferred. Assuming spherical symmetry, the mass of the cluster can be estimated by assuming that the gas is in hydrostatic equilibrium, *i.e.*

$$\frac{dp}{dr} = -\frac{G_N M(r)}{r^2}\rho(r), \tag{1.10}$$

where p is the gas pressure, and that the gas in the cluster with mean atomic weight μ follows the ideal gas law:

$$p = \frac{\rho}{\mu m_p} k_B T. \tag{1.11}$$

Then the enclosed mass within a radial distance r is

$$M(r) \approx -\frac{r}{G_N}\frac{k_B T}{\mu m_p}\frac{d\ln\rho}{d\ln r}. \tag{1.12}$$

Of course, to be able to apply (1.12) in inferring the masses of galaxy clusters, one must be able to measure the X-ray emission. However, performing ground-based measurements of these emissions is not possible since X-rays do not penetrate the atmosphere. Thus, the only way to detect X-ray emissions is to send an X-ray telescope in outer space. In 1978, the Einstein observatory was launched, and it allowed the observation of astrophysical objects and the study of the structure of galaxy clusters in the X-ray band. From X-ray observations of galaxy clusters, it was found that most of the baryonic mass actually resides in hot gas, rather than in galaxies [34]. Furthermore, based from the X-ray emission data collected from the Coma cluster, and choosing a particular ansatz for the gas density profile, Cowie, Henriksen, and Mushotzky determined the total mass in the form of gas, within 2 Mpc, to be $1.6 \times 10^{14}\, M_\odot$ [35]. Also within 2 Mpc, they provided a value of $6 \times 10^{13}\, \mathrm{M}_\odot$ for the total mass in stars and obtained a virial mass of $\sim 1.1 \times 10^{15}\, M_\odot$; the gas contribution to the total mass of the Coma cluster is around 15% the virial mass. They concluded that the range of acceptable mass-to-light ratios for the Coma cluster is 22-60 h. Similarly, but refining the analysis by not imposing assumptions about the gas equation of state, Hughes [36] found that the virial mass within $2.5\, h^{-1}$ Mpc is $0.93 \pm 0.12 \times 10^{15}\, h^{-1}$ Mpc, while the mass contained in gas comprises 16% to 53% of the virial mass. White, Navarro, Evrard, and Frenk [37] report the following values for the inferred masses in stars, hot gas, and virial mass within $1.5\, h^{-1}$ Mpc in the Coma cluster:

$$\begin{aligned} M_{gal} = 1.0 \pm 0.2 \times 10^{13} h^{-1}\,\mathrm{Mpc} \quad &, \qquad M_{gas} = 5.45 \pm 0.98 \times 10^{13} h^{-5/2}\,\mathrm{Mpc}, \\ M_{tot} \quad &= \quad 6.7 \pm 1.0 \times 10^{14} h^{-1}\,\mathrm{Mpc}. \end{aligned} \tag{1.13}$$

The gist of these results from X-ray observations is the fact that the mass-to-light ratio for the Coma cluster is lower than the initial estimates of Zwicky; nevertheless, the problem of the missing mass still persists. In addition, (1.13) implies that the baryon to DM ratio is

$$\frac{\Omega_b}{\Omega_{DM}} \approx 0.0165 + 0.0900 h^{-3/2}, \tag{1.14}$$

which gives 0.163 for $h = 0.72$, *i.e.* the baryon to DM density ratio is around 1/6. As a side comment, measurements of the primordial abundances of light elements require $\Omega_b = 0.04$, which implies that the total energy budget in matter — baryon plus DM — is roughly 0.3 times the critical density. This posed a problem for the standard CDM paradigm, where the Universe is considered to be flat and consists only of DM and baryonic matter. On the other hand, the ΛCDM paradigm accommodates an additional contribution to the Universe's energy budget: dark energy. The estimates we have just made suggest that dark energy comprises the dominant contribution to the density of the Universe, around 70% of the critical density.

Meanwhile, another method of determining the mass within a cluster is via gravitational lensing, which has long been proposed by Zwicky in his 1937 paper, alongside the use of the virial theorem [8]. Gravitational lensing is the effect in which the trajectory of a light ray is bent due to the presence of sufficiently massive objects, relative to its expected trajectory without such massive sources. This effect is a generic prediction of a class of gravitational theories, including Newtonian gravity and Einstein's general relativity (GR). The first observational evidence for gravitational lensing was provided by Eddington [38], where, during a solar eclipse in 1919, he discovered that light from a distant star grazing at the Sun's surface can be bent. By marking the relative positions of the star during the eclipse and during a normal evening, he was able to measure an angular deflection of 1.75 arcseconds, consistent with the GR prediction. Another evidence for gravitational lensing came in 1979, when Walsh, Carswell, and Weymann [39] reported the observation of two quasars with identical magnitudes, redshifts, and spectra. They proposed the more likely scenario that the two quasars are mere images of a single distant quasar, where light from that quasar is bent by an intervening galaxy, then reached the Earth in two different directions. The measured observables — angular separation of images, sizes of the images, and the amplification of the images — allowed them to infer the mass and size of the gravitational lens.

In principle, gravitational lensing can come in two types: strong gravitational lensing, in which the amount of bending of starlight allows for the formation of multiple images or even ring-like images; and weak gravitational lensing, where the intervening massive source only distorts the images but not producing multiple images. It should be realized that, compared with X-ray techniques to infer the masses of clusters, weak gravitational lensing offers a clean and powerful way of mapping the underlying matter distribution in some observable part of the Universe. The only principle that relates measurable quantities and the properties of the gravitational lens is GR, although one also operates under the assumption that GR works well in these scales.

Perhaps the strongest and most direct empirical evidence for the existence of DM is the weak lensing observation of the Bullet Cluster, by Clowe et. al. [40]. The collision of two clusters gave rise to the Bullet Cluster. Initially, the components of each cluster — galaxies, gas, and DM — trace a common gravitational potential and are spatially distributed in a way that is symmetric about a common center. For the colliding clusters, they used weak gravitational lensing of the images of background galaxies to map the underlying gravitational potential due to the clusters. On the other hand, the X-ray image of the cluster, obtained using the *Chandra* X-ray telescope, was used to map the distribution of hot gas. As shown in Fig. (1.2), it is evident that the distribution of the X-ray emitting plasma is offset relative to the underlying gravitational potential, indicating that the amount of DM in the colliding clusters must dominate

the baryonic components. Furthermore, the intracluster plasma lags behind the cluster centers, due to ram pressure. In contrast, the DM components in each cluster appear to have simply passed through each other, which demonstrates a property of DM being collisionless.

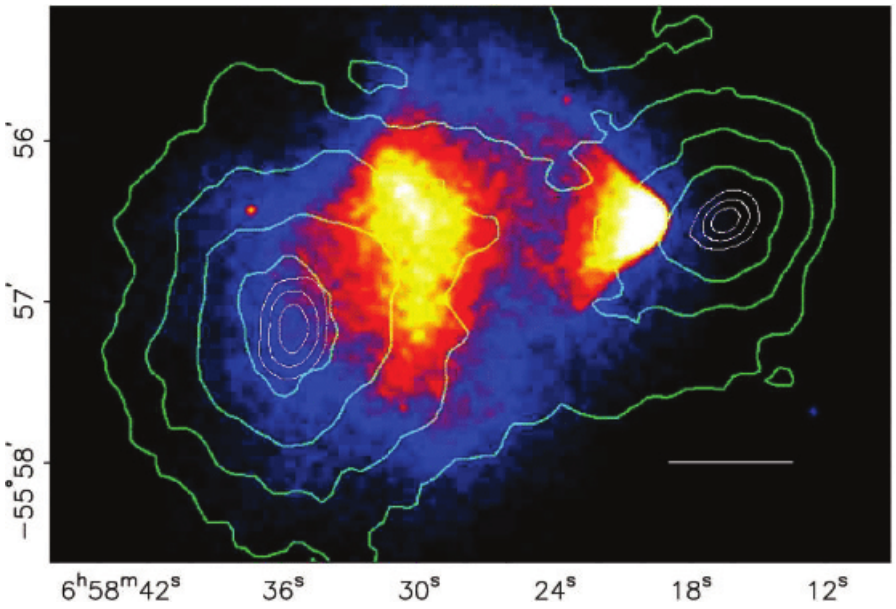

Figure 1.2: False color image of the Bullet Cluster taken from [40]. The green contours are contours of constant convergence κ, where the peaks correspond to locations of maximum surface mass density. The blue and red regions correspond to the spatial locations of the gas.

1.1.5 Features in the CMB anisotropy

It was demonstrated by Gamow that the hypothesis of an expanding Universe meant that it should have started from a hot dense state. The argument can be traced back by starting from the Friedmann equation

$$H^2 = \frac{8\pi G_N}{3}\rho, \tag{1.15}$$

where ρ consists of the matter density ρ_m and radiation density ρ_r. At very early times, radiation dominated the energy budget of the Universe, and it scales with $a(t)$, the scale factor, as

$$\rho \propto a^{-4}, \tag{1.16}$$

which simply follows from the conservation of the energy-momentum tensor for a perfect fluid with equation of state $p = \rho/3$. The Friedmann equation then implies that the evolution of the scale factor, with respect to the comoving time t, is

$$a(t) \propto t^{1/2}. \tag{1.17}$$

Noting that the energy density of radiation scales as T^4, where T is the temperature of the radiation bath, we obtain the time-temperature relation

$$T \approx \left(1.52 \times 10^{10}\,\mathrm{K}\right)\left(\frac{t}{1\,\mathrm{sec}}\right)^{-1/2} \approx \left(1.27\,\mathrm{MeV}\right)\left(\frac{t}{1\,\mathrm{sec}}\right)^{-1/2}. \tag{1.18}$$

This rough calculation, while ignoring the temperature dependence of the number of effective degrees of freedom in the primordial plasma, clearly gives us the result that the temperature of the radiation that fills the Universe, must have been very high at early times.

Related to the study of the thermal history of the early Universe, a hot Big Bang cosmology sets the ideal conditions for the synthesis of light elements through nuclear fusion. In a series of papers, Alpher, Bethe, and Gamow, laid down the necessary ingredients to tackle Big Bang nucleosynthesis (BBN). At the basic level, a network of nuclear processes must be followed in order to track the relative abundances of the light elements, starting from the formation of deuterium via the reaction

$$n + p \leftrightarrow {}^2H + \gamma. \tag{1.19}$$

While the binding energy of deuterium is $B_D = 2.2\,\mathrm{MeV}$, the large photon to baryon ratio ($\eta_B \equiv n_B/n_\gamma \approx 5 \times 10^{-10}$) pushes back the equilibrium towards a configuration of free neutrons and protons, thereby delaying nucleosynthesis to temperatures lower than B_D; this is the so-called deuterium bottleneck. Assuming that the species track their equilibrium abundances, one can show that the deuterium fraction relative to the baryon number density is

$$X_D \approx \eta_B \left(\frac{T}{m_p}\right)^{3/2} \exp(B_D/T), \tag{1.20}$$

and the deuterium fraction becomes order unity when

$$T \lesssim -\frac{B_D}{\ln \eta_B} \lesssim 0.1\,\mathrm{MeV}. \tag{1.21}$$

A more careful calculation sets the BBN temperature at $0.07\,\mathrm{MeV}$.

The early BBN analyses that were done in the late 1940s were historically important, because these were crucial in establishing early estimates of the present temperature of the CMB. In particular, Alpher and Herman [41] obtained an estimate of $5\,\mathrm{K}$. In order to obtain this value, they first started with the known measurement, by Hubble, of the present matter density ($\sim 10^{-30}\,\mathrm{g/cm^3}$). Using that as initial condition, they integrated the system of coupled Boltzmann equations, tracking the mass fractions of the different nuclear species, backwards in time to the BBN epoch; they obtained the matter density at this time ($\sim 10^{-6}\,\mathrm{g/cm^3}$). On the other hand, they knew the temperature at which BBN started to occur, which implies a radiation density of $\sim 1\,\mathrm{g/cm^3}$. From the scaling of the matter and radiation densities with respect to the scale factor, the following quantity must be a constant:

$$\rho_r \rho_m^{-4/3} = \mathrm{const.} \tag{1.22}$$

Hence, the radiation density at the present epoch can be inferred, from which one can obtain the temperature of the CMB.

Later in 1965, Peebles re-derived the CMB temperature prediction that had been previously obtained by Alpher and Herman, which prompted the construction of a radio antenna at Princeton that was designed to search for this background radiation. Similar results had been obtained by Doroshkevich and Novikov a year before, where in [42] they discussed the detectability of the CMB using radio observations. Finally, the serendipitous discovery by Penzias and Wilson in 1965 [43] of an isotropic radio signal at 4080 MHz (corresponding to a wavelength of 7.3 cm), was identified by Dicke, Roll, Peebles, and Wilkinson [44] as evidence for the leftover radiation from the Big Bang, whose present temperature they estimated to be 3.5 K. While the temperature of the CMB was inferred from radio measurements, the question of whether it follows a blackbody spectrum or not, was not yet settled: the measurement of the CMB was carried out only at a fixed wavelength. In the 1990s, the FIRAS instrument on-board the COBE satellite collected data from the CMB; subsequent analysis by Mather et. al. [45] showed that the CMB follows a perfect blackbody spectrum in the range of frequencies from 2 to 20 cm^{-1}, and the present CMB temperature is 2.726 ± 0.010 K at 95% confidence level.

Regarding the spatial distribution of the CMB in the sky, early work by Silk [46], Zel'dovich and Sunyaev [47], and Peebles and Yu [48], demonstrated that initial perturbations in the matter density, which served as seeds for the subsequent formation of structure in the Universe, will leave an imprint on the CMB in the form of temperature anisotropies at the level of 10^{-4}. The connection between matter density fluctuations and CMB temperature anisotropies can be understood by looking at the interplay between baryons, photons, (cold) DM component, and gravity. From the framework of inflationary cosmology, the quantum fluctuations of the inflaton field gave rise to scale-invariant, adiabatic fluctuations of the curvature perturbations [49]. In turn, from the Einstein field equations, fluctuations in the metric give rise to fluctuations in the matter-energy density. The evolution of the phase space densities of the different components in the system is dictated by separate Boltzmann equations for each component, generically given by

$$L[f_i] = \sum_{j \neq i} C_{ij}[f_i, f_j] \tag{1.23}$$

where f_i is the phase space density of species i, L is the Liouville operator, and C_{ij} is the collision operator. The collision operator encodes the interactions between species, *e.g.* Thomson scattering of photons with electrons, Coulomb scattering of protons with electrons, while the Liouville operator encodes the evolution of the phase space density along a geodesic in curved spacetime. From a practical standpoint, the Boltzmann equations are reduced to ordinary differential equations by taking moments with respect to momentum, and one simply tracks the evolution of the perturbations of these moments. For the system under consideration, we would like to, at least, track the following: matter density perturbations of baryons and DM, bulk velocities of baryons and DM, and temperature anisotropy of photons. The full set of Boltzmann equations can be found in, *e.g.* Ma and Bertschinger [50], Hu and Sugiyama [51], Lesgourges and Pastor [52].

Ultimately, the quantity of interest is the two-point function of the CMB temperature anisotropies. Generically the temperature anisotropy at a particular direction in the sky $\hat{n}$

can be expanded in terms of spherical harmonics, *i.e.*

$$\Theta(\hat{n}) \equiv \frac{\Delta T(\hat{n})}{T_{CMB}} = \sum_{lm} a_{lm} Y_{lm}(\hat{n}). \tag{1.24}$$

Assuming Gaussian fluctuations, the two-point function of the multipole coefficients can be written as

$$\langle a_{lm} a_{l'm'} \rangle = \delta_{ll'} \delta_{mm'} C_l, \tag{1.25}$$

where C_l is what is commonly referred to as the CMB power spectrum. From an observational perspective, C_l encodes vast amounts of information about cosmology, particularly on the relative weights Ω_i of the different matter-energy components present in the Universe. Of course, extracting Ω_i from the observed CMB power spectrum assumes some underlying cosmological framework, *i.e.* ΛCDM cosmology; in principle, a choice of Ω_i will give predictions for the CMB power spectrum, which can be fitted with observations.

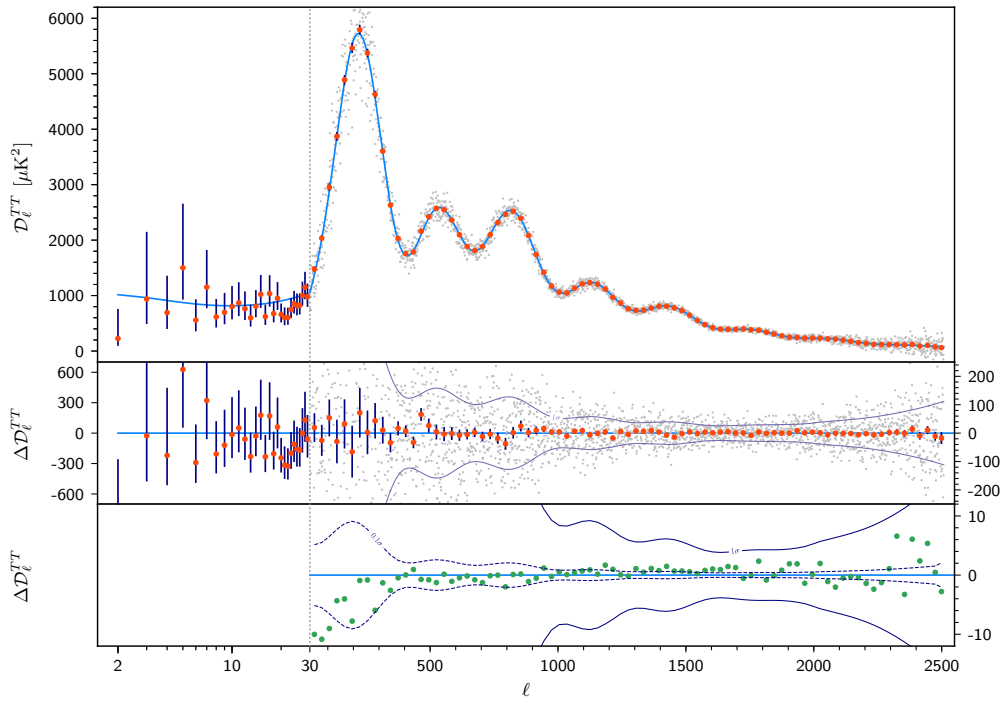

Figure 1.3: Plot of the angular power spectrum of the temperature anisotropy of the CMB from the Planck 2018 data release. The data points cover the multipoles from $l = 2$ to $l = 2508$.

Meanwhile, progress has been made in measuring the CMB temperature anisotropy since the 1980s. First generation satellites that were used to carry out the measurement of the CMB anisotropy are RELIKT-1 [53], launched in 1983, and the Cosmic Background Explorer (COBE), which carried the Differential Microwave Radiometer (DMR) instrument that was responsible for measuring the CMB anistropy [54]. In 2000, BOOMERanG, an experiment that was implemented by sending an instrument in a long duration balloon flight, reported the evidence of a

well-defined peak in the CMB power spectrum at $l = 197 \pm 6$ [55]. This was followed by the Wilkinson Microwave Anisotropy Probe (WMAP), when, in 2003, they published preliminary measurements of the CMB power spectrum in the range $2 \leq l \leq 900$ [56]. Apart from space-based observations of the CMB anisotropy, ground-based interferometers such as the Very Small Array (VSA) [57], Degree Angular Scale Interferometer (DASI) [58], and Cosmic Background Imager (CBI) [59], were capable of measuring the CMB anisotropy; these arrays of instruments also found oscillations in the CMB anisotropy, and also detected the E-mode polarization of the CMB. To date, the most accurate measurement of the CMB power spectrum comes from the Planck satellite [60].

The observed CMB power spectrum has important implications regarding the existence of DM. In particular, the locations and heights of the first three peaks in the CMB angular power spectrum shown in Fig. (1.3) are mainly affected by the relative contributions of baryons and DM in the Universe's energy budget. In order to understand the connection between the CMB peaks and the DM density in the Universe, one can go back to the era before recombination when neutral hydrogen started to form. During this time period, the primordial plasma contained baryons, free electrons, and photons. Photons and electrons are kept tightly coupled via Thomson scattering, while protons and electrons scatter efficiently via Coulomb interactions; all together, the plasma can be considered to be a single, tightly coupled entity, called the baryon-photon fluid. The moments of the temperature anisotropy satisfy a Boltzmann hierarchy, where the derivative of the l^{th} order moment depends on the $(l-1)^{\text{th}}$ and the $(l+1)^{\text{th}}$ moment; in practice, this hierarchy is truncated to obtain a closed set of equations. In the tightly coupled regime, only the monopole and dipole moments of the temperature anisotropy are relevant, while the other moments can be neglected. One can show that the relevant temperature moments satisfy an ordinary differential equation for a damped, forced oscillator [61]

$$c_s^2 \left(c_s^{-2}\Theta'\right)' + c_s^2 k^2 \Theta = -\frac{k^2}{3}\Psi - c_s^2 \left(c_s^{-2}\Phi'\right)' \equiv F(\eta), \tag{1.26}$$

where the prime denotes differentiation with respect to conformal time η, c_s^2 is the square of the sound speed given by

$$c_s^2 = \frac{1}{3}\frac{1}{1+R}, \quad R = \frac{3\rho_b}{4\rho_r}, \tag{1.27}$$

k is the Fourier scale of the perturbation, and Ψ and Φ are gauge-invariant gravitational potentials. Intuitively, (1.26) describes the physics of the baryon-photon fluid in the following manner: the term on the right hand side is the forcing due to gravity, which tends to collapse the fluid; on the other hand, the term linear in Θ corresponds to radiation pressure which acts as a restoring force to counter gravitational collapse. This tug-of-war between gravity and photon pressure gives rise to the well-known baryon acoustic oscillations (BAO). These oscillations continue until the time of last scattering ($z \approx 1100$), when photons decouple from baryons and undergo free-streaming. The oscillatory behavior of the solution to (1.26) can be formally seen by noting that Θ can be written down in terms of: the homogeneous solution, which is just a linear combination of $\sin(ks)$ and $\cos(ks)$, where $s \equiv \int d\eta\ c_s(\eta)$; and the particular solution that depends on the convolution of the forcing $F(\eta)$ with the Green's function. Knowing the formal solution to (1.26), we can make statements about the locations of the acoustic peaks and

the amplitudes of the peaks. At the time of recombination η_*, a scale k will yield maximum temperature anisotropy if

$$k_n s_* \approx n\pi, \;\; s_* \equiv \int_0^{\eta_*} d\eta \; c_s(\eta), \tag{1.28}$$

where s_* is the physical scale of the sound horizon. In turn, this length scale of perturbations is imprinted on the last scattering surface, on angular scales with size

$$\theta_n \approx \frac{2s_*}{nD_*}, \tag{1.29}$$

where D_* is the angular diameter distance to the last scattering surface. Finally, this manifests in the CMB angular power spectrum in multipoles

$$l_n \approx \frac{n\pi D_*}{s_*}. \tag{1.30}$$

On the other hand, the heights of the peaks are mainly determined by the gravitational forcing term in the right hand side of (1.26).

At this point, we can elaborate on the effects of changing the DM density $\Omega_c h^2$, as well as the baryon density $\Omega_b h^2$, on the CMB power spectrum. As we increase $\Omega_b h^2$, the sound speed decreases as one can see in (1.27). Intuitively, since the photons are tightly coupled with baryons, the bulk motion of the fluid is dragged as we increase the amount of baryons; this is known as baryon loading. As the sound speed decreases, the length scale of perturbations corresponding to acoustic peaks must decrease, implying that these perturbations appear at smaller angular scales; this is clearly shown in the left panel of Fig. (1.4). On the other hand, knowing *a posteriori* that DM dominates the matter density over baryons, DM is the main source for the gravitational potentials that control the heights of the acoustic peaks. As CMB photons propagate in space, photons encounter potential wells; to overcome gravity, photons must redshift away some of their energy. Thus, increasing $\Omega_c h^2$ will manifest mainly as loss of power in the CMB angular spectrum, as one can see in the right panel of Fig. (1.4). Finally, one can make a parameter estimate, by obtaining the predicted CMB angular power spectrum and matching it with Planck observations, to demonstrate that, at cosmological scales, there is a huge amount of DM relative to baryons; as shown in Fig. (1.5), we can precisely pinpoint the cosmological parameters entering in the ΛCDM to a high level of accuracy. In a sense, the missing mass problem resurfaces in the context of cosmology: the prediction for the CMB angular power spectrum would be vastly different from what is observed if only baryons were generating the gravitational potential wells along which photons propagate.

1.2 Particle DM paradigm

In light of the overwhelming evidences pointing to the existence of DM, it is a natural question to inquire about the composition of DM. During the early days of DM research, it was simply dismissed as a collection of astrophysical objects that are too faint to be seen: massive collapsed objects [63], M8 dwarfs [64], and massive compact halo objects (MACHOs) [65]. However, Hegyi and Olive [66] argued that the nonluminous matter that surrounds galaxies must be nonbaryonic.

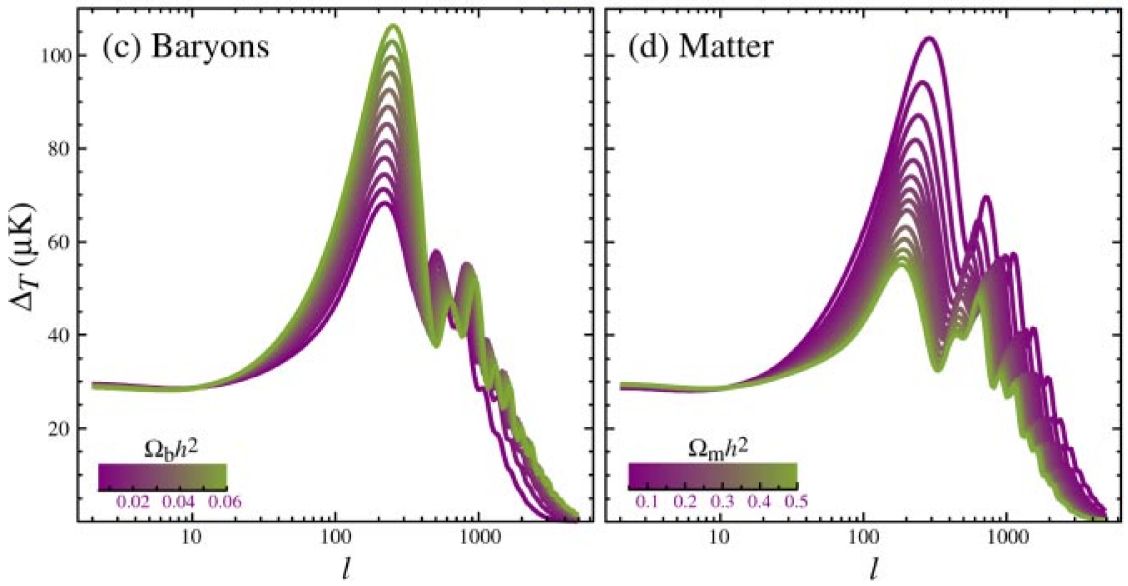

Figure 1.4: (Figure taken from [61]) Plots of the CMB angular power spectrum, upon changing $\Omega_b h^2$ (left panel), and $\Omega_m h^2$ (right panel). For each panel, the variation is taken with respect to a Λ CDM fiducial model $\Omega_{tot} = 1, \Omega_\Lambda = 0.65, \Omega_b h^2 = 0.02, \Omega_m h^2 = 0.147$, and spectral index $n = 1$. See the text for a discussion of the effects on the power spectrum upon changing the baryon and DM densities.

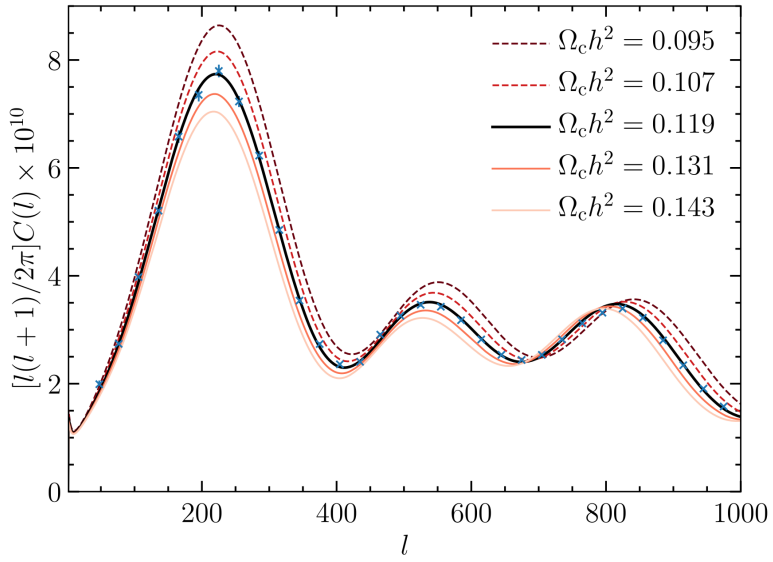

Figure 1.5: (Figure taken from [62]) Same as Fig. (1.4), but changing only $\Omega_c h^2$ while keeping the constraint $\Omega_m = 1 - \Omega_K - \Omega_\Lambda$. The blue dots correspond to binned measurements of the power spectrum by Planck [1].

Their line of argument proceeded by first considering an isothermal gas of baryons, which would collapse under its own gravity below some equilibrium temperature; on the other hand, keeping this gas of baryons stable would imply that it must emit a significant amount of X-ray radiation,

in conflict with what was known at that time regarding upper limits on the observations of the X-ray background; nowadays, the argument against baryonic DM stem from our understanding of the primordial abundance of light species from BBN, and the Universe's matter-energy budget as inferred from CMB observations. Hot intracluster gas was also considered to be a viable option to address the missing mass problem, although, as discussed in Sec. (1.1.4), it was not enough to account for the virial mass of galaxy clusters. MACHOs, which mainly consist of brown dwarfs, jupiters, white dwarfs, and black hole (BH) remnants, were considered to be strong candidates to account for the missing mass in the Universe. The proposed method to detect MACHOs was through gravitational microlensing; however, observational data showed that MACHOs can only account for less than 8% of the halo mass of the MW Galaxy [67] (see also [68] and [69]). Primordial black holes (PBHs) are attractive candidates for DM; after all, most of the properties we know about DM have come from observations and measurements of its gravitational influence on matter and spacetime, and black holes are objects that trap light and are, hence, nonluminous. The formation of black holes in the early Universe was studied by Carr and Hawking [70]. PBH formation proceeds in a similar fashion as BH formation from stellar collapse: during the radiation-dominated era, overdense regions can collapse if gravitational forces overcome the pressure due to radiation, and, furthermore, black hole formation occurs when the size of the collapsed region is smaller than its Schwarzschild radius. However the formation of PBHs is suppressed under the assumption of a scale-invariant power spectrum for initial curvature perturbations [71], and a possible way to enhance the production of PBHs is to introduce non-Gaussianties in the curvature power spectrum [72, 73].

However, the most well-studied hypothesis, and the leading paradigm for explaining the nature of DM is the particle DM hypothesis, and we shall subscribe to this umbrella framework throughout this manuscript. The connection between particle physics and the DM problem was not initially evident in the late 1970s, when the presence of nonbaryonic matter was established in light of rotation curve data. Rather, the contact was first established between particle physics and cosmology: this was made possible by the insight into the connection between neutrinos and cosmology, which allowed for the determination of upper limits to the neutrino mass, from the requirement that relic neutrinos do not overclose the Universe [74, 75]. Furthermore, the fact that the neutrino does not directly interact with SM photons makes it a very natural candidate for nonluminous DM; this possibility that relic neutrinos account for DM in the Universe was first investigated by Szalay and Marx [76]. It was soon realized, however, that neutrinos cannot be the DM, since they are regarded as hot relics, which are ruled out by structure formation. While the DM puzzle was not the primary motivation for constructing models beyond the SM (BSM), the particle physics community had become open to the possibility that new particles from BSM physics are needed to explain the nature of DM. Of course, in order for a BSM physics model to be able to explain DM, the construction of such a theory must be guided by the inferred properties of DM based on observations.

Any proposed theory of DM must provide a DM candidate/s that, at least, satisfy certain inferred properties, which were drawn from astrophysical and cosmological observations:

- DM cannot be a relativistic relic, otherwise it would be inconsistent with the observed bottom-up scenario of structure formation. Preferably, a DM relic must be cold and nonrelativistic; on the other hand, WDM scenarios could still be viable, but are also strongly constrained by Ly-α forest data [77–80].

- DM must be electromagnetically neutral: there are hypothetical scenarios in which a small kinetic mixing between SM photons and hypothetical dark photons induce a millicharge on DM [81, 82], however there are various constraints from BBN, CMB, colliders, and beam dump experiments [83].

- DM must be collisionless, as evidenced by the observations of the Bullet Cluster: this places constraints on the possible self-interactions among DM species.

- DM must be stable, since we observe signatures of DM across all cosmic epochs, and its lifetime must be at least the age of the Universe. This condition can be slightly relaxed by allowing DM to decay into, *e.g.* radiation, but the presence of extra radiation components are constrained by CMB observations [84, 85].

- The relic density of DM, relative to the critical density of the Universe, follows from the analysis of Planck data on the anisotropies in the CMB, discussed in Sec. (1.1.5), and was found to be

$$\Omega_m h^2 = 0.11933 \pm 0.00091; \tag{1.31}$$

  a model for DM must be able to reproduce this number.

This is just a shortlist of basic constraints that a hypothetical DM model must be able to satisfy, although there could be additional constraints that can be added to this list, or even modifications in this list, depending on the framework that one chooses to describe DM. For instance there are some DM candidates, *e.g.* self-interacting DM, fuzzy DM, that have been invoked in order to address apparent issues in the ΛCDM paradigm at small scales.

1.2.1 A selection of DM candidates

Given the long history of addressing the nature of DM from a particle physics perspective, it is no longer surprising that there are plenty of proposals for a model of DM. However, we would like to emphasize that initially, the DM puzzle, *i.e.* the problem of identifying the exact nature of DM, was not treated by model builders to be in equal footing with other theoretical issues within particle physics, *e.g.* hierarchy problem, electroweak stability; the presence of a DM candidate in such models was viewed as an added bonus. Over the years, the general view has changed: addressing the issue of the nature of DM now enjoys a rather elevated status as an important problem to be tackled by particle physics. As a matter of fact, the DM puzzle can be thought of as one of the main drivers of the birth of astroparticle physics, where issues in astrophysics can be studied from the point of view of particle physics, while cosmology provides a natural laboratory where particle physics models can be studied, even beyond energy scales that can be probed by terrestrial colliders. Here we list down a selection of DM candidates: our goal here is not to be exhaustive, but rather we would like to provide a brief overview of how model building can be carried out in the context of the DM problem.

Non-SM neutrinos

As we alluded to previously, the SM contains electrically neutral and long-lived particles, the neutrinos, which can be possible DM candidates. However, neutrinos have large free streaming scales that would have erased structures below a certain length scale. Nevertheless, the role of neutrinos in cosmology cannot be ignored, especially in the context of studying the thermal history of the Universe. On the other hand, the SM prediction for the neutrino mass is zero, which is in disagreement with what was observed in neutrino oscillation experiments in the late 1990s [86, 87]. There are issues in accommodating neutrino masses in the SM: for starters, a Dirac mass term can only be written down if there were a right-handed counterpart for the left-handed neutrino; a Majorana mass term, which only requires ν_L by construction, would yield a lepton number violating term. There have been theoretical investigations on the origin of neutrino masses that were carried out by, *e.g.* [88–92]; but in principle, if one insists on working only with fields present in the SM, neutrino masses can be generated through a nonrenormalizable dimension 5 Weinberg operator [93]

$$\mathcal{L}_5 \supset \frac{c_{ij}}{\Lambda}\left(l_{iL}^T C^{-1}\, i\sigma_2 H\right)\left(H^\dagger l_{jL}\right). \tag{1.32}$$

This higher dimensional operator can be realized in a UV complete theory, for instance, by introducing right handed neutrinos. On the other hand, from the context of the DM problem, one can introduce heavy sterile neutrinos as DM candidates that fulfill the limits from structure formation; an excellent review can be found in, *e.g.* [94]. Regarding past literature on this subject, Olive and Turner [95] considered obtaining bounds for the masses of light, left handed neutrinos and heavy, right handed neutrinos, from the condition that one must not overclose the Universe; here they suggested the possibility that these heavy right handed neutrinos can be the DM. Dodelson and Widrow [96] studied the scenario of $\nu_L - \nu_R$ oscillation as a means to produce sterile neutrinos.

Axions and ALPs

Axions are hypothetical bosonic particles that were introduced to address the so-called strong-CP problem, which can be developed by starting from the observation that the following CP-violating term is not forbidden in the SM:

$$\mathcal{L} \supset \frac{\theta g_s^2}{32\pi^2} G^a_{\mu\nu}\tilde{G}^{a\mu\nu}, \tag{1.33}$$

where g_s is the QCD gauge coupling, $G^{\mu\nu} = G^{a\mu\nu}t^a$ is the gluon field strength tensor, and t^a is an SU(3) generator. Actually, the physical parameter is the combination

$$\bar{\theta} \equiv \theta - \arg\,\det(M), \tag{1.34}$$

where M is the quark mass matrix; this can be seen by starting from the partition function

$$Z = \int [\mathcal{D}\psi]\left[\mathcal{D}\bar{\psi}\right] e^{i\int d^4x\, \left(\bar{\psi}i\not{D}\psi - \bar{\psi}M\psi + \frac{\theta g_s^2}{32\pi^2}G^a_{\mu\nu}\tilde{G}^{a\mu\nu}\right)}. \tag{1.35}$$

Performing a chiral rotation on the quark fields via

$$\psi \to e^{i\alpha\gamma_5}\psi \tag{1.36}$$

introduces a nontrivial transformation of the path integral measure [97], the effect of which is to shift the action by

$$\Delta S = 2\alpha \, \frac{g_s^2}{32\pi^2} G^a_{\mu\nu}\tilde{G}^{a\mu\nu}. \tag{1.37}$$

Meanwhile, the diagonalized quark mass term can be rewritten explicitly as

$$\mathcal{L}_m = -\sum_f \bar{f}_L f_R \, |m_f| e^{i\arg(m_f)} + \text{h.c.}. \tag{1.38}$$

When one performs a chiral rotation α_f on each quark field, the mass matrix transforms as

$$\arg(m_f) \to \arg(m_f) + 2\alpha_f, \tag{1.39}$$

and to go to a physical basis, one should rotate away the quark phases, which amounts to a choice $2\alpha_f = -\arg(m_f)$. Summing over quark fields gives

$$-\sum_f \arg(m_f) = -\arg\left(\prod_f m_f\right) = -\arg\,\det(M),$$

and thus we recover (1.34).

The presence of CP violating terms can contribute to the electric dipole moment (EDM) of neutrons, where current measurements point to [98]

$$|d_n| < 10^{-26} e\,\text{cm}. \tag{1.40}$$

Note that the SM, without the strong CP violating term, has CP violating terms in the quark sector, and contributes $|d_n| \sim 10^{-34} e\,\text{cm}$ [99], which is well within the above experimental limit. If we turn on the strong CP violating term, the contribution to the neutron EDM is [100]

$$d_n = 5.2 \times 10^{-16} \bar{\theta}\; e\,\text{cm}, \tag{1.41}$$

corresponding to $|\bar{\theta}| \lesssim 10^{-10}$ — an extremely small number. While the criterion of technical naturalness is an explanation for a vanishing $\bar{\theta}$ for pure QCD, *i.e.* CP symmetry is restored when $\bar{\theta} \to 0$, this is not the case when we include electroweak interactions. Then the point of the strong-CP problem is to "explain" why $\bar{\theta}$ is very small, and one proposed solution is due to Peccei and Quinn [101, 102], where they introduced a global U(1) Peccei-Quinn (PQ) symmetry that can be spontaneously broken. The resulting (pseudo)Nambu-Goldstone boson is the (QCD) axion $a(x)$, which transforms under a generic $\text{U}(1)_{\text{PQ}}$, parametrized by $\alpha(x)$, as

$$a(x) \to a(x) + f_a \alpha(x), \tag{1.42}$$

where f_a is the axion decay constant, analogous to the pion decay constant. It can be shown that under this symmetry, the following interaction is allowed:

$$\mathcal{L} \supset \frac{a(x)}{f_a} \, \frac{1}{32\pi^2} G^{a\mu\nu} G^a_{\mu\nu}. \tag{1.43}$$

By considering the low-energy effective theory for Nambu-Goldstone bosons, one can write down a potential for $a(x)$, and show that the minimum occurs at

$$\langle a(x) \rangle = -f_a \bar{\theta}; \tag{1.44}$$

this demonstrates that a dynamical solution to the strong-CP can be achieved.

Axions are good DM candidates: their stability is ensured by their very low masses (the benchmark for the QCD axion is $\sim 10^{-7}\,\mathrm{eV}$ for a coupling of $10^{-16}\,\mathrm{GeV}^{-1}$ with photons), while they can form structures, *e.g.* through Bose-Einstein condensation [103, 104]. If axions are to be regarded as DM, then one must ask how they can produce the observed relic density of DM. There are at least three possible ways of producing axions in the early Universe: thermal production, decay of topological defects, and misalignment mechanism. We shall provide a very rough sketch of how axions can be produced via misalignment mechanism. The effective Lagrangian for the QCD axion is

$$\mathcal{L}_a = \frac{1}{2}(\partial a)^2 - m_a^2 f_a^2 \left[1 - \cos\left(\frac{a}{f_a}\right)\right] \tag{1.45}$$

$$= \frac{1}{2}(\partial a)^2 - \frac{m_a^2}{2} a^2 + ... \tag{1.46}$$

The classical equation of motion for a spatially homogeneous distribution of axions, in an expanding background, is

$$\ddot{a} + 3H\dot{a} + m_a^2(T) a = 0, \tag{1.47}$$

where we emphasize that the mass of the axion m_a depends on temperature, scaling as T^{-n}, $n > 0$, at high temperatures, and tapers off to a constant at low temperatures. Initially, the Hubble parameter, which acts like a friction term, is much greater than m_a, and thus the axion field is tied to its initial value a_0. As T goes down, the axion potential starts to develop; at the time when $m_a(t_*) \approx H(t_*)$, the axion field begins to undergo oscillations. From (1.47), one can show that

$$\dot{\rho}_a = -3H\left(\rho_a + P_a\right), \tag{1.48}$$

where the energy density, ρ_a, and the pressure, P_a, are given by

$$\rho_a \equiv \frac{\dot{a}^2}{2} + \frac{m_a^2}{2} a^2 \tag{1.49}$$

$$P_a \equiv \frac{\dot{a}^2}{2} - \frac{m_a^2}{2} a^2. \tag{1.50}$$

Within one oscillation period, $\langle \dot{a}^2 \rangle = m_a^2 \langle a^2 \rangle$, and hence $\langle P_a \rangle = 0$. We are then left with $\langle \dot{\rho}_a \rangle + 3H \langle \rho_a \rangle = 0$, which implies that the axion energy density redshifts away like a matter component. To estimate the relic density of axions, we note that the present density of axions is just

$$\rho_a(t_0) = \rho_a(t_*) \frac{s(t_*)}{s(t_0)} = m_a^2 a_0^2 \frac{s(t_*)}{s(t_0)} \tag{1.51}$$

where $s(t)$ is the entropy density at time t; here we assume that the comoving entropy is conserved, and we replaced the energy density at t_* by the time-averaged value of ρ_a. By using the exact expression for the axion mass as function of temperature, and using the time-temperature relation one obtains for a radiation dominated Universe, one arrives at

$$\Omega_a h^2 \approx 0.1 \left(\frac{a_0}{2.15}\right)^2 \left(\frac{f_a}{10^{12}\,\mathrm{GeV}}\right)^{7/6}. \tag{1.52}$$

On the other hand, string theory predicts the existence of multiple axions [105], that may not necessarily correspond to the QCD axion. This provides inspiration to consider so-called axion-like particles (ALPs), which are described by a generic class of models in which they couple with gauge bosons through an $F\tilde{F}$ term analogous to the QCD axion. Reviews on the phenomenology and search efforts for ALPs can be found in, *e.g.* [106, 107].

WIMP (and FIMP) DM

Perhaps the most well-known DM candidate is the weakly interacting massive particle (WIMP), which is actually a generic DM framework that can be realized in specific BSM models such as supersymmetry (SUSY), and models that involve extra dimensions á la Kaluza-Klein. The idea of the WIMP emerged when it was realized that the DM production mechanisms for a variety of models have some common features.

We briefly focus on SUSY, where we provide a lightning introduction to SUSY and understand how a DM candidate arises from SUSY. The basic idea behind SUSY is the presence of a symmetry between bosons and fermions; in the simplest realization of SUSY case, called the minimal supersymmetric SM (MSSM), the basic particle content can be classified into: (i) chiral supermultiplet, consisting of a Weyl SM fermion and its spin-0 counterpart (*e.g.* electron-selectron, higgsino-Higgs); and (ii) vector supermultiplet, which consists of a SM gauge boson and its Weyl fermion counterpart called the gaugino. The Lagrangian describing the interactions within the MSSM can be obtained from the superpotential; in addition, since a theory where SUSY is unbroken leads to degenerate mass spectrum for particles belonging to the same supermultiplet, we have to introduce soft SUSY breaking terms to be consistent with the observed particle phenomenology. Meanwhile, apart from the condition that the soft SUSY breaking terms respect gauge invariance, additional symmetries can be imposed on them. Most notably, from constraints on baryon and lepton number violation, and limits on processes with flavor-changing neutral currents, one introduces R-symmetry, and the associated multiplicative quantum number called R-parity. All SM species are assigned to have R-parity +1, while their SUSY partners have R-parity -1. This ensures that SUSY particles are only produced in pairs, and the lightest among the superpartners (LSP) cannot decay; the latter consequence implies that LSPs are good DM candidates.

Suppose that we have a thermal distribution of WIMPs, whose temperature T is the same as the thermal bath. If WIMPs do not interact with any species at all, their number density dilutes away as the inverse cube of the scale factor, *i.e.* $a^{-3}(t)$, in a similar way as the entropy density (modulo changes in the effective number of degrees of freedom). In this case, we simply

have

$$\Omega_\chi h^2 = \frac{m_\chi s_0}{\rho_c h^{-2}} \left(\frac{n}{s}\right)_i \tag{1.53}$$

$$= \left(1.52 \times 10^6\right) \left(\frac{m_\chi}{1\,\mathrm{GeV}}\right). \tag{1.54}$$

This obviously leads us to overabundant DM, and so we then consider a very minimal assumption that a WIMP χ can undergo pair annihilation to produce a pair of SM species; the scattering of χ with SM species ensures that χ is kept in kinetic equilibrium with the thermal bath at temperature T. One can then write the Boltzmann equation describing the evolution of the number density of χ, given by

$$\dot{n}_\chi + 3Hn_\chi = -\langle\sigma v\rangle_{\chi\chi\to SMSM} n_\chi^2 + \langle\sigma v\rangle_{SMSM\to\chi\chi} n_{SM}^2, \tag{1.55}$$

where $\langle\sigma v\rangle$ is the so-called thermal cross section for a certain pair annihilation process, which is obtained by taking a thermal average of the cross section with respect to the thermal distribution function of WIMPs. The right hand side of (1.55) simply keeps track of the number-changing processes that control the number density of WIMPs: the first term refers to the depletion of WIMPs through WIMP pair annihilation into bath particles, while the second term refers to the creation of WIMPs through the reverse process. The detailed balance condition is often invoked to rewrite the last term in terms of the number density of χ, when the thermal distribution of χ follows an equilibrium distribution; this yields

$$\dot{n}_\chi + 3Hn_\chi = -\langle\sigma v\rangle(T)_{\chi\chi\to SMSM} \left[n_\chi^2 - (n_{\chi,eq}(T))^2\right]. \tag{1.56}$$

We note that a formal derivation (1.56) starts from the unintegrated Boltzmann equation, and taking moments in momentum; the evolution equation for the number density is simply the zeroth moment. Generally, one can have scenarios with several interacting components, where tracking the number density is simply not enough. In Ch. (2), we shall explore such a possibility, and we shall provide a discussion on properly writing down Boltzmann equations.

In principle, (1.56) can be recast further in a convenient form that resembles a Riccati equation. To show this, define

$$x \equiv \frac{m_\chi}{T} \tag{1.57}$$

$$\tilde{y} \equiv \left[\frac{g_\chi m_\chi^3}{2\pi^2 s(m_\chi)}\right]^{-1} y \tag{1.58}$$

$$\lambda \equiv \frac{g_\chi m_\chi^3 \langle\sigma v\rangle}{2\pi^2 H(m_\chi)}, \tag{1.59}$$

where m_χ is the mass of χ, g_χ is the number of spin degrees of freedom of χ, s is the entropy density, $y \equiv n_\chi/s$ is the comoving number density of χ. and H is the Hubble parameter. Noting that the comoving entropy is conserved, one can rewrite (1.56) as

$$\frac{d\tilde{y}}{dx} = -\frac{\lambda(x)}{x^2}\left[\tilde{y}^2 - \tilde{y}_{eq}^2(x)\right] \tag{1.60}$$

We note that λ, in general, is a function of temperature, since the thermal cross section generically has some temperature dependence. At high temperatures, the only available scale is T, and we expect $\langle \sigma v \rangle$ to go as T^{-2} on dimensional grounds. For low T, the thermal cross section will be constant in temperature for s-wave annihilation; for p-wave annihilation, it picks up a power of T. For simplicity, we consider the case of s-wave annihilation at low temperatures, so that one can write

$$\lambda(x) \sim \lambda_0 \begin{cases} x^2, \ x \ll 1 \\ \\ 1, \ x \ll 1 \end{cases} . \tag{1.61}$$

Sample solutions of $\tilde{y}$, for different values of λ_0, are shown in Fig.(1.6). At early times, the solid curves, representing the solution to the Boltzmann equation, trace the dashed curve, corresponding to the equilibrium comoving number. When the annihilation cross section is larger (which, in this case, amounts to larger λ_0), WIMPs stay longer in equilibrium with the heat bath. Alternatively, we can recover the features of the numerical solution by employing certain

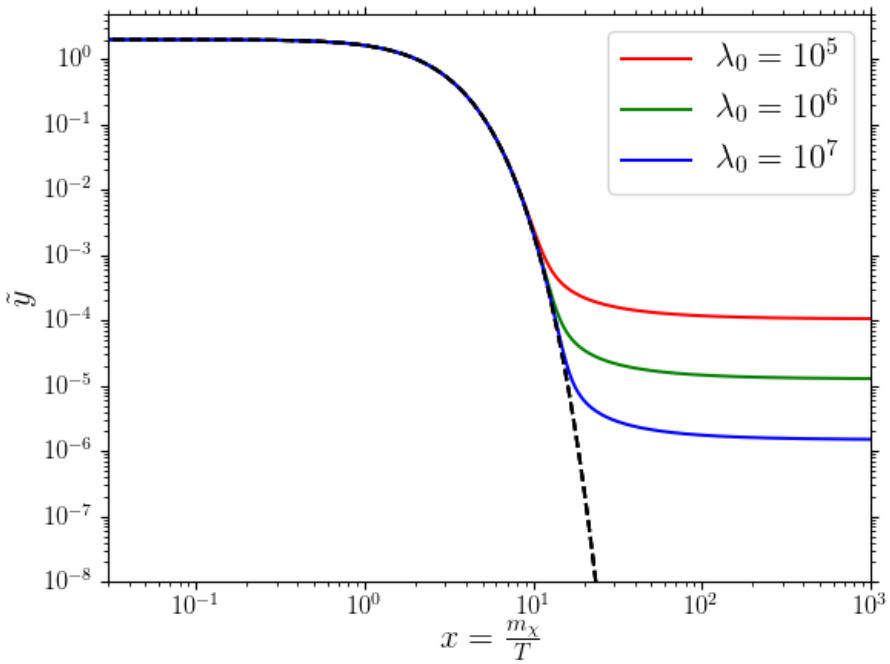

Figure 1.6: Sample plot of the rescaled comoving number $\tilde{y}$ as a function of $x \equiv m_\chi/T$, for different values of the s-wave thermal cross section. Here, λ_0 represents the s-wave thermal cross section, up to some constant factor; see the text for discussion. The dashed curve represents the equilibrium comoving number. Our goal here is to just show the general features of the solution of the Boltzmann equation.

approximations and physical insights. Note first that, at early times, WIMPs are in chemical equilibrium with the bath particles, *i.e.* the number-changing processes in the forward direction proceeds in the same rate as the reverse process. As the Universe cools down, departure from

chemical equilibrium will occur at some epoch, which is determined by the condition

$$\frac{\Gamma}{H} = \frac{n_\chi \langle \sigma v \rangle (T)_{\chi\chi \to SMSM}}{H} \sim 1; \tag{1.62}$$

where

$$\Gamma = n_\chi \langle \sigma v \rangle (T)_{\chi\chi \to SMSM}, \tag{1.63}$$

is the annihilation rate of WIMPs to SM bath particles. At the so-called decoupling temperature T_{dec}, $\Gamma/H = 1$. Noting that the equilibrium number density of χ in the nonrelativistic regime is

$$\begin{aligned} n_{\chi,eq}(T) &\approx \frac{g_\chi m_\chi^2 T}{2\pi^2} K_2\left(\frac{m_\chi}{T}\right) & (1.64)\\ &\approx g_\chi \left(\frac{m_\chi T}{2\pi}\right)^{3/2} e^{-m_\chi/T}, \quad T \ll m_\chi, & (1.65) \end{aligned}$$

and also

$$H \approx 1.66 g_*(T)^{1/2} \frac{T^2}{M_{Pl}}, \tag{1.66}$$

where $g_*(T)$ is the effective number of relativistic degrees of freedom at temperature T, the decoupling temperature satisfies

$$\frac{m_\chi}{T_{dec}} \approx \ln\left(\langle \sigma v \rangle m_\chi M_{Pl}\right) + \frac{1}{2}\ln\left(\frac{m_\chi}{T}\right), \tag{1.67}$$

where we have neglected a term that is the logarithm of an order 1 quantity.

When the rate of annihilation processes goes way below the rate of Hubble expansion, number-changing processes are said to be inefficient, and thus the comoving number of WIMPs freezes out to a constant value; this can be seen more formally when we write down the evolution equation for $y \equiv n/s$, which can be written as

$$\frac{d(\ln y)}{d(\ln a)} = -\frac{\Gamma}{H}\left[1 - \frac{y_{eq}^2(T)}{y^2}\right]. \tag{1.68}$$

When $\Gamma \ll H$, the right hand side tends to zero, so y indeed becomes constant. To estimate what this constant y is, we assume that the transition from chemical decoupling to thermal freeze out proceeds instantaneously, so that

$$y_{f.o.} \sim \left(\frac{m_\chi}{T}\right)^{3/2} e^{-m_\chi/T} \sim \frac{(m_\chi/T_{dec})}{\langle \sigma v \rangle m_\chi M_{Pl}}. \tag{1.69}$$

The relic density of WIMP DM is then

$$\begin{aligned} \Omega_\chi h^2 &\approx \frac{m_\chi y_{f.o.} s_0}{\rho_c h^{-2}} & (1.70)\\ &\approx 0.1 \left(\frac{2.5 \times 10^{-9}\,\mathrm{GeV}^{-2}}{\langle \sigma v \rangle}\right)\left[\frac{(m_\chi/T_{dec})}{10}\right]. & (1.71) \end{aligned}$$

In other words, in order to get a DM relic density that is close to (1.31), the thermal cross section must be $2.5 \times 10^{-9}\,\mathrm{GeV}^{-2}$; equivalently this thermal cross section is expressed in various units: $1\,\mathrm{pb} = 3 \times 10^{-26}\,\mathrm{cm}^3/\mathrm{s}$. Note that the relic density does not explicitly depend on the mass of the WIMP, m_χ, although it enters in T_{dec} as a weak logarithmic dependence. It can also be seen from (1.71) that a lower cross section enhances the relic density, hence the statement, "the weakest wins;" this estimate for the relic density is also consistent with the trend we see in Fig.(1.6). Also one may notice that the thermal cross section can be written in a suggestive form:

$$\langle \sigma v \rangle \approx \left(2.5 \times 10^{-9}\,\mathrm{GeV}^{-2}\right) \left(\frac{\alpha_\chi}{0.5 \times 10^{-2}}\right)^2 \left(\frac{100\,\mathrm{GeV}}{m}\right)^2 . \tag{1.72}$$

That is, if we assume that the WIMP annihilation process is mediated by some particle with mass at the weak scale, with weak scale couplings, we reproduce the correct relic density for DM: this is the celebrated WIMP miracle, although rescaling both the coupling α_χ and the mediator mass m by the same amount will work out just fine, at least from the perspective of a cosmologist who is concerned mainly on recovering the correct relic density of DM. However, the idea of the WIMP can have different meanings for different people, depending on what formal or phenomenological issue they want to address; see the discussion in [108].

One can play around with (1.72) and change the couplings and masses. However, if one wishes to go to extremely small couplings, the thermal WIMP production mechanism would require very small masses, which falls on the regime of hot DM relics. There is an alternative mechanism that can lead to relic densities at the same level as the one coming from WIMP freeze out, which can be achieved with very low couplings: FIMP freeze in [109]. Here, FIMP stands for feebly interacting massive particle, which is an appropriate name for such a relic since its production only requires very small annihilation cross sections to bath particles. The governing equation for the evolution of the number density is still (1.55), but the qualitative behavior of the solution is entirely different from thermal freeze out. Whereas the initial condition for WIMP is $y = y_{eq}$, FIMPs start out with negligible amounts relative to bath particles. At high temperatures, bath particles have enough energy to annihilate into FIMPs, thereby increasing the population of FIMPs. From a formal perspective, the last term in the right hand side of (1.55) dominates the first term, and this last term is positive, thereby increasing n_χ. Once the bath temperature goes below the FIMP mass, similar to the case of WIMPs, the process of populating FIMPs becomes inefficient, and the comoving number of FIMPs freezes in to a certain value. This qualitative picture of the evolution of the FIMP abundance can be seen in Fig.(1.7).

The relic density of FIMPs can be easily estimated by simply integrating the rate of FIMP production up to the time when the temperature falls below the FIMP mass; more precisely, the FIMP comoving number at freeze in is roughly

$$\begin{aligned} y_{f.i.} &\approx \int_0^{t_{f.i.}} dt\; n_{\chi,eq} \langle \sigma v \rangle & (1.73)\\ &\approx \frac{s(m_\chi)}{H(m_\chi)} \langle \sigma v \rangle_0 & (1.74)\\ &\approx m_\chi M_{Pl} \langle \sigma v \rangle_0 ; & (1.75) \end{aligned}$$

here we assumed that the thermal cross section at the relevant time period scales as T^{-2}, and

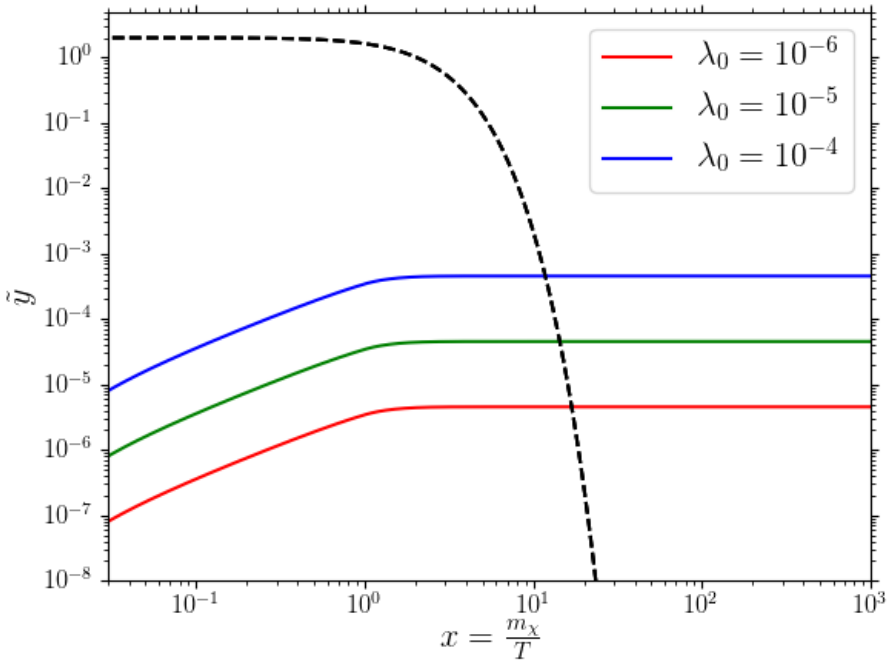

Figure 1.7: Same as in Fig.(1.6), but for the case of FIMPs.

we dropped order 1 factors like y_{eq}. We thus have

$$\left(\Omega_\chi h^2\right)_{f.i.} \approx 0.1 \left(\frac{m_\chi}{100\,\mathrm{GeV}}\right)^2 \left(\frac{\langle\sigma v\rangle_0}{3\times 10^{-33}\,\mathrm{GeV}^{-2}}\right). \tag{1.76}$$

Multicomponent dark sectors

We close this brief survey of DM models by considering the possibility that there can be more than one DM candidate. The most obvious motivation to consider this scenario ultimately comes from the fact that DM comprises the bulk component of matter, and baryons only comprise 1/6 of the matter density at the present epoch: if the baryonic component is well-described by the SM, which is based on a nontrivial gauge theory and has a rich and intricate structure especially in the lepton and quark sectors, one could entertain the possibility that the more abundant DM component may as well be described by a framework that is as complex, or even richer than the SM. The case for multicomponent dark sectors, *i.e.* models in which there can be more than one stable species, has been put forward from both theoretical and phenomenological fronts. On the one hand, the presence of extra gauge symmetries naturally arise in string theory and grand unification scenarios, and these would lead to additional discrete symmetries that could potentially give rise to multiple stable species; at the same time, multicomponent dark sectors have been considered to be viable in explaining the possible anomalies/excesses in direct and indirect DM searches [110–112]. In Ch. (2) of this manuscript, we shall feature an investigation of the cosmological impact of a framework, in which the SM is extended by introducing a dark sector containing stable species — the dark fermions — that are charged under a dark Abelian gauge group. This dark gauge group is not spontaneously broken, and the mediator, the dark

photon, remains massless. We have found promising prospects in trying to detect the dominant dark fermion species in experiments that look for signals of nuclear recoils.

1.2.2 Probes of DM

The hunt for individual DM particles has been one of the subjects of extensive research efforts in particle physics, for the past three decades. In this subsection we shall briefly look into the traditional methods of searching for DM — namely direct, indirect, and collider searches — as well as some of the other methods of inferring the properties of DM beyond the trio that we have just mentioned.

Traditional probes

The vanilla methods of searching for DM particles can be neatly summarized in a single picture, shown in Fig.(1.8). The arrows indicate the time direction, starting from the initial state particles to the final states, and each arrow corresponds to a particular mode of DM search. In this manuscript, we shall mainly focus on direct detection, which involves the scattering of DM states on SM states, but we shall briefly touch upon indirect detection and collider searches for completeness.

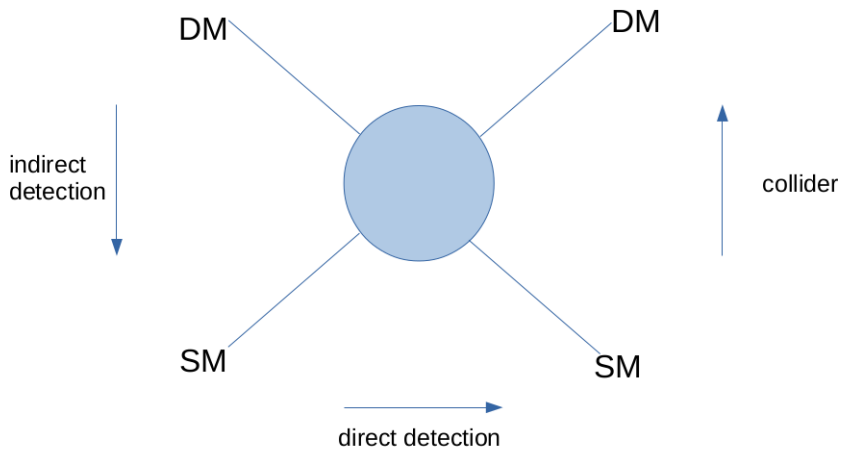

Figure 1.8: This schematic diagram summarizes the main experimental methods of detecting DM particles. See the discussion in the text for details.

- **Direct detection**
  Direct detection searches operate under the assumption that DM particles within our Galactic halo, stream through the Solar system in various directions. If DM has some hypothetical interactions with the SM, then it could be possible that nuclei can undergo elastic scattering with DM. The resulting nuclear recoil from such processes may be interpreted as conclusive detection of DM, upon proper accounting of other backgrounds and competing effects. Such proposals to detect DM in this manner have been laid down in, *e.g.* [113, 114], based on the detector concept by Drukier and Stodolsky for probing the

coupling of neutrinos with the Z boson [115]. Another possible detector design for DM direct detection involves: (i) a pure sample of a noble gas, that is kept at cryogenic temperatures in order to reduce the thermal noise in the detector, (ii) photomultiplier tubes that are capable of detecting scintillation signals, and (iii) a potential difference that allows for electrons, that could have come from ionization events, to drift inside the chamber and get detected.

In order to assess the practicability of searching DM in this manner, we must determine the expected rate at which these recoil events occur. At the very basic level, the recoil event rate per nuclei is just $R \sim n_\chi \langle \sigma v \rangle_{\chi T}$, where n_χ is the local number density of DM, and $\langle \sigma v \rangle_{\chi T}$ is the velocity-averaged cross section of DM-nucleus scattering; the velocity averaging takes into account the fact that DM particles from the Galactic halo can enter the detector in various directions and speeds. From this very simple expression, one can immediately identify the necessary ingredients to obtain the predicted rate of recoil events: (i) the local DM mass density, from which one can obtain the local DM number density upon dividing by the DM mass; (ii) the velocity distribution function of DM in the Galactic halo; (iii) the particle physics model of elementary DM-SM interactions that we would like to probe; and (iv) nuclear/atomic form factors that account for the internal structure of the nucleus/atom. For the case of nuclear recoils, the recoil spectrum, which gives the rate of recoil events per nuclei per recoil energy, is given by

$$\frac{dR}{dE_R} = \frac{\rho_\chi}{m_\chi} \int d^3\vec{v}\ |\vec{v}|\ f_E(\vec{v})\ \frac{d\sigma_{\chi T}}{dE_R}, \tag{1.77}$$

where $\vec{v}$ is the DM velocity relative to the Earth-based detector, $f_E(\vec{v})$ is the DM velocity distribution function boosted in the frame of the Earth, and $d\sigma_{\chi T}/dE_R$ is the differential DM-nucleus scattering cross section with respect to the recoil energy E_R.

Let us discuss the various uncertainties that enter in the recoil spectrum. Firstly, the particular model for DM interactions with ordinary matter could be specified as a generic interaction between DM and nuclei, or between DM and elementary SM particles. For the latter case, the conversion from DM-SM interactions to DM-nucleus interactions requires the knowledge of nuclear form factors; uncertainties in these form factors mainly come from QCD. In most discussions in the literature, DM-nucleus interactions are typically classified as spin-independent (SI) or spin-dependent (SD), mainly for simplicity. In general, however, one can start from an effective field theory (EFT) perspective and write down all the possible DM-nucleon interactions that are consistent with Galilean invariance (since we are considering nonrelativistic cold DM). This framework goes beyond the usual SI/SD interactions, in which SI/SD interactions are subsets of a wider class of possible interactions, and it captures certain features that may not be present in SI/SD interactions. A full treatment of the EFT of DM-nucleon interactions will be discussed in Ch. (2), and we shall discuss examples that call for an EFT treatment of calculating DM nuclear recoil spectra.

On the other hand, astrophysical uncertainties about the phase space distribution of DM in the Galactic halo are encoded both in the local DM density, ρ_χ, and the local velocity distribution function, $f_E(v)$. In determining the local DM density, various methods can

be employed, including the construction of mass models for the Galaxy and trying to fit the predicted circular velocities with the measured rotation curves for the Galaxy [4, 5, 116, 117]. As for the local velocity distribution function, the ansatz for an isothermal, spherical halo is used; this gives rise to a Maxwell-Boltzmann distribution. However, a slightly more realistic halo model involves truncating the distribution function beyond a certain velocity. Such a velocity distribution function, called the standard halo model (SHM), takes the form

$$f(\vec{V}) = N^{-1} \exp\left(-\frac{V^2}{2\sigma^2}\right) \Theta\left(v_{esc} - V\right), \tag{1.78}$$

where $\vec{V}$ is the DM velocity relative to the Galactic center, v_{esc} is the local escape speed, and N is a normalization factor given by

$$N = \left(2\pi\sigma^2\right)^{3/2} \left[\mathrm{erf}\left(\frac{v_{esc}}{\sigma\sqrt{2}}\right) - \sqrt{\frac{2}{\pi}}\frac{v_{esc}}{\sigma} \exp\left(-\frac{v_{esc}^2}{2\sigma^2}\right)\right]. \tag{1.79}$$

Note that $\vec{V}$ and $\vec{v}$ are related by a simple Galilean transformation

$$\vec{V} = \vec{v} + \vec{v}_E, \tag{1.80}$$

where $\vec{v}_E$ is the Earth's velocity relative to the Galactic center. The impact of astrophysical uncertainties on the predicted event rates has been discussed in the literature; see, *e.g.*, the early work of Wasserman [114], where he proposed the introduction of a velocity cutoff in the velocity distribution function. However, he argued that such a modification may have marginal effect on the resulting spectrum, at least for intermediate DM masses. On the other hand, it might be interesting to probe the impact of halo modelling on DM-electron scattering, which is actually sensitive to lower DM masses that can be probed by DM-nucleon scattering: this will be the subject of Ch. (4) of this manuscript.

As of present, there is not yet a conclusive evidence for the direct detection of Galactic DM particles, and currently there is a worldwide experimental effort in the direct detection of DM, employing a wide variety of clever experimental techniques to carry out this endeavor; for a recent account of the current status of direct detection experiments, see [118]. However, the DAMA/LIBRA collaboration reported the detection of an annual modulation signal at 7.5-σ level, using data that they collected in a span of a decade [119]; the inclusion of DAMA/LIBRA phase 2 data increased the significance discovery of annual modulation to 9.5σ [120]. An annual modulation of the DM signal is searched in connection to the fact that the Earth revolves around the Sun, and hence $\vec{v}_E$ contains not only the Sun's velocity with respect to the Galactic center, but also a quasi-sinusoidal time-dependent velocity component. On the other hand, the ANAIS experiment, a detector utilizing same material as the DAMA/LIBRA detector, recently reported a lack of annual modulation signal using 3 years worth of data [121]. Furthermore, all other direct detection experiments yield null result for DM direct detection.

- **Indirect detection**
  Turning Fig. (1.8) counterclockwise refers to indirect searches of DM. The basic hypothesis is that DM can undergo pair annihilations into SM species, which may lead to observed excesses in cosmic ray fluxes coming from the Galaxy, or other extragalatic sources.

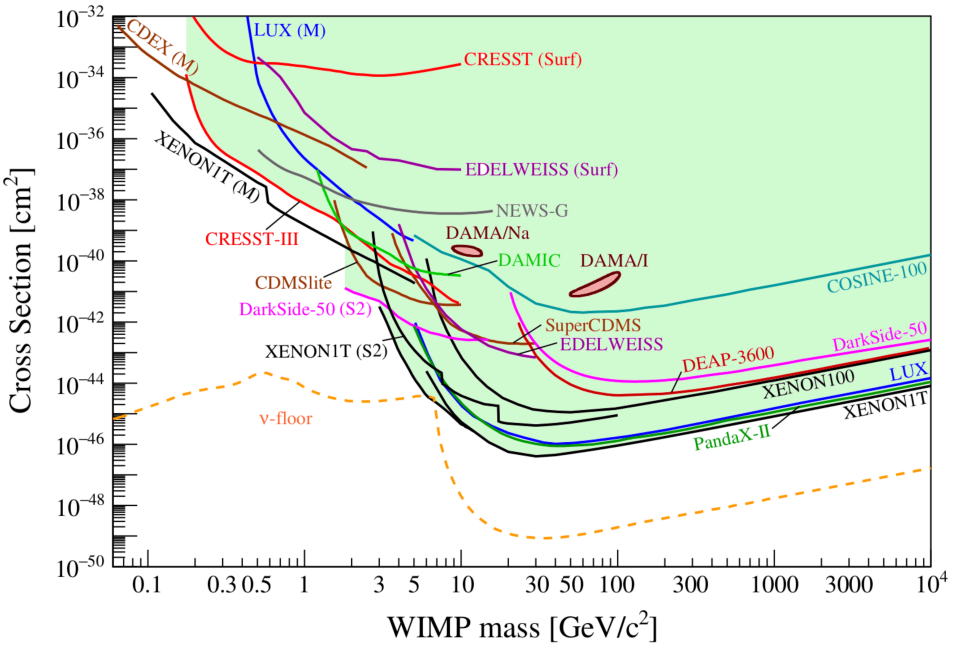

Figure 1.9: (Taken from [118]) The plot shows a summary of current limits, obtained from various direct detection experiments, for spin-independent WIMP-nucleus scattering, assuming the following astrophysical parameters: local DM density $= 0.3\,\mathrm{GeV/cm^3}$, $v_0 \equiv \sigma\sqrt{2} = 200\,\mathrm{km/s}$, and local escape velocity $= 544\,\mathrm{km/s}$.

The primary annihilation products can be, *e.g.* $b\bar{b}, W^+W^-, \mu^+\mu^-$, etc., and, in turn produce secondary proton, antiproton, gamma-ray, and/or neutrino fluxes, through decays or hadronization; these signals may come from different locations in the Galaxy, or they can be extragalactic in origin. Gamma-ray and neutrino fluxes are ideal signals for the indirect detection of DM, since are largely unaffected when they travel from the source to our telescopes, and we can also easily trace back the signal to its original source. On the other hand, for the case of charged cosmic rays (CR), their diffusive motion in the Galaxy is affected by the Galactic magnetic field; thus the predicted flux of charged CR requires a diffusion transport model to track its propagation.

For the case of gamma-ray fluxes as a means to search for DM, one must make a prediction of the gamma-ray flux spectrum, which requires the following ingredients: DM annihilation cross section to SM species, the energy spectrum of SM species, and the halo density profile. For a given direction $\hat{n}$ in the sky, and assuming that DM annihilates to some channel f which then annihilates to produce gamma rays, then the flux spectrum in photon energy E_γ measured by a telescope with opening angle $\Delta\psi$ is given by [122]

$$\frac{d\Phi_\gamma}{dE_\gamma}(E_\gamma, \hat{n}) = \frac{1}{8\pi} \int_{\Delta\psi} \frac{d\Omega}{\Delta\psi} \int_{\mathrm{l.o.s}} dl(\hat{n})\; \rho_\chi^2(\vec{r}) \left(\frac{\langle\sigma v\rangle_{\chi\chi\to f}}{m_\chi^2} \sum_f B_f \frac{dN_\gamma^f}{dE_\gamma} \right), \tag{1.81}$$

where the integration over l is along the line of sight of the telescope. Here, the terms that depend on the particle physics model are: B_f is the branching fraction to channel f,

the velocity-weighted annihilation cross section $\langle \sigma v \rangle$ to channel f, and N_γ^f is the number of photons per annihilation. Meanwhile, similar to the case of direct detection of DM, astrophysical uncertainties come from the DM velocity distribution function as well as the DM halo density profile. In particular, one can sift out the astrophysics-dependent part of the flux spectrum, called the J-factor, defined as

$$J \equiv \int_{\Delta\psi} \int_{\text{l.o.s}} dl(\hat{n})\ \rho_\chi^2(\vec{r}). \tag{1.82}$$

Perhaps the most significant systematic uncertainty in this astrophysical J-factor is the halo density profile, where its functional form is taken from some known profile, *e.g.* NFW halo profile, which is motivated by results from pure DM N-body simulations. But regardless of the choice for the density profile, one can see from (1.82) that, for a halo with size r and source distance d,

$$J = \langle \rho_\chi^2 \rangle d\Delta\Omega = \langle \rho_\chi^2 \rangle\ \frac{4\pi r^3}{3d^2}; \tag{1.83}$$

intuitively, this simply tells us that our chances of detecting signals of DM annihilation can increase if at least one of the following criteria is satisfied: the source is nearby, there is a high density of DM, or the halo distribution is spread out over a large volume [123]. Based on this argument, one can say that the perfect systems for searching DM indirect detection signals are dwarf spheroidal satellites (dSphs): these are pristine environments of low luminosity and are mostly made up of DM. One possible avenue of investigation would be to use the potential excess gamma-ray signals that can be traced back to dSphs, under the assumption that the origin of these excess signals comes from DM annihilations. As of present, there are hints of signals of DM annihilations, such as the observed Galactic center (GC) excess measured by Fermi-LAT [124], the CR positron excess measured by HEAT [125], PAMELA [126], Fermi [127], and AMS-02 [128], and the CR anti-helium excess reported by AMS-02 [129]. For the observed positron excess, it was found that the signal was most likely produced by pulsars, instead of DM annihilations [130]. On the other hand, there are interpretations for the measured GC excess, other than the DM annihilation scenario; an account of the current status of observations of the GC excess, its possible interpretations, and future efforts to discriminate among these possibilities is discussed in [131].

- **Collider searches**

  Capping off the general discussion of the trio of traditional methods of DM searches, we turn Fig. (1.8) clockwise, and consider the possibility of producing DM from smashing together SM particles in colliders. In general, the discovery of new particles in colliders, including DM, usually involve searching for events of missing energy/transverse momentum signals; in a sense, the hunt for new particles is reminiscent of how the idea of the neutrino was brought up to explain the continuous energy spectrum of electrons in beta decay. We also have to keep in mind that colliders have been valuable tools for us to discover new particles, and build the SM that we know today, and thus provides us with an interesting avenue for potentially discovering DM. Of course, the most obvious limitation

of collider searches for DM, and for any new particles, is the energy reach of the detector. At present, the Large Hadron Collider (LHC) can reach energies of 13 TeV; in principle, one of the primary motivations for constructing hadron colliders was mostly to search for SUSY particles, and SUSY offers a viable DM candidate called the neutralino, which are the physical states arising from the diagonalization of the gaugino mass matrix; details regarding this can be found, *e.g.* Baer and Tata [132].

There are several processes that can be considered in looking for SUSY particles in colliders. One process is the cascade decay of gluinos ($\tilde{g}$) to neutralinos (χ), *i.e.*

$$\tilde{g} \to g\tilde{q} \to g\tilde{q}\chi, \tag{1.84}$$

where g is a gluon, and $\tilde{q}$ is a squark. Another process involves the presence of mono-X signals, where X can be a photon, a gluon jet, W/Z boson, or even the Higgs, such that

$$q\bar{q} \to \chi\chi + X. \tag{1.85}$$

While both processes can be motivated by the interactions present in the MSSM, such processes may also arise from other scenarios involving BSM mediators other than the Higgs or Z bosons; in order to cover a wide variety of models, it is natural to consider an effective field theory (EFT) of such interactions. A review of collider searches for DM can, for instance, be found in [133], while a survey of collider constraints on DM are discussed in [134].

Additional probes

In light of advancements in instrumentation and computational power, we briefly enumerate some of the techniques that can be employed to directly, or indirectly, probe the nature of DM.

We have already mentioned in Sec.(1.1.3) the role of early N-body simulations in establishing that the HDM scenario of structure formation is in conflict with the observed clustering of galaxies in surveys of large-scale structure (LSS). With the increase in resolution of N-body simulations, it has become possible to determine the structure of halos. Navarro, Frenk, and White demonstrated that in the CDM framework, the equilibrium density profile of halos can be fitted by the following spherically symmetric density profile [135]:

$$\rho(r) = \frac{\rho_0}{(r/r_s)(1 + r/r_s)^2}, \tag{1.86}$$

where r is the distance from the center of the halo, r_s is a scale radius, and ρ_0 is a normalization factor. However, measurements of the rotation curves of low surface brightness galaxies, *e.g.* [136, 137] suggest that the inferred structure of halos in these galaxies cannot be the cuspy profile as in (1.86); instead, there is a preference for cored profiles at the center, as in the Burkert profile [138]:

$$\rho(r) = \frac{\rho_0 r_0^3}{(r + r_0)(r^2 + r_0^2)}. \tag{1.87}$$

This tension between the results of CDM-only N-body simulations and the inferred density profiles of halos from observations is one of the small-scale issues of the CDM paradigm, known

as the "core-cusp" problem. One proposed solution to alleviate this tension is to incorporate the effects of baryonic feedback in N-body simulations to yield cored halo density profiles. As shown in [139], the inclusion of baryons in simulations accounts for star formation, which eventually explode into supernovae. If these supernovae explosions are energetic enough, these can form underdense regions of DM, thereby creating cored halos. Alternatively, Spergel and Steinhardt proposed going beyond the CDM paradigm and consider the case of self-interacting DM (SIDM) [140]; a review of theories involving SIDM and their astrophysical implications can be found in, *e.g.* [141]. For CDM halos, the peak of the velocity dispersion lies at the scale radius; meanwhile, the presence of DM self-interactions facilitates heat transport within the halo, so that the cold inner region of the halo becomes hotter, making it expand.

The wealth of 6-dimensional astrometric data, *i.e.* the positions and velocities of tracers in our own Galaxy, coming from the Gaia satellite [142], will allow us to infer the underlying gravitational potential due to the mass components in our Galaxy, especialy the shape of the DM halo, and opens new possibilities in probing the nature of DM. We emphasize that, at the present level of technology, a direct mapping of the gravitational potential of the Galaxy is a challenge, if one tries to carry out this task by measuring the accelerations of tracers, which are too small to be measured (but see [143] where they propose to robustly determine the Galactic potential and the local DM density by including measurements of angular acceleration in the astrometric data). On the other hand, the position and velocity data of tracers can be used to infer the mass distribution in the Galaxy, under the assumption that the Galaxy has relaxed to dynamical equilibrium. A caveat in this approach is that the second data release from Gaia has provided evidence for the existence of unrelaxed substructures in the Galaxy, particularly the so-called Gaia sausage [144–146]; for a review of the evolution of the Galaxy and an account of the streams and substructures within it, see [147].

Finally, BSM physics models that are invoked to explain anomalies in the SM may also find their way to connect with the DM problem. Recently, the LHCb collaboration reported a signal of violation of lepton flavor universality in flavor changing neutral currents [148]. Here they measured the ratio of the branching ratios R_K of B^+ decays via

$$B^+(u\bar{b}) \to K^+(u\bar{s}) + e^+e^-, \quad B^+(u\bar{b}) \to K^+(u\bar{s}) + \mu^+\mu^-, \tag{1.88}$$

i.e., $\bar{b} \to \bar{s}$ transition, and found that $R_K = 0.846^{+0.044}_{-0.041}$: a 3.1-$\sigma$ deviation from the SM prediction. This was an indication that the electron and muon might have different interaction strengths in neutral current interactions. On the other hand, for the case of charged current processes, the BESIII detector measured the branching ration of hyperon (Λ) decay via

$$\Lambda(uds) \to p(uud) + \mu^-\bar{\nu}_\mu. \tag{1.89}$$

The BESIII collaboration reported that the branching ratio of this decay process to $\mu - \bar{\nu}_\mu$ relative to $e - \bar{\nu}_e$ is 0.178 ± 0.0028, which is consistent with the SM prediction with lepton flavor universality [149]. One possibility to account for the LHCb measurement of lepton flavor violation (LFV) involves invoking the presence of a leptoquark (LQ), which mediates interactions between quarks and leptons, but with different interaction strengths with leptons. The idea of LQs is not new, and such particles naturally arise in, *e.g.* grand unification theories (GUT) such as the Pati-Salam model [150] and SU(5) GUT where quarks and leptons belong to a field in the

fundamental representation of SU(5) [151, 152]. Meanwhile, the connection of LQs in the DM has been investigated in, *e.g.* [153–156], where LQs may serve as portals to DM.

Another recently measured anomaly in the SM involves the magnetic moment of the muon, dubbed the $g-2$ anomaly. The measurement of the muon magnetic moment was carried out in the Fermi National Laboratory (FNAL), where muons, subjected to an external magnetic field of known strength, are fed in a storage ring; the determination of the magnetic moment requires at least the measurement of the cyclotron frequency and the precession rate [157]. On the other hand, the contributions of the SM to the quantum corrections in $g-2$ come from: QED corrections to tenth order, QCD corrections such as hadronic vacuum polarizations (HVP), and electroweak (EW) processes. Defining $a_\mu \equiv (g-2)/2$ that quantifies the deviation from the $g=2$ prediction by the Dirac equation, we respectively have the FNAL measurement and the SM predictions for a_μ:

$$a_\mu(\text{FNAL}) = (116592040 \pm 54) \times 10^{-11}, \quad a_\mu(\text{SM}) = (116591810 \pm 43) \times 10^{-11}, \tag{1.90}$$

which gives $\Delta a_\mu = (23.0 \pm 6.9) \times 10^{-10}$ for the deviation of the FNAL measurement from the SM prediction. Several explanations to the $g-2$ anomaly have been proposed in the literature, even before the announcement of the FNAL measurement in 2021, *e.g.* [158–160]; a recent account of the impact of the $g-2$ anomaly in BSM physics, including its implications on DM and LHC searches can be found in [161]. In Ch.(3), we shall consider a minimal setup, inspired by the bino-slepton-lepton interactions in the MSSM, to account for the $g-2$ anomaly; this scheme involves a bino, which we take to be the DM, and we investigated, *e.g.* the impact of accounting for $g-2$ on the relic density of bino DM, and the implications of such a scheme on direct detection searches. One must keep in mind, however, that alternatives to solve the $g-2$ tension might not involve new physics. Borsanyi et. al. [162] noted that the main source of uncertainty in the SM prediction for a_μ comes from HVP; while the FNAL collaboration used dispersion relation techniques combined with low-energy data from cross sections of electron-positron annihilation to hadrons, they instead considered an ab-initio computation of the leading-order HVP, and found that the FNAL measurement matches the theoretical prediction.

1.3 Specific goals of the thesis

As we have just discussed, we have accumulated evidences that firmly established our confidence in the existence of DM in the Universe. We have also provided a survey of a selection of particle DM proposals, the ways in which we can shed light on the nature of DM, and the avenues in which the DM puzzle can be tied with observational and experimental anomalies. At this point, we would like to define the scope of the thesis by outlining the goals of the projects that we shall feature in this manuscript, and briefly discuss how these goals fit in to the entire edifice that is DM phenomenology:

- In Ch. (2), we propose a framework for a multicomponent dark sector, in which the stable species — dark fermions — are Dirac particles that are charged under a dark U(1) gauge interaction, such that this interaction is mediated by a massless dark photon. A scalar portal allows the dark fermions to communicate with SM fermions, through generic

Yukawa-like interactions. We use complementary limits, from precision physics to astrophysics, as guiding principles to pinpoint the mass hierarchy of states in the dark sector. We investigate the impact of such a dark sector model on the thermal history of the Universe, keeping in mind the peculiarity of this setup that the early Universe plasma consists of the visible and dark sector reservoirs. We explore direct detection prospects in constraining this framework, and the direct detection limits we obtain are competitive with those coming from complementary probes such as stellar cooling and precision physics.

- In Ch. (3), we study a minimal model to address the $g-2$ anomaly that was reported at FNAL, and we primarily investigate its impact on the DM puzzle. This model, inspired by the MSSM, consists of: a Majorana fermion, which acts as the DM candidate; at least a pair of scalars, where the "left" handed scalar is an SU(2) doublet, while the "right" handed scalar is a singlet; mixing between the "left" and "right" handed scalars in the scalar mass matrix; and gaugino-like interactions between the DM, scalars, and muons. We show that projected direct detection constraints on this framework, coming from planned DM direct detection experiments, might be able to constrain a part of the viable parameter space which both satisfy the $g-2$ anomaly and saturate the observed relic density of DM. We derive additional constraints on the framework, from theoretical considerations like vacuum stability and perturbative unitarity.

- In Ch. (4), we address one key astrophysical uncertainty that enters in calculating the recoil spectrum used in direct detection searches, namely the DM velocity distribution function. Prompted by the observed XENON1T excess signal in the low recoil energy region [163], we focus our attention on DM-electron interactions. The DM velocity distribution function is obtained by implementing inversion techniques, under the assumption that the overall potential of the Galaxy is axisymmetric and that it has relaxed to an equilibrium configuration. We determine the impact of halo modelling on the recoil spectrum, and direct detection constraints, both for elastic and inelastic DM-electron interactions. While we do not find significant deviations from the standard halo model, we argue that this simply is a consequence of fitting the Galactic potential with the local circular and escape velocities, and our method has the virtue of being self-consistent.

Chapter 2

Multicomponent dark sectors

2.1 Motivations and synopsis

The existence of a multicomponent *dark sector* has been extensively discussed in the literature (see [164, 165] for two recent reviews). Such framework generally includes many new states with no direct interactions with the Standard Model (SM) particles, but possibly interacting among themselves by means of new forces. Motivations for this construction have been put forward in a variety of different contexts, ranging, *e.g.*, from beyond SM physics in connection to collider data and flavor anomalies, to explaining the nature of the dark matter component of the Universe, and to addressing possible shortcomings in the SM of cosmology.

In particular, regarding the dark matter problem, any non-relativistic stable dark state can potentially contribute to the Universe's matter budget. Because of the secluded nature of the dark sector which prevents large couplings to ordinary matter, these states automatically satisfy observational properties for dark matter, mostly derived under the assumption that the only relevant interaction between dark and ordinary matter is gravity. On the other hand, given the complexity of the dark sector, the phenomenology of dark matter candidates in this context could be richer than simply looking at gravitational effects. For example, dark matter itself could be multicomponent or in composite forms; dark sector interactions may lead to macroscopic effects and, for instance, impact on the paradigm in the SM of cosmology that dark matter should be described as a collisionless fluid.

In this chapter we illustrate the interplay among different effects occurring when the dark sector contains several species. More explicitly, we will discuss the early Universe's thermal history in such a scenario and the generation of dark matter and other stable relics. One peculiarity is the fact that there are two reservoirs of states, ordinary and dark, and their temperatures are not necessarily the same. Therefore, a set of coupled Boltzmann equations, tracking at the same time the number density of the different species and the energy exchanges between the two sectors, needs to be considered.

To investigate explicitly this issue, we must first commit ourselves to a specific model of the dark sector (which we do in section 2.2 by considering a rather minimal setup). The choice of model provides an explicit spectrum of states within the dark sector, the interaction strengths among the dark states, and the strength of the portal interaction between the dark and SM states. These must be supplied in order to extract definite predictions. In particular, we shall

assume that the dark force is long range, that is mediated by an unbroken $U(1)$ gauge interaction. Regarding the particle content, besides the force carrier, a massless dark photon, we introduce a set of stable dark fermions charged under the $U(1)$. One of these may account for most of dark matter in the Universe since it is rather heavy, at the TeV scale or above, and passes upper limits from self-interaction effects [166–168]. The others are much lighter, have suppressed relic abundances, but concur in determining the ratio between dark and visible photon temperatures at late times; such ratio is constrained by cosmic microwave background (CMB) data, given that dark photons contribute as an extra radiation component to the Universe's dynamics. In this respect, the role of portal interactions between dark and visible sectors is also important: we consider scalar messengers mediating Yukawa-like interactions. The latter are also crucial for selecting the mechanism for dark matter generation and final relic densities. Such interplay is discussed in detail in section 2.3.

Direct detection, namely the attempt to measure nuclear recoils induced by dark matter scatterings, is one of the main tools to test a given dark matter scenario. In our framework, the direct-detection cross section is mostly driven, via loop induced magnetic dipole and charge radius interactions, by the massless mediators, SM and dark photons. While long-range interactions are present and boost the recoil spectrum at low recoil energies, the correlated contact terms are also contributing to the cross section and may be dominant (contrary to standard lore that contact interactions can be neglected in the presence of long-range effects). These aspects are illustrated in section 2.4, bridging also between astrophysical, cosmological, and high-energy observables and relative constraints, demonstrating once more the diversity of the phenomenological implications of introducing such a multicomponent dark sector.

2.2 A model of the dark sector

Several dark sector models have been studied in the literature and they are usually classified [165] according to the portal through which they interact with ordinary matter. We consider a model consisting of dark fermions that are, by definition, singlets under the SM gauge interactions. These dark fermions interact with the visible sector through a portal provided by scalar messengers which carry both SM and dark-sector charges. These scalars are phenomenologically akin to the sfermions of supersymmetric models.

In general, we can have as many dark fermions as there are in the SM; they can be classified conveniently according to whether they couple (via the corresponding messengers) to quarks (q_L, u_R, d_R) or leptons (l_L, e_R): we denote the former (hadron-like) Q and the latter (lepton-like) χ. The Yukawa-like interaction Lagrangian can be written as [169, 170]:

$$\mathcal{L} \supset -g_L \left(\phi_L^\dagger \bar{\chi}_R l_L + S_L^{U\dagger} \bar{Q}_R^U q_L + S_L^{D\dagger} \bar{Q}_R^D q_L\right) - g_R \left(\phi_R^\dagger \bar{\chi}_L e_R + S_R^{U\dagger} \bar{Q}_L^U u_R + S_R^{D\dagger} \bar{Q}_L^D d_R\right) + \text{h.c.}\,. \tag{2.1}$$

The L-type scalars are doublets under $\mathrm{SU}(2)_L$, while the R-type scalars are singlets under $\mathrm{SU}(2)_L$. The $S_{L,R}$ messengers carry color indices (unmarked in (2.1)), while the messengers $\phi_{L,R}$ are color singlets. The Yukawa coupling strengths are parameterized by $\alpha_{L,R} \equiv g_{L,R}^2/(4\pi)$; they can be different for different fermions and as many as the SM fermions.

In order to generate chirality-changing processes, we must have the mixing terms

$$\mathcal{L} \supset -\lambda_s S_0 \left(H^\dagger \phi_R^\dagger \phi_L + \tilde{H}^\dagger S_R^{U\dagger} S_L^U + H^\dagger S_R^{D\dagger} S_L^D \right) + \text{h.c.}\,, \tag{2.2}$$

where H is the SM Higgs boson, $\tilde{H} = i\sigma_2 H^\star$, and S_0 a scalar singlet of the dark sector. After both S_0 and H take a vacuum expectation value (VEV) (μ_S and v—the electroweak VEV—respectively), the Lagrangian in Eq. (2.2) gives rise to the mixing between right- and left-handed states.

Dark sector states interact by means of an unbroken $U(1)_D$ gauge symmetry; the corresponding massless gauge boson is the dark photon γ_D whose coupling strength we denote by $\alpha_D \equiv g_D^2/(4\pi)$. We assign different dark $U(1)_D$ charges to the various dark sector fermions to ensure, by charge conservation, their stability. There is no kinetic mixing between the ordinary and the dark photon [81, 171]. The latter is a distinctive feature of models in which the dark photon is, and remains, massless as opposed to those in which the gauge symmetry is broken and the dark photon is massive. While there is no tree-level coupling between dark fermions and SM photons, and between ordinary matter and dark photons, the mixing in Eq. (2.2) leads, through one-loop diagrams and therefore operators of dimension larger than four, to an effective coupling of ordinary matter to the dark photon as well as of the dark fermions to the ordinary photon.

When the dark sector scalar S_0 and the Higgs boson acquire VEVs, the scalar messengers must be rotated to identify the physical states. Considering first the lepton sector, while before the rotation all ϕ states have the same mass m_ϕ, after the rotation we find the mass eigenstates (labeled by $\pm$)

$$\phi_\pm \equiv \frac{1}{\sqrt{2}} \left(\phi_{Le} \pm \phi_R \right)\,, \tag{2.3}$$

with masses $m_{\phi_\pm} = m_\phi \sqrt{1 \pm \eta_s}$, where we defined the mixing parameter:

$$\eta_s \equiv \frac{\lambda_s \mu_S v}{m_\phi^2}\,. \tag{2.4}$$

We must have $\eta_s < 1$ in order for the ϕ_- state to be physical. In the new basis, the interaction terms in Eq. (2.1) in the lepton sector is given by

$$\mathcal{L}^{(lep)} \supset -g_L \phi_{L\nu}^\dagger \left(\bar{\chi}_R \nu_L \right) - \frac{g_L}{\sqrt{2}} \left(\phi_+^\dagger + \phi_-^\dagger \right) \left(\bar{\chi}_R e_L \right) - \frac{g_R}{\sqrt{2}} \left(\phi_+^\dagger - \phi_-^\dagger \right) \left(\bar{\chi}_L e_R \right) + \text{h.c.}\,. \tag{2.5}$$

The picture in the hadronic sector is perfectly specular; in the following we will indicate generically with m_S the mass for the eigenstates S_{Ld}^U and S_{Lu}^D before the rotation, and keep η_s as mixing parameter for the physical eigenstates:

$$S_\pm^U \equiv \frac{1}{\sqrt{2}} \left(S_{Lu}^U \pm S_R^U \right) \quad \text{and} \quad S_\pm^D \equiv \frac{1}{\sqrt{2}} \left(S_{Ld}^D \pm S_R^D \right)\,. \tag{2.6}$$

Looking at (2.5), we can see that for χ to be a stable dark-sector species, its mass must be at most $m_{\phi_-} + m_e$. Similarly, for a dark-sector species Q, the mass must be no heavier than

$m_{S_-} + m_q$, where m_q is the mass of the SM species corresponding to Q. This sets an upper bound for the mixing η_s:

$$\eta_s < 1 - \left(\frac{M_{\chi,Q}}{m_{\phi,S}}\right)^2 , \tag{2.7}$$

where $M_{\chi,Q}$ stands for the mass of the heaviest stable dark-sector species and $m_{\phi,S}$ for the mass parameter of the corresponding messenger. We assume that $M_{\chi,Q}$ is much heavier than any SM species. The upper bound in Eq. (2.7) also guarantees that the scalar messengers are heavier than the dark fermion into which they can thus decay.

This model can be considered as a template for many models of the dark sector with the scalar messenger as stand-in for more complicated portals. It is a simplified version of the model in [169], which might provide a natural solution to the SM flavor-hierarchy problem. It has been used to predict new decays for the Higgs boson [172–174], neutral Kaons [175] and the Z-boson [176] as well as invisible decays for the neutral K- and B-mesons [177].

Models of self-interacting dark matter charged under Abelian or non-Abelian gauge groups and interacting through the exchange of massless as well as massive particles have a long history [166–169, 178–196]. We have relied in particular on [166, 168, 183, 184]—the constraints of which we recover in our framework where dark matter is only a component among the many of the dark sector within the specific underlying model defined by Eqs. (2.1)–(2.2). Interacting dark matter can form bound states. The phenomenology of such atomic dark matter [186] has been discussed in the literature (see [167] and references therein). In this chapter, we shall only consider the case in which these bound states, if they exist, are mostly ionized.

2.2.1 Constraining the model

Several limits on the parameter space of the model are known from high-energy physics and tests in astrophysical and cosmological environments. We list below the most severe constraints and the relative implications for mass parameters and coupling constants, as a preliminary outline of the regions in parameter space which will be relevant in the analysis of dark matter candidates within this framework. These constraints will be discussed further in Section 2.4, when examining current limits and projected sensitivities from dark matter direct detection experiments.

Contrary to the case of a massive dark photon, constraints from flavor and precision physics, as well as radiative emission in astrophysical bodies, come from one-loop order corrections providing the coupling to SM fermions. Under the assumption of CP conservation in the dark sector, the limits quoted below are mostly derived from the effective magnetic moment of SM fermions with respect to the dark photon or the ordinary photon, induced by dark fermion - scalar messenger loops. Since a change in the chirality of the fermions is required, the limits are strongly dependent to the mixing η_s. Depending on the process under consideration, the experimental limits only constrain particular combinations of couplings and masses in the dark sector. At this level, it is then more useful to quote results for Yukawa couplings and dark-sector masses for specific flavors, rather than taking them to be universal as in Eq. (2.1).

- Precision physics: Magnetic dipole moments of leptons provide a deeper insight on the parameter space. From the experimental measurement of the electron magnetic dipole

moment [197], we find:

$$\frac{(m^e_{\phi^-})^2}{m^e_\chi}\frac{0.01}{\eta_s\sqrt{\alpha^e_L\alpha^e_R}} \gtrsim 2\times 10^3\,\text{TeV}, \tag{2.8}$$

where m^e_χ stands for the mass of corresponding dark fermion. A comparable limit can be found from the experimental measurement of the muon magnetic dipole moment [198]:

$$\frac{(m^\mu_{\phi^-})^2}{m^\mu_\chi}\frac{0.01}{\eta_s\sqrt{\alpha^\mu_L\alpha^\mu_R}} \gtrsim 4\times 10^2\,\text{TeV}. \tag{2.9}$$

Since the measurement of the tau magnetic dipole moment is experimentally challenging, the corresponding limit is much less relevant, at about the GeV level.

Except for tau-like dark sector species, these limits point to lepton-like scalar messengers at a heavy scale, say 10 TeV or above, and lepton-like dark fermions significantly lighter, say at 1 TeV or below - unless the couplings α_L or α_R gets suppressed, or the mixing parameter η_s is small.

- Collider physics: Direct searches for charged scalar particles at the LHC [199] set a limit [177]

$$m^i_S \gtrsim 940\ \text{GeV}\,, \tag{2.10}$$

for the messenger mass related to the dark fermions Q^U and Q^D, while [200] have set constraints on the mass of sleptons, which give the following lower bound on the mass of lepton-like scalar messengers:

$$m^e_\phi \gtrsim 290\,\text{GeV}. \tag{2.11}$$

The limit increases to 1.5 TeV if more families are included. No limits exist for the masses of the dark fermions from events in which they are produced because they are SM singlets and do not interact directly with the detector.

- Astrophysics probes: Dark sector species can change the energy transport in astrophysical environments. Constraints for models with a massless dark photon from astrophysics have been discussed in [201–203]. The most stringent limit comes from stellar cooling in globular clusters by dark-photon Bremsstrahlung emission of electrons scattering on ^{4}He nuclei; for a standard choice of environmental parameters, and an upper value of 10 erg g^{-1} s^{-1} on the extra cooling rate by exotic processes [204], we find:

$$\frac{(m^e_{\phi^-})^2}{m^e_\chi}\frac{1}{\eta_s}\frac{0.1}{\sqrt{\alpha_D}}\frac{0.01}{\sqrt{\alpha^e_L\alpha^e_R}} \gtrsim 3\times 10^3\,\text{TeV}. \tag{2.12}$$

This limit applies specifically to the Yukawa coupling to electrons and the corresponding messenger state, and affects regions in parameter space analogous to the limit in Eq. (2.8). When considering, instead, extra cooling effects in supernovae, the most relevant process is the dark photon emission in nucleon-nucleon Bremsstrahlung. From the neutrino signal of supernova 1987A one can deduce:

$$\frac{(m^i_S)^2}{m_{Q^i}}\frac{0.001}{\eta_s\sqrt{\alpha_D\alpha^i_L\alpha^i_R}} \gtrsim 2.4\times 10^2\,\text{TeV}\,. \tag{2.13}$$

The above limit applies to the Yukawa couplings of u and d quarks and the corresponding messenger states. This sets an impact on the parameter space analogous to the leptonic sector, except that, for quark-like dark fermions, we will also explore the possibility of larger mass splittings with respect to the messenger states, with m_Q even at the GeV scale.

- Self-interactions for dark matter particles: As already anticipated, our scenario gets severely constrained for light dark matter candidates because of the long-range self-interactions induced by the $U(1)_D$ gauge symmetry. The most severe observational limits come from the impact on the dark matter density distribution in collapsed dark matter structures, rather than effects in the early Universe or the early stages of structure formation [166, 167, 184]. Bounds have been derived from the dynamics in merging clusters, such as the Bullet Cluster [205], the tidal disruption of dwarf satellites along their orbits in the host halo, and kinetic energy exchanges among dark matter particles in virialized halos. Among these limits, the latter turns out to be the most constraining: energy exchanges through dark matter self-interactions tend to isotropize dark matter velocity distributions, while there are galaxies whose gravitational potentials show a triaxial structure with significant velocity anisotropy. A limit has been derived by estimating an isotropization timescale (via hard scattering and cumulative effects of many interactions, with Debye screening taken into account) and comparing that timescale to the estimated age of the object [184]: a refinement of this limit involves tracking the evolution of the velocity anisotropy due to the energy transfer [168]. The ellipticity profile inferred for the galaxy NGC720, according to Ref [168] (see Fig. 4) sets a limit of about:

$$m_\chi \left(\frac{0.01}{\alpha_D}\right)^{2/3} \gtrsim 300\,\mathrm{GeV} \tag{2.14}$$

where m_χ here stands for the dark matter mass — anticipating that we will focus on a lepton-like dark fermion as dark matter candidate — and the α_D scaling quoted this equation is approximate and comes from the leading m_χ over α_D scaling in the expression for the isotropization timescale. Note that the limit quoted here is subject to a number of uncertainties and assumptions; it is less stringent than earlier results, such as the original bound quoted from [166], as well about a factor of 3.5 weaker than [184] (see also, *e.g.*, [206, 207]). On the other hand, results on galaxies from N-body simulations in self-interacting dark matter cosmologies [208], taking into account predicted ellipticities and dark matter densities in the central regions, seem to go in the direction of milder constraints, at about the same level or slightly weaker than the value quoted in Eq. (2.14). This result is also subject to uncertainties, such as the role played by the central baryonic component of NGC720.

  As benchmark avoiding self-interaction constraints we will consider cases with dark matter mass about 1 TeV and $\alpha_D \simeq 10^{-2}$.

  We wish to reiterate that all throughout the history of the Universe, the dark sector is ionized. In our situation, we have multiple dark components: a dominant component consisting of heavy species and a subdominant component consisting of light species. Since

both species are charged under the dark U(1), there is additional interaction between the heavy and light species apart from the self-interaction between identical species.

Investigating the effect of having multiple dark matter components on structure formation at small and large scales is an interesting possibility that is beyond the scope of our work, but it could be a potential avenue for further exploration. Instead, we shall assume that we are working in the regime in which the multicomponent feature has negligible effect on structure formation.

2.2.2 Reference framework and parameter space

Taking into account the emerging picture, we will consider a scenario with: *i)* scalar messengers as the heaviest states in the dark-sector, *ii)* a lepton-like dark fermion χ playing the role of dark matter, lighter than scalar messengers but at a comparable mass scale, and *iii)* two dark fermions Q^U and Q^D coupled to the quarks, which are much lighter than χ and representative of the light dark sector (we shall see that the masses of the light dark species turn out to be indirectly constrained by CMB limits on exotic radiation components). Unless comparing to specific observables, to keep the model numerically tractable — but also without losing any of the main trends — we will adopt a set of simplifying assumptions. We restrict ourselves to the case in which all messenger states have a degenerate mass spectrum defined by a single mass parameter $m_\phi = m_S$ and a single mixing parameter η_s. For simplicity, the Yukawa couplings of all the dark fermions are also taken to be equal, and with $\alpha_L = \alpha_R$. The extra parameters we need to deal with are the mass of the dark matter candidate m_χ, the common mass m_Q for the two light quark-like dark fermions and the dark photon coupling α_D.

The remainder of the chapter is devoted to additional constraints coming from the thermal history of the Universe and dark matter searches.

2.3 Thermal history and relic density

2.3.1 General picture

The aim is to compute the cosmological relic density for the stable species in the dark sector. The technical calculation, via a set of coupled Boltzmann equations, is discussed in the next section. However, it is useful to illustrate first a few features characterizing our setup.

The lightest fermions of given dark charge, lepton-like or hadron-like, are stable, and their number density in the early Universe heat bath changes through processes involving pair productions and pair annihilations; initially in equilibrium (*chemical* equilibrium; see the discussion below for a clarification on this point), they decouple in the non-relativistic regime. Thus, they have a relic density which can be approximated by the celebrated "WIMP miracle" formula, which we have already seen in (1.71):

$$\Omega_{\chi,Q} h^2 \sim 0.1 \left(\frac{2.5 \times 10^{-9}\,\mathrm{GeV}^{-2}}{\langle v\sigma_{\chi\bar{\chi},Q\bar{Q}} \rangle} \right) , \tag{2.15}$$

where $\langle v\sigma_{\chi\bar{\chi},Q\bar{Q}} \rangle$ is the thermal average of the pair annihilation cross section for either χ or Q, including all kinematically allowed final states. However, there are two elements which make

the computation in the case at hand more involved than in other WIMP setups. First, while one usually deals only with SM final states, the pair annihilation may involve both particles belonging to the dark sector and to the SM sector; the leading processes are into two dark photons and a pair of SM fermion-antifermion of the corresponding type, as shown in Fig. 2.1 for the $Q\bar{Q}$ initial state. Assuming that s-wave processes dominate, the thermal average of the

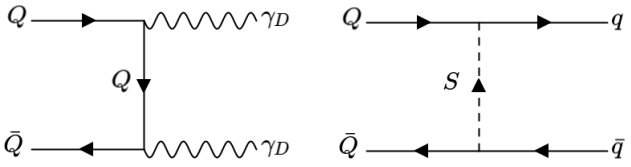

Figure 2.1: The Feynman diagrams giving the dominant contributions to the total pair annihilation rate of hadron-like dark sector fermions; diagrams contributing to the process for lepton-like dark fermions are analogous.

pair annihilation cross sections, in the limit of small temperature corrections and massless final states, are approximately given by:

$$\langle v\sigma_{\chi\bar{\chi},Q\bar{Q}\to\gamma_D\gamma_D}\rangle \sim \frac{\alpha_D^2}{m_{\chi,Q}^2} \quad \text{and} \quad \langle v\sigma_{\chi\bar{\chi},Q\bar{Q}\to f\bar{f}}\rangle \sim \frac{\alpha_L^2}{m_{\phi,S}^2}\left(\frac{m_{\chi,Q}}{m_{\phi,S}}\right)^2 . \tag{2.16}$$

Substituting these approximate expressions into Eq. (2.15), one can find the preferred mass ranges for which Ω_χ is at the level of the cosmological dark matter abundance, while Ω_Q is instead negligible (fulfilling the scheme emerging from the set of constraints discussed in the previous section). Taking α_D and α_L to be $O(10^{-2})$, and messenger scalars lying around 10 TeV, we find that $\Omega_\chi h^2 \sim 0.1$ if m_χ is in the 1-10 TeV range; χs predominantly annihilate into dark photons (SM fermions) if $(\alpha_L/\alpha_D)^2\,(m_\chi/m_\phi)^4$ is much less than (greater than) unity. Requiring that Ω_Q is at most 1% of the Universe's matter density, we find as a conservative upper bound on the masses of the hadron-like species $m_Q \lesssim 100\,\text{GeV}$; Qs predominantly annihilate into dark photons.

The second point we need to pay attention to is the fact that "thermal bath" effects, neglected so far, can actually have a significant impact on the overall picture. Analogously to the photon in the SM sector, the dark photon is crucial in keeping dark sector particles at a common temperature via, *e.g.*, the large energy exchanges in Compton-like dark fermion - dark photon elastic scatterings. These elastic scattering processes maintain *kinetic* equilibrium within the dark sector. Moreover, being a stable massless particle, the dark photon can potentially give a sizable contribution to the budget for the energy density in radiation in the Universe, even at epochs, such as recombination, at which extra radiation components are tightly constrained. The general picture is given schematically in Fig. 2.2. Assuming that the $U(1)_D$ coupling α_D is perturbative but still sufficiently large, dark photon interactions (or, eventually, a chain of processes involving additional interactions with other mediators/forces in the dark sector) enforce that all dark sector particles in the thermal bath have a common temperature T_d. Analogously, Compton scattering between SM photons and SM particles maintains kinetic equilibrium within the visible sector. However, the temperature T of the visible sector may be different from T_d.

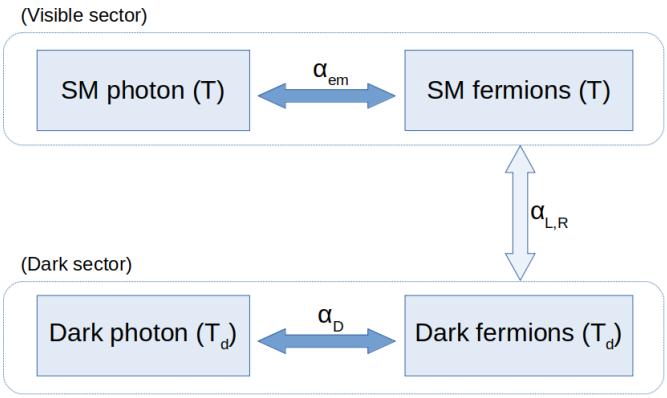

Figure 2.2: Schematic diagram of the interactions between the different reservoirs of states. $\alpha_{em} \equiv e^2/(4\pi)$ and $\alpha_D \equiv g_D^2/(4\pi)$ are, respectively, the electromagnetic and dark photon interaction strengths. The coupling $\alpha_{L,R}$ are defined by the Lagrangian in Eq. (2.1). Ordinary and dark photons do not talk directly to each other.

In the regime at which messenger scalars are non-relativistic, and with their number densities suppressed, the communication between visible and dark sectors (both at the level of particle number-changing processes and elastic scatterings) is mostly regulated by the Yukawa-like interactions in Eq. (2.1). Let us first turn off the portal interactions, *i.e.* $\alpha_L = \alpha_R = 0$. In this case the thermal bath in the visible and dark sectors evolve independently, and one can track T and T_d by imposing entropy conservation separately in each of the two sectors, see, *e.g.* [183]. The cooling process goes as the inverse of the scale factor plus a correction due to the change in effective number of relativistic degrees of freedom, when particles becoming non-relativistic transfer their entropy to lighter, relativistic states of the corresponding sector. We define the temperature ratio between dark and visible sectors at a given time t to be

$$\xi(t) \equiv \frac{T_d(t)}{T(t)} \tag{2.17}$$

and consider some initial time t_0, with the temperature in the visible sector denoted by T_0, at which two sectors are already decoupled. Assuming that entropy densities in the dark and visible sectors, which are respectively given by:

$$s_d = \frac{2\pi^2}{45} g_{*S_d}(T_d) T_d^3 \qquad \text{and} \qquad s_v = \frac{2\pi^2}{45} g_{*S_v}(T) T^3, \tag{2.18}$$

are separately conserved in a comoving volume, one finds that the temperature ratio at the CMB epoch is given by:

$$\xi_{CMB} = \left[\frac{g_{*S_d}(\xi_0 T_0)}{g_{*S_d}(\xi_{CMB} T_{CMB})} \frac{g_{*S_v}(T_{CMB})}{g_{*S_v}(T_0)} \right]^{1/3} \xi_0 \,, \tag{2.19}$$

where $g_{*S_v}(T)$ counts the number of internal degrees of freedom (fermionic species are weighted by 7/8) for all SM particles that are relativistic at temperature T, and $g_{*S_d}(T_d)$ is the analogous quantity in the dark sector. Evaluating this ratio is relevant since this is the epoch at which extra radiation components are most severely constrained by cosmological observables. The limit is usually given in terms of N_{eff}, the effective number of neutrino-like species, *i.e.* fully

relativistic fermions with two internal degrees of freedom, and with a temperature which is a factor of $(4/11)^{1/3}$ cooler than photons. N_{eff} is related to the radiation energy density by:

$$\rho_r(t) \equiv \rho_\gamma(T(t)) \left[1 + \frac{7}{8}\left(\frac{4}{11}\right)^{4/3} N_{eff}(t)\right] . \tag{2.20}$$

The Planck satellite has measured N_{eff} at the CMB epoch to be [9]: $N_{eff} = 3.27 \pm 0.15$, 68% CL. Subtracting out the contribution from the three standard model neutrinos [209] $N_{eff}^{SM} = 3.046$, and assuming that the dark photon is the only dark sector relativistic state at the CMB epoch, giving rise to the extra radiation component $\rho_{r,d}(T_d(t)) = \rho_\gamma(T(t))\,\xi^4(t)$, we can translate the upper limit on N_{eff} from Planck into a limit on the temperature ratio at the CMB epoch; one finds:

$$\xi_{CMB} < 0.54, \quad 68\%\ CL \tag{2.21}$$

The 2σ and 3σ upper limits are, respectively, about 0.59 and 0.63. Our reference dark sector framework consists of: the dark photon, one lepton-like Dirac fermion χ, and N_Q light hadron-like Dirac fermions Q being relativistic at the initial time t_0. From Eq. (2.19) we obtain $g_{*S_d}(\xi_0 T_0)/g_{*S_d}(\xi_{CMB} T_{CMB}) = (7N_Q + 11)/4$. Even for a single family of dark hadrons ($N_Q = 2$) we find $\xi_{CMB} \approx 0.61\,\xi_0$, in tension with the limit quoted in (2.21) if $\xi_0 = 1$ (namely $T = T_d$ at $t = t_0$). As we increase the number of light species in the dark-sector, this problem gets more severe. A possible way out is to relax the initial condition. In principle the picture with decoupled sectors can be extrapolated to T_0 as high as, say, the reheating temperature. One can then assume an initial temperature mismatch between the two sectors, with a cooler dark sector (*i.e.* $\xi_0 < 1$), and thus the dark photon contribution to the radiation component of the Universe can be made small relative to the visible sector contribution. Similar conclusions (for various implementations of the dark-sector portal) were reached in, *e.g.*, [166, 183, 202, 210–213].

On the other hand, when the messenger portal is turned back on, allowing for non-vanishing Yukawa couplings α_L and α_R, energy (and entropy) can be exchanged between visible and dark sectors. Regardless of what is assumed for ξ_0, even if the system is not initially in kinetic equilibrium, for couplings sufficiently large, we expect it to relax to a maximum entropy configuration with the two temperature in the two sectors that will tend to become equal. This brings back the problem of satisfying the bound on extra radiation component associated to the dark photon at the CMB epoch, and will effectively translate on an upper bound on the Yukawa couplings. Since α_L and α_R both enter in the discussion for kinetic and chemical equilibrium, these two aspects have to be considered at the same time, as we will do with the set of coupled Boltzmann equations that we introduce in the next subsection and solve numerically.

2.3.2 Boltzmann equations

Having highlighted above that SM and dark sector states may have, in general, different temperatures, T and T_d respectively, it is useful to keep track of them separately. Hence, in what follows, we adopt the following notation: i_d will generically indicate a species in the dark sector, while species in the visible sector will be denoted by i_v; i will, in general, stand for any species in either sector. To track the distribution function of a state i_d, we follow [214, 215] and consider the generic Boltzmann equation

$$L[f_{i_d}] = C[f_{i_d}] , \tag{2.22}$$

where f_{i_d} is the occupation number for the particle i_d, L is the Liouville operator tracking the evolution in the Friedmann-Robertson-Walker (FRW) background, and C is the collision operator. The Liouville operator takes the form

$$L[f_{i_d}] = E_{i_d}\left(\frac{\partial f_{i_d}}{\partial t} - H\vec{p}\cdot\frac{\partial f_{i_d}}{\partial \vec{p}}\right) , \tag{2.23}$$

where $\vec{p}$ is the physical momentum of i_d and H is the Hubble rate. In the early Universe, the Hubble rate is dominated by radiation components coming from the visible and dark sectors. The first Friedmann equation tells us that

$$H^2(t) \approx \frac{4\pi^3}{45M_{Pl}^2}\left[g_{*v}(T)T^4 + g_{*d}(T_d)T_d^4\right] . \tag{2.24}$$

In the dilute limit, the collision operator acting on f_{i_d} is driven by $2 \to 2$ processes, such as $i_d + j \leftrightarrow k + l$. It is then obtained by summing terms of the form:

$$\begin{aligned} C_{i_d+j\leftrightarrow k+l}[f_{i_d}(p_{i_d})] \;=\; & \frac{1}{2}\int d\Pi_j(p_j)d\Pi_k(p_k)d\Pi_l(p_l)(2\pi)^4\delta^{(4)}(p_{i_d}+p_j-p_k-p_l) \\ & \times\Big\{ -\Big|\mathcal{M}(i_d+j\to k+l)\Big|^2 f_{i_d}(p_{i_d})f_j(p_j)[1\pm f_k(p_k)][1\pm f_l(p_l)] \\ & +\Big|\mathcal{M}(k+l\to i_d+j)\Big|^2 f_k(p_k)f_l(p_l)[1\pm f_{i_d}(p_{i_d})][1\pm f_j(p_j)]\Big\} , \end{aligned} \tag{2.25}$$

where $d\Pi_j(p_j) \equiv d^3\vec{p}_j/[(2\pi)^3\, 2\, E_j(p_j)]$ are the usual phase-space integration factors.

When tracking chemical equilibrium, *i.e.* the evolution of the number density of i_d, only inelastic processes are relevant. Given the structure of our model, the relevant number changing processes for χ and Q states (for T_d not too large) are all in the form of particle-antiparticle pair annihilation or creation (see Fig. 2.1), namely

$$C^{(in)}[f_{id}] = \sum_{j_v} C_{i_d+\bar{i}_d\leftrightarrow j_v+\bar{j}_v}[f_{id}] + \sum_{j_d\neq i_d} C_{i_d+\bar{i}_d\leftrightarrow j_d+\bar{j}_d}[f_{id}]. \tag{2.26}$$

The expression for $C^{(in)}[f_{i_d}]$ can be simplified under the standard set of assumptions: (i) **CP invariance** in the process $i_d + \bar{i}_d \to j_d + \bar{j}_d$, so that $|\mathcal{M}_{\to}|^2 = |\mathcal{M}_{\leftarrow}|^2$ (strictly true in our model); (ii) **dilute limit**, with $f_i \ll 1$, $1 \pm f_i \approx 1$, and equilibrium distributions with occupation numbers approximated as

$$f_i^{(eq)} = f_i^{(eq)}(E_i, T) \approx \exp\left(-\frac{E_i - \mu_i}{T}\right) ; \tag{2.27}$$

and (iii) **kinetic equilibrium** among dark sector states as enforced by elastic scatterings on the dark photon. Following from (ii), one can safely assume that standard model states follow equilibrium distributions and, using conservation of energy, formally rewrite their occupation numbers in terms of thermal distributions for the dark sector states in the form

$$\begin{aligned} f_{i_v}f_{\bar{i}_v} &= f_{i_v}^{(eq)}(E_{i_v}, T)f_{\bar{i}_v}^{(eq)}(E_{\bar{i}_v}, T) = \exp\left(-\frac{E_{i_v}+E_{\bar{i}_v}}{T}\right) \\ &= \exp\left(-\frac{E_{i_d}+E_{\bar{i}_d}}{T}\right) = f_{i_d}^{(eq)}(E_{i_d}, T)f_{\bar{i}_d}^{(eq)}(E_{\bar{i}_d}, T). \end{aligned} \tag{2.28}$$

Note that we have T rather than T_d in the last expression. As for (iii), this implies that, for any dark sector state, one may assume that there is an overall scaling – only dependent on time – of the occupation numbers of dark sector species with respect to equilibrium distributions:

$$f_{i_d}(E_{i_d},t) \simeq \frac{n_{i_d}(t)}{n_{i_d}^{(eq)}(t)} f_{i_d}^{(eq)}(E_{i_d},T_d(t)) \equiv A_{i_d}(t)\, f_{i_d}^{(eq)}(E_{i_d},T_d(t))\,, \tag{2.29}$$

with n_{i_d} and $n_{i_d}^{(eq)}$ being the number densities of i_d obtained by integrating f_{i_d} and $f_{i_d}^{(eq)}$, respectively.

To find the evolution equations for the number densities n_{i_d} of the relevant dark-sector fermions, we take the zeroth-order moment of the Boltzmann equation to obtain

$$\begin{aligned} \dot{n}_{i_d} + 3Hn_{i_d} &= \sum_{i_v} \left[-\langle\sigma v\rangle_{i_d\bar{i}_d\to i_v\bar{i}_v}(T_d) n_{i_d}^2 + \langle\sigma v\rangle_{i_d\bar{i}_d\to i_v\bar{i}_v}(T) n_{i_d,eq}^2(T) \right] \\ &+ \sum_{j_d\neq i_d} \left[-\langle\sigma v\rangle_{i_d\bar{i}_d\to j_d\bar{j}_d}(T_d) n_{i_d}^2 + \langle\sigma v\rangle_{j_d\bar{j}_d\to i_d\bar{i}_d}(T_d) n_{j_d}^2 \right] . \end{aligned} \tag{2.30}$$

It is understood that the sum over j_d includes the dark photon. The thermally averaged cross section $\langle\sigma v\rangle$ in (2.30) is defined, in terms of the corresponding Møller cross section, as

$$\langle\sigma v\rangle_{i\bar{i}\to j\bar{j}}(\tilde{T}) \equiv \frac{\int \frac{d^3\vec{p}_1}{(2\pi)^3}\frac{d^3\vec{p}_2}{(2\pi)^3}\ (\sigma v)_{i\bar{i}\to j\bar{j}}\, f_i^{(eq)}(p_1;\tilde{T}) f_{\bar{i}}^{(eq)}(p_2;\tilde{T})}{\int \frac{d^3\vec{p}_1}{(2\pi)^3}\frac{d^3\vec{p}_2}{(2\pi)^3}\ f_i^{(eq)}(p_1;\tilde{T}) f_{\bar{i}}^{(eq)}(p_2;\tilde{T})}. \tag{2.31}$$

Looking at (2.30), there are three independent variables: t, T, and T_d. In the standard approach, one closes the system by assuming entropy conservation; this leads to a time-temperature relation. In our current set-up, however, the two sectors are allowed to exchange energy and entropy, and thus the entropy of either sector is neither conserved. Nevertheless, the time evolution of the entropies of both sectors will allow us to obtain a well-posed ODE system.

In tracking the entropy of both sectors, we first need to introduce the definition of entropy of species i in terms of the occupation number f_i. This is given by

$$s_i = -\int \frac{d^3\vec{p}}{(2\pi)^3}\,(f_i \ln f_i - f_i)\,. \tag{2.32}$$

Its evolution can be obtained by differentiating s_i with respect to time, and then using Boltzmann equation. We have

$$\dot{s}_i + 3Hs_i = -\int \frac{d^3\vec{p}}{(2\pi)^3}\ C[f_i]\ln f_i. \tag{2.33}$$

We then take the sum of (2.33) over dark-sector species. Using kinetic equilibrium and dilute limit assumptions, one obtains:

$$\dot{s}_d + 3Hs_d = \frac{1}{T_d}\sum_{i_d}\int \frac{d^3\vec{p}}{(2\pi)^3}\, E\, C^{(in)}[f_{i_d}] + \frac{1}{T_d}\sum_{i_d}\int \frac{d^3\vec{p}}{(2\pi)^3}\, E\, C^{(el)}[f_{i_d}] - \sum_{i_d}\ln A_{i_d}(t)\int \frac{d^3\vec{p}}{(2\pi)^3}\, C^{(in)}[f_{i_d}], \tag{2.34}$$

where A_{i_d} has been defined in Eq. (2.29) above, and $C^{(el)}[f_{i_d}]$ is the elastic part of the collision operator. Similarly, for s_v, we have:

$$\dot{s}_v + 3Hs_v \;=\; \frac{1}{T}\sum_{i_v}\int \frac{d^3\vec{p}}{(2\pi)^3}\; E\; C^{(in)}[f_{i_v}] + \frac{1}{T}\sum_{i_v}\int \frac{d^3\vec{p}}{(2\pi)^3}\; E\; C^{(el)}[f_{i_v}] \tag{2.35}$$

In the sum over dark-sector/visible sector species, we only take those processes that involve the transfer of entropy from one sector to the other. To proceed further, it is appropriate to digress into the discussion of the elastic part of the collision operator. It encodes the processes of type $i + B \leftrightarrow i + B$, where i is some species scattering from bath particles B, which also contribute to the entropy transfer between the two sectors. As demonstrated in [216], it can be written as

$$C^{(el)}[f_i] = \sum_B C_{i+B\leftrightarrow i+B}[f_i] \tag{2.36}$$

where $C_{i+B\leftrightarrow i+B}[f_i]$ is a Fokker-Planck type operator, given by

$$C_{i+B\leftrightarrow i+B}[f_i] \equiv \frac{\partial}{\partial\vec{p}_i}\cdot\left[\gamma_{iB}(E_i,T_B)\left(E_iT_B\frac{\partial f_i}{\partial\vec{p}_i}+\vec{p}_if_i\right)\right] = \frac{\partial}{\partial\vec{p}_i}\cdot\left[\gamma_{iB}(E_i,T_B)E_i\frac{\partial f_i}{\partial\vec{p}}\right](T_B-T_i)\,. \tag{2.37}$$

In obtaining this expression, it is assumed that the momentum transfer between i and B is much smaller than the typical momentum of either species. The momentum transfer rate can be shown to be given by:

$$\gamma_{iB}(E_i,T_B) = \frac{1}{48\pi^3E_i^2T_B\,(1-|\vec{v}_i|^2/3)}\int_{m_B}^{\infty}dE_B\; f_B(E_B,T_B)\;\frac{p_B}{\sqrt{E_i^2E_B^2-m_i^2m_B^2}} \times\left[\frac{1}{16}\int_{-4p_{CM}^2}^{0}dt\;|\mathcal{M}|^2(-t)\right], \tag{2.38}$$

where $4p_{CM}^2 \equiv [s_0-(m_i+m_B)^2][s_0-(m_i-m_B)^2]/s_0$ and $s_0 \equiv m_i^2+m_B^2+2E_iE_B$. Using (2.37), we have

$$\int\frac{d^3\vec{p}_i}{(2\pi)^3}\;E_i\;C^{(el)}[f_i] = -\,(T_B-T_i)\int\frac{d^3\vec{p}_i}{(2\pi)^3}\;\gamma_{iB}\,(E_i,T_B)\;\;\vec{p}_i\cdot\frac{\partial f_i}{\partial\vec{p}_i} = 3n_i\,(T_B-T_i)\,\langle\gamma_{iB}\rangle(T_i,T_B), \tag{2.39}$$

where we identify the thermal average of the momentum transfer rate

$$\langle\gamma_{iB}\rangle(T_i,T_B) \equiv \frac{\int\frac{d^3\vec{p}_i}{(2\pi)^3}\;\gamma_{iB}\,(E_i,T_B)\;\;\vec{p}_i\cdot\frac{\partial f_i}{\partial\vec{p}_i}}{\int\frac{d^3\vec{p}_i}{(2\pi)^3}\;\vec{p}_i\cdot\frac{\partial f_i}{\partial\vec{p}_i}} = \frac{\int_{m_i}^{\infty}dE_i\;\;(E_i^2-m_i^2)^{3/2}\,\gamma_{iB}\,(E_i,T_B)\;\;f_i^{(eq)}(E_i,T_i)}{\int_{m_i}^{\infty}dE_i\;\;(E_i^2-m_i^2)^{3/2}\;\;f_i^{(eq)}(E_i,T_i)}\,. \tag{2.40}$$

At this point we would like to emphasize the following: if the species i were non-relativistic, $T_i \ll m_i$, one could ignore the dependence of γ_{iB} on energy, and the thermal average may be safely replaced as $\langle\gamma_{iB}\rangle(T_i,T_B) \approx \gamma_{iB}(E_i = m_i, T_B)$. For instance, this applies for the case of scatterings of non-relativistic DM particles from a bath of relativistic SM species (this is the limit applied, *e.g.*, in [217]). In our scenario, however, we would also like to account for entropy transfers from the dark-sector to the visible sector; this situation corresponds to the case where

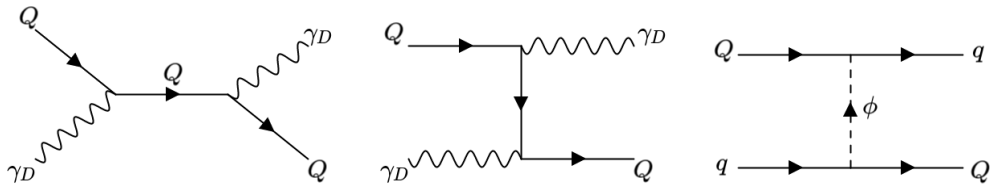

Figure 2.3: The Feynman diagrams for the elastic amplitudes of the dark sector fermions with dark photons (left and center) and with SM fermions (right). Only the contribution of the diagram on the right is included in the numerical solutions since the two Compton-like diagrams are by assumption in equilibrium.

the dark-sector species act as bath particles for scatterings of visible sector species. When the scattering species are relativistic, one needs to take into account the energy dependence of γ_{iB} and perform the thermal average at each step in the numerical solution of the system of coupled differential equations; further details about the technical implementation of this term are given Appendix A.2.

We are now in the position to write down the evolution equations for the entropies in the visible and dark sectors; we have (see also the analogous set of equations in [218])

$$\begin{aligned}
\dot{s}_v + 3Hs_v &\approx \frac{1}{T}\sum_{i_v}\sum_{i_d}\left[-\langle\sigma vE\rangle_{i_v\bar{i}_v\to i_d\bar{i}_d}(T)n^2_{i_v,eq}(T) + \langle\sigma vE\rangle_{i_d\bar{i}_d\to i_v\bar{i}_v}(T_d)n^2_{i_d}\right] \\
&\quad -3\sum_{i_v}\sum_{i_d}\langle\gamma_{i_v i_d}\rangle(T,T_d)\left(\frac{T-T_d}{T}\right)n_{i_v,eq}(T)\,, \\
\dot{s}_d + 3Hs_d &\approx \frac{1}{T_d}\sum_{i_d}\sum_{i_v}\Big[-\left(\langle\sigma vE\rangle_{i_d\bar{i}_d\to i_v\bar{i}_v}(T_d) - \langle\sigma v\rangle_{i_d\bar{i}_d\to i_v\bar{i}_v}(T_d)\;T_d\ln A_{i_d}\right)n^2_{i_d} \\
&\qquad\qquad + \left(\langle\sigma vE\rangle_{i_v\bar{i}_v\to i_d\bar{i}_d}(T) - \langle\sigma v\rangle_{i_v\bar{i}_v\to i_d\bar{i}_d}(T)\;T_d\ln A_{i_d}\right)n^2_{i_v,eq}(T)\Big] \\
&\quad +3\sum_{i_d}\sum_{i_v}\langle\gamma_{i_d i_v}\rangle(T_d,T)\left(\frac{T-T_d}{T_d}\right)n_{i_d}\,,
\end{aligned} \tag{2.41}$$

where we have introduced yet another thermal average

$$\langle\sigma vE\rangle_{i\bar{i}\to j\bar{j}}(\tilde{T}) \equiv \frac{\int\frac{d^3\vec{p}_1}{(2\pi)^3}\frac{d^3\vec{p}_2}{(2\pi)^3}\;(\sigma v)_{i\bar{i}\to j\bar{j}}\left[E_i(p_1)+E_{\bar{i}}(p_2)\right]f_i^{(eq)}(p_1;\tilde{T})f_{\bar{i}}^{(eq)}(p_2;\tilde{T})}{\int\frac{d^3\vec{p}_1}{(2\pi)^3}\frac{d^3\vec{p}_2}{(2\pi)^3}\;f_i^{(eq)}(p_1;\tilde{T})f_{\bar{i}}^{(eq)}(p_2;\tilde{T})}. \tag{2.42}$$

From Eq. (2.41) it is transparent that if $T = T_d$ at early times the entropy exchange processes balance out, as expected from the condition of thermal equilibrium. Also, once the dark sector particles decouple, the entropies of the two sectors are separately conserved. The approach to kinetic equilibrium between the two sectors will then be relevant if we start with an initial temperature asymmetry and when the heavy dark sector species are still relativistic.

We choose to solve the system of coupled differential equations using the scale factor a as the independent variable. Using Eq. (2.18), we rewrite the evolution equations for the entropies

as evolution equations for the temperatures:

$$\begin{aligned}
\frac{d(\ln T)}{d(\ln a)} &= -\frac{1}{h_{*S_v}(T)} + \frac{s_v(T)}{3T\,H(T,T_d)\,h_{*S_v}(T)} \sum_{i_v}\sum_{i_d}\Bigg[-\langle\sigma v E\rangle_{i_v\bar{i}_v\to i_d\bar{i}_d}(T) Y^2_{i_v,eq}(T) \\
&\quad +\langle\sigma v E\rangle_{i_d\bar{i}_d\to i_v\bar{i}_v}(T_d)\; Y^2_{i_d}\Bigg] - \frac{1}{H(T,T_d)\,h_{*S_v}(T)} \sum_{i_v}\sum_{i_d}\langle\gamma_{i_v i_d}\rangle(T,T_d)\left(\frac{T-T_d}{T}\right) Y_{i_v,eq}(T)\,, \\
\frac{d(\ln T_d)}{d(\ln a)} &= -\frac{1}{h_{*S_d}(T_d)} + \frac{s_v^2(T)}{3T_d\,H(T,T_d)\,s_d(T_d)\,h_{*S_d}(T_d)} \sum_{i_d}\sum_{i_v}\Big\{ -\big[\langle\sigma v E\rangle_{i_d\bar{i}_d\to i_v\bar{i}_v}(T_d) \\
&\quad -\langle\sigma v\rangle_{i_d\bar{i}_d\to i_v\bar{i}_v}(T_d)\; T_d \ln A_{i_d}\big] Y^2_{i_d} \\
&\quad +\big[\langle\sigma v E\rangle_{i_v\bar{i}_v\to i_d\bar{i}_d}(T) - \langle\sigma v\rangle_{i_v\bar{i}_v\to i_d\bar{i}_d}(T)\; T_d \ln A_{i_d}\big] Y^2_{i_v,eq}(T)\Big\} \\
&\quad +\frac{s_v(T)}{H(T,T_d)\,s_d(T_d)\,h_{*S_d}(T_d)} \sum_{i_d}\sum_{i_v}\langle\gamma_{i_d i_v}\rangle(T_d,T)\left(\frac{T-T_d}{T_d}\right) Y_{i_d}\,,
\end{aligned} \tag{2.43}$$

where we have written explicitly that the Hubble rate H depends both on T and T_d, see Eq. (2.24), we have defined

$$h_{*S_v}(T) \equiv 1 + \frac{1}{3}\frac{d(\ln g_{*S_v})}{d(\ln T)} \quad \text{and} \quad h_{*S_d}(T_d) \equiv 1 + \frac{1}{3}\frac{d(\ln g_{*S_d})}{d(\ln T_d)}\,, \tag{2.44}$$

and have normalized all number densities to the entropy density in the visible sector, defining $Y_i \equiv n_i/s_v$, with i being any species – in the visible sector or in the dark sector. For such variables and again using the scale factor a as independent variable, the Boltzmann equation (2.30) takes the form:

$$\begin{aligned}
\frac{dY_{i_d}}{d(\ln a)} &= -3Y_{i_d}\left[1 + h_{*S_v}(T)\frac{d(\ln T)}{d(\ln a)}\right] + \frac{s_v(T)}{H(T,T_d)}\Big\{\sum_{i_v}\big[-\langle\sigma v\rangle_{i_d\bar{i}_d\to i_v\bar{i}_v}(T_d)\; Y^2_{i_d} \\
&\quad +\langle\sigma v\rangle_{i_d\bar{i}_d\to i_v\bar{i}_v}(T)\; Y^2_{i_d,eq}(T)\big] + \sum_{j_d\neq i_d}\big[-\langle\sigma v\rangle_{i_d\bar{i}_d\to j_d\bar{j}_d}(T_d)\; Y^2_{i_d} + \langle\sigma v\rangle_{j_d\bar{j}_d\to i_d\bar{i}_d}(T_d)\; Y^2_{j_d}\big]\Big\}.
\end{aligned} \tag{2.45}$$

Equations (2.43) and (2.45) constitute the closed system of differential equations to be solved.

2.3.3 Numerical results

As mentioned at the end of Section 2.2, we will consider a dark sector framework with the following fermionic content: (i) one lepton-like dark fermion χ, with mass m_χ, which acts as our dark matter candidate, and (ii) two hadron-like states, with masses m_{Q^U} and m_{Q^D}, that are lighter than χ. The evolution of the number density of each dark sector fermionic species is governed by Eq. (2.45). Regarding scalar messengers, we assume them to be degenerate in mass such that they are specified by a single mass parameter m_S, and a universal mixing η_S. Meanwhile, the other parameters relevant for the discussion are: (i) the $U(1)_D$ gauge coupling α_D, and (ii) the Yukawa-like couplings α_L and α_R, which are taken to be equal for simplicity. Despite

the model residing in a seven-dimensional parameter space, main trends can be illustrated on benchmark cases. In particular, unless explicitly stated, we will start illustrating the framework by focusing on the following choice of parameters:

$$m_{Q^U} = 10\,\text{GeV}, \quad m_{Q^D} = 20\,\text{GeV}, \quad m_S = 10\,\text{TeV}, \quad \alpha_D = 10^{-2}, \quad \text{and} \quad \eta_S = 0. \tag{2.46}$$

We will then vary the Yukawa-like coupling α_L and properly adjust m_χ, so that the relic density of χ approximately matches the dark matter density in the Universe as measured from cosmological observations. In Fig. 2.4 we present results for the numerical solution of the Boltzmann code

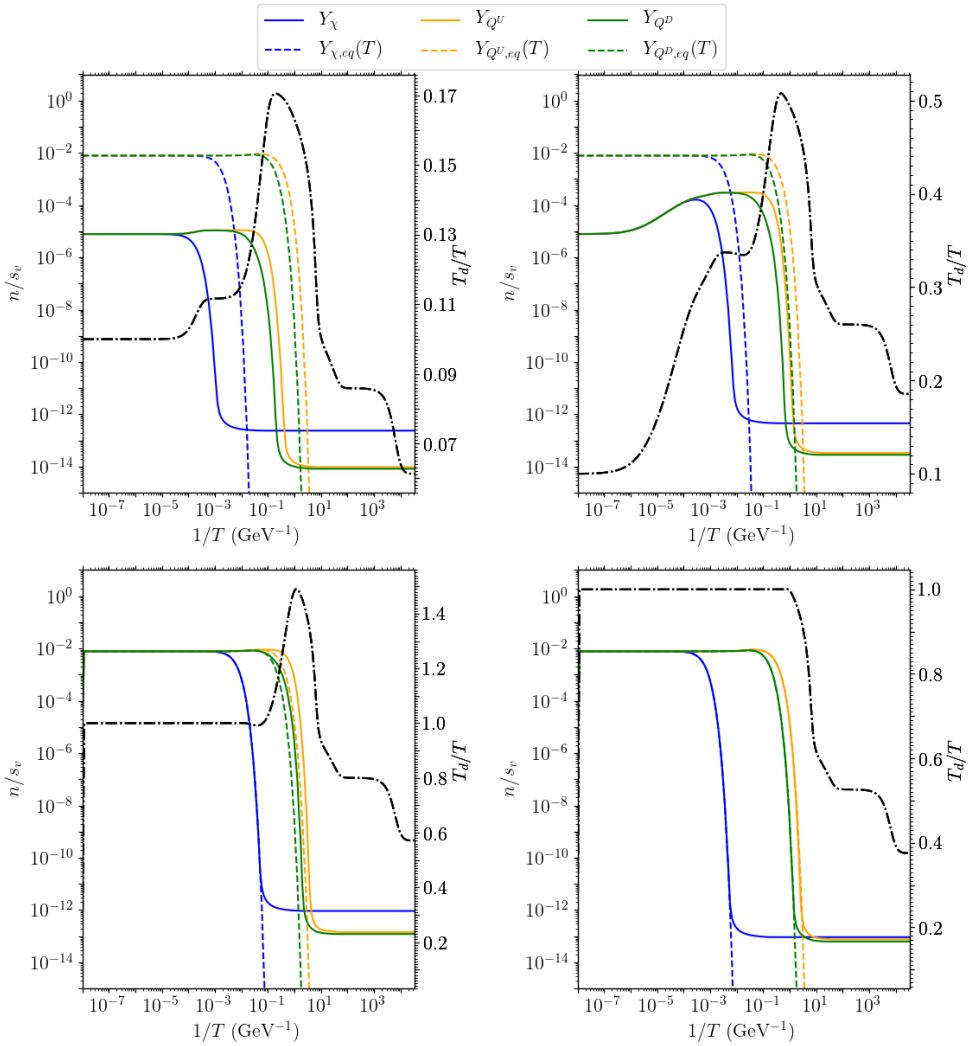

Figure 2.4: Solutions of the Boltzmann equations for four different benchmark point in parameter space, as specified in Table 2.1. These are representative of the four regimes labelled region I, II, III, and IV (from left to right and top to bottom) and described in the text. The solid lines track Y_{i_d}, the comoving number density normalized over the visible sector entropy, for each fermionic dark species i_d. The dashed lines indicate the value of Y_{i_d} if i_d were in chemical equilibrium with the visible sector heat bath at temperature T. The dash-dotted line shows the evolution of $\xi \equiv T_d/T$, the ratio of the dark-to-visible sector temperatures.

Region	Coupling		Species	Mass (GeV)	Relic density (Ωh^2)	Temp. ratio at CMB
I	$\alpha_L = 10^{-11}$		χ	1850	0.1183	0.0613
			Q^U	10	2.573×10^{-5}	
			Q^D	20	4.457×10^{-5}	
II	$\alpha_L = 1.75 \times 10^{-8}$		χ	1000	0.1221	0.1856
			Q^U	10	8.948×10^{-5}	
			Q^D	20	1.520×10^{-4}	
III	$\alpha_L = 10^{-4}$		χ	480	0.1192	0.5712
			Q^U	10	3.866×10^{-4}	
			Q^D	20	6.499×10^{-4}	
IV	$\alpha_L = 0.35$		χ	5000	0.1239	0.3757
			Q^U	10	2.039×10^{-4}	
			Q^D	20	3.372×10^{-4}	

Table 2.1: Numerical values of the couplings and masses used to generate the plots in Fig. (2.4), as well as their corresponding results for the relic densities and temperature ratio at CMB. We have chosen the couplings and masses such that χ would give a relic density that is close to the measured value of the matter density: $\Omega h^2 = 0.1186$. In all cases, we have taken $\alpha_D = 10^{-2}$ and $m_s = 10\,\text{TeV}$.

for four different sets of pairs (α_L, m_χ). In each panel a solid line shows, as a function of the inverse of the temperature in the visible sector T, the evolution of the number density for χ, Q^U and Q^D, normalized to the entropy density in the visible sector; such evolution is followed from an initial time t_0, with initial temperature $T_0 = 10^8\,\text{GeV}$, to some low temperature at which all comoving number densities are frozen to their relic values. Y_{i_d} for each dark fermion species i_d is compared to the corresponding $Y_{i_d,eq}(T)$, namely the ratio between the equilibrium number density $n_{i_d,eq}(T_d)$ – assuming $T_d = T$ – and again $s_v(T)$, which is shown as a dashed line. This comparison is relevant since the case of Y_{i_d} tracking $Y_{i_d,eq}$ corresponds to the species i_d being in chemical equilibrium as well as kinetic equilibrium between visible and dark sectors. In each panel we also show, with a dash-dotted line, the temperature ratio between dark and visible sectors; values of $\xi(t) = T_d/T$ can be read on the vertical scale on the right-hand side – notice that, to show more clearly its variation over time, the range of values displayed is adjusted in each panel (while the displayed range for Y_{i_d}, on the left-hand side of each panel, is kept fixed). Following the general discussion in Section 2.3.1, for all benchmark models considered in the plot, it is assumed that at t_0 the dark sector is significantly colder than the visible sector, starting the numerical solution with $\xi(t_0) = 0.1$.

In the four panels of Fig. 2.4, going from left to right and top to bottom, α_L is progressively increased from a relatively small value for which the entropy exchanges between dark and visible sector are inefficient at any time, up to a regime at which kinetic equilibrium between the two sectors is reached at the very beginning of the numerical solution and maintained at temperatures lower than the chemical decoupling temperature of the lightest dark fermion. The values of the couplings, the dark fermion mass spectrum, as well as the results of the relic densities of the three dark fermions, and the value ξ_{CMB} of the temperature ratio at the CMB epoch, are given in Table 2.1. To explain trends in Fig. 2.4, considering the same benchmark cases and focusing on χ, in Fig 2.5 the effective interaction rates for relevant processes in Eqs. (2.43) and

(2.45) are compared to the Universe's expansion rate H (as usual, as a rule of thumb, a given process is efficient only when the ratio is larger than one). The pair annihilation rates into dark photons and/or SM leptons, which are shown separately, drive chemical decoupling; the role of χ in restoring and maintaining kinetic equilibrium can be sketched from the effective energy transfer rate from dark fermion annihilations and χ elastic scattering on SM leptons, *i.e.* the combinations one obtains when factorizing out $Y_{i_d}^2/H$ and Y_{i_d}/H in, respectively, the second and third term on the r.h.s. of Eq. (2.43). In the same plot we also show that, for all benchmark models, the scattering rate of χ on dark photons is much larger than H at any temperature, justifying the assumption of kinetic equilibrium among dark sector states.

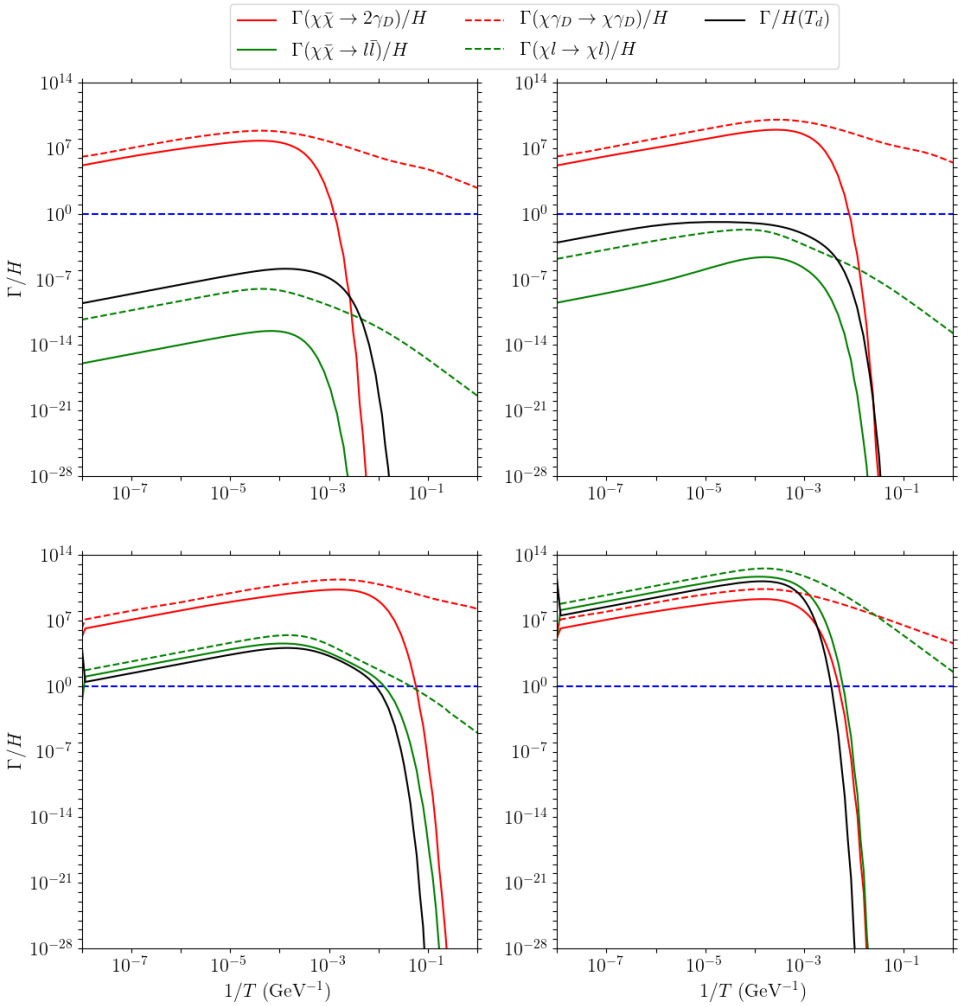

Figure 2.5: Rates (normalized over the Hubble constant) of annihilation (solid lines) and scattering processes (dashed lines) involving the lepton-like heavy dark fermion (see Eq. (2.30)) into dark photons (γ_D) and SM states. The rate of entropy exchange is also plotted (see Eq. (2.41)), and is labelled by $\Gamma/H(T_d)$. The plot refers to the same four benchmark models displayed in Fig. 2.6 and specified in Table 2.1, as representative of regions I, II, III, and IV in the parameter space (from left to right and top to bottom).

The four panels in Figs. 2.4 and 2.5 correspond to four different regimes in the parameter space. These are:

- Region I (top-left plots) This is the regime in which the portal between dark and visible sectors is virtually absent, and the pair annihilation into dark photons enforces chemical equilibrium of fermions in the dark sector at large temperatures. In this case the relic density of χ can be estimated as the thermal freeze-out of a non-relativistic species from the dark sector, which is analogous to the freeze-out of a standard WIMP from the visible sector: Y_χ at freeze-out can be shown to be

$$Y_{\chi,f.o.} \simeq \frac{\xi_{f.o.}(m_\chi/T_d)_{f.o.}}{\langle\sigma v\rangle_{\gamma_D} m_\chi M_{Pl}}, \tag{2.47}$$

with the dark-sector freeze-out temperature being about

$$\left(\frac{m_\chi}{T_d}\right)_{f.o.} \simeq \ln\left(\xi_{f.o.}^2 \langle\sigma v\rangle_{\gamma_D} m_\chi M_{Pl}\right) + \frac{1}{2}\ln\ln\left(\xi_{f.o.}^2 \langle\sigma v\rangle_{\gamma_D} m_\chi M_{Pl}\right) . \tag{2.48}$$

The relic density of χ is then

$$\Omega_\chi h^2 = \Omega_\chi h^2\big|_{\xi_{f.o.}=1} \frac{\xi_{f.o.}(m_\chi/T_d)_{f.o.}}{(m_\chi/T_d)_{f.o.}|_{\xi_{f.o.}=1}} . \tag{2.49}$$

In this regime, the evolution of ξ is obtained by assuming that the entropies of the dark and visible sectors are separately conserved. Note that due to the Universe's expansion, both T_d and T decrease; the temperature ratio $\xi = T_d/T$ increases whenever T_d decreases slower than T. This occurs when a dark species becomes non-relativistic and heats up the dark photon plasma. The ratio reaches a peak at around $T = m_{Q^U}$, and then decreases since SM photons are heated up by SM degrees of freedom becoming non-relativistic, and, especially, at the QCD phase transition when quarks and gluons are transformed into bound-state hadrons.

- Region II (top-right plots): The moderate increase in α_L is still insufficient to reach kinetic equilibrium between the two sectors. The effective energy transfer rate and the elastic scattering rates are still smaller than H at all temperatures, see Fig. 2.5. Nevertheless, the entropy leakage between the two sectors cannot be ignored, as one can see in the partial readjustment of ξ in the top-right panel of Fig. 2.4. Meanwhile in this regime, the relic density for χ, while still mostly determined by χ pair annihilations into dark photons, is also dictated by pair annihilations of visible sector particles populating the dark-sector with more dark fermions. This scheme is reminiscent of the freeze-in production mechanism for feebly interacting massive particles (FIMPs) [109]. As an approximate expression, Eq. (2.49) still applies, with however a slight increase in the thermal bath reservoir within which the freeze out of the thermal component is taking place and a shift in $\xi_{f.o.}$.

- Region III (bottom-left plots): This is the regime in which α_L is large enough to enforce kinetic equilibrium between the two sectors from the very first steps of the numerical solution, up to the freeze out temperature of the dark matter component (but – for the specific parameter choice displayed – not up to the temperature at which the light fermions become non-relativistic). It is however still too small for the χ pair annihilation into SM leptons to play a role in setting the dark matter relic density; the annihilation into dark

photons is still the dominant channel and the standard WIMP formula, Eq. (2.15) applies. Notice that the peak in the temperature ratio exceeds unity, since the light fermions become non-relativistic after kinetic decoupling. It follows that this is the benchmark case with largest ξ_{CMB}, slightly above the 1 σ bound from Planck.

- Region IV (bottom-right plots): This scenario is similar to region III, except that, concerning the relic density of χ, α_L is sufficiently large for SM lepton-anti-lepton pairs to be the dominant final state in the annihilation rate driving the WIMP rule-of-thumb formula Eq. (2.15). In the case at hand, α_L is also large enough to ensure kinetic equilibrium between dark and visible sectors at all temperatures at which dark fermions are relativistic, hence ξ becomes 1 immediately after t_0 and is not increasing further.

The four regions are also shown in the left panel of Fig. 2.6, where the relic density of χ is plotted as a function of α_L. We have kept m_χ, α_D, and η_S fixed for each curve. As expected from the previous discussion, $\Omega_\chi h^2$ is not necessarily a monotonic function of α_L and so there are multiple values of α_L giving the same relic density. In regions I and III, $\Omega_\chi h^2$ is independent of α_L, since in both regimes it is the annihilation to dark photons that determines the relic density of χ. Note that region I is the regime where the dark sector out of kinetic equilibrium with respect to the visible sector at all times, while region III is the regime where kinetic equilibrium holds until, at least, the chemical freeze-out of χ. Region II is the transition region between I and III: since the energy/entropy transfers and freeze-in effects become more efficient as α_L increases, $\Omega_\chi h^2$ increases as well. Region IV is the regime in which annihilations into SM leptons become dominant: following from Eqs. (2.15) and (2.16), we have $\Omega_\chi h^2 \propto \alpha_L^{-2}$. The change in m_χ produces a vertical shift of regions I, II, and III. This follows from the fact that, for these regimes, the relic density of χ is determined by the annihilation to dark photons, and thus $\Omega_\chi h^2 \propto m_\chi^2$. The trend changes for region IV; we have $\Omega_\chi h^2 \propto m_\chi^{-2}$. We also include the case where the left-right mixing between scalar messengers is maximal, *i.e.* $\eta_S = 1 - (m_\chi/m_\phi)^2$; this makes one of the scalar messengers lighter. A lighter scalar messenger increases the rate of processes enforcing kinetic equilibrium, which slightly changes the transition in region II; it also increases the annihilation rate to SM fermions, leading to the transition from region III to IV at a smaller α_L, as well as it leads to a decrease in the relic density in region IV. The value α_{L*} of the transition between regions III and IV can be roughly estimated by imposing that the annihilation cross section to SM species is about the same as the annihilation to dark photons; this leads to

$$\alpha_{L*} \simeq \alpha_D \left(\frac{m_S}{m_\chi}\right)^2 (1 - \eta_s) \ . \tag{2.50}$$

For instance, if $\eta_s = 0$, $\alpha_D = 10^{-2}$, and $m_S/m_\chi = 2$ (as in the blue curve in the left panel of Fig. 2.6), we have $\alpha_{L*} \simeq 4 \times 10^{-2}$.

In the right panel of Fig. 2.6 we explore how the relic density of the lighter dark fermions change with their masses. Given the constraints on light particles with long-range interactions in DM halos, such relic densities must be much suppressed compared to $\Omega_\chi h^2$, at the level of about 1% or lower. In general, the lighter the dark fermion, the more efficient the pair production/annihilation is into dark photons; since chemical decoupling is regulated by this final state, the relic density decreases accordingly. The right panel of Fig. 2.6 indeed shows

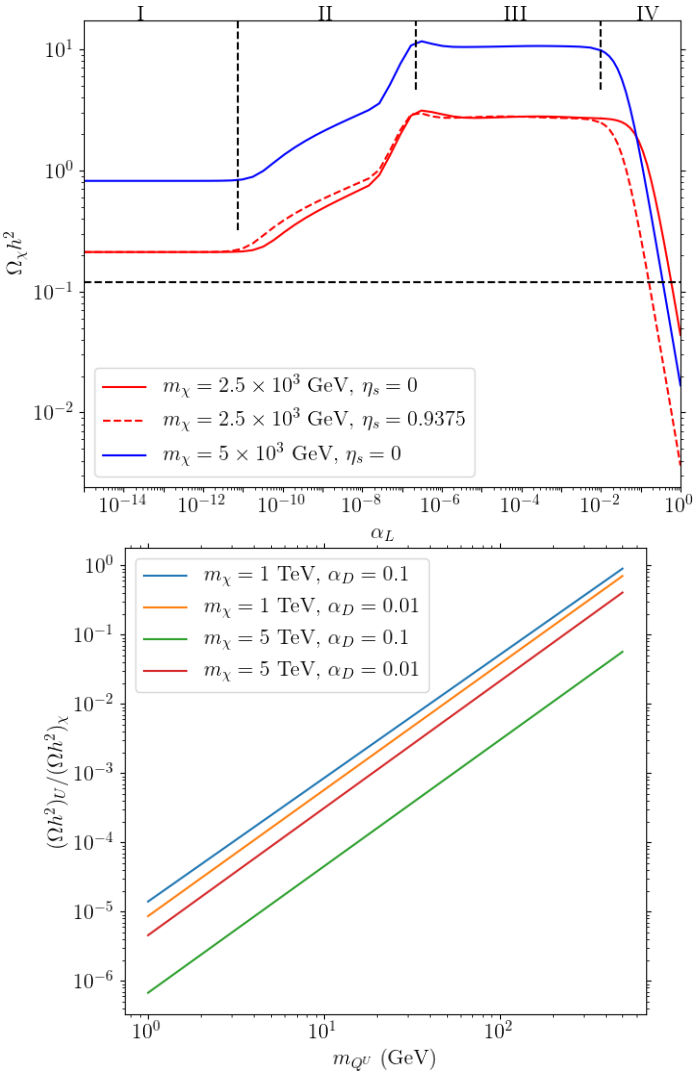

Figure 2.6: Top panel: Relic density $\Omega_\chi h^2$ of the DM candidate χ vs α_L, for fixed $\alpha_D = 10^{-2}$ and initial temperature ratio $\xi_0 = 0.1$. One can see the effect of changing m_χ and the effect of changing the left-right mixing for messenger scalars. The four marked regions are discussed in the text. Bottom panel: Relic density of Q^U relative to the relic density of χ, as a function of m_{Q^U}. As expected, $\Omega_U h^2$ increases with m_{Q^U} since the annihilation cross section to dark photons goes as $m_{Q^U}^{-2}$. The Yukawa coupling is taken everywhere to be $\alpha_L = 0.1$.

the expected scaling $\Omega_U h^2 \propto m_{Q^U}^2$, for each choice of the parameters α_D and m_χ. In general a contribution to the matter density below one percent can be obtained for $m_Q \lesssim 500\,\text{GeV}$. For example, for $\alpha_D = 0.1$ and $m_\chi = 1\,\text{TeV}$, this upper value is 40 GeV, while for $m_\chi = 5\,\text{TeV}$ the upper value shifts up to 195 GeV. For $\alpha_D = 0.01$, the upper values are 50 GeV and 70 GeV, for $m_\chi = 1\,\text{TeV}$ and $m_\chi = 5\,\text{TeV}$, respectively. The ratio of the relic densities of Q^U over χ is weakly dependent on α_L.

In the left panel of Fig. 2.7, we show the temperature ratio at the CMB as a function of α_L, for fixed α_D, m_χ, and m_ϕ, while N_Q, the number of light dark quarks, and m_Q, the common mass of the dark quarks, are allowed to change individually. On the right panel of Fig. 2.7, we present

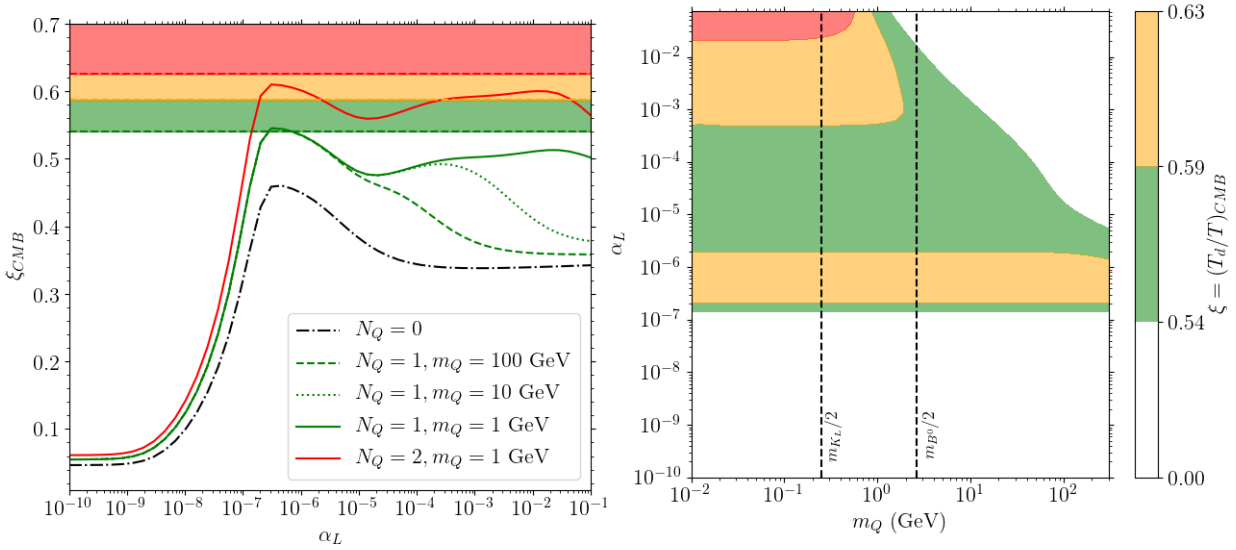

Figure 2.7: (Left) Plot of ξ_{CMB} versus α_L, for varying m_Q at fixed $N_Q = 1$, and for varying N_Q at fixed $m_Q = 1\,\text{GeV}$. The colored regions correspond to $2-\sigma$ (green), $3-\sigma$ (orange), and > 3-σ (red) bands. Here we have taken $m_s = 10\,\text{TeV}$, $m_\chi = 1\,\text{TeV}$, and $\alpha_D = 10^{-2}$. (Right) Contour plot of ξ_{CMB} on the $\alpha_L - m_Q$ plane, taking the same values of m_s, m_χ and α_D as in the left panel. Each colored regions correspond to $2-\sigma$ (green), $3-\sigma$ (orange), and > 3-σ (red) bands. The remaining regions correspond to ξ_{CMB} that are not excluded at 1σ by the current CMB limit on N_{eff}. The vertical lines correspond to half the masses of the neutral mesons K_L and B^0, which could decay into a particle-anti-particle pair of dark quarks. (*e.g.*, see [177]).

a contour plot of ξ_{CMB} in the $m_Q - \alpha_L$ plane, for fixed $\alpha_D = 10^{-2}$, $m_\chi = 1\,\text{TeV}$, and $N_Q = 2$. The contour plot has been generated by performing a scan of m_Q from 10 MeV to 300 GeV, and α_L values from 10^{-10} to 10^{-1}. All results in Fig. 2.7 are obtained in numerical solutions of the Boltzmann code assuming as initial temperature ratio $\xi_0 = 0.1$. As previously mentioned in Sec. 2.3.1, bounds on N_{eff} constrain extra contributions to the amount of radiation energy density. This constraint translates to an upper bound on the temperature ratio at CMB, given by Eq. (2.21).

There are a few features emerging from Fig. 2.7. As expected, at any given α_L, the ratio ξ_{CMB} increases as the number of light species N_Q increases. In particular, in the limit of vanishing Yukawa coupling α_L, *i.e.* when the two sectors do not communicate with each other, ξ_{CMB} depends on N_Q only. For our reference model, the scaling is $\xi_{CMB} \propto (7N_Q + 11)^{1/3}$. This follows from the fact that entropy is injected into the dark sector bath when dark species become non-relativistic. Since the CMB epoch occurs at relatively late times, ξ_{CMB} does not depend on m_Q. Recall also that in this limit, $\xi_{CMB} \propto \xi_0$ and we are assuming a rather small ξ_0.

Starting from a vanishingly small α_L, entropy exchanges between visible and dark sectors, that tend to equilibrate the mismatch ξ_0 in the initial temperatures, become more efficient as we increase α_L. This leads to increasing ξ_{CMB}. In the left panel of Fig. 2.7 this is the rising branch at $\alpha_L \lesssim 10^{-6}$. The largest increase is obtained at some intermediate α_L for which kinetic equilibrium is reached at early times, but is not maintained at the epoch at which χ or the

light dark fermions become non-relativistic. When these particles become non-relativistic, they transfer their entropies mainly to dark photons, which makes $\xi(t)$ become larger than 1 at some intermediate temperatures.

If instead α_L is large enough to maintain kinetic equilibrium when dark fermions become non-relativistic, entropy injections are shared by the SM degrees of freedom and the result is a decrease in ξ_{CMB}. At the same time the reverse effect occurs: SM states becoming non-relativistic and injecting entropy into the dark sector, rather than just heating SM photons, with then an increase in ξ_{CMB}. The efficiency in these two-direction exchanges clearly depends on all parameters regulating kinetic equilibrium between the two sectors, including m_χ, m_Q, and the messenger masses m_ϕ and m_S, as well as on the parameters setting the temperatures at which the dark fermions become non-relativistic (regulated also by m_χ and m_Q). In the left panel of the figure, we show in particular the α_L dependence of ξ_{CMB} for different values m_Q and $N_Q = 1$, while the case $N_Q = 2$ is illustrated for a sample value in the left panel and in the full range $m_Q \in (10\,\mathrm{MeV}, 300\,\mathrm{GeV})$ in the right panel. As the entropy transfer is particularly large at the QCD phase transition, at a temperature of about 150 MeV [219], it is crucial whether, at this epoch, Q are relativistic and/or visible and dark sectors are in kinetic equilibrium.

As seen from Fig. 2.7, the CMB limits on N_{eff} turn out to be a very severe constraint on the content of light fermions in the dark sector. Assuming an α_L of at least 10^{-2}, a favorable situation in order to satisfy the CMB limits at 1-σ level would be to keep $N_Q \leq 2$ and take m_Q to be at least 5 GeV. Future tighter constraints on N_{eff} will impact on the parameter space even more severely.

2.4 Direct detection searches

Direct searches test the interactions of dark matter particles with ordinary matter. As a preliminary step to project direct detection limits into our framework, we need to write down the effective coupling between dark leptons and quarks. Scattering processes are mostly driven by massless mediators: SM and dark photons. Since there is no kinetic mixing between the SM and the dark photon, the leading contributions appear at one-loop order, as shown in Fig. 2.8.

Computing the diagrams in Fig. (2.8) yields the following dimension 5 (magnetic dipole) and dimension 6 (charge-radius) effective operators[1]:

$$\mathcal{L}_5 \supset g_D \frac{d^{(q)}_{M,\gamma_D}}{2\Lambda^{(q)}_{D,\gamma_D}} (\bar{q}\sigma^{\mu\nu} q)\, X_{\mu\nu} + e \frac{d^{(\chi)}_{M,\gamma}}{2\Lambda^{(\chi)}_{D,\gamma}} (\bar{\chi}\sigma^{\mu\nu}\chi)\, F_{\mu\nu} \tag{2.51}$$

$$\mathcal{L}_6 \supset -g_D \frac{c^{(q)}_{CR,\gamma_D}}{[\Lambda^{(q)}_{CR,\gamma_D}]^2} (\bar{q}\gamma^{\nu} q)\, \partial^\mu X_{\mu\nu} - e \frac{c^{(\chi)}_{CR,\gamma}}{[\Lambda^{(\chi)}_{CR,\gamma}]^2} (\bar{\chi}\gamma^{\nu}\chi)\, \partial^\mu F_{\mu\nu} \tag{2.52}$$

where $F_{\mu\nu}$ and $X_{\mu\nu}$ are, respectively, the field strength associated with the SM photon and the dark photon. The dipole and charge-radius couplings, denoted by d_M/Λ_D and $c_{CR}/[\Lambda_{CR}]^2$, respectively, carry additional labels. These additional labels specify: the fermion they are associated with, and the massless gauge boson such fermion is coupled to. In the discussion below

[1] We assume for simplicity that CP invariance is respected in the dark-sector and there are no electric dipole moments.

we will both show results referring to a generic framework in which dipole and charge-radius couplings are treated independently of each other, as well as focus on our specific framework; in the latter case, they are given in terms of our model parameters and strong correlations appear. In particular, assuming universal couplings and $g_L = g_R$, we have

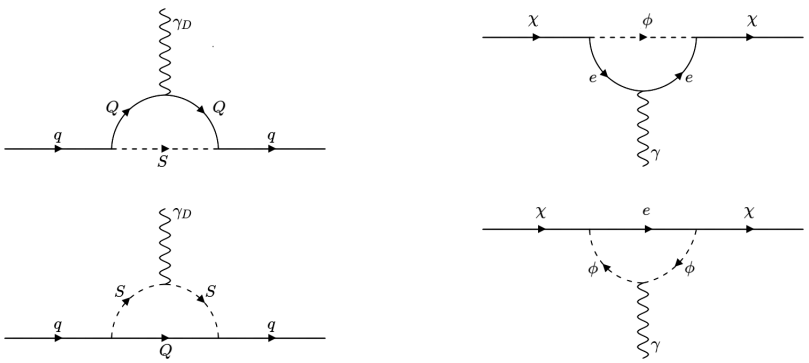

Figure 2.8: Feynman diagrams for the leading (one-loop) contributions to the the coupling between quarks and the dark photon (left) and (lepton-like) dark fermions and the ordinary photon (right).

$$\frac{d^{(\chi)}_{M,\gamma}}{\Lambda^{(\chi)}_{D,\gamma}} = \frac{\alpha_L}{4\pi}\frac{m_\chi}{m^2_{\phi_-}} F^{(\chi)}_{D,\gamma}\left(m_l, m_{\phi_-}, m_{\phi_+}\right) \quad , \qquad \frac{c^{(\chi)}_{CR,\gamma}}{[\Lambda^{(\chi)}_{CR,\gamma}]^2} = \frac{\alpha_L}{4\pi}\frac{1}{m^2_{\phi_-}} F^{(\chi)}_{CR,\gamma}\left(m_l, m_{\phi_-}, m_{\phi_+}\right)$$
$$\frac{d^{(q)}_{M,\gamma_D}}{\Lambda^{(q)}_{D,\gamma_D}} = \frac{\alpha_L}{4\pi}\frac{m_Q}{m^2_{S_-}} F^{(q)}_{D,\gamma_D}\left(m_Q, m_{S_-}, m_{S_+}\right) \quad , \qquad \frac{c^{(q)}_{CR,\gamma_D}}{[\Lambda^{(q)}_{CR,\gamma_D}]^2} = \frac{\alpha_L}{4\pi}\frac{1}{m^2_{S_-}} F^{(q)}_{CR,\gamma_D}\left(m_Q, m_{S_-}, m_{S_+}\right). \tag{2.53}$$

The exact expressions for the functions F_D and F_{CR}, which are either of order 1 or logarithmically-enhanced, are given in Appendix A.3. Here we just quote useful approximate expressions assuming that $m_l \ll m_{\phi_-}$ and $m_Q \ll m_{S_-}$:

$$\begin{aligned}
F^{(\chi)}_{D,\gamma}\left(m_l, m_{\phi_-}, m_{\phi_+}\right) &\simeq -\left(1 + \frac{m^2_{\phi_-}}{m^2_{\phi_+}}\right) \\
F^{(\chi)}_{CR,\gamma}\left(m_l, m_{\phi_-}, m_{\phi_+}\right) &\simeq -\left[\frac{1}{3}\ln\left(\frac{m_{\phi_-}}{m_l}\right) - \frac{1}{4}\right] - \left[\frac{1}{3}\ln\left(\frac{m_{\phi_+}}{m_l}\right) - \frac{1}{4}\right]\left(\frac{m_{\phi_-}}{m_{\phi_+}}\right)^2 \\
F^{(q)}_{D,\gamma_D}\left(m_Q, m_{S_-}, m_{S_+}\right) &\simeq \left[4\ln\left(\frac{m_{S_-}}{m_Q}\right) - 2\right] - \left[4\ln\left(\frac{m_{S_+}}{m_Q}\right) - 2\right]\left(\frac{m_{S_-}}{m_{S_+}}\right)^2 \\
F^{(q)}_{CR,\gamma_D}\left(m_Q, m_{S_-}, m_{S_+}\right) &\simeq \frac{1}{36}\left[13 - 12\ln\left(\frac{m_{S_-}}{m_Q}\right)\right] + \frac{1}{36}\left[13 - 12\ln\left(\frac{m_{S_+}}{m_Q}\right)\right]\left(\frac{m_{S_-}}{m_{S_+}}\right)^2.
\end{aligned} \tag{2.54}$$

If we plug-in typical values of dark-visible couplings and particle masses in the dark sector (where

we take $m_{\phi_+} = m_{S_+} = 10^3\,\text{TeV}$), we have

$$\begin{aligned}
\frac{d^{(\chi)}_{M,\gamma}}{\Lambda^{(\chi)}_{D,\gamma}} &\simeq \left(-1.59\times10^{-8}\,\text{GeV}^{-1}\right)\left(\frac{\alpha_L}{10^{-1}}\right)\left(\frac{m_\chi}{200\,\text{GeV}}\right)\left(\frac{10\,\text{TeV}}{m_{\phi_-}}\right)^2 \\
\frac{c^{(\chi)}_{CR,\gamma}}{[\Lambda^{(\chi)}_{CR,\gamma}]^2} &\simeq \left(-4.26\times10^{-10}\,\text{GeV}^{-2}\right)\left(\frac{\alpha_L}{10^{-1}}\right)\left(\frac{10\,\text{TeV}}{m_{\phi_-}}\right)^2 \\
g_D^2\frac{d^{(q)}_{M,\gamma_D}}{\Lambda^{(q)}_{D,\gamma_D}} &\simeq \left(2.56\times10^{-9}\,\text{GeV}^{-1}\right)\left(\frac{\alpha_D}{10^{-2}}\right)\left(\frac{\alpha_L}{10^{-1}}\right)\left(\frac{m_Q}{10\,\text{GeV}}\right)\left(\frac{10\,\text{TeV}}{m_{S_-}}\right)^2 \\
g_D^2\frac{c^{(q)}_{CR,\gamma_D}}{[\Lambda^{(q)}_{CR,\gamma_D}]^2} &\simeq \left(-1.94\times10^{-11}\,\text{GeV}^{-2}\right)\left(\frac{\alpha_D}{10^{-2}}\right)\left(\frac{\alpha_L}{10^{-1}}\right)\left(\frac{10\,\text{TeV}}{m_{S_-}}\right)^2 .
\end{aligned} \tag{2.55}$$

A further correlation is with the additional contribution to the magnetic dipole moment of SM leptons predicted in our framework; this involves a single class of loop diagrams in which the virtual messenger scalars couple with the SM photon, which is analogous with the bottom-right diagram in Fig. (2.8) with the particles χ and e exchanged. Such contribution is given by

$$\frac{d^{(l)}_{M,\gamma}}{\Lambda^{(l)}_{D,\gamma}} = \frac{\alpha_L}{4\pi}\frac{m_\chi}{m^2_{\phi_-}}F^{(l)}_{D,\gamma}\left(m_\chi, m_{\phi_-}, m_{\phi_+}\right) \tag{2.56}$$

where again F_D is order one and can be approximated as

$$F^{(l)}_{D,\gamma}\left(m_\chi, m_{\phi^-}, m_{\phi^+}\right) \approx \begin{cases} -2\left\{1+8\left(\frac{m_\chi}{m_{\phi^-}}\right)^2\left[1-\ln\left(\frac{m_{\phi^-}}{m_\chi}\right)\right]\right\}\left(\frac{m_{\phi^+}}{m_{\phi^-}}-1\right), & m_\chi \ll m_{\phi^-} \lesssim m_{\phi^+} \\ -\frac{1}{3}+\frac{m^2_{\phi^-}}{m^2_{\phi^+}}-\frac{1}{3}\left(1-\frac{m_\chi}{m_{\phi^-}}\right), & m_\chi \lesssim m_{\phi^-} \ll m_{\phi^+}. \end{cases} \tag{2.57}$$

In the following we will first analyze separately the cases in which DM-nucleus scattering is mediated by: *(a)* the SM photon, and *(b)* the dark photon. Case (a) has already been discussed in the literature, and some results are reproduced here (see, *e.g.*, [220–224]; see [225] for another possible long-range interaction for dark matter). Case (b), in which nuclei carry a (dark) magnetic moment, is explored here for the first time. We discuss the differential recoil rates, exclusion curves and projected sensitivities that one obtains considering each of the two massless mediators. Since both cases (a) and (b) involve dipole-vector interactions between DM and nucleons, one expects a term in the scattering amplitude which scales as the inverse of the momentum transfer, giving it an enhancement in the recoil rate at small recoil energies. On the other hand, we demonstrate here that one cannot naively conclude that the latter is the dominant effect and neglect other terms. While the enhancement is indeed present, it may get dominant over other terms only at extremely small recoil energies. It follows that, for what regards the phenomenology of the model, dimension 5 operators are not always playing the main role.

2.4.1 Direct detection analysis: an overview

The direct detection differential recoil rate, namely the number of scattering events per unit time, detector mass and recoil energy, can be generally written as

$$\frac{dR}{dE_R} = \sum_T c_T \frac{\rho_0}{m_\chi m_T} \int_{|\vec{v}|\geq v_{min}} d^3\vec{v}\ |\vec{v}|\ f(\vec{v}) \frac{d\sigma_T}{dE_R}. \tag{2.58}$$

In this equation the product of $|\vec{v}|$, the modulus of the velocity of the DM particle in the detector frame, times the local DM particle number density, expressed in terms of the ratio between the local DM density ρ_0 and the DM mass m_χ, gives the flux of DM particles in the detector at given $|\vec{v}|$. Such flux is weighted over the velocity distribution for DM particles in the detector frame $f(\vec{v})$ and convolved with the DM-nucleus differential cross section $d\sigma_T/dE_R$. The sum in the equation is over target nuclear isotopes T, with mass m_T and relative abundance c_T. The integral includes any $|\vec{v}|$ large enough to give a recoil energy E_R, *i.e.*, larger than $v_{min} = |\vec{q}|/(2\mu_{\chi T})$, where $\mu_{\chi T}$ is the target nucleus-DM reduced mass, $\mu_{\chi T} = m_\chi m_T/(m_\chi + m_T)$, and the momentum transfer $|\vec{q}|$ is related to the value of the recoil energy via $E_R = |\vec{q}|^2/(2m_T)$. In what follows, for the astrophysical dependent quantities ρ_0 and $f(\vec{v})$, we just refer to the standard assumptions in the direct detection community: a local DM halo density of $0.3\,\mathrm{GeV/cm^3}$ and a Maxwellian velocity distribution in the Galactic frame, with standard values of the velocity dispersion, and of the circular and escape velocities at the position of the Sun. While results are mildly dependent on these assumptions, they do not affect in any way the general discussion.

The DM-nucleus differential cross section $d\sigma_T/dE_R$ is derived in steps. Given the coupling of DM with quarks, one retrieves the effective coupling of DM with nucleons. The general formalism developed to describe non-relativistic EFT interactions goes as follows: the non-relativistic reduction of the Lagrangian density for the elastic scattering of a heavy DM particle on a proton or a neutron at rest can be written in terms of a set of 15 hermitian, leading-order operators (see *e.g.*, [226, 227]), *i.e.*:

$$\mathcal{L}_{NREFT} = \sum_{i=1}^{15} \sum_{N=p,n} c_i^{(N)} \mathcal{O}_i^{(N)} \left(\vec{q}, \vec{v}^{\perp}, \vec{S}_\chi, \vec{S}_N \right). \tag{2.59}$$

Each $\mathcal{O}_i^{(N)}$ is built out of a different contraction of four three-vectors: the momentum transfer $\vec{q}$; the transverse component of the DM particle velocity $\vec{v}^{\perp}$ ($\vec{v}^{\perp} \cdot \vec{q} = 0$); the spin of the DM particle and of the nucleon, respectively $\vec{S}_\chi$ and $\vec{S}_N$. The second step is mapping the single-nucleon interactions into nuclear interactions; the general structure for the differential cross section takes the form:

$$\frac{d\sigma_T}{dE_R} = \frac{m_T}{2\pi|\vec{v}|^2} \sum_{\alpha=1}^{8} \sum_{\tau,\tau'=0,1} S_\alpha^{(\tau\tau')} \left(|\vec{v}_\perp|^2, |\vec{q}|^2 \right) \widetilde{W}_\alpha^{(\tau\tau')}(|\vec{q}|^2), \tag{2.60}$$

where the proton-neutron basis has been replaced by the isospin basis, τ and τ' are isospin indices, S_α are the dark-matter response functions containing contractions of $\mathcal{O}_i^{(N)}$ terms and depend on the coefficients appearing in (2.59), $\vec{v}_\perp \equiv \vec{v} + \vec{q}/(2\mu)$, and $\widetilde{W}_\alpha$ are the nuclear response functions which are essentially form factors accounting for the composite structure of the nucleus.

Once we have the differential recoil rate, the expected number of direct detection events can be computed using [228]:

$$N_p = MT_E \int_0^\infty \phi(E_R) \frac{dR}{dE_R} dE_R \,, \tag{2.61}$$

where M is the mass of the detector, T_E is the exposure time, and $\phi(E_R)$ is the efficiency curve specific to a particular experiment. We can then use the data on the observed number of scattering events in a direct detection experiment, to constrain DM-nucleon interactions. To obtain the usual exclusion curves with some specified confidence level $1-\alpha$, one must, in principle, obtain the confidence interval $[0, N_{p*}]$ from the posterior probability distribution of N_p, given the observed number of events N_o. A fixed value of N_{p*} corresponds to a contour in the space of parameters that we are trying to constrain. Alternatively, to obtain exclusion plots, we use here the likelihood ratio test. First compute the Poisson likelihood functions:

$$\mathcal{L}\left(N_o, b|N_p\right) = \frac{(b+N_p)^{N_o}}{N_o!} e^{-(b+N_p)} \,, \tag{2.62}$$

where b is the number of background events, and then obtain the test statistic

$$\lambda \equiv -2 \ln \frac{\mathcal{L}\left(N_o = 0, b|N_p\right)}{\mathcal{L}\left(N_o, b|N_p\right)}. \tag{2.63}$$

The test statistic λ follows a half-chi-squared distribution with one degree of freedom. The exclusion region will then correspond to those values of N_p, which give probabilities above the confidence level: for 90% CL, we reject those values of N_p which give $\lambda \lesssim -1.64$. In what follows we shall use DDCalc [228, 229], a package written specifically for dark-matter direct detection calculations, including the calculation of differential recoil rates and likelihoods needed for obtaining parameter constraints at some specified confidence level. We will apply the procedure above to compare against the latest results from the XENON collaboration, which has produced the strongest upper limits in the DM particle mass range of interest for our framework [230], and to infer projected sensitivities of one of the proposed next-generation direct detection experiments, the DARWIN experiment [231], as representative of nearly final target for the direct detection field. In both cases we have checked that our results match closely published results when the DM nucleus interaction is assumed to be mediated by the standard spin independent operator.

2.4.2 SM photon-mediated processes

We consider first interactions mediated by SM photons (abbreviated as γm in the following). The dipole and charge radius effective coupling between dark leptons and SM quarks can be readily extracted from the effective operators in Eqs. (2.51) and (2.52):

$$\mathcal{L}_\gamma = e^2 \left\{ \frac{d^{(\chi)}_{M,\gamma}}{\Lambda^{(\chi)}_{D,\gamma}} \frac{1}{q^2} \left(\bar{\chi} i\sigma^{\mu\nu} q_\nu \chi\right) + \frac{c^{(\chi)}_{CR,\gamma}}{[\Lambda^{(\chi)}_{CR,\gamma}]^2} \left(\bar{\chi}\gamma^\mu \chi\right) \right\} \left(\frac{2}{3} \bar{u}\gamma_\mu u - \frac{1}{3} \bar{d}\gamma_\mu d \right), \tag{2.64}$$

where q^μ is the transfer four-momentum. We map the quark operators to the nucleon operators by using the form factors in [232]. We have

$$\bar{q}(k_2)\gamma^\mu q(k_1) \;\; \to \;\; \bar{N}(k_2) \left[F_1^{(q/N)}(q^2)\gamma^\mu + \frac{i}{2m_N} F_2^{(q/N)}(q^2) \sigma^{\mu\nu} q_\nu \right] N(k_1), \tag{2.65}$$

where $N = n, p$, and the $F_i^{(q/N)}$ coefficients are QCD matrix elements. Applying (2.65) to the quark vector current in (2.64) we get

$$\frac{2}{3}\bar{u}\gamma_\mu u - \frac{1}{3}\bar{d}\gamma_\mu d \;\rightarrow\; \bar{p}\gamma_\mu p + \frac{1}{2m_p}\left[\frac{2}{3}F_2^{(u/p)} - \frac{1}{3}F_2^{(d/p)}\right](\bar{p}i\sigma_{\mu\alpha}q^\alpha p) + \frac{1}{2m_n}\left[\frac{2}{3}F_2^{(u/n)} - \frac{1}{3}F_2^{(d/n)}\right](\bar{n}i\sigma_{\mu\alpha}q^\alpha n). \tag{2.66}$$

Following the prescription for mapping dark-matter-nucleon operators to their non-relativistic counterparts [226, 233], the effective, non-relativistic DM-nucleon interaction is

$$\begin{aligned}\mathcal{L}_\gamma \;=\; & e^2\frac{d_{M,\gamma}^{(\chi)}}{\Lambda_{D,\gamma}^{(\chi)}}\left[\frac{2m_p}{|\vec{q}|^2}\mathcal{O}_5^{(p)}\right] \\ & + e^2\frac{d_{M,\gamma}^{(\chi)}}{\Lambda_{D,\gamma}^{(\chi)}}\left[-\frac{1}{2m_\chi}\mathcal{O}_1^{(p)}\right] + e^2\frac{c_{CR,\gamma}^{(\chi)}}{[\Lambda_{CR,\gamma}^{(\chi)}]^2}\mathcal{O}_1^{(p)} + e^2\frac{d_{M,\gamma}^{(\chi)}}{\Lambda_{D,\gamma}^{(\chi)}}F^{(N)}\left[\frac{2}{m_N}\mathcal{O}_4^{(N)} - \frac{2m_N}{|\vec{q}|^2}\mathcal{O}_6^{(N)}\right].\end{aligned} \tag{2.67}$$

Here we have adopted the standard operator numbering

$$\mathcal{O}_1^{(N)} \equiv 1_\chi 1_N, \quad \mathcal{O}_4^{(N)} \equiv \vec{S}_\chi \cdot \vec{S}_N, \quad \mathcal{O}_5^{(N)} \equiv i\vec{S}_\chi \cdot \left(\frac{\vec{q}}{m_N} \times \vec{v}^\perp\right), \quad \mathcal{O}_6^{(N)} \equiv \left(\vec{S}_\chi \cdot \frac{\vec{q}}{m_N}\right)\left(\vec{S}_N \cdot \frac{\vec{q}}{m_N}\right), \tag{2.68}$$

where $\mathcal{O}_1$ and $\mathcal{O}_4$ are the operators commonly labelled as, respectively, *spin-independent* and *spin-dependent* couplings, and

$$F^{(p)} \equiv 1 - \frac{2}{3}F_2^{(u/p)} + \frac{1}{3}F_2^{(d/p)} \approx -0.772, \qquad F^{(n)} \equiv -\frac{2}{3}F_2^{(u/n)} + \frac{1}{3}F_2^{(d/n)} \approx 1.934. \tag{2.69}$$

Notice that we have organized the terms in (2.67) in powers of $|\vec{q}|$; the first line is of order $1/|\vec{q}|$, while the second line is of order $|\vec{q}|^0$. Looking at (2.67), we see that the γm dipole interaction gives an $\mathcal{O}_5$ contribution, which is long-range and coherent, a $\mathcal{O}_1$ contribution, which is a contact term and coherent, and other short-range, incoherent contributions. On the other hand, the γm CR interaction gives only a contact, coherent $\mathcal{O}_1$ contribution. We summarize these information in Table 2.2.

Coherent terms are likely to provide the largest contributions to the recoil spectrum. Depending on the relative size of the corresponding couplings, the recoil spectrum can either be dominated by dipole or charge-radius interactions. We address this issue by treating first the two couplings, namely $d_{M,\gamma}^{(\chi)}/\Lambda_{D,\gamma}^{(\chi)}$ and $c_{CR,\gamma}^{(\chi)}/[\Lambda_{CR,\gamma}^{(\chi)}]^2$, as independent free parameters. In the bottom panel of Fig. 2.9, assuming that only one of them is non-zero, we show the 90% confidence level exclusion curve from XENON1T data and the projected sensitivity curve for DARWIN as a function of the dark matter mass m_χ. Solid lines refer to the case when the γm CR interaction is switched off, with values of γm dipole coupling shown on vertical axis on the left-hand side; on the other hand, dashed lines assume that γm dipole interactions are negligible, with values of the γm CR coupling displayed on the scale on the right-hand side. In the top panel of Fig. 2.9,

Mediator	DM-nucleon operator			coherent	incoherent
SM photon	$(\bar{\chi} i\sigma^{\mu\nu} q_\nu \chi)(\bar{N}\gamma_\mu N)$		long-range	$\mathcal{O}_5$	none
			contact	$\mathcal{O}_1$	$\mathcal{O}_4, \mathcal{O}_6$
	$(\bar{\chi}\gamma^\mu \chi)(\bar{N}\gamma_\mu N)$		long-range	none	none
			contact	$\mathcal{O}_1$	none
Dark photon	$(\bar{N} i\sigma^{\mu\nu} q_\nu N)(\bar{\chi}\gamma_\mu \chi)$		long-range	none	$\mathcal{O}_3$
			contact	$\mathcal{O}_1$	$\mathcal{O}_4, \mathcal{O}_6$
	$(\bar{N}\gamma^\mu N)(\bar{\chi}\gamma_\mu \chi)$		long-range	none	none
			contact	$\mathcal{O}_1$	none

Table 2.2: Types of DM-nucleon interactions mediated by Standard Model and dark photons, and classifications of the non-relativistic operators generated from such interactions. For a given relativistic operator in the second column, the corresponding non-relativistic interactions are listed as effectively long-range/contact (*i.e.* of order $1/|\vec{q}|$ or $|\vec{q}|^0$) and coherent/incoherent.

we show instead exclusion and sensitivity curves in the plane $d^{(\chi)}_{M,\gamma}/\Lambda^{(\chi)}_{D,\gamma}$ versus $c^{(\chi)}_{CR,\gamma}/[\Lambda^{(\chi)}_{CR,\gamma}]^2$ for a few representative values of the DM mass m_χ: 200 GeV (dot-dashed lines), 1 TeV (dashed lines), and 2 TeV (solid lines). In this plot the solid diagonal line, which runs through the area where exclusion and sensitivity curves bend, approximately marks the separation between the *dipole-dominated* (region above the line) and the *CR-dominated* regimes (region below the line). In fact, looking at the expression for the recoil rate contribution from γm dipole interactions, this is mostly driven by the long-range and coherent $\mathcal{O}_5$ operator and can be approximated as:

$$\left(\frac{dR}{dE_R}\right)_{dip,\gamma} \simeq \mathcal{C}\,\alpha_{em}^2 \left(\frac{d^{(\chi)}_{M,\gamma}}{\Lambda^{(\chi)}_{D,\gamma}}\right)^2 \frac{4 s_\chi\,(s_\chi+1)}{3}\frac{1}{4\pi E_R} Z^2\,; \tag{2.70}$$

the γm CR contribution is instead of the form:

$$\left(\frac{dR}{dE_R}\right)_{CR,\gamma} \simeq \mathcal{C}\,\alpha_{em}^2 \left(\frac{c^{(\chi)}_{CR,\gamma}}{[\Lambda^{(\chi)}_{CR,\gamma}]^2}\right)^2 \frac{m_T}{2\pi v^2} Z^2\,. \tag{2.71}$$

Using Xe as nuclear target, and considering experiments which lose sensitivity below a recoil energy of few keV, we find:

$$\left(\frac{dR}{dE_R}\right)_{dip,\gamma} \Bigg/ \left(\frac{dR}{dE_R}\right)_{CR,\gamma}\Bigg|_{E_R\simeq 5\,\mathrm{keV}} \gtrsim 1 \quad\Longrightarrow\quad \frac{d^{(\chi)}_{M,\gamma}}{\Lambda^{(\chi)}_{D,\gamma}} \Bigg/ \frac{c^{(\chi)}_{CR,\gamma}}{[\Lambda^{(\chi)}_{CR,\gamma}]^2} \gtrsim 50\,\mathrm{GeV} \tag{2.72}$$

which is about the delimiter shown in the plot.

There are additional information displayed in Fig. 2.9. The orange polygonal region in the top panel denotes the pairs of dipole-CR coefficients obtainable in our model assuming $\alpha_L = 10^{-1}$, $m_\chi \in [200\,\mathrm{GeV}, 2\,\mathrm{TeV}]$, $m_{\phi_-} \in [1\,\mathrm{TeV}, 100\,\mathrm{TeV}]$, $m_{\phi_+} \in \{11\,\mathrm{TeV}, 10^3\,\mathrm{TeV}\}$, and $m_\chi \leq m_{\phi_-} \leq m_{\phi_+}$. As it can be seen, there are models in our framework that are excluded by XENON1T data, while DARWIN will cut deeper into the parameter space. The full region is within the area delimited by the condition in (2.72). Hence we can infer that within our

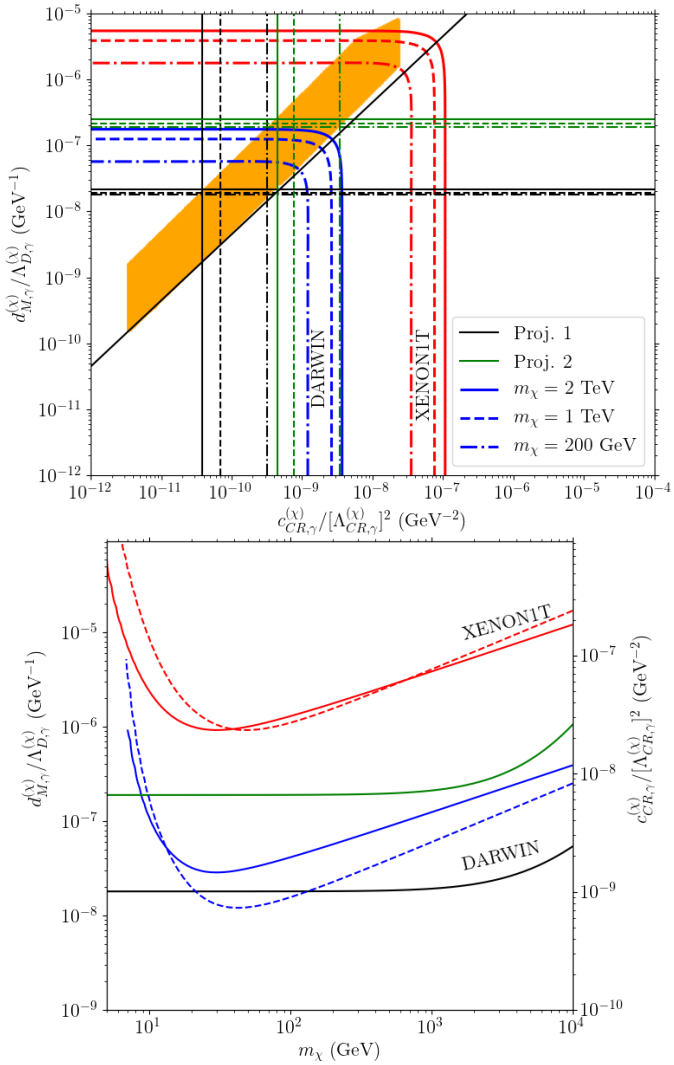

Figure 2.9: (Top) 90% confidence level exclusion curves from XENON1T data and the projected sensitivity curves for DARWIN for a few values of the dark matter mass m_χ in the plane dipole coupling versus CR coupling. The diagonal line gives a visual guidance to separate the regime in which, for a Xenon target and typical detector setups, direct detection rates are dominated by γm dipole interactions or γm CR interactions. The orange region is the area spanned by a large sample of models within our dark sector setup. The horizontal and vertical lines represent a projection of the muon magnetic dipole moment limit into a limit on, respectively, the dipole and CR coefficients, within our framework and for two representative cases: a model with large mixing for scalar messenger (Proj. 1) and one with small mixing (Proj. 2), see the text for details; the intersection points only should be compared with the result for XENON1T and DARWIN. (Bottom) Exclusion and projected sensitivity curves (90% CL) versus dark matter mass in case of either γm dipole interactions only (solid lines, referring to the vertical scale displayed on the left-hand side) or γm CR interactions only (dashed lines, referring to the vertical scale displayed on the right-hand side); also shown are the limits on the γm dipole coefficient derived within our framework and the same parameter choices as in the top panel.

framework, for what concerns γm interactions, the dipole term contributes more to the direct detection rate than the CR term, although the latter can be relevant as well. Note that this statement depends on the type of the nuclear target and on the range of recoil energies at which the experiment is sensitive.

Finally, in Fig. 2.9 we try to compare the direct detection limits and projected sensitivities with other constraints. There is no other process in which the operators introduced in Eq. (2.64) are tested at a significant level, and hence a model independent comparison is not possible. On the other hand, as described above, within our framework the loop diagrams giving rise to these interactions are closely related to the loop diagrams contributing to the magnetic dipole moments of leptons, which in turn are providing among the tightest constraints on our model, recall the discussion in Section 2.2.1. For reference, we consider the case in which the dark matter particle χ is coupled to muons (stronger constraints would follow in case of coupling to electrons; the limits get essentially irrelevant in case of coupling to tau leptons). The relation between coefficients of the different operators is simply:

$$\frac{d^{(\chi)}_{M,\gamma}}{\Lambda^{(\chi)}_{D,\gamma}} = \frac{F^{(\chi)}_{D,\gamma}\left(m_\mu, m_{\phi_-}, m_{\phi_+}\right)}{F^{(\mu)}_{D,\gamma}\left(m_\chi, m_{\phi_-}, m_{\phi_+}\right)} \frac{d^{(\mu)}_{M,\gamma}}{\Lambda^{(\mu)}_{D,\gamma}}, \quad \frac{c^{(\chi)}_{CR,\gamma}}{[\Lambda^{(\chi)}_{CR,\gamma}]^2} = \frac{1}{m_\chi} \frac{F^{(\chi)}_{CR,\gamma}\left(m_\mu, m_{\phi_-}, m_{\phi_+}\right)}{F^{(\mu)}_{D,\gamma}\left(m_\chi, m_{\phi_-}, m_{\phi_+}\right)} \frac{d^{(\mu)}_{M,\gamma}}{\Lambda^{(\mu)}_{D,\gamma}}\,. \tag{2.73}$$

Comparing against the experimental measurement of the muon magnetic dipole moment [198], we find:

$$\frac{d^{(\mu)}_{M,\gamma}}{\Lambda^{(\mu)}_{D,\gamma}} \leq 1.80 \times 10^{-8}\,\mathrm{GeV}^{-1}\,. \tag{2.74}$$

We project this limit into a limit on the γm dipole and γm CR coefficients (hence comparing at this level against direct detection) choosing two representative set of values for the masses of the corresponding scalar messenger: in the first — to which we refer as projection 1 — we choose a large mixing configuration $\left(m_{\phi_-}, m_{\phi_+}\right) = (10\,\mathrm{TeV}, 10^3\,\mathrm{TeV})$, while in the other — to which we refer as projection 2 — we consider a small mixing case $\left(m_{\phi_-}, m_{\phi_+}\right) = (10\,\mathrm{TeV}, 11\,\mathrm{TeV})$. In the top panel of Fig. 2.9 derived limits on γm dipole and γm CR coefficients are shown, respectively, as horizontal and vertical lines; the line-style reflects again the three sample choices for m_χ and the position of the crossing point of horizontal and vertical lines for the same model configuration should be compared to the corresponding direct detection curves (crossing points correspond to physical models in our framework, and, as expected, they all lie in the dipole dominated region). We see that in general, within our framework, the muon magnetic dipole moment limit is more constraining than the current direct detection limit. On the other hand, future detectors will be more sensitive to smaller dark matter dipole moments. Note that the effective dipole operator requires a change in the chirality of the external fermion, either through a sizable η_s or a mass insertion on the external leg. When η_s is sufficiently small, *i.e.* $\eta_s \ll m_\mu/m_\chi$, the muon dipole is proportional to m_μ while the dark matter dipole is proportional to m_χ: in this case the muon dipole tends to be much smaller than the dark matter dipole. The projected limits on the γm dipole are also shown in the bottom panel of Fig. 2.9; given that physical models in our framework have a direct detection rate mostly driven by γm dipole interactions to a first approximation the displayed limits can be compared to the direct detection curves shown in this plot is the case $c^{(\chi)}_{CR,\gamma}/[\Lambda^{(\chi)}_{CR,\gamma}]^2 = 0$, reinforcing the picture just described.

2.4.3 Dark photon-mediated processes

The same procedure outline above can be applied to compute the recoil rate in case of processes that are dark photon-mediated (in the following: $\gamma_D m$); we start with the effective SM quark-dark lepton interaction:

$$\mathcal{L}_{\gamma_D} = g_D^2 \frac{d^{(q)}_{M,\gamma_D}}{\Lambda^{(q)}_{D,\gamma_D}} \frac{1}{q^2} \left(\bar{q} i\sigma^{\mu\nu} q_\nu q\right) \left(\bar{\chi}\gamma_\mu \chi\right) + g_D^2 \frac{c^{(q)}_{CR,\gamma_D}}{[\Lambda^{(q)}_{CR,\gamma_D}]^2} \left(\bar{q}\gamma^\mu q\right) \left(\bar{\chi}\gamma_\mu \chi\right). \tag{2.75}$$

Borrowing the terminology from the previous section, we identify the first and second terms in (2.75) as $\gamma_D m$ *dipole* and *charge-radius* (CR) interactions, respectively. We then map the quark vector and tensor currents to nucleonic operators. The non-relativistic reduction of the effective DM-nucleon interaction yields

$$\begin{aligned}\mathcal{L}_{\gamma_D} &= g_D^2 \frac{d^{(N)}_{M,\gamma_D}}{\Lambda^{(N)}_{D,\gamma_D}} \left[-\frac{2m_N}{|\vec{q}|^2}\mathcal{O}_3\right] \\ &\quad + g_D^2 \left[\frac{d^{(N)}_{M,\gamma_D}}{\Lambda^{(N)}_{D,\gamma_D}} \frac{1}{2m_N} + \frac{d^{(N)}_{M,\gamma_D,1}}{\Lambda^{(N)}_{D,\gamma_D}} \frac{1}{m_N}\right] \mathcal{O}_1 + g_D^2 \frac{c^{(N)}_{CR,\gamma_D}}{[\Lambda^{(N)}_{CR,\gamma_D}]^2} \mathcal{O}_1 + g_D^2 \frac{d^{(N)}_{M,\gamma_D}}{\Lambda^{(N)}_{D,\gamma_D}} \left[\frac{2}{m_\chi}\mathcal{O}_4 - \frac{2m_N^2}{m_\chi |\vec{q}|^2}\mathcal{O}_6\right],\end{aligned} \tag{2.76}$$

where $\mathcal{O}_1, \mathcal{O}_4$, and $\mathcal{O}_6$ are defined in Eq. (2.68), and

$$\mathcal{O}_3 \equiv i\vec{S}_N \cdot \left(\frac{\vec{q}}{m_N} \times \vec{v}^\perp\right). \tag{2.77}$$

Using the numerical values of QCD matrix elements obtained from lattice calculations [232], the coefficients in Eq. (2.76) are in the form

$$\frac{d^{(N)}_{M,\gamma_D}}{\Lambda^{(N)}_{D,\gamma_D}} \equiv f_T \left\langle \frac{d^{(q)}_{M,\gamma_D}}{\Lambda^{(q)}_{D,\gamma_D}} \right\rangle, \quad \frac{d^{(N)}_{M,\gamma_D,1}}{\Lambda^{(N)}_{D,\gamma_D}} \equiv f_{T1} \left\langle \frac{d^{(q)}_{M,\gamma_D}}{\Lambda^{(q)}_{D,\gamma_D}} \right\rangle, \quad \frac{c^{(N)}_{CR,\gamma_D}}{[\Lambda^{(N)}_{CR,\gamma_D}]^2} \equiv f_1 \left\langle \frac{c^{(q)}_{CR,\gamma_D}}{[\Lambda^{(q)}_{CR,\gamma_D}]^2} \right\rangle, \tag{2.78}$$

with

$$f_T = 0.59 \pm 0.023, \qquad f_{T1} = 0.79, \qquad f_1 = 3, \tag{2.79}$$

and angle brackets denoting weighted averages that can be safely removed if $\gamma_D m$ dipole and CR coefficients are about the same for all light quarks. Analogously to the previous case, we organized the terms in Eq. (2.76) in powers of $|\vec{q}|$, with the first line of order $1/|\vec{q}|$ and the second of order $|\vec{q}|^0$. In the non-relativistic reduction, the $\gamma_D m$ dipole interaction has led to: (i) a long-range, incoherent $\mathcal{O}_3$ term, (ii) a contact, coherent $\mathcal{O}_1$ term, and (iii) other short-range, incoherent terms; the $\gamma_D m$ CR interaction has generated only one leading operator corresponding to a contact, coherent $\mathcal{O}_1$ term. A summary with relativistic operators and the corresponding non-relativistic reductions is given in Table 2.2.

Similarly to what has been done above for the γm case, we consider first the $\gamma_D m$ dipole and CR couplings to a quark as two independent coefficients, without any reference to our

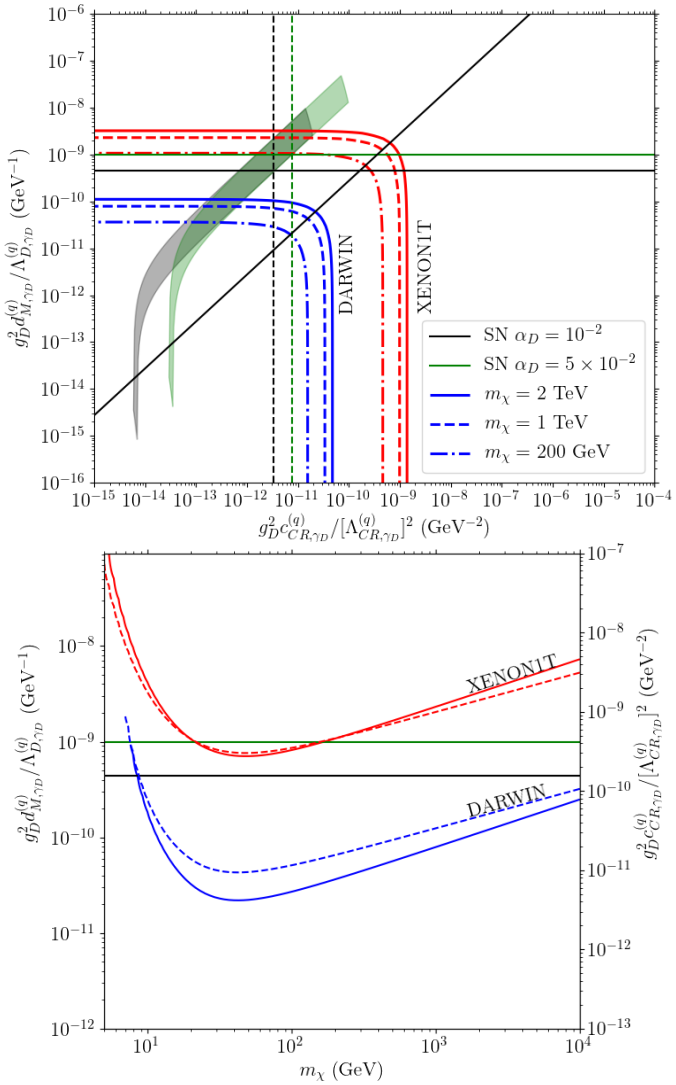

Figure 2.10: 90% CL exclusion curves from XENON1T data and projected sensitivity curves for DARWIN in case of γ_D-mediated DM-nucleus scatterings, in the plane dipole-CR coefficients (top panel) or when assuming that only one of the two coefficients is non-zero (bottom panel, solid lines and the vertical scale on the left side refer to the $\gamma_D m$ dipole operator, while dashed lines and the vertical scale on the right side refer to the $\gamma_D m$ CR operator). Model-independent supernova cooling limit on the $\gamma_D m$ dipole for quarks are displayed as horizontal solid lines for two representative values of α_D: 10^{-2} (black) and 5×10^{-2} (green). Also shown in the top panel are two results specific for our dark sector framework: vertical dashed lines represent the projection of the supernova limit on the $\gamma_D m$ CR coefficient - the intersection points with horizontal lines should be compared against direct detection results; the coloured regions correspond to two representative scans in the model parameter space, see the text for details.

scheme. In the top panel of Fig. 2.10, 90% confidence level exclusion curve from XENON1T data and projected sensitivity curves for DARWIN are shown in the plane $g_D^2\, d_{M,\gamma_D}^{(q)}/\Lambda_{D,\gamma_D}^{(q)}$ versus $g_D^2\, c_{CR,\gamma_D}^{(q)}/[\Lambda_{CR,\gamma_D}^{(q)}]^2$ for a few sample values of the dark matter mass: $m_\chi = 200\,\text{GeV}, 1\,\text{TeV}, 2\,\text{TeV}$. In the bottom panel they are shown instead versus mass, assuming that only one among the

two coefficients are different from zero. The solid diagonal line in the top panel marks again the separation between the dipole-dominated region and CR-dominated region, as we can check looking at the expressions for the differential recoil rate. As in the previous case, CR interactions contributes with the coherent term in the form

$$\left(\frac{dR}{dE_R}\right)_{CR,\gamma_D} \simeq \mathcal{C}' \left(g_D^2 \frac{c^{(q)}_{CR,\gamma_D}}{[\Lambda^{(q)}_{CR,\gamma_D}]^2}\right)^2 \frac{m_T}{2\pi v^2}\, f_1^2 A^2\,, \tag{2.80}$$

where A is the atomic number of the target nucleus. On the other hand and contrary to the previous case, for $\gamma_D m$ dipole interaction we cannot a priori assume that the long-range effects dominate: given that the long-range $\mathcal{O}_3$ term is incoherent, we need to keep also the short-range coherent $\mathcal{O}_1$ term, getting

$$\left(\frac{dR}{dE_R}\right)_{dip,\gamma_D} \simeq \mathcal{C}' \left(g_D^2 \frac{d^{(q)}_{M,\gamma_D}}{\Lambda^{(q)}_{D,\gamma_D}}\right)^2 \frac{f_T^2}{2\pi}\left[\frac{2}{3\,E_R}\left\langle \vec{S}_N^2\right\rangle + \frac{4\,m_T}{v^2\,m_N^2}\left\langle \left(\vec{L}\cdot\vec{S}_N\right)^2\right\rangle + \frac{A^2\,m_T}{v^2\,m_N^2}\left(\frac{1}{2}+\frac{f_{T1}}{f_T}\right)^2\right], \tag{2.81}$$

where S_N is the spin operator for the valence nucleon (which is usually relevant for odd-even nuclei) and L is the angular momentum associated with the internal motion of the valence nucleon. Among the three contributions on the right-hand-side, although the first has a m_N/E_R enhancement, this has to compete with the large A^3 and $1/v^2$ enhancements in the third term; moreover, the second term is most often sub-leading compared to the third given that $\langle(\vec{L}\cdot\vec{S}_N)^2\rangle \approx l_{max}^2$, where l_{max} is the maximum angular quantum number attained by the valence nucleon, typically much less than A. Comparing first and third contributions, one finds that the long-range $1/E_R$ enhancement takes over only at recoil energies

$$E_R \lesssim \left(1.5\times 10^{-7}\,\mathrm{keV}\right)\left[\frac{s_N(s_N+1)}{3/4}\right]\left(\frac{v}{10^{-3}}\right)^2\left(\frac{100}{A}\right)^3, \tag{2.82}$$

i.e. in a range which is irrelevant for a Xe target (as well as any target presently considered) and current detector technologies. Hence the third term is the leading one, and when taking the ratio between the rate in Eq. (2.81) and that in Eq. (2.80) one finds

$$\left(\frac{dR}{dE_R}\right)_{dip,\gamma_D} \Bigg/ \left(\frac{dR}{dE_R}\right)_{CR,\gamma_D} \simeq \left(g_D^2 \frac{d^{(q)}_{M,\gamma_D}}{\Lambda^{(q)}_{D,\gamma_D}} \Bigg/ g_D^2 \frac{c^{(q)}_{CR,\gamma_D}}{[\Lambda^{(q)}_{CR,\gamma_D}]^2}\right)^2 \frac{f_T^2}{m_N^2\, f_1^2}\left(\frac{1}{2}+\frac{f_{T1}}{f_T}\right)^2. \tag{2.83}$$

It follows that:

$$\left(\frac{dR}{dE_R}\right)_{dip,\gamma_D} \Bigg/ \left(\frac{dR}{dE_R}\right)_{CR,\gamma_D} \gtrsim 1 \quad\Longrightarrow\quad g_D^2 \frac{d^{(q)}_{M,\gamma_D}}{\Lambda^{(q)}_{D,\gamma_D}} \Bigg/ g_D^2 \frac{c^{(q)}_{CR,\gamma_D}}{[\Lambda^{(q)}_{CR,\gamma_D}]^2} \gtrsim 2.8\,\mathrm{GeV}\,, \tag{2.84}$$

which is the delimiter shown as a solid diagonal line in the top panel of Fig. 2.10.

Turning now to constraints competing with direct detection results, contrary to the γm case, there is a strong model-independent bound impacting directly on the first operator in Eq. (2.75). In fact, the $\gamma_D m$ dipole for quarks can be responsible for enhancing the cooling rate in supernovae, allowing for nucleon-nucleon Bremsstrahlung emission of dark photons; as

discussed in Section 2.2.1, there is a tight constraint one can extrapolate from the observed neutrino flux from SN1987A. The detailed derivation of the limit is rather involved and beyond the scope of this study; we consider instead an extrapolation from analogous scenarios. In particular, Raffelt [204] computed the energy loss rate due to nucleon-nucleon Bremsstrahlung with axion emission, with the axion entering through a derivative coupling with the nucleon axial current. More recently an improved calculation has been implemented in [234]. For the case of γ_D emission, Dobrescu [202] assumed that the rate of energy loss is two times larger than in the case of axion emission, given that the dark photon has two propagating degrees of freedom. If one writes the effective nucleon-γ_D interaction as

$$\mathcal{L}_{N\gamma_D} = \frac{g_{N\gamma_D}}{4m_N} \bar{N}\sigma^{\mu\nu} N \; X_{\mu\nu}, \tag{2.85}$$

following Raffelt and imposing that the extra energy loss rate per unit mass induced by the novel Bremsstrahlung process cannot exceed $10^{19}\,\mathrm{erg\ g^{-1}\ s^{-1}}$, we find:

$$g_{N\gamma_D} \lesssim 1.414 \times 10^{-9} \; f^{1/2}. \tag{2.86}$$

Here, f is a fudge factor accounting for the deviation from the Dobrescu assumption on the cooling rate when actually using (2.51) (in the following we will just set it to 1). Mapping the quantity $g_{N\gamma_D}$ to the quark dipole moment in (2.51), and then mapping to the $\gamma_D m$ dipole coefficient constrained by direct detection, we have

$$g_D^2 \frac{d^{(q)}_{M,\gamma_D}}{\Lambda^{(q)}_{D,\gamma_D}} \lesssim \left(4.18 \times 10^{-10}\,\mathrm{GeV}^{-1}\right) f^{1/2} \left(\frac{\alpha_D}{10^{-2}}\right)^{1/2} \left(\frac{g^{(lim)}_{N\gamma_D}}{1.414 \times 10^{-9}}\right) \left(\frac{1\,\mathrm{GeV}}{m_N}\right) \left(\frac{0.6}{f_T}\right). \tag{2.87}$$

This limit is shown with horizontal solid lines in the top and bottom panels of Fig. 2.10, for $\alpha_D = 10^{-2}$ (black) and $\alpha_D = 5 \times 10^{-2}$ (green). As it can be seen, at face value, the supernova limit is constraining $\gamma_D m$ dipole of quarks at a comparable level with respect to current direct detection data, while, regarding future sensitivities, direct detection experiments are going to be more competitive. On the other hand, the validity of the supernova limit has been recently questioned [235] since it relies on a mainstream picture for the explosion mechanism of core-collapse supernovae which is still, to a large extent, not well-established; in alternative scenarios the limit in Eq. (2.86) simply does not apply. In this respect, information on the $\gamma_D m$ dipole of quarks derived from direct detection searches seem more reliable.

While the $\gamma_D m$ CR operator does not contribute the dark photon emission via nucleon-nucleon Bremsstrahlung, a constraint can be indirectly derived within our framework implementing

$$g_D^2 \frac{c^{(q)}_{CR,\gamma_D}}{[\Lambda^{(q)}_{CR,\gamma_D}]^2} = \frac{1}{m_Q} \frac{F^{(q)}_{CR,\gamma_D}\left(m_Q, m_{S_-}, m_{S_+}\right)}{F^{(q)}_{D,\gamma_D}\left(m_Q, m_{S_-}, m_{S_+}\right)} \; g_D^2 \frac{d^{(q)}_{M,\gamma_D}}{\Lambda^{(q)}_{D,\gamma_D}}. \tag{2.88}$$

In the top panel of Fig. 2.10, limits on the $\gamma_D m$ CR coefficient, as derived from the supernova limit on the $\gamma_D m$ dipole, are shown with dashed vertical lines; these projections are obtained assuming $m_Q = 10\,\mathrm{GeV}$, $m_{S_-} = 10\,\mathrm{TeV}$, and $m_{S_+} = 10^3\,\mathrm{TeV}$. Note that vertical and horizontal lines cross in the dipole-dominated regime, hence the relevant comparison with direct detection

rates is still in the limit of vanishing CR coefficient. Dipole dominance is typical for the parameter space in our scheme. In the top panel of Fig. 2.10 we show the regions in the dipole-CR plane corresponding to a scan with $\alpha_L = 10^{-1}$, $m_Q \in [10\,\text{GeV}, 50\,\text{GeV}]$, $m_{S_-} \in [10\,\text{TeV}, 10^3\,\text{TeV}]$, $m_{S_+} = 1.001 \times 10^3\,\text{TeV}$, and either $\alpha_D = 10^{-2}$ (grey region) or $\alpha_D = 5 \times 10^{-2}$ (green region); in scanning the model space, we ensured that $m_Q \leq m_{S_-} \leq m_{S_+}$. Most models are in the dipole-dominated area, with only tails extending into the CR-dominated regime in case the $\gamma_D m$ dipole gets severely suppressed when S_- and S_+ are very close in mass and hence the mixing η_s is very small.

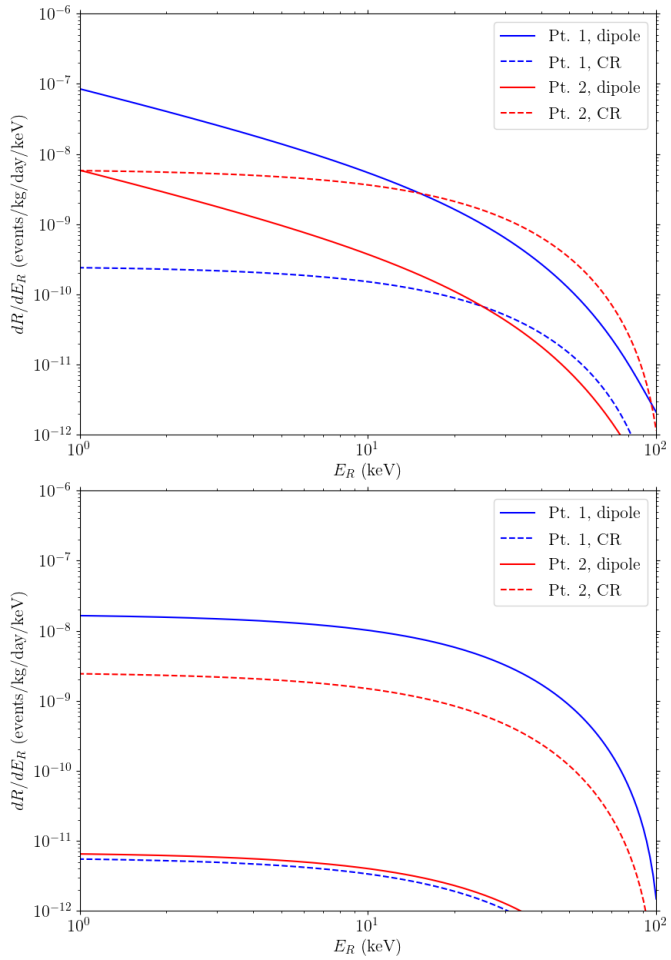

Figure 2.11: Recoil spectra due to γm interactions (top panel) and $\gamma_D m$ interactions (bottom panel) for sample models in our dark sector framework. For each of the two cases, representative points in the parameter space have been chosen to have either a dipole-dominated spectrum (Pt. 1), or a CR-dominated spectrum (Pt. 2); model parameters are specified in Table 2.3. Contributions to the rate due to the dipole operator and the CR operators are shown separately, respectively with solid and dashed lines. Note the long-range $1/E_R$ enhancement appears only in case of γm dipole interactions.

In Fig. 2.11, we plot recoil spectra in case of γm interactions (top panel) and $\gamma_D m$ interactions (bottom panel) for sample models in our dark sector framework. For each mediator, we have chosen two representative points such that "Pt. 1" lies in the corresponding dipole-dominated region, while "Pt. 2" in the CR-dominated regime: the corresponding model parameters are

Mediator	Model parameters	Dipole (GeV^{-1})	CR (GeV^{-2})
γ (Pt. 1)	$\alpha_L = 0.1, m_\chi = 1\,\mathrm{TeV}$ $m_{\phi_-} = 10\,\mathrm{TeV}, m_{\phi_+} = 11\,\mathrm{TeV}$	1.45×10^{-7}	5.21×10^{-10}
γ (Pt. 2)	$\alpha_L = 0.1, m_\chi = 50\,\mathrm{GeV}$ $m_{\phi_-} = 5\,\mathrm{TeV}, m_{\phi_+} = 6\,\mathrm{TeV}$	2.70×10^{-8}	1.81×10^{-9}
γ_D (Pt. 1)	$\alpha_L = 0.1, \alpha_D = 10^{-2}, m_Q = 10\,\mathrm{GeV}$ $m_{S_-} = 50\,\mathrm{TeV}, m_{S_+} = 10^3\,\mathrm{TeV}$	1.28×10^{-10}	9.95×10^{-13}
γ_D (Pt. 2)	$\alpha_L = 0.1, \alpha_D = 10^{-2}, m_Q = 10\,\mathrm{GeV}$ $m_{S_-} = 14\,\mathrm{TeV}, m_{S_+} = 14.014\,\mathrm{TeV}$	2.55×10^{-12}	2.09×10^{-11}

Table 2.3: List of representative models chosen for generating the recoil spectra in Fig. 2.11.

specified in Table 2.3. Contributions to the differential rate of the dipole and CR operators are shown separately. Notice the qualitatively different shapes of the dipole contribution in the two cases: the $1/E_R$ scaling due to long-range interactions can be seen in the γm case, while contact interactions dominate in the $\gamma_D m$ case. Notice also that Pt. 2 in the γm case is rather peculiar, since to find a model within the CR-dominated regime we were forced to consider a relatively small m_χ, below the range considered for the scan displayed in Fig. 2.10 and what we expect typically in our framework.

2.4.4 Comparison with relic density limits

We are now ready to combine direct detection results with the constraints on our framework obtained by imposing that the relic density of χ matches the observed abundance of DM in the Universe, $\Omega_{DM}h^2 = 0.1200 \pm 0.0012$ [9]. We refer to our minimal 6-parameter setup, slicing the parameter space along the $m_\chi - \alpha_L$ plane for reference values of the dark photon coupling α_D, of the common scalar messenger mass parameter $m_\phi = m_S$ and mixing η_s, and of the mass m_Q for light quark-like dark fermions. In Fig. 2.12, along the curves labelled "relic" the dark matter relic density matches the observed dark matter density. In the "south-east" direction, *i.e.* towards larger m_χ and smaller α_L, the χ relic density exceeds the observed dark matter density, assuming that α_D is fixed. In the opposite direction, the χ relic density is a fraction of the observed dark matter density. These portions of the parameter space could be, in principle, recovered referring to, *e.g.*, non-thermal production of dark matter or non standard cosmological frameworks, see, *e.g.*, [236, 237]).

In the top-left panel a maximal scalar mixing $\eta_s = 1 - (m_\chi/m_\phi)^2$ has been considered, while in the top-right panel it is tuned to zero; results for two representative values of α_D are displayed, namely 10^{-2} (solid lines) and 5×10^{-2} (dashed lines), while the other parameters are fixed to $m_Q = 10\,\mathrm{GeV}$ and $m_S = 10\,\mathrm{TeV}$. Each isolevel curve for $\Omega_\chi h^2$ exhibits the features described by the decoupling regimes for χ discussed in Sec. 2.3.3. The upper branch corresponds to region IV, where the $\chi\bar{\chi}$ annihilation to SM leptons controls the final relic density of χ. The vertical branch corresponds to region III where the annihilation to γ_D determines the final relic density of χ: note that, in order to have the same relic density, increasing α_D requires increasing m_χ as well, which is consistent with the expectation from Eq. (2.16). The remaining branch corresponds

to region II, where the final relic density is still determined by the γ_D channel, but in the relic density regime given by Eq. (2.49), where a larger α_L leads to larger $\xi_{f.o.}$ and thus m_χ must decrease accordingly (since $\langle\sigma v\rangle_{\gamma_D}$ goes as m_χ^{-2}). The branch for region I is not shown in these plots, but would simply correspond to a vertical line at lower values of α_L.

Concerning direct detection limits and projected sensitivities, in the top-left panel of Fig. 2.12, the XENON1T and DARWIN curves (solid lines corresponding again to $\alpha_D = 10^{-2}$, while dashed lines to 5×10^{-2}) are driven by the $\gamma_D m$ dipole operator, given that in the large mixing scenario this gives a larger event rate than the $\gamma_D m$ CR operator: we find that a large part of the upper branches with correct value of the relic density is already excluded by current direct detection limits, while a larger portion of region III will be tested with DARWIN. On the other hand, in the top-right panel $\eta_s = 0$ suppresses the role of the $\gamma_D m$ dipole operator and the $\gamma_D m$ CR operator provides instead the bulk of the direct detection events: while current esperiments do not test this regime, DARWIN will be able to probe the branch with correct relic density in the region IV snd a portion of the one in region III. Note however that these results depend to some extent on the assumption of universality in the scalar messenger sector: the displayed direct detection curves would shift to larger values of α_L in case some hierarchy between ϕ and S is assumed, with a larger m_S relaxing the direct detection limits, without any significant impact on the result for the relic density of χ, given that the S scalars only interact with SM quarks.

A tighter connection appears with limits and projected sensitivities when including γm interactions; having artificially switching off $\gamma_D m$ interactions, in the bottom panel of Fig. 2.12 we show the curves stemming from the γm dipole coupling, together again with the relic density isolevel curves in case of both $\eta_s = 1 - (m_\chi/m_\phi)^2$ and $\eta_s = 0$ (in this plot we are always the *dipole-dominated* region in Fig. 2.9, hence the γm CR coupling plays a minor role). Such results look less constraining than for $\gamma_D m$ interactions, however they do not depend on m_S or η_s, and hence can be more solidly compared against the relic density lines: we find that XENON1T data are in fact excluding part of the upper branch at small η_s which was not tested via the $\gamma_D m$ operators, as well as that DARWIN will have a sizable impact in probing our scenario.

2.5 Summary and conclusions

It is plausible that the solution to the dark matter problem may be in a context in which, on top of one or more particles accounting for dark matter, there are several extra states and/or extra forces. In this work, we have considered a toy model realization of a multicomponent dark sector, with an additional unbroken U(1) gauge interaction, mediated by a massless dark photon, and with portal interactions between dark fermions and SM fermions through scalar messengers. The model is characterized by: (i) the dark U(1) coupling α_D, (ii) the Yukawa-like portal couplings $\alpha_{L,R}$, and (iii) the masses of the scalar messengers and the dark fermions. Despite its simplicity, this model has a rich dynamics and several phenomenological consequences. Its stable relics can provide a significant additional radiation component, as well as match the measured dark matter density in the Universe, with dark components having sizable interactions with ordinary matter as well as non-negligible self-interactions.

To characterize these features and have reliable estimates of final particle densities and temperatures, we have introduced a properly extended system of coupled Boltzmann equations, which track simultaneously the number density of several particle species, as well as entropy

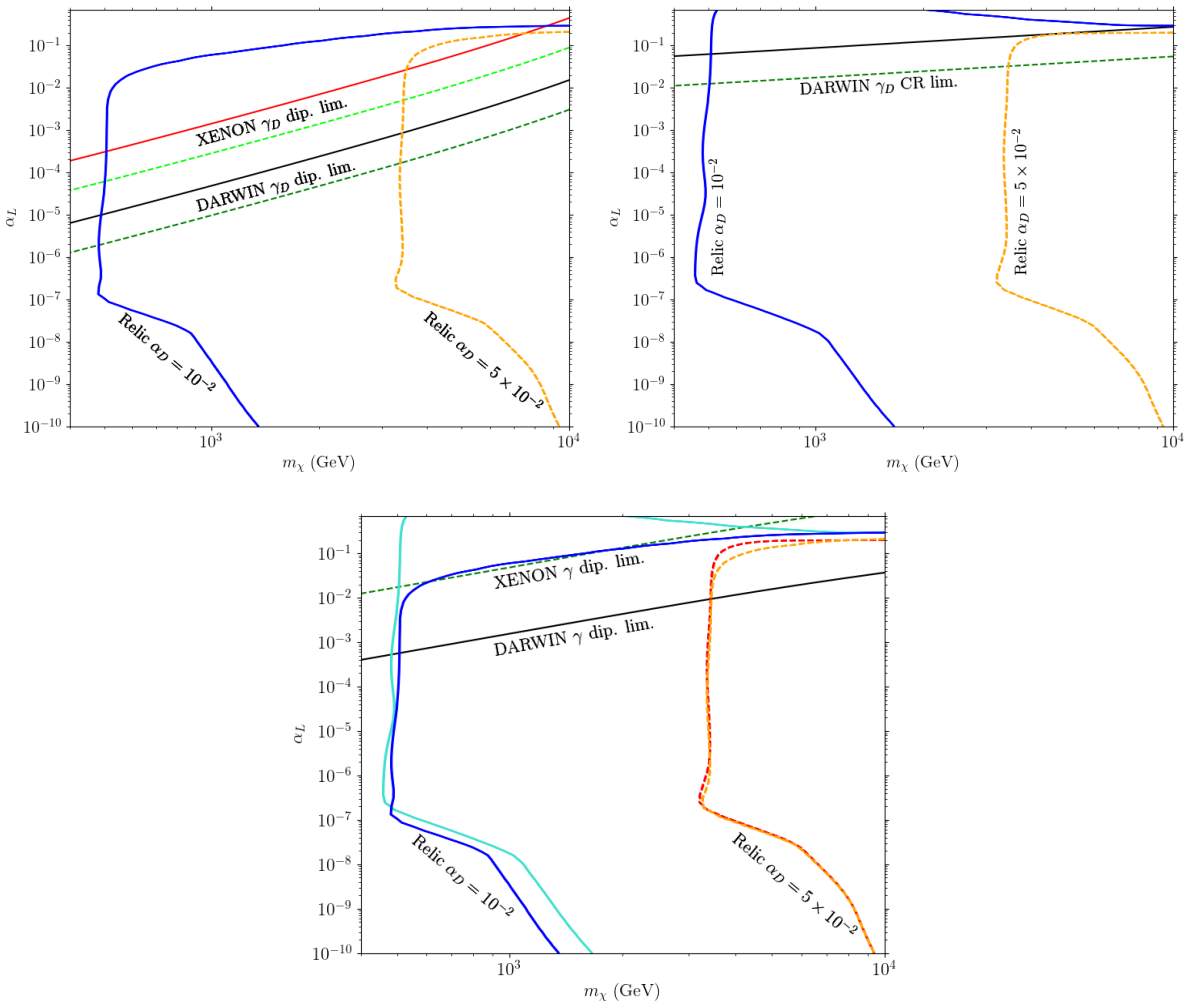

Figure 2.12: The lines labelled "relic" correspond to model parameters α_L and m_χ for which the relic density of χ matches the abundance of dark matter in the Universe. In the top-left panel the case of maximal mixing for scalar messengers is considered, while in the top-right a case with $\eta_s = 0$ is displayed; in these two panels solid lines refer to the choice of $\alpha_D = 10^{-2}$ and dashed lines to $\alpha_D = 5 \times 10^{-2}$, while the other parameters the model are fixed to sample values, see the text for details. Also displayed in two top panels are XENON1T limits and DARWIN sensitivity curves due to $\gamma_D m$ interactions, mainly due to the dipole operator in case of large mixing and the CR operator in case of zero mixing; solid and dashed lines refer again to the two sample values of α_D. In the bottom panel the four relic density isolevel curves from the top panels are reproduced to be shown against XENON1T and DARWIN results in case γm interactions are included while $\gamma_D m$ interactions are switched off (by *e.g.*, raising the mass scale for scalar messengers in the quark sector); the dipole term is dominant and results do not depend on η_s or α_D.

and energy exchanges between the dark and visible sectors. We have solved it numerically, implementing a few procedures allowing for fast - but very accurate - solutions. The target is to have a lepton-like dark fermion χ as the dark matter candidate, a requirement which selects viable regions in the model parameter space, without however singling out a definite scheme

for the dark matter generation in the early Universe. In fact, depending on the strength of the Yukawa portal between visible and dark sector, we have identified four different regimes for the χ production, ranging from the limit of a WIMP-like scenario in a totally decoupled dark sector, to a FIMP-like generation in case of intermediate coupling, and up to a standard WIMP framework when the two sectors come and stay in kinetic equilibrium all the way through the chemical decoupling of all dark sector species. As a consequence, our framework is not very predictive regarding the mass scale of the dark matter candidate, which we can only point to be rather heavy, in the range, say, 500 GeV-10 TeV, with portal couplings all the way from about $\alpha_L \simeq 10^{-2}$-1, down to around 10^{-9}-10^{-7}.

The result on the relic density for lepton-like dark fermion χ is weakly dependent on the choice for the masses of the lighter quark-like dark fermions Q. The latter can have a negligible contribution to the Universe matter density, say below 1% with respect to the heavy dark lepton contribution, if there is a sizable mass splitting between χ and Q, say $m_Q \lesssim 100\,\text{GeV}$ for $m_\chi \gtrsim 1\,\text{TeV}$. On the other hand, the presence of light dark fermions enters critically in setting the temperature ratio ξ between dark photons and SM photons at the kinetic decoupling between the two sectors; this is one of the most critical observables in our model, since the CMB constraint on the amount of extra radiation in the Universe (usually given in terms of the effective number of neutrino-like species N_{eff}) limits ξ to be at most 0.6 (at the 3-σ level). For a given portal coupling, constraints on the number and masses of light quark-like dark fermions follow: *e.g.*, in a scenario with two light dark quarks ($N_Q = 2$) and the early-time temperature ratio initialized to $\xi_0 = 0.1$, the limit on ξ_{CMB} is satisfied at 1-σ level for any dark quark mass m_Q if $\alpha_L \lesssim 10^{-7}$; for $\alpha_L \simeq 10^{-3}$, m_Q lighter than 10 GeV (2 GeV) are excluded at 1-σ (at 2-σ); if $\alpha_L \simeq 10^{-1}$, Q lighter than about 0.5 GeV are excluded at more than 3-σ.

Regarding other constraints on our scenario, we checked its testability with direct detection searches. The elastic scattering of the dark matter candidate χ on a nucleus can be mainly driven by dipole (dimension 5) or charge radius (dimension 6) interactions mediated by either the SM photon or the dark photon. We have analyzed on general grounds the interplay among the different operators, discussing features in the recoil spectrum and enlightening that long-range effects are not always predominant (as usually assumed in this context). After deriving current limits and projected sensitivities for next-generation detectors in terms of generic dipole and charge radius couplings, we have applied the results to our specific toy model, showing, *e.g.*, that the DARWIN experiment will cover a significant portion of the parameter space in which χ is a viable dark matter candidate, as well as it will be competitive against the tightest (but model-dependent) constraints at present, including extra contributions to the magnetic dipole moments of leptons and extra cooling of stellar systems.

This exploratory work on a particular realization of a multicomponent dark sector model, can be extended further by investigating more general early-time initial conditions as well as a further extension of the particle content or more general particle interactions. Furthermore aspects are also not discussed here, such as its mapping on precision and accelerator physics, or further cosmological and astrophysical implications, including, *e.g.*, the level of dark matter self-interactions. Some of this directions will be investigated in future work.

Chapter 3

Minimal SUSY framework for $g-2$

In Sec.(1.2.2) we have briefly touched upon the Fermilab measurement of the magnetic moment of the muon, and found that the experimental measurement of the g-factor differs from the SM prediction by an amount that is quantified by a_μ, whose current value is

$$a_\mu \equiv \frac{g_\mu - 2}{2} = (23.0 \pm 6.9) \times 10^{-10}. \tag{3.1}$$

We note again that $g_\mu = 2$ is the prediction from the Dirac equation, and the theoretical prediction from the SM accounts the various quantum corrections from QED, QCD, and the electroweak sector. The goal of this section is to account for this anomaly from the context of new physics. This is achieved by considering a minimal model, inspired by the interactions and particle content within the framework of the minimal supersymmetric SM (MSSM). In our setup, the new physics model consists of the following particles: a bino-like Majorana fermion, $\tilde{B}$, that is taken to be a singlet under the SM; a lepton-like scalar $\tilde{l}_L$ (containing the muon sneutrino $\tilde{\nu}$ and smuon left $\tilde{\mu}_L$), analogous to the left handed sleptons in the MSSM, with the same quantum numbers as its corresponding left handed lepton doublet; and a lepton-like scalar $\tilde{\mu}_R$, the right handed smuon, which is the partner of the right handed muon. Meanwhile, we introduce the bino-slepton-lepton interaction in this setup via

$$\mathcal{L} \supset -\lambda_L \tilde{l}_L^\dagger \bar{B}_R l_L - \lambda_R \tilde{\mu}_R^\dagger \bar{B}_L \mu_R + \text{h.c.} \tag{3.2}$$

In principle, the couplings λ_L and λ_R can be arbitrary complex parameters; in the MSSM, (3.2) arises from the gaugino interactions, and these couplings take the form

$$\lambda_{L,R} = \sqrt{2}\, g_Y Y_{L,R}. \tag{3.3}$$

Notice the resemblance of (3.2) with the portal interactions (2.1) that we have introduced in the multicomponent dark sector framework: the scalar messengers in the previously discussed dark sector model correspond to sleptons in this minimal framework, while the dark fermions correspond to the bino. The important difference between the current setup with the multicomponent dark sector is, in this minimal framework we are considering, the bino is a Majorana fermion that is neutral and cannot have any kind of charge, in contrast with the dark fermions that are charged under the dark U(1) gauge interaction.

In what follows, we assume that the CP-violating phases of λ_L and λ_R are set to zero. In addition to the gaugino-like interactions (3.2), we have the mass matrix for the left- and right-handed sleptons given by

$$\mathcal{L} \supset -\begin{pmatrix}\tilde{\mu}_L^\dagger & \tilde{\mu}_R^\dagger\end{pmatrix}\begin{pmatrix}m_{LL}^2 & m_{LR}^2 \\ m_{LR}^2 & m_{RR}^2\end{pmatrix}\begin{pmatrix}\tilde{\mu}_L \\ \tilde{\mu}_R\end{pmatrix} - m_{LL}^2\tilde{\nu}_L^\dagger\tilde{\nu}_L. \tag{3.4}$$

In the MSSM, the various contributions to the slepton mass parameters in (3.4) are set by the different terms appearing in the MSSM Lagrangian. First, the soft-SUSY breaking mass terms given by

$$\mathcal{L} \supset -m_{LL,soft}^2\tilde{l}_L^\dagger\tilde{l}_L - m_{RR,soft}^2\tilde{\mu}_R^\dagger\tilde{\mu}_R. \tag{3.5}$$

Additional contributions can also come from the so-called D-terms, which also give rise to the Higgs quartic potential; for a gauge group schematically represented by α, whose generators are t_A, the associated D-term is generically given by

$$\mathcal{L}_D = -\frac{1}{2}\sum_A\left|\sum_i \mathcal{S}_i^\dagger g_\alpha t_A^{(\alpha)}\mathcal{S}_i\right|^2, \tag{3.6}$$

where $\mathcal{S}_i$ is any scalar field in some representation of the gauge group. In principle, the D-terms in the Lagrangian arise in the MSSM from eliminating the nondynamical D_a field through its equation of motion, and replacing it with an expression involving the dynamical fields in the theory. On the other hand, one can think of the individual D-terms as additional renormalizable operators that are allowed by symmetries; the coefficients that appear in the D-terms can be completely arbitrary, only that SUSY imposes that these coefficients are related to the gauge couplings. If we adhere to this choice of the couplings, one can show that

$$\mathcal{L}_D = -\frac{g_Y^2}{2}\left|\sum_i Y_i\mathcal{S}_i^\dagger\mathcal{S}_i\right|^2 - \frac{g^2}{4}\left[\mathrm{tr}\left\{M^2\right\} - \frac{1}{2}\left(\mathrm{tr}\left\{M\right\}\right)^2\right], \tag{3.7}$$

where g_Y and g are the U(1) and SU(2) gauge couplings, respectively, Y_i is the hypercharge of $\mathcal{S}_i$ in which we take the normalization such that:

$$Q_i = T_{3i} + Y_i, \tag{3.8}$$

where Q_i is the electromagnetic charge of species i, and

$$M_{AB} \equiv \sum_i \mathcal{S}_{iA}\mathcal{S}_{iB}^\dagger; \tag{3.9}$$

the indices in uppercase Roman letters refer to SU(2) indices in the fundamental representation. We further assume that there is only one Higgs doublet, which one can write in the unitary gauge as

$$H = \frac{1}{\sqrt{2}}e^{i\vec{\pi}\cdot\vec{t}/v}\begin{pmatrix}0 \\ v+h\end{pmatrix}, \tag{3.10}$$

where the $\vec{\pi}$ are the Nambu-Goldstone bosons and v is the nonzero vacuum expectation value of the Higgs field. Note that the situaton of a single Higgs doublet is in contrast with the case in the MSSM where there are two Higgs doublets, as required by the holomorphicity of the superpotential and anomaly cancellation. One can then show that the scalar-neutral Higgs interaction is given by

$$\mathcal{L} \supset m_Z^2 \sum_j \mathcal{S}_j^\dagger \left(\hat{T}_3 - \hat{Q}_{em} s_W^2\right) \mathcal{S}_j \ \left(1 + \frac{h}{v}\right)^2 - \frac{m_{LR}^2}{v} h(\tilde{\mu}_L \tilde{\mu}_R^\dagger + \text{h.c.}), \tag{3.11}$$

where the last term, in principle, is put in by hand, but it arises from the A-terms in the superpotential from an MSSM context. The diagonal elements of the smuon mass matrix are then given by

$$m_{LL}^2 = m_{LL,soft}^2 - m_Z^2 \left(-\frac{1}{2} + s_W^2\right) \tag{3.12}$$

$$m_{RR}^2 = m_{RR,soft}^2 - m_Z^2 s_W^2, \tag{3.13}$$

while the sneutrino mass parameter is

$$m_{\tilde{\nu}}^2 = m_{LL,soft}^2 - \frac{m_Z^2}{2}. \tag{3.14}$$

Note that $s_W \equiv \sin\theta_W$, where θ_W is the weak mixing angle. One can introduce a convenient parametrization for the mass parameters in terms of the mass eigenvalues m_1 and m_2, where $m_1 < m_2$, and the mixing angle θ via

$$m_{LL}^2 = m_1^2 c_\theta^2 + m_2^2 s_\theta^2 \tag{3.15}$$

$$m_{RR}^2 = m_1^2 s_\theta^2 + m_2^2 c_\theta^2 \tag{3.16}$$

$$m_{LR}^2 = |m_2^2 - m_1^2||c_\theta s_\theta|, \tag{3.17}$$

where $c_\theta \equiv \cos\theta$, $s_\theta \equiv \sin\theta$. The mass eigenstates can then be expressed in terms of the interaction states written as

$$\tilde{\mu}_1 = \tilde{\mu}_L c_\theta - \tilde{\mu}_R s_\theta, \quad \tilde{\mu}_2 = \tilde{\mu}_L s_\theta + \tilde{\mu}_R c_\theta. \tag{3.18}$$

This completes the construction of the reference model. Then, in principle, the input parameters in the model are: M_B, the mass of the bino; m_1 and m_2, the masses of the lighter and the heavier smuons, respectively; and the mixing angle θ.

3.1 $g-2$ anomaly

In our reference framework, the additional bino-slepton-lepton interaction contributes to the magnetic dipole moment of the muon through the one-loop diagram shown in Fig. (3.1), where the virtual states running in the loop are the bino and smuons, and that the external photon attaches to the smuon. This extra contribution, parametrized by Δa_μ, is given in this reference

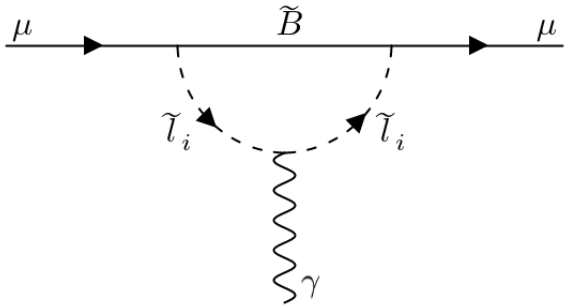

Figure 3.1: One-loop Feynman diagrams from which one can calculate the quantum corrections to the muon magnetic dipole moment under this framework.

framework by

$$\Delta a_\mu = -\frac{1}{32\pi^2}\lambda_L\lambda_R \sin(2\theta)\ \frac{m_\mu}{M_B}\left[L(x_1) - L(x_2)\right], \tag{3.19}$$

where

$$L(x) \equiv \frac{x}{(1-x)^2}\left[1 + x + \frac{2x\ln x}{(1-x)}\right], \quad x_i \equiv \frac{M_B^2}{m_i^2}; \tag{3.20}$$

in the limiting cases $x \to 0$ and $x \to 1^-$, we have

$$L(x) \approx \begin{cases} x, & x \ll 1 \\ 1/3 + (x-1)/6, & x \sim 1 \end{cases}. \tag{3.21}$$

It is rather convenient to introduce auxiliary parameters r and y, defined as

$$r \equiv \frac{m_1 - M_B}{M_B}, \quad y \equiv \frac{m_2^2 - m_1^2}{4m_W^2}|\sin(2\theta)|; \tag{3.22}$$

this definition for y is motivated by the form of m_{LR}^2, which, in (3.17), we have expressed in terms of the mass eigenvalues m_1 and m_2, and the mixing angle θ. Then we can trade m_1 with r and m_2 with y. For a given bino mass M_B, one can choose the mixing angle such that the $g-2$ contribution coming from (3.19) matches with the FNAL measurement; here we take the reference value $\Delta a_\mu = 25 \times 10^{-10}$. In Fig. 3.2 we plot the required mixing angle θ, for a given bino mass M_B, that gives the correct $g-2$ contribution that matches the one from FNL. Each color code corresponds to a different value of y, while the linestyle corresponds to the choice of the bino-smuon 1 mass splitting r. One may notice that for a pair of r and y values, there is a maximum allowed M_B, which simply comes from the fact that we are saturating the largest possible value of $\sin(2\theta)$. Far from the maximal mixing case, we can identify two branches in Fig. (3.2). The branch where θ is close to zero refers to the "left handed" branch, where, from (3.18), the lighter smuon ($\tilde{\mu}_1$) is purely left handed. In this case, we have $m_1^2 \approx m_{LL}^2$, $m_2^2 \approx m_{RR}^2$, and $m_{\tilde{\nu}}^2 = m_{LL}^2 - m_W^2 \approx m_1^2 - m_W^2$; $\tilde{\mu}_1$ and $\tilde{\nu}$ are nearly degenerate. On the other hand, the branch where θ is close to $\pi/2$ refers to the "right handed" branch, where, from (3.18), the lighter smuon ($\tilde{\mu}_1$) is purely right handed. The mass spectrum changes, so that $\tilde{\mu}_2$ and $\tilde{\nu}$ are nearly degenerate.

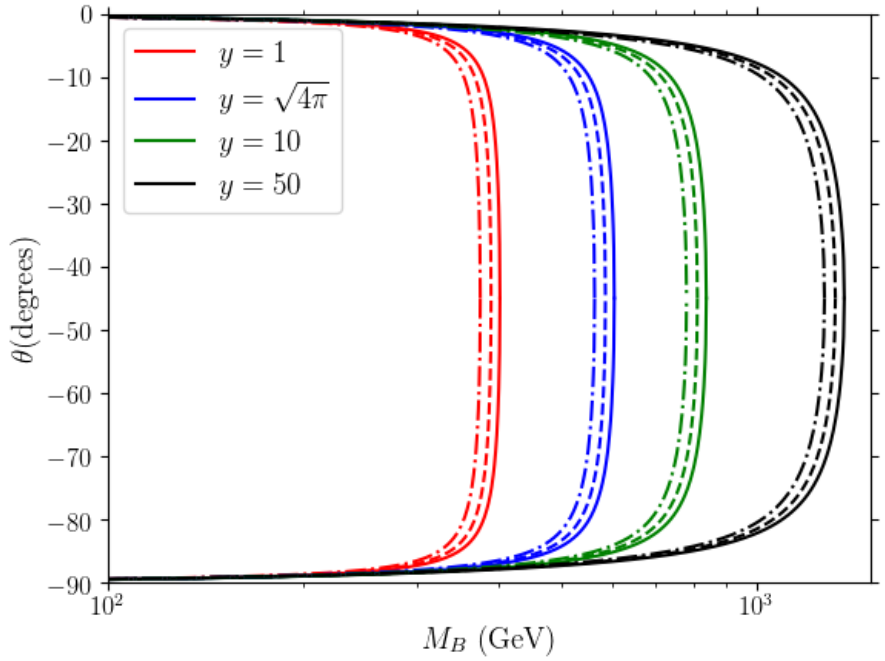

Figure 3.2: Plot of the mixing angle θ, in degrees, that give the $g-2$ contribution that matches with FNL, given a choice of M_B, r, and y. The linestyles correspond to different values of r: 1% (solid), 5% (dashed), and 10% (dot dashed).

3.2 Relic density scan

As in the study of the multicomponent dark sector we carried out in Ch. (2), we would like to see the DM implications of this minimal framework. We take the DM candidate to be the bino, and assuming that it is a thermal relic, its relic density is set by annihilations to final state leptons, assuming no coannhilations. Its stability is ensured by assuming that R-symmetry is respected in our framework, and its stability is also ensured by requiring it to be the lightest supersymmetric particle (LSP). The standard lore is the s-wave cross section of the bino, and for any Majorana DM in general, going to final state SM fermions is chirality suppressed: the initial state bino-bino pair has $S = 0$, while the final state $f_L \bar{f}_R$ has $S = 1$. One requires a chirality flip in order to conserve angular momentum and yield an s-wave cross section: this is typically achieved through the mass term of f, or, additionally, in the case of our model, left-right mixing among smuons. The diagrams associated with bino annihilation to muons is shown in Fig. (3.3). It can be shown that the s-wave cross section is given by [238]

$$\langle \sigma v \rangle_0 = \frac{M_B^2}{32\pi} \left[\lambda_L \lambda_R \sin(2\theta)\right]^2 \left(\frac{1}{m_1^2 + M_B^2} - \frac{1}{m_2^2 + M_B^2} \right)^2 . \tag{3.23}$$

In our framework, the combination $\lambda_L \lambda_R \sin(2\theta)$ appears in the s-wave annihilation cross section for bino pair annihilation to muons given in (3.23): this combination also appears in the $g-2$

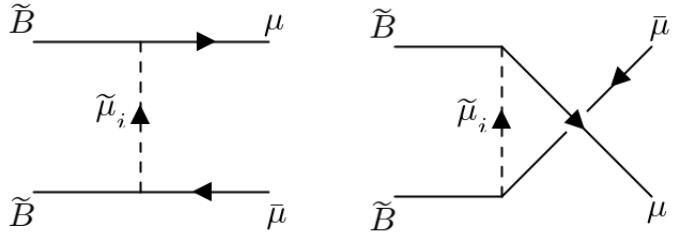

Figure 3.3: t-channel and u-channel diagrams, shown respectively in the left and right panels, that contribute to the amplitude for the $\tilde{B}\tilde{B} \to \mu\bar{\mu}$ annihilation process.

contribution, given in (3.19), so that one can rewrite

$$\langle \sigma v \rangle_0 = \frac{32\pi^3}{m_\mu^2} (\Delta a_\mu)^2 \mathcal{F} \tag{3.24}$$

$$= \left(2.25 \times 10^{-4}\,\text{pb}\right) \left(\frac{\Delta a_\mu}{25 \times 10^{-10}}\right)^2 \mathcal{F}, \tag{3.25}$$

where

$$\mathcal{F} \equiv \frac{1}{\left[L(M_B^2/m_1^2) - L(M_B^2/m_2^2)\right]^2} \left(\frac{1}{1 + m_1^2/M_B^2} - \frac{1}{1 + m_2^2/M_B^2}\right)^2. \tag{3.26}$$

Assuming only the s-wave contributes to the annihilation cross section, it can be shown that the factor $\mathcal{F}$ can be maximized when $m_2 \gg M_B$ and $m_1 \to M_B$, so it can only be at most order 1. Hence one cannot achieve the desired picobarn annihilation cross section for a thermal relic. The p-wave cross section dominates the cross section [238], however, the cross section is still suppressed at freeze out and this yields overabundant DM.

There is still a viable regime that can be explored, and this is the coannihilation regime in which some species are nearly degenerate with the LSP. We revisit the computation of the relic density in this setup, following the first papers that appeared in the literature which discusses this improvement in the relic density calculation [239, 240]. For each species i, the Boltzmann equation tracking its number density is

$$\frac{dn_i}{dt} + 3Hn_i = -\sum_j \langle \sigma v \rangle_{ij} \left(n_i n_j - n_{i,eq} n_{j,eq}\right) - \sum_j \left[\Gamma_{ij} \left(n_i - n_{i,eq}\right) - \Gamma_{ji} \left(n_j - n_{j,eq}\right)\right], \tag{3.27}$$

where $\langle \sigma v \rangle_{ij}$ is the thermal cross section associated with the annihilation of i and j to bath particles, and Γ_{ij} is the decay rate from i to j and a bath particle. The assumption here is the particles decay, at a rate that is faster than the Hubble parameter, into the stable DM candidate; in the MSSM, this is the LSP. The final number density of the LSP is then

$$n = \sum_i n_i. \tag{3.28}$$

Summing (3.27) over i gives

$$\frac{dn}{dt} + 3Hn = -\sum_{i,j} \langle \sigma v \rangle_{ij} \left(n_i n_j - n_{i,eq} n_{j,eq}\right). \tag{3.29}$$

The right hand side can be further rewritten in terms of n. Note that the distribution of species i is still thermal since the scattering of i with the bath particles remain efficient even after i becomes nonrelativistic. Using (2.29), we have

$$\frac{n_i}{n} \approx \frac{A_i(T)\exp(-E_i/T)}{\sum_j A_j(T)\exp -E_j/T} \approx \frac{\exp\left(-E_i/T\right)}{\sum_j A_j(T)/A_i(T)\exp\left(-E_j/T\right)} \approx \frac{n_{i,eq}}{n_{eq}}. \tag{3.30}$$

Then (3.29) becomes

$$\frac{dn}{dt} + 3Hn = -\langle\sigma v\rangle_{eff}\left(n^2 - n_{eq}^2\right), \tag{3.31}$$

where

$$\langle\sigma v\rangle_{eff} \equiv \sum_{ij}\langle\sigma v\rangle_{ij}\frac{n_{i,eq}n_{j,eq}}{n_{eq}^2}. \tag{3.32}$$

The quantity in (3.32) is the effective annihilation cross section. Using the expression for the equilibrium number density of species i in the nonrelativistic regime, *i.e.*

$$n_{i,eq}(T) = g_i\left(\frac{m_iT}{2\pi}\right)^{3/2}e^{-m_i/T}, \tag{3.33}$$

and defining

$$\Delta_i \equiv \frac{m_i - m_{LSP}}{m_{LSP}}, \quad x \equiv \frac{m_{LSP}}{T}, \tag{3.34}$$

we have

$$\langle\sigma v\rangle_{eff} = \sum_{ij}\langle\sigma v\rangle_{ij}r_ir_j, \tag{3.35}$$

$$r_i \equiv \frac{\frac{g_i}{g_{\rm LSP}}\left(1+\Delta_i\right)^{3/2}\exp\left(-x\Delta_i\right)}{1+\sum_{k\neq{\rm LSP}}\frac{g_k}{g_{\rm LSP}}\left(1+\Delta_k\right)\exp\left(-x\Delta_k\right)}. \tag{3.36}$$

Assuming that the LSP undergoes thermal freeze out, chemical decoupling occurs roughly at $x \sim 20$: the exponential term in the numerator of (3.36) is nonnegligible when the mass splitting Δ_i is, *e.g.* less than 5%. In other words, looking at the effective annihilation cross section, coannhilation effects are important in the regime of small mass splittings, since the Boltzmann suppression factors at chemical equilibrium are weak.

In solving (3.31), one must include all processes from all possible pairs of supersymmetric initial states, to all possible SM final states; these annihilation channels are listed down in Table (3.1). The relic density calculation was carried out using a proper implementation of `DarkSUSY` [241]; in parallel, we have also attempted an alternative implementation by interfacing `SARAH` [242] and `micromegas` [243]. As before, we have traded m_1 and m_2 with r and y, so that the set of input model parameters are M_B, r, y, and θ. The scan is then carried out in the $r - M_B$ plane, for a fixed y, and θ is chosen such that the contribution to Δa_μ is enough to satisfy the $g-2$ anomaly. Since we want to fall under the coannihilation regime, we take the bino

Initial states	Final states
$\tilde{B}\tilde{B}$	$\mu^-\mu^+$, $\nu_\mu\bar{\nu}_\mu$
$\tilde{\mu}_i\tilde{\mu}_j^*$	$f\overline{f}$, $\gamma\gamma$, W^+W^-, ZZ, hh, $Z\gamma$, $h\gamma$, hZ
$\tilde{\mu}_i\tilde{\mu}_j$	$\mu^-\mu^-$
$\tilde{\nu}_\mu\tilde{\nu}_\mu^*$	$f\overline{f}$, $\nu_\mu\bar{\nu}_\mu$, $\nu_\mu\nu_\mu$, W^+W^-, ZZ, hh, hZ
$\tilde{B}\tilde{\mu}_i$	$\mu^-\gamma$, μ^-Z, μ^-h, $\nu_\mu W^-$
$\tilde{B}\tilde{\nu}_\mu$	$\nu_\mu Z$, $\nu_\mu h$, μ^-W^+
$\tilde{\mu}_i^*\tilde{\nu}_\mu$	$\mu^+\nu_\mu$, W^+Z, $W^+\gamma$, W^+h, $f_u\overline{f}_d$
$\tilde{\mu}_i\tilde{\nu}_\mu$	$\mu^-\nu_\mu$

Table 3.1: A table summarizing all the processes that enter in computing the effective annihilation rate. Here f is any fermion in the SM, while f_u and f_d refer to the upper and lower components of f if it is an SU(2) doublet. The corresponding processes involving charge conjugated states are implied. Here, the indices i and j refer to the mass eigenstates of the smuon.

to be nearly degenerate with $\tilde{\mu}_1$, hence we take values of r below 5%. The results of the relic density scan are shown in Fig.(3.4), where we separately considered the left handed (top panel) and right handed (bottom panel) branches. For the left handed branch, we also included the relative mass splitting between the sneutrino and the bino, to show that there are cases in which the next-to-LSP (NLSP) can be the sneutrino. The curves in the relic density are contours on the parameter space which reproduces the observed DM relic density, and each individual curve corresponds to a value of y, which we have chosen to be between $y = 1$ and $y = 50$.

One can make observations on the relic density contours and provide physical explanations to such behaviors. The most apparent one is the increase in bino mass as the bino-$\tilde{\mu}_1$ mass splitting is decreased, for moderate values of y. This behavior can be understood by recognizing that coannihilations become important for relatively smaller mass splittings, and the dominant annihilation channels mainly involve sleptons. The individual cross sections, for the dominant processes, that enter (3.32) scale with the light smuon mass roughly as m_1^{-2}. As r is decreased, the Boltzmann suppression is weakened and the cross section must go down to keep the same same effective annihilation cross section; this is achieved by increasing m_1, or just M_B since the bino and $\tilde{\mu}_1$ are nearly degenerate. For the left handed branch, one can identify the cases in which the NLSP is the sneutrino. First, note that the sneutrino mass is given by

$$m_{\tilde{\nu}}^2 = m_1^2 + \left(m_2^2 - m_1^2\right) s_\theta^2 - m_W^2 = m_1^2 + m_W^2 \left(2y|t_\theta| - 1\right), \tag{3.37}$$

where $t_\theta \equiv \tan\theta$. For a specified value of y, one finds that there is a critical absolute value of the mixing angle $|\theta_*| = \arctan(1/(2y))$, below which the sneutrino becomes the NLSP. The condition that the sneutrino is the NLSP can be easily achieved for low to moderate values of y and for relatively low bino masses, since the required mixing angles to satisfy $g-2$ in such a regime are typically close to zero, as shown in Fig. (3.2). The amplitudes for the annihilation processes involving sneutrinos, with final states listed in Table (3.1), do not depend on the mixing angle (except for the case with W^+W^- final states which involves a t-channel sneutrino exchange) and hence the cross sections have a very mild dependence on y; evidently, the dashed curves in Fig. (3.4), representing the bino-sneutrino splitting versus bino contour, do not vary much in y,

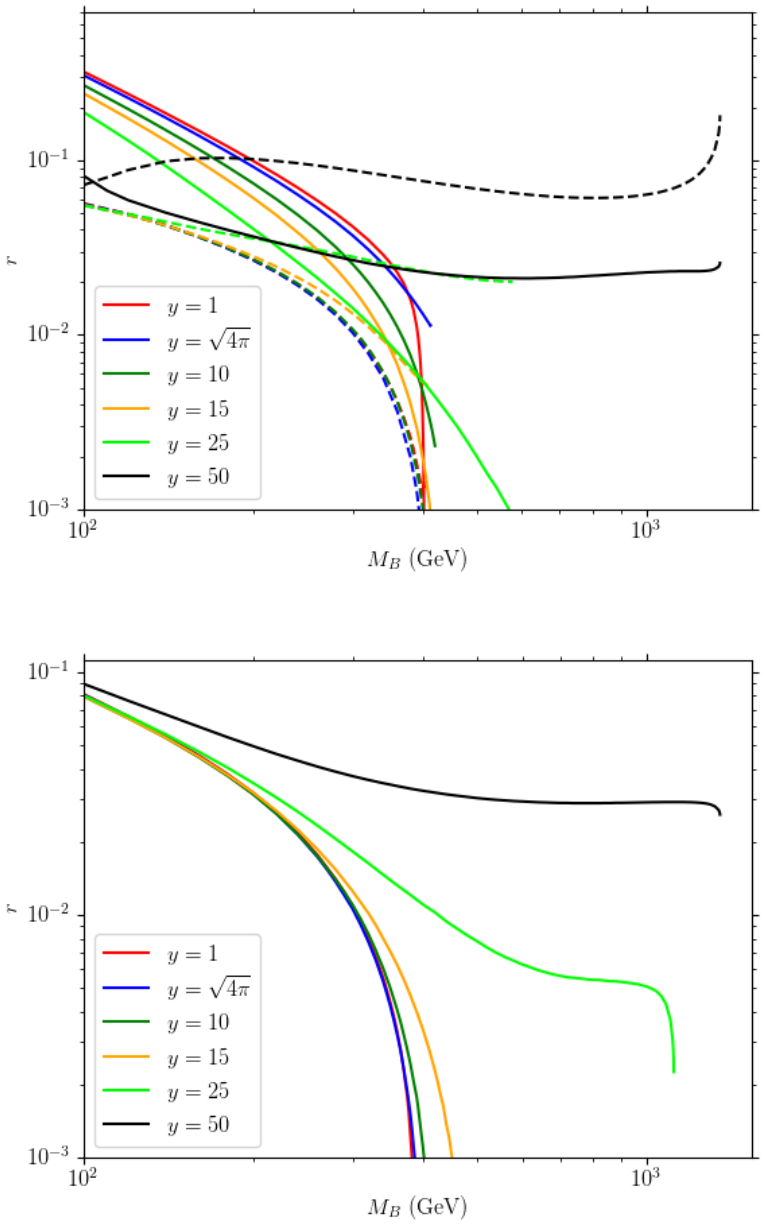

Figure 3.4: Relic density scans in the $r - M_B$ plane, for the left-handed branch (top panel) and for the right-handed branch (bottom panel). For the plot on the top panel, we included the relative mass splitting between the sneutrino and the bino as dashed lines.

for y from 1 to 10. If we focus on this range of y values, we see that the maximum bino mass of $\sim 400\,\text{GeV}$, that is required for saturating the observed relic density, is consistent with what has been mentioned in, *e.g.* [244], where they quote an upper limit of 600 GeV. For moderate values of y, *e.g.* $y = 15$ and $y = 25$, we observe a cross over between the dashed and solid lines. This indicates that the lighter smuon $\tilde{\mu}_1$ now plays the role of the NLSP; here we then expect that the solid line contours will shift to larger bino masses (for a fixed r) as y is increased, since

annihilation cross sections involving $\tilde{\mu}_1$ depend on the mixing. On the other hand, for the right handed branch, the sneutrino is nearly degenerate with $\tilde{\mu}_2$, and both species are sufficiently above the bino mass so that coannihilations between the bino and $\tilde{\mu}_2$ are unimportant. In both branches, the reach in bino mass implied by the relic density scans could potentially be relevant for new physics searches in future lepton colliders such as the International Linear Collider (ILC), where it is expected to have an energy reach up to 1 TeV [245]. Meanwhile, we observe a different behavior in the relic density contour for $y = 50$: the required mass splitting for saturating the desired DM relic density mainly stays flat when M_B is increased, indicating that the dominant cross section roughly remains constant for increasing values of m_1, at least up to around 1 TeV.

3.3 Perturbative unitarity check

Gauge invariance guarantees that tree level amplitudes remain finite in the high energy limit, *i.e.* when the center of mass energy $\sqrt{s}$ is much larger than the masses of all external states, so that the external states are practically massless. However, in the opposite limit where the momenta of external particles are much less than the masses of the external particles, potential issues may arise. To illustrate this point, note that unitarity imposes an upper limit on the partial wave cross sections, with angular momentum J, of annihilating particles with initial common mass m, given by [246]

$$(\sigma v_{rel})_J \leq \frac{4\pi(2J+1)}{m^2 v_{rel}}. \tag{3.38}$$

On the other hand, consider the annihilation process $\tilde{\mu}_i\tilde{\mu}_j^* \to W^-W^+$, and analytically compute the squared amplitude in the zero momentum limit. The motivation behind computing the amplitude squared in the limit of vanishing momentum is the fact that the zero momentum cross section corresponds roughly to thermal cross section at thermal freeze out, when the bino is highly nonrelativistic. For initial state $\tilde{\mu}_i\tilde{\mu}_j^*$ going to W^-W^+, the full annihilation amplitude is given by

$$\begin{aligned}
\mathcal{M}_{tot} &= \frac{2g^2V_{ij}}{t-m^2_{\tilde{\nu}_L}}p_1^\lambda p_2^\nu \epsilon_\lambda(p_1')\epsilon_\nu^*(p_2') + \frac{g^2V_{ij}}{2}\eta^{\lambda\nu}\epsilon_\lambda(p_1')\epsilon_\nu^*(p_2') \\
&- \frac{e^2Q_{\tilde{l}}m_Z^2\delta_{ij}}{s(s-m_Z^2)}\mathcal{K}^{\lambda\nu}\epsilon_\lambda(p_1')\epsilon_\nu^*(p_2') + \frac{g^2T_{3L}(\tilde{\mu}_L)V_{ij}}{s-M_Z^2}\mathcal{K}^{\lambda\nu}\epsilon_\lambda(p_1')\epsilon_\nu^*(p_2') \\
&- \frac{g^2m_W^2}{c_W}\frac{V_{ij}^{(h)}}{s-m_h^2}\eta^{\lambda\nu}\epsilon_\lambda(p_1')\epsilon_\nu^*(p_2'),
\end{aligned} \tag{3.39}$$

where

$$\mathcal{K}^{\lambda\nu} \equiv (p_1-p_2)_\mu[2p_1'^\nu\eta^{\mu\lambda} + (p_2'-p_1')^\mu\eta^{\nu\lambda} - 2p_2'^\lambda\eta^{\mu\nu}], \tag{3.40}$$

$$V_{ij} \equiv \begin{pmatrix} c_\theta^2 & c_\theta s_\theta \\ c_\theta s_\theta & s_\theta^2 \end{pmatrix}_{ij}, \tag{3.41}$$

$$V_{LL}^{(h)} \equiv \frac{1}{c_W}Q_Z(\tilde{\mu}_L), \quad V_{RR}^{(h)} \equiv \frac{1}{c_W}Q_Z(\tilde{\mu}_R), \quad V_{LR}^{(h)} \equiv -\frac{c_W m_{LR}^2}{2m_W^2} = -2yc_W, \tag{3.42}$$

and

$$V_{ij}^{(h)} = [R^T(\theta)V^{(h)}R(\theta)]_{ij}, \quad R(\theta) \equiv \begin{pmatrix} c_\theta & s_\theta \\ -s_\theta & c_\theta \end{pmatrix}. \tag{3.43}$$

We ignored the superpotential contributions to $h\tilde{\mu}_L\tilde{\mu}_L^*$ and $h\tilde{\mu}_R\tilde{\mu}_R^*$, which are just proportional to m_μ^2/m_W^2 and are mainly subdominant. Also, we have introduced

$$T_{3L}(\tilde{\mu}_L) = -\frac{1}{2}, \quad Q_Z(\tilde{\mu}_L) \equiv -\frac{1}{2} + s_W^2, \quad Q_Z(\tilde{\mu}_R) \equiv s_W^2. \tag{3.44}$$

In the zero momentum limit, the squared amplitude can be written as

$$|\mathcal{M}|^2(p \to 0) = |\mathcal{M}|_0^2 + |\mathcal{M}|_h^2 \tag{3.45}$$

where

$$|\mathcal{M}|_0^2 = C_1^2\mathcal{A}_{11} + C_2^2\mathcal{A}_{22} + C_1C_2\mathcal{A}_{12}, \quad |\mathcal{M}|_h^2 = \left(C_h^2 + 2C_2C_h\right)\mathcal{A}_{22} + C_1C_h\mathcal{A}_{12}, \tag{3.46}$$

$$C_1 \to \frac{2g^2V_{ij}}{m_W^2 - m_im_j - m_{\tilde{\nu}_L}^2}, \quad C_2 \to \frac{g^2V_{ij}}{2}, \quad C_h \to -\frac{g^2m_W^2}{c_W}\frac{V_{ij}^{(h)}}{(m_i+m_j)^2 - m_h^2} \tag{3.47}$$

and

$$\mathcal{A}_{11} \to \frac{m_i^2m_j^2}{16m_W^4}[(m_i+m_j)^2 - 4m_W^2]^2 \quad , \qquad \mathcal{A}_{22} \to 2 + \frac{1}{4m_W^4}[(m_i+m_j)^2 - 2m_W^2]^2 \tag{3.48}$$

$$\mathcal{A}_{12} \to m_im_j \qquad \left[\frac{(m_i+m_j)^4 - 6m_W^2(m_i+m_j)^2 + 8m_W^4}{4m_W^4}\right]. \tag{3.49}$$

For the special case $i = j = 1$, one can show that

$$\begin{aligned} |\mathcal{M}|^2(p \to 0) &\approx (g^2c_\theta^2)^2\left(\frac{m_{\tilde{\nu}}^2/m_1^2 - 1}{m_{\tilde{\nu}}^2/m_1^2 + 1}\right)^2\frac{m_1^4}{m_W^4} \\ &+ g^4\left[-c_\theta^4\left(\frac{m_{\tilde{\nu}}^2/m_1^2 - 1}{m_{\tilde{\nu}}^2/m_1^2 + 1}\right)^3 - \frac{V_{11}^{(h)}}{c_W}c_\theta^2\left(\frac{m_{\tilde{\nu}}^2/m_1^2 - 1}{m_{\tilde{\nu}}^2/m_1^2 + 1}\right)\right]\frac{m_1^2}{m_W^2} \\ &+ \mathcal{O}((m_1/m_W)^0). \end{aligned} \tag{3.50}$$

Using (3.37), one can show that

$$\left(\frac{m_{\tilde{\nu}}^2/m_1^2 - 1}{m_{\tilde{\nu}}^2/m_1^2 + 1}\right) = \left(\frac{m_W^2}{m_1^2}\right)\frac{y|t_\theta| - \frac{1}{2}}{1 + \left(\frac{m_W^2}{m_1^2}\right)\left(y|t_\theta| - \frac{1}{2}\right)}. \tag{3.51}$$

We then further expand in m_1/m_W, to yield

$$|\mathcal{M}|^2(p \to 0) \approx \left[g^2c_\theta^2\left(y|t_\theta| - \frac{1}{2}\right)\right]^2 + \mathcal{O}\left(\frac{m_W^2}{m_1^2}\right). \tag{3.52}$$

If then require that the first term remains at order m_W^2/m_1^2 or below, we then have a rough criterion that y must satisfy; this is given by

$$y \lesssim \frac{1}{|t_\theta|}\left(\frac{1}{2} + \frac{m_W^2/m_1^2}{g^2 c_\theta^2}\right). \tag{3.53}$$

In other words, if we do not want to upset the inequality (3.38), then y cannot exceed a certain value. This then provides a hint that the perturbative unitarity condition can impose theoretical limits on the allowed masses of the species in the setup, most especially the masses of the sleptons. Such a criterion based on a basic principle has been used, for instance, in [247] to obtain an upper bound on the Higgs mass, long before its discovery. Constraints on dimensionless couplings, *i.e.* quartic couplings for scalars, can easily be obtained by simply noting that such an expansion parameter in perturbation theory must be less than order unity, and this can be shown to be consistent with perturbative unitarity. On the other hand, our setup contains a dimensionful Higgs-slepton trilinear coupling. We have the weak scale at hand to define the dimensionless parameter $y = \frac{m_{LR}^2}{2m_W^2}$, and we have derived a condition on this dimensionless parameter to ensure that the $\tilde{\mu}_i\tilde{\mu}_j^* \to W^-W^+$ amplitude stays at order m_W^2/m_1^2. However, in general, it might not be clear with which mass scale should a dimensionful coupling, coming from a relevant operator, be compared.

Ultimately, we would like to obtain some kind of criterion that is based on a general principle, and we derive it on the basis of the unitarity of the S-matrix, which implies that the transition matrix elements T_{fi} must satisfy [248]

$$\mathrm{Im}\,\{T_{fi,J}\} = \sum_k T^*_{kf,J} T_{ki,J}, \tag{3.54}$$

where

$$T_{fi,J} \equiv \frac{\lambda_f^{1/4}\lambda_i^{1/4}}{32\pi s}\int_{-1}^{1} d(\cos\theta)\; T_{fi}(\sqrt{s},\cos\theta)\; P_J(\cos\theta), \tag{3.55}$$

and the λs are functions of s and the squares of the masses of the initial (i)/final (f) states given by

$$\lambda(x,y,z) \equiv x^2+y^2+z^2-2xy-2yz-2xz \tag{3.56}$$

$$\lambda_i \equiv \lambda(s,m_{i1}^2,m_{i2}^2) \quad , \quad \lambda_f \equiv \lambda(s,m_{f1}^2,m_{f2}^2). \tag{3.57}$$

This implies that the eigenvalues $\hat{T}_i(s)$ of the transition matrix must satisfy

$$\mathrm{Im}\,\{\hat{T}_i(s)\} = |\hat{T}_i(s)|^2 \Rightarrow \left(\mathrm{Re}\,\{\hat{T}_i(s)\}\right)^2 + \left(\mathrm{Im}\,\{\hat{T}_i(s)\} - \frac{1}{2}\right)^2 = \frac{1}{4}. \tag{3.58}$$

Treating $\hat{T}_i(s)$ as a complex parameter, (3.58) determines the so-called unitarity circle in the complex $\hat{T}_i(s)$ plane; any transition amplitude that satisfies unitarity must lie on this circle. In all our calculations of the cross sections for the relic density computation, we have used tree level amplitudes that are always real. Since in this case the transition matrix is real and symmetric,

the eigenvalues are always real, and the tree level amplitude will always lie outside the unitarity circle. In principle, one will approach the unitarity circle if one includes corrections from all orders in perturbation theory, including loop contributions, to the amplitude [249]. An estimate of the amount of loop corrections to the tree level amplitude, in order to satisfy unitarity, can be obtained by taking the closest distance d between the unitarity circle and the tree level amplitude that lies on the real axis. The criterion that one can adopt to ensure perturbative unitarity is to set

$$a \equiv \frac{d}{\max\{|\mathrm{Re}\,\{\lambda_i(s)\}|\}} \tag{3.59}$$

$$= \frac{\sqrt{1+4\lambda_{max}^2}-1}{2\lambda_{max}} \tag{3.60}$$

to be less than some arbitrary value. Here, i runs over all the eigenvalues of the S-matrix. Note that the maximum eigenvalue λ_{max} is taken over all S-matrix eigenvalues and over all physically allowed s. Alternatively, [248] adopts $|\mathrm{Re}\,\{\lambda\}| \leq 1/2$ for perturbative unitarity, and $|\mathrm{Re}\,\{\lambda\}| \leq 1/6$ to ensure the smallness of the Born amplitude; each criterion corresponds, respectively, to at least 41% and 16% corrections from higher orders to ensure unitarity.

To facilitate the perturbative unitarity check, we perform the scan over the bino mass, while the other parameters r, y, and θ are determined by satisfying $g-2$ and saturating the required relic density for DM. Using these parameters, one constructs the S-matrix where the entries are the $J=0$ tree-level amplitudes for all possible 2-particle initial and final states. One then obtains the maximum eigenvalue of the S-matrix scanning over all s, and impose either 1/2 or 1/6 to the maximum eigenvalue. This procedure we have just outlined can be efficiently implemented by first specifying the model in `SARAH` [242], and then generate the `SPheno` [250, 251] code. The model parameters can be specified in the SUSY Les Houches Accord (SLHA) input file, and this is fed into `SPheno`, which returns the maximum eigenvalue of the S-matrix. It is important to choose an appropriate range and number of values of the center of mass energies $\sqrt{s}$ on which `SPheno` will perform the scan to correctly determine the maximum eigenvalue of the S-matrix. The results of the `SPheno` scans are shown in Fig. 3.5, where we plotted the maximum possible eigenvalue of the S-matrix as a function of the bino mass. The left/right panel corresponds to the left/right handed branch. Essentially, the free parameter is just the bino mass, while the other parameters are fixed by requiring that our reference model yields the correct $g-2$ contribution to close the anomaly, while also providing the correct relic density for DM. If we take $\lambda_{max} \leq 1/6$ as our criterion for ensuring that perturbative unitarity is satisfied, we find that there are certain values of y in which all bino masses are still within the perturbative unitarity constraint. For the left handed branch, choosing $y = 50$ gives an upper bound of $\sim 400\,\mathrm{GeV}$ for the bino mass, while in the right handed branch, $y = 50$ yields an upper bound of $\sim 900\,\mathrm{GeV}$. One can also notice that the left handed branch yields stronger constraints on the bino mass than for the right handed branch. This can be explained simply from the fact that there are more low-lying species, with masses close to the bino, in the left handed branch, than in the right handed branch; in the latter case, the threshold for most processes is around the mass of the heavier smuon.

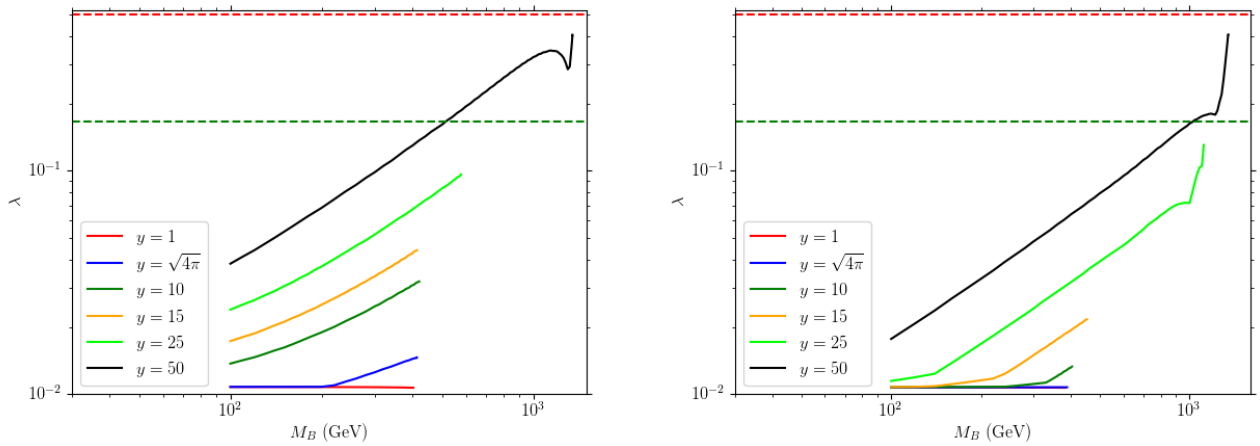

Figure 3.5: Plots of the maximum possible eigenvalue of the S-matrix as a function of the bino mass. In both panels, each point on all curves corresponds to a set of model parameters that yield the desired $g-2$ contribution and the relic density for DM. The left panel corresponds to the left handed branch, while the right panel corresponds to the right handed branch.

3.4 Vacuum stability

There is another way of imposing theoretical limits on our framework, and it concerns the minima of the resulting potential in the presence of scalar fields other than the Higgs. Essentially, in order to reproduce the known phenomenology of electroweak (EW) symmetry breaking, we must ensure that the global minimum of the scalar potential must be the electroweak vacuum. This kind of analysis has been implemented in, *e.g.* [252, 253]; in particular, [253] showed that staus can be as heavy as $\sim 1\,\text{TeV}$ for maximum stau mixing.

To proceed with the analysis of vacuum stability, we first write down the tree-level potential given by

$$V_{tot} = V_H + V_D^{(1)} + V_D^{(2)} + V_{mix}, \tag{3.61}$$

where

$$V_H = \mu^2 H^\dagger H \quad , \quad V_{mix} = k_s \left(H^\dagger \tilde{l}_L \tilde{\mu}_R^\dagger + \tilde{l}_L^\dagger \tilde{\mu}_R \right), \tag{3.62}$$

$$V_D^{(1)} = \frac{g_Y^2}{2} \left| \sum_i Y_H H^\dagger H + Y_L \tilde{l}_L^\dagger \tilde{l}_L + Y_R \tilde{\mu}_R^\dagger \tilde{\mu}_R \right|^2 \tag{3.63}$$

$$V_D^{(2)} = \frac{g^2}{4} \left\{ \text{tr}\left(M^2\right) - \frac{1}{2} \left[\text{tr}(M)\right]^2 \right\} \tag{3.64}$$

$$V_2 = m_{LL}^2 \tilde{l}_L^\dagger \tilde{l}_L + m_{RR}^2 \tilde{\mu}_R^\dagger \tilde{\mu}_R, \tag{3.65}$$

and

$$M \equiv H H^\dagger + \tilde{l}_L \tilde{l}_L^\dagger. \tag{3.66}$$

Here, the parameter k_s is related to m_{LR}^2 via

$$k_s = \frac{\sqrt{2} m_{LR}^2}{v}. \tag{3.67}$$

We can work in the unitary gauge so that we can write the Higgs field as in (3.10), and perform SU(2) rotations on the Higgs and slepton left doublet. Then we rewrite any field ϕ in terms of its real and imaginary parts, such that

$$\phi = \frac{1}{\sqrt{2}}\phi_R + \frac{i}{\sqrt{2}}\phi_I; \tag{3.68}$$

the normalization factor $1/\sqrt{2}$ ensures that we have canonical kinetic terms for ϕ_R and ϕ_I. A phase rotation on a field does not change the total potential, and hence we can simply work with the real parts of the different scalar fields. Letting h to be the real component of the neutral Higgs, X and Y to be the real parts of $\tilde{\nu}$ and $\tilde{\mu}_L$, respectively, and Z to be the real part of $\tilde{\mu}_R$, we have

$$V_H = \frac{\mu^2}{2}h^2, \quad V_{mix} = \frac{k_s}{\sqrt{2}}hYZ \quad , \qquad V_2 = \frac{m_{LL}^2}{2}\left(X^2 + Y^2\right) + \frac{m_{RR}^2}{2}Z^2 \tag{3.69}$$

$$V_D^{(1)} = \frac{g_Y^2}{32}\left[h^2 - \left(X^2 + Y^2\right) + 2Y_R Z^2\right]^2 \quad , \qquad V_D^{(2)} = \frac{g^2}{32}\left[h^4 - 2h^2\left(X^2 - Y^2\right) + \left(X^2 + Y^2\right)^2\right]. \tag{3.70}$$

Since we would like to determine the conditions in which the EW vacuum gives the global minimum for the scalar potential, it is convenient to shift the neutral Higgs field by the EW vacuum expectation value (VEV), so that we can rewrite

$$h = v + \tilde{h}. \tag{3.71}$$

In this way, the EW vacuum corresponds to $\tilde{h} = 0$. We can then introduce a convenient coordinate transformation, following [254], in such a way that the total potential can be written as a quartic potential in $\tilde{h}$. Defining

$$\tilde{X} \equiv \frac{X}{\tilde{h}}, \quad \tilde{Y} \equiv \frac{Y}{\tilde{h}}, \quad \tilde{Z} \equiv \frac{Z}{\tilde{h}}, \tag{3.72}$$

one can show that

$$V_{tot}(\tilde{X}, \tilde{Y}, \tilde{Z}, \tilde{h}) = m^2(\tilde{X}, \tilde{Y}, \tilde{Z})\tilde{h}^2 - A(\tilde{X}, \tilde{Y}, \tilde{Z})\tilde{h}^3 + \lambda(\tilde{X}, \tilde{Y}, \tilde{Z})\tilde{h}^4, \tag{3.73}$$

where

$$
\begin{aligned}
m^2(\tilde{X},\tilde{Y},\tilde{Z}) &\equiv \frac{m_{LL}^2}{2}\left(\tilde{X}^2+\tilde{Y}^2\right)+\frac{m_{RR}^2}{2}\tilde{Z}^2+\frac{k_s v}{\sqrt{2}}\tilde{Y}\tilde{Z}+\frac{g_Y^2 v^2 Y_R}{8}\tilde{Z}^2-\frac{(g^2+g_Y^2)\,v^2}{16}\tilde{X}^2 \\
&+ \frac{(g^2-g_Y^2)\,v^2}{16}\tilde{Y}^2+\frac{(g^2+g_Y^2)\,v^2}{8}, \qquad (3.74)\\
A(\tilde{X},\tilde{Y},\tilde{Z}) &\equiv \frac{(g^2+g_Y^2)\,v}{8}\tilde{X}^2+\frac{(-g^2+g_Y^2)\,v}{8}\tilde{Y}^2-\frac{k_s}{\sqrt{2}}\tilde{Y}\tilde{Z} \\
&- \frac{g_Y^2 v Y_R}{4}\tilde{Z}^2-\frac{(g^2+g_Y^2)\,v}{8}, \qquad (3.75)\\
\lambda(\tilde{X},\tilde{Y},\tilde{Z}) &\equiv \frac{g^2}{32}\left[\tilde{X}^4+2\tilde{X}^2\left(-1+\tilde{Y}^2\right)+\left(1+\tilde{Y}^2\right)^2\right]+\frac{g_Y^2}{32}\left(-1+\tilde{X}^2+\tilde{Y}^2-2Y_R\tilde{Z}^2\right)^2. \qquad (3.76)
\end{aligned}
$$

Note that V_{tot} has a term linear in $\tilde{h}$, which simply sets the value of the μ^2 parameter in the Higgs potential to

$$\mu^2=-\frac{(g^2+g_Y^2)\,v^2}{8}. \qquad (3.77)$$

There is also a constant term, which could be relevant when dealing with the cosmological constant problem, but we simply ignore for our purposes. In the following discussion, the EW vacuum corresponds to zero potential value.

From (3.73), one can determine the local minima in the $\tilde{h}$ direction: the EW minimum, corresponding to $\tilde{h}=0$, and the false minimum at $\tilde{h}=\tilde{h}_*$, where $\tilde{h}_*$ satisfies

$$4\lambda\tilde{h}_*^2-3A\tilde{h}_*+2m^2=0. \qquad (3.78)$$

There are two solutions for $\tilde{h}_*$, and one should take the solution which gives a local minimum, *i.e.* from the condition that the second derivative must be positive, $\tilde{h}_*>3A/(8\lambda)$, assuming that $\lambda>0$. By plugging this solution $\tilde{h}_*$ to the potential, and requiring that the potential be positive, we have $4m^2\lambda-A^2>0$. Of course, the left hand side of this inequality depends on the other field directions $\tilde{X}$, $\tilde{Y}$, and $\tilde{Z}$, and thus we have the condition

$$\min_{\{\tilde{X},\tilde{Y},\tilde{Z}\}}\left[4\lambda(\tilde{X},\tilde{Y},\tilde{Z})m^2(\tilde{X},\tilde{Y},\tilde{Z})-A(\tilde{X},\tilde{Y},\tilde{Z})\right]>0. \qquad (3.79)$$

In other words, in order to guarantee that the EW vacuum corresponds to the global minimum of the potential, the minimum value of the quantity $4\lambda m^2-A$, which we shall refer to as the discriminant D, must be positive. We shall take this as our criterion for absolute vacuum stability. The goal is to then perform a scan over an appropriate section of the parameter space (m_1,m_2,θ) and identify which points can be accommodated by vacuum stability. Since we would like to, at least, close the $g-2$ anomaly, we consider a fixed value of the bino-$\tilde{\mu}_1$ mass splitting r, choose certain values of y, and determine the locations of the viable points in the $\theta-M_B$ plane. In determining the minimum of the discriminant in the $(\tilde{X},\tilde{Y},\tilde{Z})$ direction, we used the HOM4PS2 program [255] to numerically solve the set of polynomial equations $\vec{\nabla}_i D=\vec{0}$, where $\vec{x}_i=(\tilde{X},\tilde{Y},\tilde{Z})$. Among the roots obtained by HOM4PS2, we picked the purely real roots, and

selected the one that gives the smallest D. The result of such a scan is shown in the top panel of Fig. (3.6). Here we are assuming $r = 10^{-2}$ for the relative bino-$\tilde{\mu}_1$ splitting. We can see that for low values of y, *e.g.* 1 and $\sqrt{4\pi}$, all the parameter points that can close the $g-2$ anomaly are allowed by absolute vacuum stability. Moving on to larger values of y, we observe tightening constraints on the allowed bino mass and mixing angle θ; for $y = 10$, masses below $\sim 620\,\text{GeV}$ are viable from the point of view of absolute vacuum stability, while the upper limit for bino masses is $\sim 230\,\text{GeV}$ for $y = 25$. This can be explained by noting that y is related to k_s via

$$k_s = \sqrt{2} g^2 v y \ \text{sgn}\left(s_\theta c_\theta\right), \tag{3.80}$$

i.e. k_s is fixed by y. Meanwhile, k_s enters in the cubic coefficient of the potential, as seen from (3.75). For sufficiently large y, V_{tot} tips over to large $\tilde{h}$ field values, which can potentially lead to the scenario of having a deeper minimum at nonzero $\tilde{h}$. This situation is illustrated in the bottom panel of Fig. (3.6), for $y = 25$, $r = 10^{-2}$, and $M_B = 1\,\text{TeV}$; this point in parameter space is excluded by imposing absolute vacuum stability, and the potential develops a global minimum away from the EW vacuum. In cases where the the EW vacuum is not providing the global minimum for the total potential, the corresponding parameter region can still be accommodated if the tunneling time from the EW vacuum to the global minimum is longer than the age of the Universe; the EW vacuum is said to be in a metastable state. The lifetime of the metastable vacuum is given by

$$\tau_m = \left(\frac{\Gamma}{V_S}\right)^{-1/4}, \tag{3.81}$$

where Γ/V_S is the decay rate per spatial volume of the metastable vacuum. Early calculations of Γ/V_S were carried out in [256, 257], for the case of a single scalar field subjected to a potential $U(\phi)$. This potential has minima at $\phi = \phi_\pm$, where the metastable vacuum is at $\phi = \phi_+$, while the global minimum is at $\phi = \phi_-$. Through a semiclassical computation, it was shown that

$$\frac{\Gamma}{V_S} = K e^{-B} \tag{3.82}$$

where B, the so-called bounce action, is computed by evaluating the Euclidean action

$$S_E = 2\pi^2 \int_0^\infty \rho^3 d\rho \ \left[\frac{1}{2}\left(\frac{d\phi}{d\rho}\right)^2 + U(\phi)\right], \tag{3.83}$$

where $\rho \equiv \sqrt{\tau^2 + |\vec{x}|^2}$, τ is the Wick rotated time coordinate, and ϕ is a field configuration that satisfies

$$\frac{d^2\phi}{d\rho^2} + \frac{3}{\rho}\frac{d\phi}{d\rho} = \frac{dU(\phi)}{d\phi}, \tag{3.84}$$

with boundary conditions

$$\lim_{\rho\to\infty} \phi(\rho) = \phi_+, \quad \left.\frac{d\phi}{d\rho}\right|_{\rho=0} = 0. \tag{3.85}$$

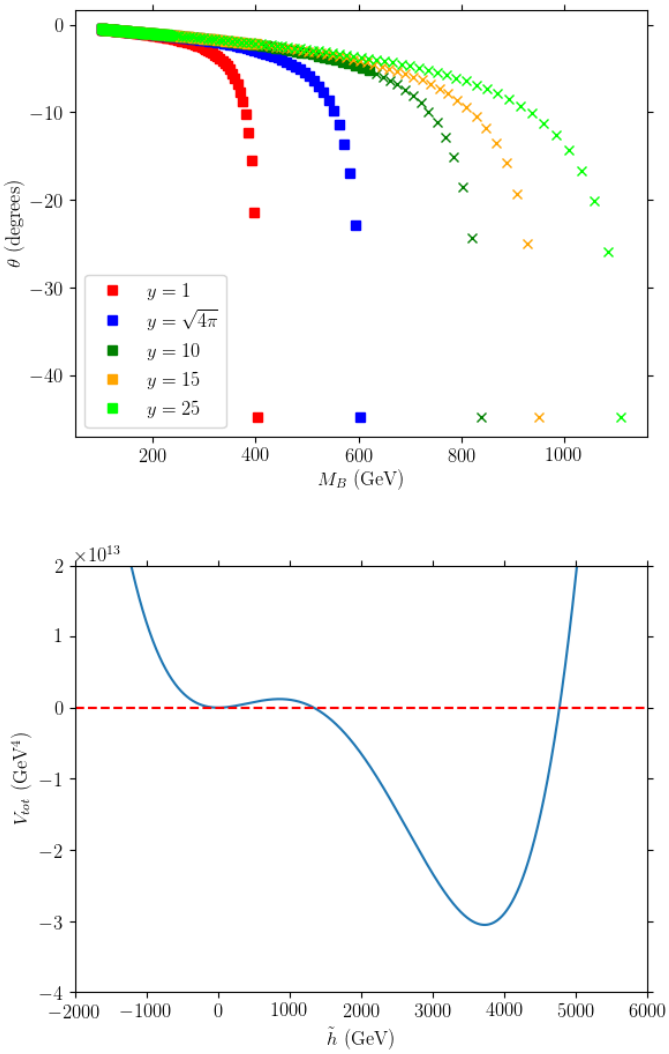

Figure 3.6: (Top panel) Result of the scan along each contour of constant y, in the $\theta - M_B$ plane, where the square markers indicate points that are allowed by absolute vacuum stability, while the cross markers lead to a vaccum distinct from the EW one. (Bottom panel) Sample plot of the total potential, for a benchmark point $y = 25$, $r = 10^{-2}$, and $M_B = 1\,\text{TeV}$, that is excluded on grounds of absolute vacuum stability.

The generalization of this discussion is straightforward for the case of multiple scalar fields $\vec{\phi}$, where one simply makes the replacement $\phi \to \vec{\phi}$, and the one-dimensional derivative of the potential with the gradient of $U(\vec{\phi})$ over $\vec{\phi}$. Methods have been devised to solve the resulting system of coupled differential equations and compute the bounce action, *e.g.* [258–261]. Here we follow the procedure in [254], which is based on calculating the bounce action using a polynomial approximation obtained by [262]. This method is sufficient for our purposes, and this is convenient when performing scans over the parameter space of the model. The semianalytic result for the bounce action is

$$B = \frac{\pi^2}{3\bar{\lambda}}(2-\delta)^{-3}\left(13.832\delta - 10.819\delta^2 + 2.0765\delta^3\right), \tag{3.86}$$

where

$$\delta \equiv \frac{8\bar{m}^2\bar{\lambda}}{\bar{A}^2}, \tag{3.87}$$

$$f \equiv 1 + \tilde{X}_i^2, \quad \bar{m}^2 \equiv \frac{m^2(\tilde{X}_i)}{f}, \quad \bar{\lambda} \equiv \frac{A(\tilde{X}_i)}{f^{3/2}}, \quad \bar{\lambda} \equiv \frac{\lambda(\tilde{X}_i)}{f^2}, \tag{3.88}$$

and $\tilde{X}_i$ is the point in the reduced field space $(\tilde{X}, \tilde{Y}, \tilde{Z})$ that gives the minimum value of the discriminant D. The criterion for determining whether a metastable vacuum is long-lived then reduces to a criterion on the value of the bounce action; in [254], they considered $B > 440$, which we shall also adopt in this work. In Fig. (3.7), we show a scan on the same $\theta - M_B$ space as in the left panel of Fig. (3.6), and we see that a significant part of the parameter space opens up; the circle markers, previously excluded on grounds of absolute vacuum stabilty, correspond to points in the parameter space that lead to a long-lived, metastable EW vacuum.

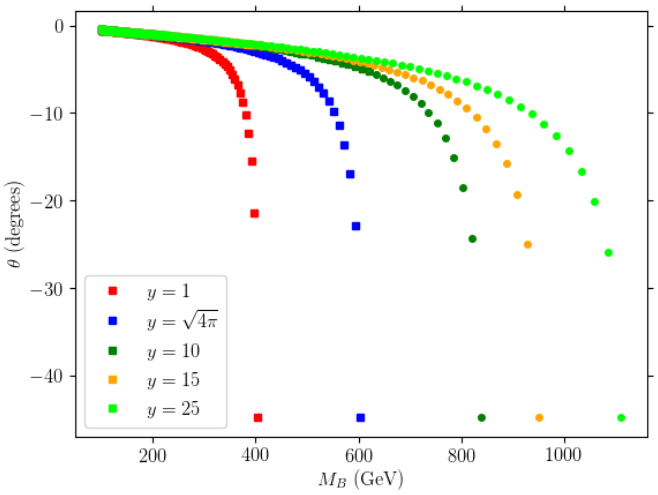

Figure 3.7: Same as in the left panel of Fig. (3.6), but now including the criterion for having a long-lived metastable EW vacuum. The circle points correspond to model parameters that yield a a long-live metastable EW vacuum; in the case of imposing absolute vacuum stability, these points were previously excluded.

3.5 Direct detection

We start from the EFT of bino-quark interactions, where we only consider Higgs, Z, and photon exchanges, and we follow the discussion in [263]. By mapping the quark operators to their nucleonic counterparts via QCD form factors, we have

$$\mathcal{L}_{BN} = \sum_{N=p,n} \sum_{q=u,d} \left[c_q^{(0)} \bar{B}B \; m_N f_{q,N}^{(0)} \bar{N}N + c_q^{(1)} \bar{B}\gamma_\mu\gamma^5 B \; f_{q,N}^{(1)} \bar{N}\gamma^\mu\gamma^5 N \right] + e c_A(q^2) \bar{B}\gamma_\mu\gamma^5 B \; \bar{p}\gamma^\mu p, \tag{3.89}$$

where the QCD form factors are

$$f_{u,N}^{(0)} = \frac{R_{ud}}{1+R_{ud}}\frac{\Sigma_{\pi N}}{m_N}(1+\xi_N) \tag{3.90}$$

$$f_{d,N}^{(0)} = \frac{1}{1+R_{ud}}\frac{\Sigma_{\pi N}}{m_N}(1-\xi_N) \tag{3.91}$$

$$\xi_N = \frac{1+R_{ud}}{1-R_{ud}}\frac{\Sigma_{-,N}}{2\Sigma_{\pi N}}, \tag{3.92}$$

$$\Sigma_{\pi N} = 44\,\mathrm{MeV}, \quad R_{ud} = 0.49 \pm 0.13, \quad \Sigma_{-,N} = \begin{cases} 2\,\mathrm{MeV}, & N = p \\ \\ -2\,\mathrm{MeV}, & N = n \end{cases}, \tag{3.93}$$

$$f_{u,p}^{(1)} = 0.75, \quad f_{d,p}^{(1)} = -0.51. \tag{3.94}$$

For $f^{(1)}$, the coefficients are related by isospin, *i.e.* $u \leftrightarrow d$ is to $p \leftrightarrow n$. The Wilson coefficients $c_q^{(0)}$, $c_q^{(1)}$, and $c_A(q^2)$ can be found in the Appendix of [263]. Once we have the EFT for DM-nucleon interactions, we need to perform a nonrelativistic reduction in order to use `DDCalc` [228, 229] to calculate the recoil spectrum. It can be shown that

$$\mathcal{L}_{NREFT} = \sum_{N=p,n}\left[c_N^{(0)}\mathcal{O}_1^{(N)} - 4c_N^{(1)}\mathcal{O}_9^{(N)}\right] - e\mathcal{A}\left[2\mathcal{O}_8^{(p)} - 2\mathcal{O}_9^{(p)}\right], \tag{3.95}$$

where $\mathcal{O}_1$ is just the identity operator acting on isospin space, while

$$\mathcal{O}_8 \equiv \vec{S}_\chi \cdot \vec{v}^{\perp}, \quad \mathcal{O}_9 \equiv i\vec{S}_\chi \cdot \left(\vec{S}_N \times \frac{\vec{q}}{m_N}\right). \tag{3.96}$$

The coefficients c_N are defined as

$$c_N^{(0)} \equiv m_N \sum_{q=u,d} c_q^{(0)} f_{q,N}^{(0)}, \quad c_N^{(1)} \equiv \sum_{q=u,d} c_q^{(1)} f_{q,N}^{(1)}, \tag{3.97}$$

while the exact expression for $\mathcal{A}$ is given in [263] and will be written down here for completeness:

$$\mathcal{A}(q^2) = \frac{e}{8\pi^2}\sum_{i=1,2}\alpha_\mu^{(i)}\beta_\mu^{(i)}\int_0^1 dx\int_0^{1-x} dy\left[\frac{y(2y+x-2)}{\Delta(x,y,M_B,m_i,m_\mu;q^2)} + \frac{(2y-1)(2y+x-1)}{2D(x,y,M_B,m_i,m_\mu;q^2)}\right], \tag{3.98}$$

where

$$\Delta(x,y,M_B,m_i,m_\mu;q^2) \equiv xm_i^2 + (1-x)m_\mu^2 - x(1-x)M_B^2 - y(1-x-y)q^2 \tag{3.99}$$

$$D(x,y,M_B,m_i,m_\mu;q^2) \equiv (1-x)m_i^2 + xm_\mu^2 - x(1-x)M_B^2 - y(1-x-y)q^2. \tag{3.100}$$

Also, the coefficients α_μ and β_μ are defined from the bino-slepton-lepton interaction via

$$\mathcal{L} \supset \sum_{i=1,2}\left\{\tilde{\mu}_i\bar{\mu}\left[\alpha_\mu^{(i)} + \beta_\mu^{(i)}\gamma_5\right]\tilde{B} + \mathrm{h.c.}\right\}. \tag{3.101}$$

While the trilinear interaction $h\tilde{\mu}_L\tilde{\mu}_R$ could potentially give rise to a large coupling that might boost the Higgs contribution to the recoil signal, one should note that the Higgs contributes only to $c_q^{(0)}$; from Eq. (D6) of [263], and slightly modifying it for the case of s/leptons, we have

$$c_q^{(0)} = \frac{\lambda_\mu^h/m_\mu}{8\pi^2 m_h^2}\left(\sum_{i\leq j} M_{ij} + \sum_i M_i\right),\ i,j=1,2. \tag{3.102}$$

The Higgs-slepton trilinear coupling enters in M_{ij}, given by

$$\begin{aligned} M_{ij} &\equiv \frac{1}{1+\delta_{ij}}\frac{\mu_h^{(ij)}}{m_i^2-m_j^2}\int_0^1 dx\Big[\alpha_\mu^{(i)}\alpha_\mu^{(j)}\left((1-x)m_\chi+m_\mu\right) \\ &+ \beta_\mu^{(i)}\beta_\mu^{(j)}\left((1-x)m_\chi-m_\mu\right)\Big]\ln\left(\frac{\Delta_i}{\Delta_j}\right), \end{aligned} \tag{3.103}$$

where

$$\Delta_i \equiv xm_\mu^2 + (1-x)m_i^2 - x(1-x)M_B^2, \tag{3.104}$$

the α_i and β_i are the coefficients appearing in (3.101), while μ_h and λ_μ^h appear in the Lagrangian as

$$\mathcal{L} \supset \sum_{i\leq j}\frac{\mu_h^{(ij)}}{1+\delta_{ij}} h\left(\tilde{\mu}_i\tilde{\mu}_j^\dagger + \text{h.c.}\right) + \lambda_\mu^h h\bar{\mu}\mu. \tag{3.105}$$

Looking at the coefficient of (3.103) for $i=1, j=2$, we have

$$\frac{\mu_h^{(12)}}{m_2^2-m_1^2} = \frac{1}{m_2^2-m_1^2}\left[\frac{c_\theta^2\left(-1/2+s_W^2\right)}{c_W} + \frac{s_\theta^2 s_W^2}{c_W} + \frac{c_\theta s_\theta c_W m_{LR}^2}{m_W^2}\right]. \tag{3.106}$$

The dangerous term containing m_{LR}^2 is cancelled by the mass squared difference in the denominator, so that we have $m_{LR}^2/(m_2^2-m_1^2) = c_\theta s_\theta \leq 1/2$. On the other hand, the dominant contribution to the recoil rate comes from the anapole moment, as one can see in Fig. (3.8).

We are in a position to project the direct detection limits on the $r-m_B$ plane. As in Sec.(2.4), the limits are obtained by computing a test statistic λ and setting it to -1.64 to get the direct detection limit at 90% CL. Along the direct detection limit curve, for each y, the mixing angle is chosen such that the contribution to $g-2$ is sufficient to close the $g-2$ anomaly. The left panel of Fig. 3.9 corresponds to the left-handed branch, while the right panel corresponds to the right-handed branch. We find that limits from direct detection provides stronger constraints for the right-handed branch than the left-handed branch. In particular, for the right-handed branch, future direct detection experiments can be sensitive to bino masses up to $\sim 600\,\text{GeV}$.

One can try to understand why the direct detection limits to the anapole moment is sensitive to very degenerate spectra. In the limit where the momentum transfer is much smaller than the mass of the fermion, which in our case is the muon, one can drop the momentum dependence in the anapole moment and write it as

$$\mathcal{A} \approx \frac{e}{48\pi^2}\sum_{i=1,2}\alpha_\mu^{(i)}\beta_\mu^{(i)}\int_0^1 dx\frac{3x-2}{x+(1-x)t_i-x(1-x)\eta_i}, \tag{3.107}$$

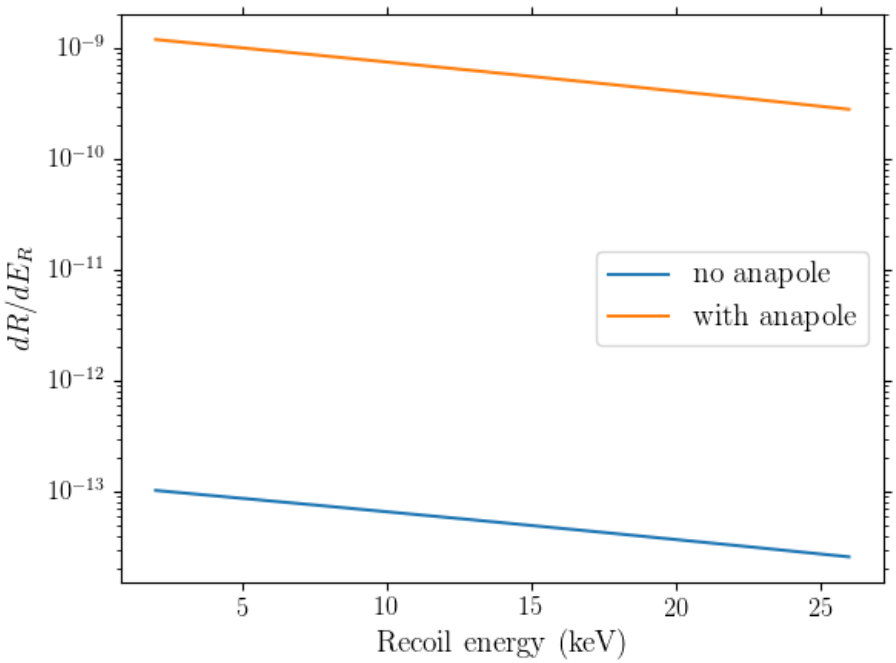

Figure 3.8: Sample plot of the recoil spectrum as a function of the recoil energy, given a representative point $y = 1$, $r = 10^{-2}$, and $m_B = 200\,\text{GeV}$. The blue/orange curve corresponds to the case where the anapole contribution is not included/included.

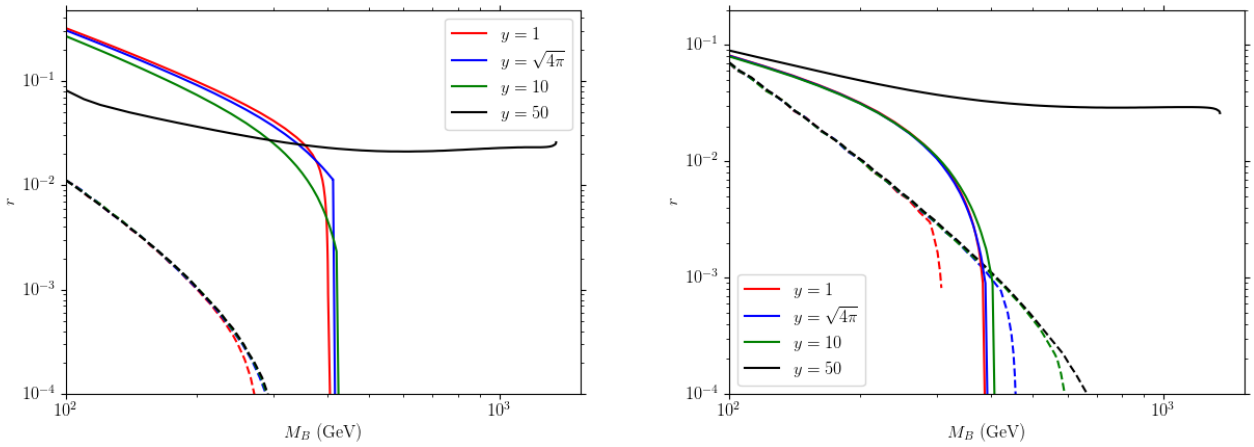

Figure 3.9: Combined plots of the relic density contours (solid) and the 90% CL limits (dashed) from future projections from DARWIN. The excluded regions of the parameter space lie below the dashed lines. The left/right panel corresponds to the left-handed/right-handed branch.

where $t_i \equiv m_\mu^2/m_i^2$ and $\eta_i \equiv m_\chi^2/m_i^2$. The above integral can be approximated by first noting that typically $t_i \ll 1$: the term containing t_i in the denominator can essentially be dropped,

provided

$$\frac{x}{1-x} \gg t_i, \tag{3.108}$$

implying that $x \gg t_i$. One can replace the lower limit in (3.107) with t_i, and one can show that the integral becomes

$$\begin{aligned}
\int_0^1 dx \frac{3x-2}{x+(1-x)t_i - x(1-x)\eta_i} &\approx \frac{2}{1-\eta_i}\ln t_i - \left(\frac{3}{\eta_i} + \frac{2}{1-\eta_i}\right)\ln\left[(1-\eta_i)+t_i\eta_i\right] && (3.109)\\
&\approx \left(2 - \frac{2}{t_i} - 3\ln t_i\right) + \left(4 + \frac{1}{t_i^2} - \frac{5}{t_i} - 3\ln t_i\right)(1-\eta_i)\\
&+ \mathcal{O}((1-\eta_i)^2), && (3.110)\\
&\approx (3 - 3t_i + 2\ln t_i) + \left(\frac{7}{2} - 5t_i + \frac{3t_i^2}{2} + 2\ln t_i\right)\eta_i\\
&+ \mathcal{O}(\eta_i^2). && (3.111)
\end{aligned}$$

It is then transparent that as one of the lighter smuons becomes nearly degenerate with the bino, $\eta_i \to 1$, the anapole moment receives enhancement due to the large hierarchy between the smuons and the muon; in the opposite regime where $\eta_i \to 0$, this enhancement is only a mild logarithmic factor.

3.6 Summary and conclusions

In this brief project, we have looked into a minimal model, inspired by the MSSM, to address the muon $g-2$ anomaly. We have studied the implications of this framework on reproducing the DM relic density and direct detection prospects, as well as the additional bounds imposed on this model by perturbative unitarity and vacuum stability.

For this setup, we have the bino-like Majorana fermion interacting with SM muons via the left handed slepton doublet $\tilde{l}_L$ and the right handed smuon $\tilde{\mu}_R$. The left and right handed smuons can mix together through a trilinear coupling with the Higgs, which can be chosen arbitrarily in principle. The introduction of this mixing term is crucial in providing a nonzero contribution to the $g-2$ anomaly, since a dipole operator requires a chirality flip. In this framework, the main parameters that can be tweaked are: the bino mass M_B, the masses m_1 and m_2 of the smuon eigenstates, and the mixing angle θ. We have found that satisfying the $g-2$ anomaly leads to two mixing regimes: the left handed branch, where the lighter smuon is approximately the $\tilde{\mu}_L$ interaction state; and the right handed branch, where the lighter smuon is mostly $\tilde{\mu}_R$.

We have looked into the impact of this minimal framework on DM, by considering the bino $\tilde{B}$ as the LSP such that it reproduces the observed relic density of DM. Here we have identified the relevance of coannihilations in determining the relic density of bino DM, and we have taken the relative mass splittings of the LSP and the NLSP to be $\mathcal{O}\left(10^{-3} - 10^{-1}\right)$. By requiring that we always yield the correct contribution to close the $g-2$ tension, we have found that the two mixing regimes lead to different coannihilation scenarios. This can be explained by noting that, in the left handed case, the bino, $\tilde{\mu}_1$, and $\tilde{\nu}$ are nearly degenerate in mass while in the right handed case, $\tilde{\nu}$ is degenerate only with the heavier $\tilde{\mu}_2$. We have used `DarkSUSY` to compute

the relic density, and we performed a scan over the r-M_B plane: the mixing angle θ and m_2 are both determined by choosing a fixed Higgs-smuon L-smuon R coupling, which amounts to choosing a value for the dimensionless variable y, and from requiring $g-2$. We have shown that for $y \leq 10$, and for LSP-NLSP mass splittings of 0.1%, the maximum bino mass is 400 GeV for both branches. These results are concurrent with earlier investigations on coannihilations in the MSSM and its related incarnations, and we commented on the interesting possibility that such predictions from relic density can be probed in future lepton colliders. On the other hand, increasing y leads to a regime in which the cross section of the dominant annihilation process remains approximately constant as m_1 is increased, and the required mass splitting tapers off to a roughly constant value.

Apart from phenomenological constraints on this minimal model, we have obtained limits from theoretical considerations, namely perturbative unitarity and vacuum stability. The condition of perturbative unitarity amounts to setting a limit on the the largest possible eigenvalue λ of the S-matrix containing tree-level amplitudes. We have found that the constraints on our framework from perturbative unitarity depends on the criterion for the allowed maximum eigenvalue of the S-matrix. If we take the conservative choice of taking the real part of λ to be at most $1/2$, perturbative unitarity guarantees that the viable parameters that saturate both $g-2$ and the DM relic density are still acceptable. On the other hand, if we impose a stronger limit of $1/6$ on the real part of λ, then both the left and right handed branches can cross this limit for $y \geq 50$. This implies that we have an upper bound of ~ 500 GeV in the left handed case, and ~ 1 TeV for the right handed case. On the other hand, we used absolute vacuum stability as a means to provide constraints on our framework. In our setup, the scalar particle content are the sleptons and a lone Higgs doublet. Carrying out vacuum stability analysis, requires the specification of the scalar potential: apart from the quadratic part of the Higgs potential, we have kept the D-terms as in the MSSM, so that the Higgs acquires a quartic coupling from such terms. Imposing absolute vacuum stability is equivalent to the condition that the cubic term in the potential cannot be so large as to cause the development of a minimum that is deeper than the EW vacuum. For the set of parameter points that we have explored, which all satisfy $g-2$, we have shown that absolute vacuum stability provides stronger constraints on the upper limit of bino masses than perturbative unitarity; as y increases starting from 10, the upper limit on the bino mass, for fixed bino-$\tilde{\mu}_1$ relative mass splitting, decreases. On the other hand, taking into account the tunneling rate from the EW vacuum to the false vacuum, and requiring such a tunneling process to occur longer than the age of the Universe, seem to point to more relaxed constraints and opens up a wider region of parameter space in the theory.

Finally, we looked into constraints that direct detection can impose on our framework. We considered the case of bino scattering with nuclei, through 1-loop processes that involve the exchange of the Higgs, Z boson, and γ. We showed that the process mediated by γ, which gives rise to an anapole moment for the bino, provides the dominant contribution to the recoil spectrum. We demonstrated the enhancement of the anapole moment for very degenerate bino and $\tilde{\mu}_1$. We derived direct detection limits using future projections from DARWIN, and plotted these constraints on the $r - M_B$ plane. While direct detection can be sensitive to bino masses as large as ~ 650 GeV, the constraints from direct detection are relevant only for very small bino-$\tilde{\mu}_1$ relative mass splittings, and are less constraining than other complementary limits we explored.

Chapter 4

Halo model and direct detection

4.1 Introduction

The further tightening of constraints for GeV-scale WIMPs from DM direct detection searches has given us motivation to explore the sub-GeV mass regime. If we stick to the DM-nucleon scattering framework, the maximum recoil energy that a sub-GeV DM candidate can impart on a nuclear target of mass m_T is

$$E_R^{(max)} = (2 \times 10^{-4}\,\mathrm{keV}) \left(\frac{m_\chi}{100\,\mathrm{MeV}}\right)^2 \left(\frac{100\,\mathrm{GeV}}{m_T}\right) \left(\frac{v}{10^{-3}}\right)^2, \tag{4.1}$$

which is way below the energy recoil thresholds of most detectors that are sensitive to nuclear recoils. On the other hand, searching for atomic ionization signals due to DM-electron scattering could be a promising avenue for probing sub-GeV DM. The process of atomic ionization through DM-electron scattering has a peculiar feature of being inherently inelastic, in contrast with the conventional DM-nucleon scattering where it is typically assumed that the nucleus does not get excited. In studying the kinematics of DM-electron scattering for ionization processes, the electron is initially in an atomic bound state, and then goes to a continuum final state. If the deposited energy to the electron is ΔE_e, then conservation of energy yields

$$\Delta E_e \;=\; \vec{q}\cdot\vec{v} - \frac{\vec{q}^2}{2\mu_{\chi T}} = -\frac{1}{2\mu_{\chi T}}|\vec{q} - \mu_{\chi T}\vec{v}|^2 + \frac{\mu_{\chi T}\vec{v}^2}{2}, \tag{4.2}$$

where $\vec{q}$ is the momentum transfer, $\vec{v}$ is the relative velocity between DM and the target atom, and $\mu_{\chi T}$ is the reduced mass of the DM-atom system. From the energy conservation relation (4.2), we find that the maximum energy that can be deposited to an electron is

$$(\Delta E_e)_{max} \;=\; (25\,\mathrm{eV}) \left(\frac{m_\chi}{50\,\mathrm{MeV}}\right) \left(\frac{v}{10^{-3}}\right)^2, \tag{4.3}$$

assuming that $\mu_{\chi T} \approx m_\chi$. As in DM-nucleon scattering, where there is a threshold energy for detectable nuclear recoil, there is a threshold for experiments probing DM-electron scattering. For instance, in the case of xenon, there is a minimum outgoing electron energy required to create at least one quantum — around 13 eV — and for the valence shell of xenon with binding

energy around 12 eV, one should have a deposited energy of at least 25 eV. In the limit where the deposited energy is much smaller than the threshold, we have

$$\Delta E_e \approx \vec{q} \cdot \vec{v}, \tag{4.4}$$

i.e. the recoil energy of the DM can be neglected. In principle, the momentum transfer q can take any value due to the fact that the electron is initially bound in the atom, but it typically takes the value $q = \alpha Z_{eff} m_e = (4\,\mathrm{keV}) Z_{eff}$, where Z_{eff} is the effective nuclear charge seen by the bound electron. A larger momentum transfer can lead to more energetic electrons, but it turns out that the atomic form factor is suppressed in this regime. On the other hand, more high velocity DM particles can also lead to an enhancement of the electronic recoil signal — such a scenario can be realized if there were a modification of the DM velocity function, especially at its high velocity tail. Turning this argument around, it can be seen that changes in the high velocity tail of the DM distribution function can have an impact on the expected electronic recoil signal.

Currently, the Standard Halo Model (SHM) is widely used in calculations of direct-detection rates to characterize the local velocity distribution of DM in the Milky Way (MW). Its form is given by

$$f_{SHM}(\vec{v}) = \frac{1}{(\pi v_0^2)^{3/2} N_{esc}} \exp\left(-\frac{\vec{v}^2}{v_0^2}\right) \theta\left(v_{esc} - |\vec{v}|\right), \tag{4.5}$$

where

$$N_{esc} \equiv \mathrm{erf}\left(\frac{v_{esc}}{v_0}\right) - \frac{2}{\sqrt{\pi}} \left(\frac{v_{esc}}{v_0}\right) \exp\left(-v_{esc}^2/v_0^2\right). \tag{4.6}$$

The Gaussian part of the velocity distribution function (VDF) is a generic result that follows from the assumption of an isothermal halo. Such a halo is motivated by the fact that it leads to a spherically symmetric density profile that produces a flat rotation curve at large distances. The hard, escape velocity cutoff ensures that the halo has finite extent. As one can see, the SHM requires v_0 and v_{esc} as external inputs to specify the VDF. While the SHM has been the VDF of choice for a very long time, refinements to it have come about in light of recent data obtained from kinematic tracers of the underlying MW gravitational potential. It is also subject to further scrutiny due to the presence of non-equilibrium substructures. Evans et. al. [264] used updated data for v_0 and v_{esc} from Gaia, and then included the contribution of the so-called "Gaia sausage," a highly flattened structure containing metal-rich stars, to the total local DM velocity distribution. They concluded that the impact of such modifications on DM-nucleon direct-detection limits is marginal, while features of the sausage could manifest in a detector equipped with directional sensitivity. Necib et. al. [265] obtained the velocity distribution of DM, inferred from an isotropic halo stellar population and a highly radial stellar population, sampled from SDSS-Gaia DR2 data. They then demonstrated that, in the context of direct-detection limits, their modified VDFs will have an impact on models that are sensitive to the high velocity tail of the distribution.

Although we have evidence for the presence of non-thermal substructure in our neighborhood, much of the DM still resides in equilibrium structures. In such cases, the full phase space distribution function (PSDF) is a solution of the collisionless Boltzmann equation. Furthermore, it

can be easily shown that the PSDF is a function of integrals of motion. The Maxwell-Boltzmann distribution, which provides the basic form of the SHM, is an example of an equilibrium PSDF for a system with spherical symmetry. However, to be consistent with the spirit of attempting to build realistic PSDFs for the DM in the MW, we must take note that the MW potential is dominated in the inner regions by baryonic components that are not spherically symmetric, but, rather, exhibit axial symmetry. A flattening of the potential would definitely have an impact on the overall shape and kinematical distribution of virialized DM in the MW, in such a way that the DM inherits this axial symmetry. Thus, it is natural to consider axisymmetric PSDFs for the DM in the MW.

The construction of axisymmetric PSDFs is done through the so-called Hunter-Qian (HQ) inversion [266], which is a generalization of Eddington inversion [267] for spherically symmetric systems. An axisymmetric PSDF is a function of two integrals of motion, namely the relative energy $\mathcal{E}$ and the angular momentum along the symmetry axis L_z; in terms of phase space coordinates, they are given by

$$\mathcal{E} = \psi(R^2, z^2) - \vec{v}^2/2, \quad L_z = Rv_\phi, \tag{4.7}$$

where ψ is the relative potential and R is the cylindrical radial coordinate. In order to construct the PSDF, it is necessary to specify the mass model for the system. For the MW, we break it down into components, each associated with either a density profile ρ_i or a potential ψ_i: for a self-consistent model, ρ_i and ψ_i are related via Poisson equation

$$\nabla^2\psi_i = -4\pi G_N \rho_i. \tag{4.8}$$

The PSDF for any component i (which, for our purposes, is the DM component) can then be obtained by feeding the mass model, along with the azimuthal velocity profile for the component i, into the HQ inversion scheme. Note that DM particles that are bound to the halo satisfy $\mathcal{E} \geq 0$; this criterion leads to a value of the escape velocity that can directly be obtained from the total potential, and this is an added virtue of self-consistent axisymmetric modelling.

The main goal of this chapter is to assess the impact of axisymmetric modelling on the theoretical ionization rates due to DM-electron scattering in xenon, prompted by observed excess recoil events in XENON1T at low recoil energies, which are attributed to DM-electron scattering [163]. In turn, we would like to determine how sensitive the exclusion limits are to the choice of the PSDF.

4.2 Ingredients in the recoil spectrum

In what follows, we lay down the groundwork in computing the ionization rate due to DM-electron scattering. Such ionization rates are relevant in computing expected event counts, which are then converted into photoelectron (PE) yields — a quantity that is directly measurable from experiment. Here we follow the discussion in [268] to develop an expression for the total ionization rate. For an electron with initial bound state nl that transitions to a final continuum state $k'l'$, the ionization rate of a single atomic target due to a flux of DM particles is given by

$$\mathcal{R}_{nl\to k'l'} = \frac{n_\chi}{16 m_\chi^2 m_e^2} \int \frac{d^3\vec{q}}{(2\pi)^3} \int d^3\vec{v}\; f_\chi(\vec{v})\; (2\pi)\delta\left(\Delta E_{nl\to k'l'} + \frac{\vec{q}^2}{2m_\chi} - \vec{q}\cdot\vec{v}\right) \langle|\mathcal{M}_{nl\to k'l'}|^2\rangle, \tag{4.9}$$

where n_χ and m_χ are, respectively, the local number density and mass of DM, $\vec{q}$ is the momentum transfer imparted by the DM on the electron, $\vec{v}$ is the velocity of DM relative to Earth, $f_\chi(\vec{v})$ is the local velocity distribution of DM in the frame of the Galactic center, $\Delta E_{nl\to k'l'}$ is the energy deposited on the electron, and $\langle|\mathcal{M}_{nl\to k'l'}|^2\rangle$ is the squared amplitude for the ionization process, summed over final states and averaged over initial electron and DM states. The delta function simply enforces energy conservation. Typically, we specify the microscopic DM-electron interaction, but the electron distribution inside the atom must be taken into account when computing the ionization amplitude. In this case we have

$$\mathcal{M}_{nlm\to k'l'm'} = \int \frac{d^3\vec{k}}{(2\pi)^3}\psi^*_{k'l'm'}(\vec{k}+\vec{q})\mathcal{M}(\vec{k},\vec{p};\vec{k}+\vec{q},\vec{p}-\vec{q})\psi_{nlm}(\vec{k}), \tag{4.10}$$

where $\vec{p}$ is the initial momentum of the DM, while $\psi_{k'l'm'}$ and ψ_{nlm} are the final and initial electron wavefunctions, respectively.

There are a few assumptions at our disposal that will simplify the computation of the recoil spectrum. Firstly, we assume that the scattering amplitude only depends on the magnitude of the momentum transfer, and that it can be factorized as

$$\mathcal{M} = \mathcal{M}_{free}(|\vec{q}| = \alpha m_e)F_{DM}(q). \tag{4.11}$$

In principle, one can establish an EFT framework that captures all possible DM-electron interactions, similar to the EFT of DM-nucleon interactions, and find that there is a subclass of interactions in which this factorization is possible. The event rate (4.9) can then be rewritten as

$$\begin{aligned}\mathcal{R}_{nl\to k'l'} &= \frac{\rho_\chi}{m_\chi}\frac{\bar{\sigma}_e}{\mu^2_{\chi e}}\int\frac{d^3\vec{q}}{(2\pi)^3}\int d^3\vec{v}\; f_\chi(\vec{v})\;(2\pi)\delta\left(\Delta E_{nl\to k'l'} + \frac{\vec{q}^2}{2m_\chi} - \vec{q}\cdot\vec{v}\right)\\ &\times\; |F_{DM}(q)|^2\langle|f_{nl\to k'}(k',q)|^2\rangle,\end{aligned} \tag{4.12}$$

where ρ_χ is the local DM density, $\bar{\sigma}_e$ is the DM-free electron scattering cross section at $q = \alpha m_e$, $\mu_{\chi e}$ is the reduced mass of the DM-electron system, defined as

$$\frac{1}{\mu_{\chi e}} \equiv \frac{1}{m_\chi} + \frac{1}{m_e}, \tag{4.13}$$

and $f_{nl\to k'}$ is the so-called *atomic form factor*, given by

$$f_{nl\to k'}(k',q) = \int\frac{d^3\vec{k}}{(2\pi)^3}\psi^*_{k'l'm'}(\vec{k}+\vec{q})\psi_{nlm}(\vec{k}) = \int d^3\vec{x}\;\psi^*_{k'l'm'}(\vec{x})\psi_{nlm}(\vec{x})e^{i\vec{q}\cdot\vec{x}}. \tag{4.14}$$

Another assumption that enters in computing the ionization rate concerns the calculation of the atomic form factor. Here we are treating electrons as nonrelativistic, and this assumption is actually made implicit when we labelled the electronic orbitals as nl. While it is generally true that outer shell electrons are nonrelativistic, this assumption might not apply for inner shell electrons: one can see this by noting that the typical electron velocity in an atom goes as $v_{typ}/c \approx \alpha Z_{eff}$, where α is the fine structure constant and Z_{eff} is the effective nuclear charge seen by a bound electron, accounting for the screening of the nucleus by the surrounding electron

cloud. A nonrelativistic treatment of computing the form factor requires solving the bound states of the Hamiltonian for a multielectron system. The problem of determining the bound states is made tractable by introducing an ansatz for the bound state wavefunctions as a Slater determinant of orbital wavefunctions, each satisfying the so-called Hartree-Fock equations; for the relativistic case, one must solve the Dirac-Hartree-Fock equations. In [269], they solved the orbital wavefunctions ψ_{nl} for atoms with atomic number up to 54, *i.e.* from helium ($Z = 2$) to xenon ($Z = 54$): they expressed the orbital wavefunctions as linear combinations of primitive Slater-type orbitals and tabulated the coefficients that enter in those linear combinations. This is the approach adopted by [270]. As for the continuum wavefunction for the outgoing electron, one can assume outgoing plane wave states, with a corrective Fermi factor which accounts for the Coulomb distortion of the plane wave. Alternatively, and this is the method prescribed in [270], one can construct the effective potential $V_{eff}^{(nl)}$, of which ψ_{nl} is a bound state, and then solve the Schrödinger equation for a continuum energy E', orbital nl, and potential $V_{eff}^{(nl)}$. Meanwhile, [271] and [272] considered the case of relativistic electron wavefunctions. While they essentially followed a similar approach as [270], they instead solved the Dirac-Hartree-Fock equations for the bound state wavefunctions, and then obtained the solution to the Dirac equation for the continuum state wavefunctions, given the effective potential in the frozen-core approximation. It turns out that, for the case of a xenon target, event rates computed using relativistic form factors are 2-10 times greater than for the case of nonrelativistic form factors. Hence, when one commits to using nonrelativistic atomic form factors, the resulting direct detection limits are conservative bounds [273]. In this work, we shall focus on xenon targets, and we use the nonrelativistic atomic form factors of xenon tabulated by [270] for different values of the momentum transfer q and outgoing electron momentum k'.

Finally, from (4.12), the total recoil spectrum which comes from adding the contribution of each electron bound state orbital to the ionization rate, is given by

$$\frac{dR}{d(\ln E')} = N_T \frac{\rho_\chi}{m_\chi} \bar{\sigma}_e \sum_{n,l} \left[\frac{1}{8\mu_{\chi e}^2} \int q \; dq \; |F_{DM}(q)|^2 \langle |f_{nl}^{(ion)}(k', q)|^2 \rangle \eta(v_{min}(q, \Delta E_e)) \right], \tag{4.15}$$

where N_T is the total number of target atoms,

$$\eta(v_{min}(q, \Delta E_e)) \equiv \int \frac{d^3\vec{v}}{v} f_\chi(\vec{v}) \theta(v - v_{min}) \tag{4.16}$$

is the mean inverse velocity, while

$$v_{min}(q, \Delta E_e) \equiv \frac{\Delta E_e}{q} + \frac{q}{2m_\chi} \tag{4.17}$$

is the minimum velocity required for the DM to impart a momentum transfer q and deposited energy ΔE_e to the electron. Regarding the limits of integration over q, note that DM has a maximum velocity v_{max} in the Galactic halo, which restricts the kinematically allowed values for the momentum transfer in the range $[q_{min}, q_{max}]$, where

$$q_{min} \equiv \text{sgn}(\Delta E_e) \left(m_\chi v_{max} - \sqrt{m_\chi^2 v_{max}^2 - 2 m_\chi \Delta E_e} \right), \quad q_{max} \equiv m_\chi v_{max} + \sqrt{m_\chi^2 v_{max}^2 - 2 m_\chi \Delta E_e}. \tag{4.18}$$

From (4.16), it can be seen that the mean inverse velocity depends on the local velocity distribution function (VDF) of DM, boosted to the local frame of the Earth-based detector. If we use the VDF for the SHM given in (4.5) on (4.16), and accounting for the Earth velocity $\vec{v}_E$ relative to the Galactic center, we have [274]

$$\eta(v_{min}) = \begin{cases} \frac{1}{v_0 y}, \ x < |y-z| \text{ and } z < y \\ \frac{1}{2N_{esc}v_0 y}\left[\text{erf}(x+y) - \text{erf}(x-y) - \frac{4}{\sqrt{\pi}} y \exp(-z^2)\right], \ x < |y-z| \text{ and } z > y \\ \frac{1}{2N_{esc}v_0 y}\left[\text{erf}(z) - \text{erf}(x-y) - \frac{2}{\sqrt{\pi}}(y+z-x)\exp(-z^2)\right], \ x > |y-z| \text{ and } x < y+z, \end{cases} \tag{4.19}$$

where

$$x \equiv v_{min}/v_0, \quad y \equiv v_E/v_0, \quad z \equiv v_{esc}/v_0, \tag{4.20}$$

and

$$N_{esc} \equiv \text{erf}(z) - \frac{2z}{\sqrt{\pi}}\exp(-z^2). \tag{4.21}$$

It should then be apparent that the main astrophysical uncertainties enter in the rate calculation through the mean inverse velocity, which can be obtained once we know the PSDF.

4.3 Hunter-Qian inversion

In this work, we advocate the use of two-integral axisymmetric PSDFs. Such PSDFs can be reconstructed from axisymmetric density-potential pairs using the so-called Hunter-Qian (HQ) inversion [275]. This is a generalization to axisymmetric systems of the well-known Eddington inversion formula [267], used to reconstruct the PSDF of spherically symmetric mass models. Essentially, such inversion schemes are rooted in solving f in integral equations of the form

$$\rho\langle g(\vec{v})\rangle = \int d^3\vec{v}\ g(\vec{v}) f(\vec{v}), \tag{4.22}$$

where the left hand side is known *a priori*. In general, it follows from the collisionless Boltzmann equation that an equilibrium PSDF is a function of integrals of motion. For the axisymmetric case, the PSDF is a function of the relative energy $\mathcal{E}$ and angular momentum L_z along the symmetry axis: these integrals of motion can be expressed in terms of position and velocity coordinates as

$$\mathcal{E} = \psi(R^2, z^2) - \frac{v_R^2 + v_\phi^2 + v_z^2}{2}, \quad L_z = R v_\phi, \tag{4.23}$$

where the velocities are taken *with respect to the Galactic frame*.

The complete axisymmetric PSDF cannot just be obtained solely from inverting the zeroth moment of the PSDF, *i.e.* from

$$\rho = \int d^3\vec{v}\; f(\mathcal{E}, L_z). \tag{4.24}$$

The inversion of the expression above only yields the even part of the PSDF, $f_+(\mathcal{E}, L_z)$, *i.e.* the part of the PSDF that is even in L_z. Additional information regarding the rotation of the mass component must be supplied in order to get the odd part of the PSDF, $f_-(\mathcal{E}, L_z)$. The HQ inversion formulae are then given by

$$f_+(\mathcal{E}, L_z) = \frac{1}{2\sqrt{2}\pi^2}\mathrm{Im}\left\{\int_C \frac{d\xi}{(\xi-\mathcal{E})^{1/2}}\frac{d^2\rho}{d\psi^2}\bigg|_{R^2=\frac{L_z^2}{2(\xi-\mathcal{E})},\xi=\psi}\right\} \tag{4.25}$$

$$f_-(\mathcal{E}, L_z) = \frac{\mathrm{sgn}(L_z)}{4\pi^2}\mathrm{Im}\left\{\int_C \frac{d\xi}{(\xi-\mathcal{E})}\frac{d^2(\rho\langle v_\phi\rangle)}{d\psi^2}\bigg|_{R^2=\frac{L_z^2}{2(\xi-\mathcal{E})},\xi=\psi}\right\}, \tag{4.26}$$

where ρ and $\langle v_\phi\rangle$ are, respectively, the density profile and the mean rotational velocity of the mass component under consideration, while ψ is the total potential obtained by summing the contribution of each mass component in the system. The contour C is shown in the right panel of Fig. (4.1); note that the evaluation of the integrals (4.25) and (4.26) requires us to carry out an analytic continuation, to the complex plane, of the functions appearing in the integrand, such as the density and the potential. Upon exploiting the analyticity of the integrands of the contour integrals, it is sufficient to perform the integration over the portion of the contour lying on the upper half plane.

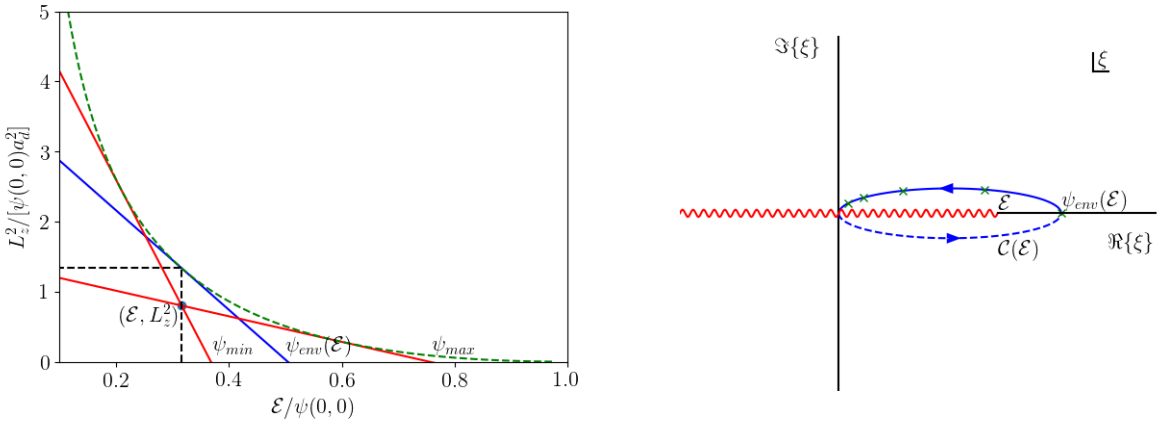

Figure 4.1: The physically relevant region in the $\mathcal{E} - L_z^2$ plane is the area under the dotted green curve, which we refer to as the *critical line*, in the left panel. This critical line is constructed from all lines $L_z^2 = 2R^2[\psi(R^2, 0) - \mathcal{E}]$. On the right panel, we have the contour along which we perform the integration to carry out the HQ inversion.

We make a few comments regarding the details of the inversion scheme. Firstly, we note that the PSDF is zero outside the physical region. From (4.23), this physical region is defined by

$$L_z^2 \leq 2u(\psi - \mathcal{E}), \quad 0 \leq \mathcal{E} \leq \psi, \tag{4.27}$$

for fixed $u \equiv R^2$ and $v \equiv z^2$, and for the case of a finite mass model. On the $\mathcal{E} - L_z^2$ plane, the physical region lies under the dotted green curve, the *critical curve* denoted by $L_z^2 = L_c^2(\mathcal{E})$, in the left panel of Fig. (4.1). Given a point in the physical region, $P(\mathcal{E}, L_z^2)$, one can construct the line tangent to the critical curve at $\mathcal{E}$; the $\mathcal{E}$-intercept is denoted by $\psi_{env}(\mathcal{E})$. Physically, this is the value of the relative potential for a circular orbit on the Galactic plane corresponding to a relative energy $\mathcal{E}$. Regarding the calculation of the contour integrals (4.25) and (4.26), one can use an elliptical contour, where

$$\xi(\theta) = \psi_{env}(\mathcal{E}) \left(\frac{1 + \cos\theta}{2} \right) + ih \sin\theta, \quad 0 \leq \theta \leq \pi. \tag{4.28}$$

The value of h is usually chosen to be $0.1\psi_{env}(\mathcal{E})$. One may also notice that the integrand involves the second derivative with respect to ψ. In principle, the density and potential are functions of u and and v. However, operating under the assumption that the potential ψ, for fixed u, is a monotonic decreasing function of v, we can trade v with ψ. It is then convenient to rewrite

$$\frac{\partial^2 f}{\partial \psi^2} = \left(\frac{\partial \psi}{\partial v} \right)^{-3} \left(\frac{\partial \psi}{\partial v} \frac{\partial^2 f}{\partial v^2} - \frac{\partial f}{\partial v} \frac{\partial^2 \psi}{\partial v^2} \right). \tag{4.29}$$

Finally, we have the issue of inverting v from the equation

$$\xi = \psi \left(u = \frac{L_z^2}{2(\xi - \mathcal{E})}, v \right). \tag{4.30}$$

In principle, this is a transcendental equation, which can be solved using Newton's method, or by a root-finding algorithm based on optimization schemes, *e.g.* [276]. Here we have devised a method of addressing this problem by first solving v for $\theta = 0$; note that we have

$$\xi(\theta = 0) = \psi_{env}(\mathcal{E}) = \psi \left(u = \frac{L_c^2(\mathcal{E})}{2(\psi_{env}(\mathcal{E}) - \mathcal{E})}, 0 \right) = \psi \left(u = \frac{L_z^2}{2(\psi_{env}(\mathcal{E}) - \mathcal{E})}, v \right), \tag{4.31}$$

where $0 \leq L_z^2 \leq L_c^2(\mathcal{E})$. Once we have $v(\theta = 0)$, we can build a table of values of v along the elliptical contour. We can simply obtain $v(\theta)$ by interpolating from this table. Note that as θ approaches π, ξ approaches 0, which implies that v must be very large. Consequently, the integrands in (4.25) and (4.26) become extremely small, so the integration over θ is carried only up to $\pi(1 - \epsilon)$, for some sufficiently small parameter ϵ, typically taken around 0.05.

4.4 Milky Way mass modelling

A necessary input to the HQ inversion scheme, which we will use to recover the PSDF for the DM component in the Milky Way (MW), is the MW mass model. The modelling of the MW

has been the subject of studies carried out over the years, where collated observational data on the MW were used to constrain such mass models. There are a variety of models used to describe the MW, *e.g.* [277, 278], but the mass components of the MW is generally split into: the baryonic disk and bulge components, which dominate the potential in the inner regions of the Galaxy; and a nonbaryonic DM halo which dominates the outskirts of the Galaxy. In this chapter, we shall follow the modelling done in [279] where the MW is split into its disk, bulge, and halo components, and specifying either the density profile or the potential that is sourced by one component. Each mass component is modelled by a particular potential/density profile, which is conveniently summarized in Table 4.1. For the Galactic disk, instead of breaking it further into the thin stellar, thick stellar, and gaseous disk components, *e.g.* [278], it is modelled as a single Miyamoto-Nagai potential

$$\psi_{MN}(u,v) = \frac{GM_d}{\sqrt{u + \left(a_d + \sqrt{v + b_d^2}\right)^2}}, \tag{4.32}$$

which provides a satisfactory fit to the disk potential. For the Galactic bulge, we have the Hernquist model

$$\psi_{HQ}(u,v) = \frac{GM_b}{\sqrt{u+v} + a_b}. \tag{4.33}$$

Regarding the MW DM halo, its inferred structure is quite uncertain, as literature sources do not seem to converge to a single coherent picture. Typically, the NFW profile is adopted to model the halo; the density profile is given by

$$\rho(r) = \frac{\rho_s}{x^\gamma (1+x)^{3-\gamma}},\ x \equiv r/r_s, \tag{4.34}$$

where by default, the logarithmic slope is $\gamma = 1$. An axisymmetric generalization of the NFW profile is to replace r with the spheroidal coordinate $m \equiv \sqrt{R^2 + z^2/q^2}$, to yield

$$\rho(m) = \frac{\rho_s}{x^\gamma (1+x)^{3-\gamma}},\ x \equiv m/r_s, \tag{4.35}$$

where $q > 1$ (< 1) corresponds to a prolate (oblate) halo. For any spheroidal density profile $\rho(m^2)$ the potential is given by

$$\psi(u,v) = 2\pi G_N q \int_0^\infty \frac{dx}{(1+x)\sqrt{q^2+x}} \int_{U(x)}^\infty \rho(m^2) d(m^2), \quad U(x) \equiv \frac{u}{1+x} + \frac{v}{q^2+x}. \tag{4.36}$$

For the spherical NFW potential, *i.e.* the case $q = 1$, an exact analytic result can be obtained and is given by

$$\psi_{NFW,q=1}(u,v) = 4\pi G_N \rho_s r_s^2 \frac{\ln(1 + r/r_s)}{r/r_s}, \quad r^2 = u + v. \tag{4.37}$$

From the point of view of N-body simulations of purely collisionless cold DM (CCDM), the structure of halos is triaxial. It is claimed by [280] that CDM simulations indicate that haloes

are highly non-spherical — mass accretion into haloes is directional and clumpy, thus one should not expect a spherical halo. However, as mentioned in [281], accounting for the condensation of baryons in the central regions of the Galaxy leads to rounder halos. Furthermore, baryonic effects can have an impact on the logarithmic slope of the density profile, in which it could be driven away from $\gamma = 1$.

The Sagittarius (Sgr) dwarf galaxy, and the morphology of the stream that resulted from its disruption, has been useful in inferring the mass distribution in the MW. In [282], where they carried out simulations of the stripping of the Sgr progenitor, they noted that the trajectory of the stream is mostly sensitive to the properties of the halo, since the Sgr dwarf orbits at large Galactocentric distances where the baryonic components are known to be subdominant: they eventually concluded that the Galactic DM halo is close to spherical. Fellhauer et. al. [283] pointed out the presence of a bifurcation in the Sgr remnant, and that there are four distinct branches of material. Depending on the heliocentric distance, these branches are situated at different angular declinations. A difference in angular declinations would indicate that these stream branches lie on different orbital planes. If the underlying potential were exactly spherical, the precession of the orbital plane would not be possible, and one is forced to consider aspherical potential models, which could be attributed to the bulge/disk and/or halo. However, too much oblateness would make the branches more diffuse, which would run in tension with observations. Fellhauer et. al. then demonstrated that an NFW halo with $q = 1$ provides the best fit to the observed bifurcation of streams. In contrast, [284] introduced the hypothesis that the DM halo might be triaxial. This is motivated by the apparent disagreement between the preferred halo structure implied by the precession of the Sgr leading arm (spherical/slightly oblate halo) and radial velocities of the arm (prolate halo). Here they considered axisymmetric disk and bulge components (Miyamoto-Nagai and Hernquist spheroid), while the halo component is specified by a logarithmic triaxial potential. They have found that within 60 kpc, the axial ratios are $p = 0.83$ and $q = 0.67$. Still following the approach of halo modelling by fits to the Sgr stream, [285] showed, using an optimized stream-fitting algorithm which avoids performing N-body simulations, that spherical haloes are still viable. However, this leads to a rising circular velocity curve that eventually flattens out beyond $\sim$50 kpc, albeit still being consistent with observations. Finally, [286] have taken into account the passage of the Large Magellanic Cloud in tracking the Sgr stream, and the hypothesis of a twisted halo — axisymmetric in the inner part, and then becoming triaxial in the outer region — seems to fit the observed properties of the stream. This result of a twisted halo is in agreement with an earlier study by [287], where they analyzed MW analogs in the EAGLE simulation; they claim that the formation of twisted haloes is a generic prediction of ΛCDM. The shape of the inner part of the halo is sensitive to baryonic physics, since baryons dominate the central parts of the galaxy. On the other hand, the tight connection between the shape of the outer part of the halo and satellite orbits, is an indication that gravitational collapse play a dominant role in determining the halo structure in the outskirts of the Galaxy.

Inferring the halo structure has also been performed using astrophysical observations other than modeling the Sgr stream. Again, there is some disagreement in the inferred halo structure, although a slight deviation from $q = 1$ is generally suggested. Olling and Merrifield [288] used two techniques to infer the shape of the MW DM halo: stellar kinematics (essentially just the rotation curve) and flaring gas-layer method; both methods consistently estimate the q-parameter of the

halo to be 0.8. Sesar et. al. [289] considered axisymmetric halo models and determined the best fit parameters that agree with the stellar halo distribution from the CFHT Legacy Survey data. Here they take into account enhancements due to the Sagittarius and Monoceros streams. They find $q = 0.84$, *i.e.* a slightly oblate halo. Nitschai et. al. [290] used Jeans axisymmetric modelling [291] alongside 6-dimensional phase space data of giant stars from Gaia DR2 to obtain constraints on: the MW stellar disk (double exponential model), bulge, and DM halo (the latter two being modeled by a generalized NFW profile with tunable inner slope and axial ratio). Their analysis suggests a slightly prolate halo ($q = 1.14$) and an inner slope $\gamma = 1.53$; they further claim that the NFW halo would produce an inconsistent circular velocity profile that is already excluded by Gaia data.

Due to this apparent lack of consensus regarding halo shape, we shall instead adhere to the case of an NFW profile with $\gamma = 1$ and $q = 1$, while allowing the possibility of the axial ratio q to slightly deviate from unity. At this point, we have a family of MW models, where a particular realization amounts to specifying the values of the parameters that enter in each mass component. In line with building models that reflect observational data, we would like to select a realization of the mass model which best fits astrophysical data, *e.g.* kinematic data for tracers of the underlying gravitational potential. In [292], kinematic data — namely rotation curve, vertical force, and surface density measurements — together with flat priors on the parameters of the MW mass model, were used to generate posterior distributions over the mass model parameters via Markov Chain Monte Carlo (MCMC) sampling. We then take the median of the single parameter posteriors as the fiducial values of the mass model parameters in [292], which we list down in Table 4.1. In changing the q value away from unity, we take the simplified

Component	Model	Parameters	Best fit values
Disk	Miyamoto-Nagai	M_d	$6.7 \times 10^{10} M_\odot$
		a_d	$3.4\,\mathrm{kpc}$
		b_d	$0.39\,\mathrm{kpc}$
Bulge	Hernquist	M_b	$0.7 \times 10^{10} M_\odot$
		a_b	$0.5\,\mathrm{kpc}$
DM Halo	Oblate NFW	ρ_s	$10^{7.2} M_\odot\,\mathrm{kpc}^{-3}$
		r_s	$13\,\mathrm{kpc}$
		q	1

Table 4.1: A list of Milky Way (MW) mass components and the parameters which specify a particular mass model. The values we report here were taken from the median of the single parameter posteriors obtained by [292].

approach of keeping the halo length scale r_s fixed while rescaling the density normalization ρ_s, so as to match with the local circular velocity prediction $V_c(R_\odot)$ of the mass model with the fiducial values. Note that

$$V_c^2(R_\odot) = -2u \frac{\partial \psi}{\partial u}\bigg|_{u=R_\odot^2,\ v=0}, \tag{4.38}$$

where we take $R_\odot = 8.122\,\mathrm{kpc}$. In the fiducial model, $V_c(R_\odot) = 230.3\,\mathrm{km/s}$. Changing q to 0.61, which is a reference value we take from [286], requires setting $\rho_s = 2.15 \times 10^7 M_\odot\,/\mathrm{kpc}^3$.

In Fig. (4.2) we show the plot of the circular velocity arising from these two models. Notice that there is excellent agreement in the inner parts of the Galaxy. In the outer region the oblate halo predicts a slightly lower circular velocity: this is due to the flattening of the density profile, which leads to a slightly lower enclosed mass compared to the spherical case.

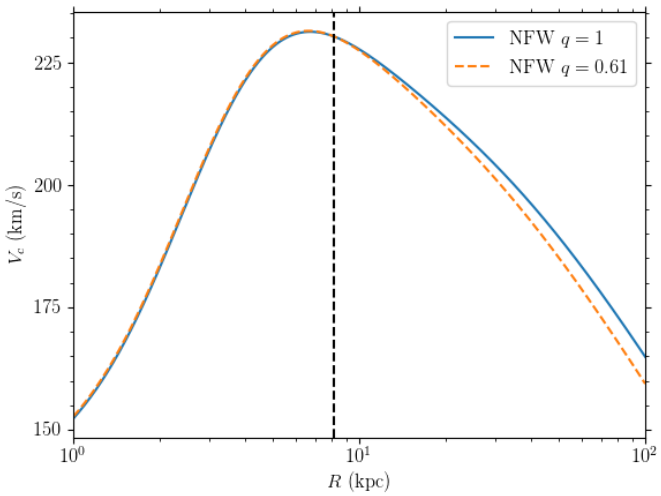

Figure 4.2: Plot of the circular velocity V_c on the Galactic plane as a function of distance R from the Galactic center, for the fiducial mass model (solid) and a modified halo profile (dashed) where $q = 1$ and ρ_s is tuned to achieve agreement with V_c at $R = R_\odot$.

4.5 Sanity check for the HQ inversion

The inversion formulae, (4.25) and (4.26), can be used to obtain the PSDF for any of the three MW mass components. Since we are interested in eventually computing the mean inverse velocity of DM, which enters the calculation of the recoil spectrum, we shall obtain the PSDF for the DM halo. Given the density profile (4.35) for the DM halo, the even part f_+ can be obtained using (4.25). On the other hand, from (4.26), the mean azimuthal velocity $\langle v_\phi \rangle$ must be supplied in order to obtain f_-. However, $\langle v_\phi \rangle$ for the DM component is largely unknown or is poorly constrained from kinematical data from luminous tracers. One approach that can be done is to simply write the odd part as

$$f_- = \alpha_0 \frac{L_z}{\sqrt{L_z^2 + L_{z*}^2}} f_+, \quad 0 \leq \alpha_0 \leq 1, \tag{4.39}$$

for some sufficiently small L_{z*}. Here α_0 is a rotation parameter. If we are assuming that the halo is spherical, i.e. $q = 1$, it has been demonstrated in [293], using a Maxwell's demon-type argument, that a spherical halo, initially having zero overall rotation, can have a nonzero mean azimuthal rotation while still retaining its shape. This argument works, provided we allow for violation of angular momentum conservation. In the same paper, it was also shown

that the resulting halo is stable. From a technical standpoint, one should note that, for our context, the PSDF from HQ inversion is only useful when it appears in the calculation of velocity moments. Performing numerical integration to compute these velocity moments requires several function calls to the PSDF. Hence it is useful to build a two-dimensional table of the PSDF values over $\mathcal{E}$ and L_z, and approximate the PSDF as a function which interpolates over such table. Furthermore, it is convenient to work with a rectangular grid, and thus one can make a coordinate transformation from $(\mathcal{E}, L_z)$ to (ϕ, y), where

$$\mathcal{E} = \psi - \frac{y^2}{2R^2} \tag{4.40}$$

$$L_z = y \sin\phi, \tag{4.41}$$

so that

$$-\frac{\pi}{2} \leq \phi \leq \frac{\pi}{2}, \quad 0 \leq y \leq \sqrt{2R^2\psi}. \tag{4.42}$$

The grid is constructed by creating a mesh of points from one-dimensional arrays along ϕ and y. To keep the density of points along y to be fairly uniform, we have implemented an adaptive scheme which changes the number of points as we change R.

At this point, it pays to perform a sanity check on the PSDF, as well as on the interpolation scheme. This can be done by comparing the density profile ρ, obtained by integrating the PSDF over velocities, with the actual density profile in (4.35), which we temporarily denote by $\bar{\rho}$. Note that from the PSDF, the density profile is

$$\rho = \frac{2\pi}{R} \int d\mathcal{E} dL_z \; f_+(\mathcal{E}, L_z), \tag{4.43}$$

where the integration is performed over the physical region. This integral can be computed either by using a general-purpose integrator, or by a Monte Carlo sampling method which only involves using the tabulated values of the PSDF. The absolute relative error between ρ and $\bar{\rho}$, as a function of R, is shown in Fig. (4.3).

4.6 Mean inverse velocity and velocity moments — axisymmetric case

For the case of an axisymmetric distribution, one can derive a general expression for the velocity moments, that is conveniently expressed as an integral over $\mathcal{E}$ and L_z. In this manner, one can directly pin down the values of $\mathcal{E}$ and L_z from which one constructs the table of PSDF values required for the interpolation. The velocity moments are then given by the compact expression (a derivation of this expression can be found in Appendix B)

$$\langle v^{k-1} \rangle = \frac{4}{R\rho} \int d\mathcal{E} dL_z \; f(\mathcal{E}, L_z) \; \left[v_+^2 + (L_z/R - v_{E\phi})^2 \right]^{(k-1)/2} \; \mathcal{K}_k(\mathcal{E}, L_z) \tag{4.44}$$

$$\rho = \frac{2\pi}{R} \int d\mathcal{E} dL_z \; f(\mathcal{E}, L_z), \tag{4.45}$$

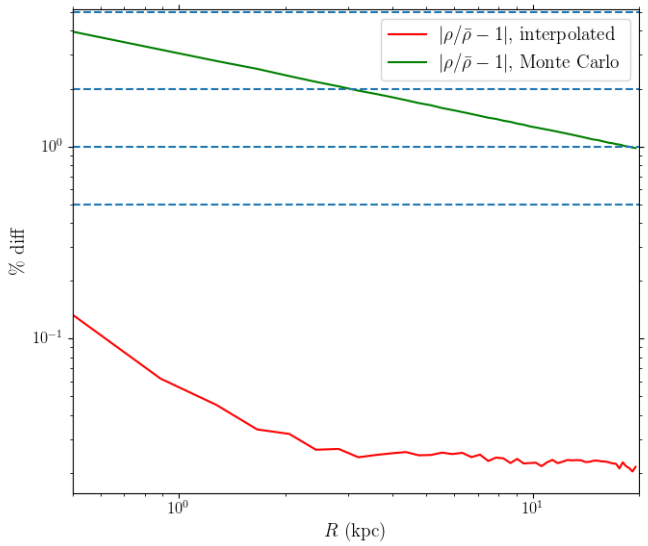

Figure 4.3: Plot of the percent difference, as a function of R, between the actual DM density and: (i) density from integrating the interpolated PSDF (red) and (ii) density from Monte Carlo integration (green). The horizontal lines correspond to: 0.5%, 1%, 2%, and 5% levels. Here we are using halo parameters from Table 4.1, and $z = 0$. All MW components contribute to the total potential as well.

where the integration region is

$$0 \leq \mathcal{E} \leq \psi, \quad L_z^2 \leq 2R^2(\psi - \mathcal{E}) \tag{4.46}$$

for a finite mass model. Also

$$v_\pm \equiv \sqrt{v_{ER}^2 + v_{Ez}^2} \pm \sqrt{2\left(\psi - \mathcal{E} - \frac{L_z^2}{2R^2}\right)}, \tag{4.47}$$

and the kernel is

$$\mathcal{K}_k(\mathcal{E}, L_z) \equiv \int_0^{\pi/2} d\phi \ \left(1 - \gamma^2 \sin^2\phi\right)^{(k-1)/2} \ \theta\left(\sqrt{1 - \gamma^2 \sin^2\phi} - \beta_{min}\right), \tag{4.48}$$

where

$$\gamma^2 \equiv \frac{v_+^2 - v_-^2}{v_+^2 + (L_z/R - v_{E\phi})^2}, \quad \beta_{min} \equiv \frac{v_{min}}{\sqrt{v_+^2 + (L_z/R - v_{E\phi})^2}}. \tag{4.49}$$

Typically we only consider the cases $k = 0$ and $k = 2$; the kernels for such cases reduce to elliptic integrals. More precisely, we have

$$\mathcal{K}_0(\mathcal{E}, L_z) = \begin{cases} F(\gamma^2), \ 0 \leq \beta_{min} \leq \sqrt{1 - \gamma^2} \leq 1 \\ \\ F(\gamma^2, \phi_{min}), \ \sqrt{1 - \gamma^2} \leq \beta_{min} < 1 \end{cases} \tag{4.50}$$

where $F(m)$ is the complete elliptic integral of the first kind, while $F(m, \phi_0)$ is the incomplete elliptic integral of the first kind, and

$$\phi_{min} \equiv \arcsin\left(\sqrt{1-\beta_{min}^2}/\gamma\right). \tag{4.51}$$

For $k = 2$, simply replace F by E, the elliptic integral of the second kind. These functions can be efficiently computed using various means; here we are using the routines developed in [294]. As a final remark, note that β_{min} can be at most 1 if we want the kernel in (4.48) to be nonzero. In the case of a finite mass model, one can show that

$$v_+^2 + \left(\frac{L_z}{R} - v_{E\phi}\right)^2 \leq \left(v_E + \sqrt{2\psi}\right)^2 \tag{4.52}$$

so that the kernel will naturally have a cutoff at

$$v_{min,*} = v_E + \sqrt{2\psi}. \tag{4.53}$$

In computing the velocity moments for an axisymmetric model, we shall use the PSDF that is obtained from HQ inversion. From a numerical standpoint, however, the HQ inversion could sometimes lead to an unphysical situation where the PSDF becomes negative; this issue has been pointed out in the context of Eddington inversion in [295]. On the other hand, the velocity moments, which are explicit functions of v_{min}, can be easily shown to be monotonically decreasing in $v_{min}$for a physical PSDF. This criterion is actually a useful sanity check to see if the HQ inversion leads to a physical PSDF. In cases where we encounter a negative PSDF, we simply reset it to be zero. In Fig. (4.4) we plot the mean inverse velocity as a function of v_{min} for: (i) the standard halo model (SHM) with $v_0 = 220\,\mathrm{km/s}$ and $v_{esc} = 544\,\mathrm{km/s}$, and (ii) the axisymmetric PSDF of a nonrotating DM halo, *i.e.* $\alpha_0 = 0$, for the mass model summarized in Table (4.1).

We would like to emphasize that the Earth velocity prescription for both cases still follows the decomposition

$$\vec{v}_E \;=\; \vec{V}_{LSR} + \vec{V}_\odot + \vec{v}_{E,\odot}, \tag{4.54}$$

where $\vec{V}_{LSR}$ is the Local Standard of Rest (LSR), $\vec{V}_\odot$ is the peculiar velocity of the Sun relative to the LSR, and $\vec{v}_{E,\odot}$ is the heliocentric velocity of the Earth. We shall use the prescription outlined in [296] for the Earth's heliocentric velocity, while the Sun's peculiar velocity is taken to be

$$\vec{V}_\odot = -(11\,\mathrm{km/s})\hat{e}_R + (12\,\mathrm{km/s})\hat{e}_\phi + (7\,\mathrm{km/s})\hat{e}_z. \tag{4.55}$$

As for $\vec{V}_{LSR}$, we take this to be the local circular velocity; for the axisymmetric case, we will use the self-consistent prediction for $V_c(R_\odot)$ instead of the v_0 value from SHM.

The Earth's velocity is a function of time since the Earth revolves around the Sun, and this causes a modulation in the mean inverse velocity. By performing Fourier analysis, one can determine the mean values and the amplitudes of modulation of the Earth's speed, the Earth's tangential velocity, and the Earth's speed projected on the meridional plane; we tabulate these values in Table (4.2). These values are the ones we will plug-in to the mean inverse velocity.

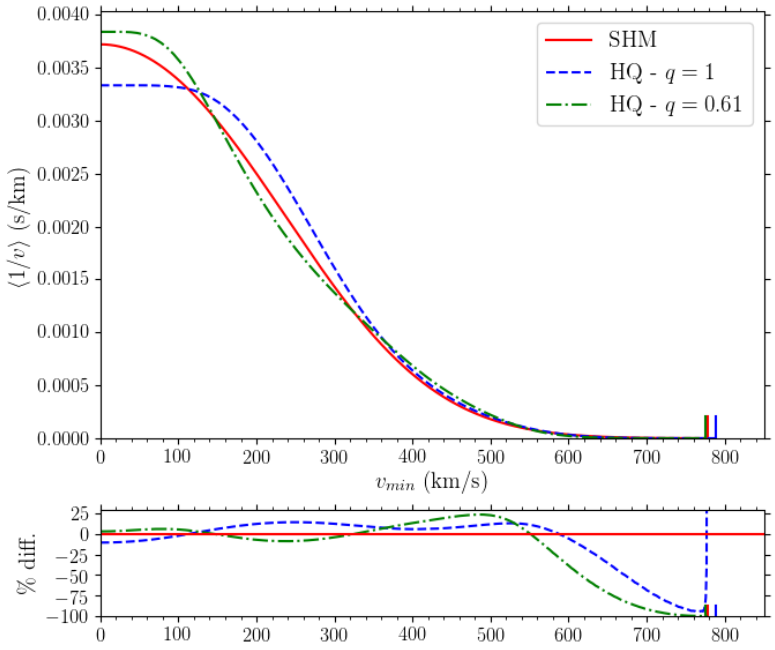

Figure 4.4: Top panel: Plot of the mean inverse velocity as a function of v_{min} for the standard halo model (SHM, dashed red curve), and for the PSDF from the HQ inversion of the axisymmetric model with parameters listed in Table 4.1 (solid blue curve). Bottom panel: Percent deviation of the axisymmetric model prediction for the mean inverse velocity relative to the SHM.

VDF model	Quantity	Mean (km/s)	Amplitude of modulation (km/s)
SHM	$\lvert\vec{v}_E\rvert$	233.9039	16.0869
HQ	$v_{E,\phi}$	242.4601	15.3044
	$v_{E,\perp}$	26.8743	13.0041

Table 4.2: Mean values and amplitudes of modulation of certain velocity quantities, relative to the Galactic center. The mean and modulation amplitudes for $v_{E,\phi}$ and $v_{E,\perp}$ for the axisymmetric case is the same for both $q = 1$ and $q = 0.61$ since we have explicitly matched their respective predictions for the local circular velocity.

4.7 Non-astrophysics part of the spectrum

Before we present the exclusion limits on $\bar{\sigma}_e$ vs m_χ, let us sift out the portion of the integrand of the recoil spectrum (4.15), that is independent of the DM halo distribution; we shall refer to it as $P(q)$. It is convenient to plot $P(q)$ as a function of v_{min}, so we can compare it with the mean inverse velocity — a quantity that is explicitly a function of v_{min}. Using (4.17) we can trade q

with v_{min}, so that we have

$$dv_{min}\ \tilde{P}(v_{min}) = dq\ q\ |F_{DM}(q)|^2 \langle |f_{nl}^{(ion)}(k',q)|^2 \rangle, \tag{4.56}$$

$$\tilde{P}(v_{min}) = \frac{1}{\sqrt{v_{min}^2 - 2\Delta E/m_\chi}} \sum_{q \in \{q_-(v_{min}), q_+(v_{min})\}} \left[q^2\ |F_{DM}(q)|^2 \langle |f_{nl}^{(ion)}(k',q)|^2 \rangle \right], \tag{4.57}$$

where

$$q_\pm(v_{min}) \equiv \left| m_\chi v_{min} \pm \sqrt{m_\chi^2 v_{min}^2 - 2 m_\chi \Delta E} \right|. \tag{4.58}$$

Note that within the physical range of momentum transfers q there is a minimum value of v_{min} for a given orbital nl, outgoing electron energy, and DM mass m_χ, so that

$$\sqrt{\frac{2\Delta E}{m_\chi}} \leq v_{min} \leq v_{max}; \tag{4.59}$$

the minimum v_{min} is obtained when $q = q_* \equiv \sqrt{2 m_\chi \Delta E}$. As always, we shall consider a xenon

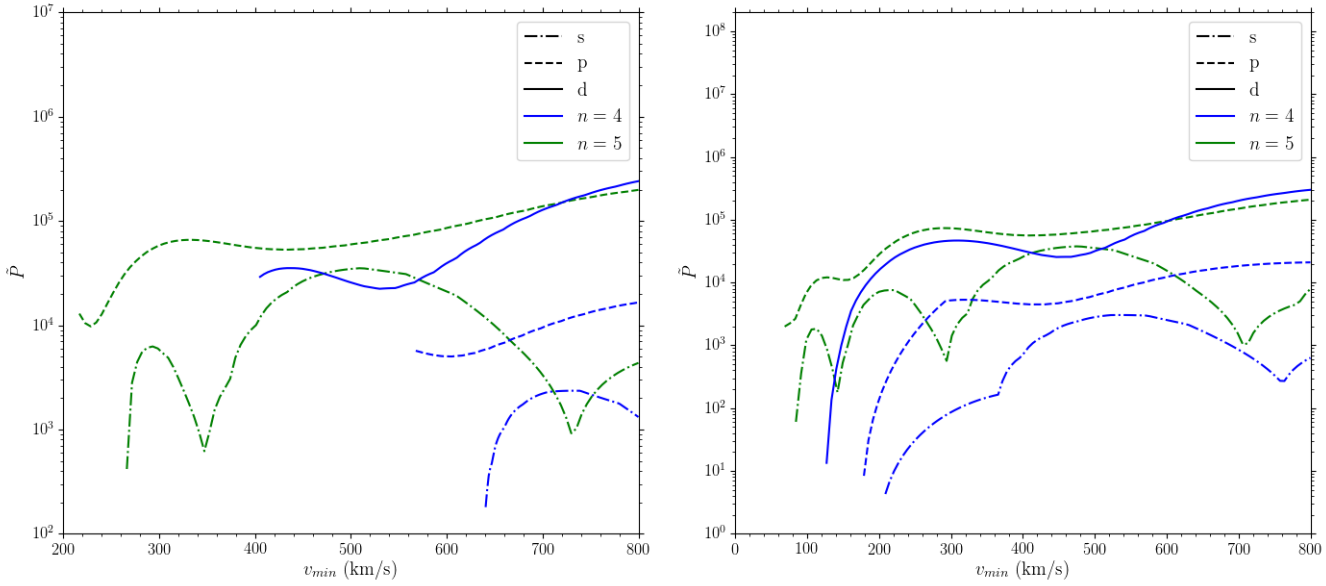

Figure 4.5: Plot of $\tilde{P}$, the part of the integrand of the recoil spectrum independent of astrophysical information, as a function of v_{min}, for two different values of DM mass: 100 MeV (left panel) and 1 GeV (right panel). Here we assume $F_{DM} = 1$. In both cases, the outgoing electron momentum is $k' = \alpha m_e = 3.74\,\text{keV}$. Each curve on both panels corresponds to a particular xenon orbital: the color code refers to the principal quantum number while the linestyle corresponds to the orbital quantum number.

detector, and also consider both $F_{DM} = 1$ and $F_{DM} = (\alpha m_e)^2/q^2$, *i.e.* respectively, contact and long-range DM-electron interactions. As benchmark, however, we only consider contact

interactions in Fig. (4.5), where we plot $\tilde{P}(v_{min})$ as a function of v_{min} for two different DM masses: 100 MeV and 1 GeV. For each DM mass, we plot $\tilde{P}(v_{min})$ for different orbitals of xenon that significantly contribute to the recoil spectrum, namely the $4s$, $4p$, $4d$, $5s$, and $5p$ orbitals. Firstly, one can notice the presence of a low velocity cutoff for all cases. This cutoff can be easily computed from the minimum value of v_{min} in (4.59); note first that for an orbital nl,

$$\Delta E_{nl} = \frac{k'^2}{2m_e} - E_{nl} = (13.6\,\mathrm{eV}) \left(\frac{k'}{\alpha m_e}\right)^2 + |E_{nl}|\,, \tag{4.60}$$

where E_{nl} is the (negative) bound state energy of the nl orbital. The absolute bound state energies of these orbitals are listed down in Table 4.3. Then the minimum v_{min}, which we denote as v_{min*}, will have a typical value of

$$v_{min*} \approx (300\,\mathrm{km/s}) \left(\frac{\Delta E}{50\,\mathrm{eV}}\right)^{1/2} \left(\frac{100\,\mathrm{MeV}}{m_\chi}\right)^{1/2}, \tag{4.61}$$

corresponding to a momentum transfer

$$q_* = \sqrt{2m_\chi \Delta E} = 26.8\ \alpha m_e \left(\frac{m_\chi}{100\,\mathrm{MeV}}\right)^{1/2} \left(\frac{\Delta E}{50\,\mathrm{eV}}\right)^{1/2}. \tag{4.62}$$

The value of v_{min*} decreases for outer shell electronic orbitals, or heavier DM; for such cases, the accessible range of v_{min} values becomes wider. Note that some values of v_{min} in Fig. (4.5) may correspond to q values that lie outside the range of momentum transfer values in the form factor table of [270]; in such cases, we extrapolate atomic form factors by assuming outgoing plane waves, endowed with a corrective Fermi factor to account for the long-range effect of the nucleus on the electron, and rescaling these values to match with [270].

We can make a statement about the sensitivity of DM-electron scattering on the deviation of the mean inverse velocity from the SHM prediction. As seen from (4.61) and from the right panel of Fig. (4.5), larger DM masses are sensitive to a wider range of v_{min} values. On the other hand, Fig. (4.4) shows that, in the range around $0 - 500\,\mathrm{km/s}$, the prediction for the mean inverse velocity using our MW mass model is above the SHM prediction around the range $120 - 380\,\mathrm{km/s}$, with a maximum deviation of $\sim$20%: in the remaining intervals, the MW mass model gives a lower mean inverse velocity than SHM. The cross over of the relative difference in mean inverse velocity from negative to positive induces a cancellation effect: we expect that the total ionization rate from the two PSDFs under consideration will differ by a few percent.

As for smaller DM masses, we can only access a narrow range of v_{min} values. Looking at Fig. (4.4), beyond 500 km/s up to the escape velocity cutoff, the relative deviation between the SHM and MW mass model predictions for the mean inverse velocity goes down all the way to -100%. While this v_{min} range features the largest relative deviation between the predictions to the mean inverse velocity from the two PSDFs under consideration, the mean inverse velocity itself is very small to give a sizable event rate.

4.8 Direct detection limits

We are now in a position to derive the direct detection limits on the scattering cross section $\bar{\sigma}_e$, using XENON10 and XENON100 data, and we follow the procedure outlined in [270]. Firstly,

Orbital	Binding energy (eV)
4s	214.643
4p	164.154
4d	75.895
5s	25.802
5p	12.493

Table 4.3: Absolute values of the bound state energies of xenon orbitals.

one must convert the recoil spectrum in outgoing electron energy E' into a spectrum in n_e, the electron yield. To convert electronic recoil energies E' into electron yields, we must adhere to a stochastic model of ionization inside the detector filled with liquid xenon. Note that a DM scattering event will produce quanta of photons and electrons: the total number of quanta is

$$N_q(E') = n_1 + n_2, \tag{4.63}$$

where n_1 is the number of quanta due to primary ionization, given by

$$n_1 = \left\lfloor \frac{E'}{W} \right\rfloor. \tag{4.64}$$

Here, we take the fiducial value of W to be 13.8 eV. On the other hand, n_2 is the number of secondary quanta, which arise from the de-excitation of electrons in the outer shell of xenon as its inner shell is ionized: n_2 is given by

$$n_2 = \left\lfloor \frac{E_i - E_j}{W} \right\rfloor \tag{4.65}$$

where i and j are, respectively, the outer and inner xenon orbitals under consideration.

A portion of the total number of quanta N_q produced comes from the contribution of the electron yield n_e, which, in turn, can be decomposed as

$$n_e = n'_e + n''_e. \tag{4.66}$$

Here, n'_e is the number of free electrons that recombine with an ionized xenon atom; the recombination process with $n'_e = 1$ occurs with probability f_R, while $n'_e = 0$ occurs with probability $1 - f_R$. Meanwhile, n''_e is, in principle, a discrete random variable that can take values from 0 to N_q; this random variable follows a binomial distribution with success probability f_e. Hence the total number of events with electron yield n_e is

$$N(n_e) = \int d(\ln E') \ \left[f_R P(n_e; N_q(E')) + (1 - f_R) P(n_e - 1; N_q(E')) \right] \frac{dR}{d(\ln E')}, \tag{4.67}$$

where

$$P(n_e; N) \equiv \binom{N}{n_e} f_e^{n_e} (1 - f_e)^{N - n_e}. \tag{4.68}$$

Here we take $f_R = 0$ and $f_e = 0.83$ as fiducial values [270]. We then convert this into an event spectrum over photoelectron (PE) yields, which are the actual experimental observables. This done by convolving $N(n_e)$ with a Gaussian response function

$$\mathcal{P}(PE|n_e) = \frac{1}{\sqrt{2\pi\sigma^2 n_e}} \exp\left[-\frac{(PE - n_e\mu)^2}{2\sigma^2 n_e}\right]. \tag{4.69}$$

The values of μ and σ depend on the experiment, and are listed in Table (4.4). This spectrum over PE must then be multiplied by the trigger $t(PE)$ and acceptance ϵ_a (taken to be 0.92 for the XENON10 experiment, while, for the XENON100 experiment, we interpolate over a table of efficiency values) efficiencies. Thus we have

$$\frac{dN}{d(PE)} = \epsilon_a(PE)t(PE)\sum_{n_e}\mathcal{P}(PE|n_e)N(n_e). \tag{4.70}$$

We perform a binned analysis to get the final 90% exclusion limits. We bin the total number of events in PE bins starting from PE_0, and in bins of width ΔPE; the values of PE_0 and ΔPE are both dependent on the experiment, and are also listed in Table (4.4). In the i^{th} bin, the expected number of events is

$$N_i = \int_{PE_i}^{PE_{i+1}} d(PE)\ \frac{dN}{d(PE)}. \tag{4.71}$$

On the other hand, the observed number of events per PE bin from either experiment is known, from which one can determine the mean number of events λ_i, under a Poisson distribution, corresponding to 90% CL. The 90% CL for $\bar{\sigma}_e$ is taken to be N_i/λ_i multiplied by $10^{-39}\,\text{cm}^2$.

Experiment	exposure (kg yr)	μ	σ	PE_0	ΔPE
XENON10	0.041	27	6.2	14	27
XENON100	29.8	19.7	6.9	80	20

Table 4.4: Values of the parameters that are dependent on experiment.

VDF model	ρ_{DM} (GeV/cm^3)	v_{esc} (km/s)	v_E (km/s)	v_{max} (km/s)
SHM	0.400	544.0	233.9	777.9
HQ, $q = 1$	0.357	544.1	243.9	788.1
HQ, $q = 0.61$	0.496	531.6	243.9	775.5

Table 4.5: Values of the local DM density, local escape velocity, and maximum speed in the detector frame for the SHM, and those obtained self-consistently from the mass model.

Then the overall limit per m_χ is just the minimum $\bar{\sigma}_e$ across bins: this is shown in Fig. (4.6). The exclusion limits in Fig. (4.6) are color coded based on the PSDF, while the line style corresponds to the detector. At the high mass end of the exclusion plot, where we expect the number density to dominate the recoil rate, we see that the blue curve ($q = 1$), is slightly above

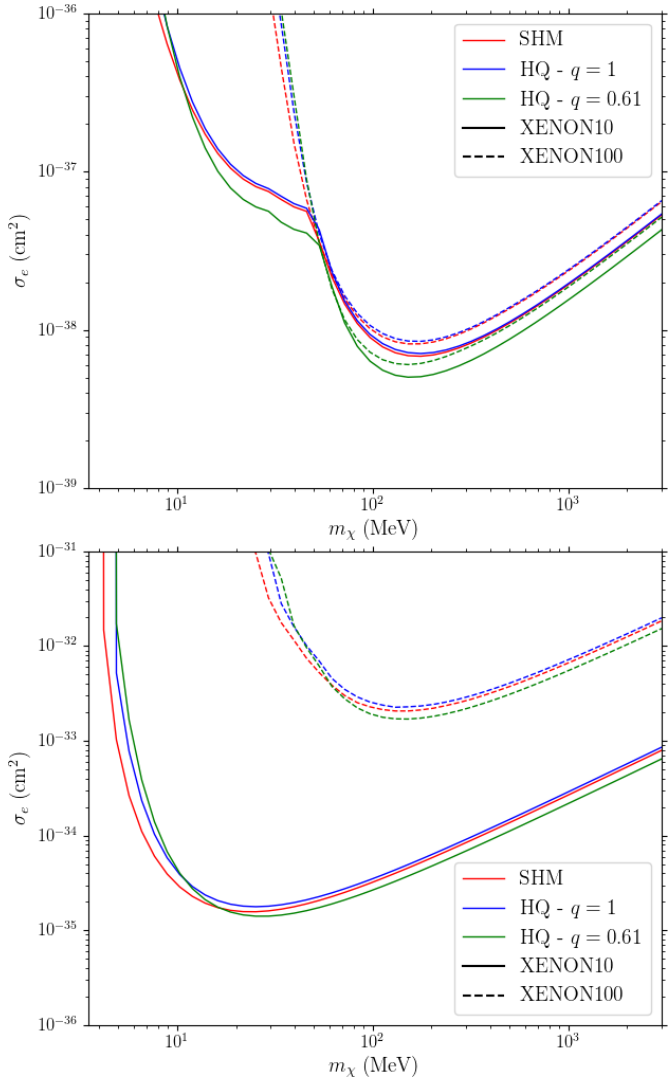

Figure 4.6: 90% exclusion limits on the scattering cross section $\bar{\sigma}_e$ vs m_χ, for the case of $F_{DM} = 1$ (top panel) and $F_{DM} = (\alpha m_e)^2/q^2$ (bottom panel). The red curve assumes the SHM for the PSDF, while the green curve is the result of using the PSDF from HQ inversion of our MW mass model. We have taken data from XENON10 (solid curves) and XENON100 (dashed curves).

the red curve for the SHM limits, while there is a noticeable split of the green curve ($q = 0.61$) relative to both blue and red curves: this hierarchy can be easily explained by referring to Table 4.5, where the three models are assigned with different local DM density values. The ρ_{DM} for the SHM and $q = 1$ cases differ by 10.75%, whereas the ρ_{DM} for $q = 0.61$ deviates by as much as 28%.

From (4.59) we note that the DM masses in the range

$$m_\chi \gtrsim (8\,\mathrm{MeV}) \left(\frac{\Delta E}{25\,\mathrm{eV}}\right) \left(\frac{750\,\mathrm{km/s}}{v_{max}}\right)^2 \tag{4.72}$$

can be probed, and thus we should see the impact of the maximum speed in the detector frame on the exclusion limits by looking at how much the low mass tail wiggles around. From Table

(4.5), we see that, although the SHM and $q = 1$ agree on the local escape velocity at per mille levels, the Earth velocity prescriptions are quite different, and thus their maximum DM speeds differ by tens of km/s: the SHM case is expected to be less sensitive than the $q = 1$ case in the low mass regime. However, the local DM density for SHM is slightly larger than the value from $q = 1$, which introduces a compensating effect on the sensitivity of SHM to low mass DM. On the other hand, if we compare the two axisymmetric models, we expect that the $q = 0.61$ case, which gives a lower maximum DM speed, will be less sensitive to low mass DM than the $q = 1$ case: however, the larger estimate from $q = 0.61$ for the local DM density compensates for this loss of sensitivity by predicting a slightly larger recoil rate than $q = 1$. These arguments reflect what are shown in the low mass regions of both exclusion limits in Fig. (4.6).

4.9 Inelastic DM-electron scattering

An interesting possibility that can be explored is the case of initial and final DM states with a mass splitting, *i.e.* $\chi_1 + e^-(nl) \to \chi_2 + e^-(k'l)$. The mass splitting δ between these DM states is defined as

$$\delta \equiv m_{\chi_2} - m_{\chi_1}. \tag{4.73}$$

Following [297], the case $\delta > 0$ (< 0) will be referred to as "inleastic" ("exothermic") DM. In either scenario, only the kinematics changes; the energy conservation relation is simply given by

$$\Delta E_{nl} = \vec{q} \cdot \vec{v} - \frac{\vec{q}^2}{2m_\chi} - \delta. \tag{4.74}$$

For the case of exothermic DM, the mere presence of a DM mass splitting allows energy to be deposited into the bound electron even for very small momentum transfers; this implies that the recoil spectrum is enhanced relative to the elastic case, and one expects to obtain tighter bounds on $\bar{\sigma}_e$. On the other hand, the opposite result is expected for the inelastic case: for fixed DM velocity, a larger momentum transfer is required to impart the same energy on an electron compared to the elastic case. Less phase space is accessible for the DM, which reduces the recoil spectrum, thereby leading to looser bounds on $\bar{\sigma}_e$. In Fig. 4.7, we precisely see the impact of the change in kinematics brought about by inelastic/exothermic DM; note here that the minimum value of v_{min} now becomes

$$v_{min*} = \begin{cases} \sqrt{\frac{2(\Delta E + \delta)}{m_\chi}}, & \Delta E > -\delta \\ \\ 0, & \Delta E \leq -\delta \end{cases} . \tag{4.75}$$

In turn, we recompute the exclusion limits on σ_e, but now accommodating nonzero δ. In Fig. (4.8), we present the exclusion limits on σ_e vs δ, for representative values of the DM mass. We have chosen them to be $m_\chi = 12.5\,\text{MeV},\ 40\,\text{MeV}$, and $300\,\text{MeV}$: these values correspond, respectively, to light, intermediate, and heavy DM masses. In the top panel, we show the limits using both XENON10 and XENON100 data, assuming only the SHM. On the other hand, the bottom panel shows the exclusion limits, using only XENON100 data, that one obtains from both SHM and axisymmetric modelling. Clearly, in both panels, we see the expected trend of weaker bounds for $\delta > 0$ and stronger bounds for $\delta < 0$.

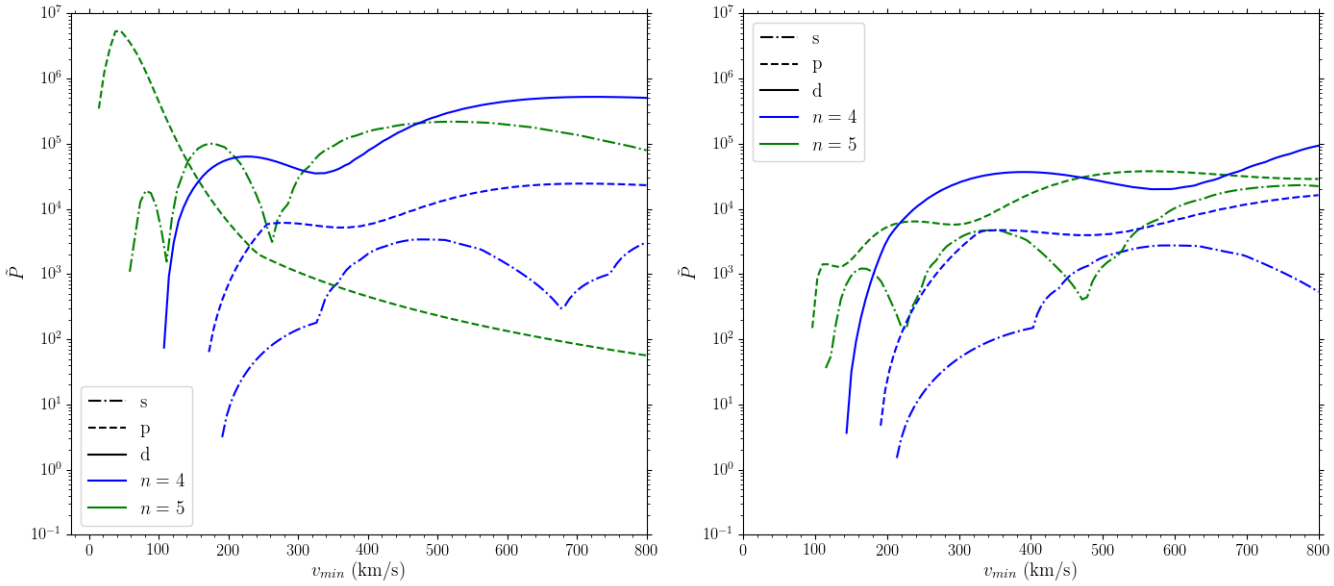

Figure 4.7: Same as in Fig. 4.5, but for $\delta = -25\,\text{eV}$ (left panel) and $\delta = 25\,\text{eV}$ (right panel). In both panels we have taken $m_\chi = 1\,\text{GeV}$.

4.10 Migdal effect

We also consider the possibility of producing an ionization signal outside the context of direct DM-electron scattering, through the so-called Migdal effect. Initially this effect was considered in the case of nuclear decay. As the nucleus decays, it picks up a velocity relative to the surrounding electron cloud; the electrons need time to catch up with the recoil nucleus, which may cause the atom to get ionized with a nonzero probability [298]. Meanwhile, Ibe et. al. discussed the detectability of light GeV DM via the Migdal effect, where the ionization signal is produced when the electrons lag behind the nucleus when a DM scatters from the nuclear target [299]. In order for this to occur, the interaction must happen fast enough. From this condition, one can obtain a criterion for the mass of the mediator m_A. The interaction time is $\sim m_A^{-1}$, while the light crossing time across the electron cloud is $r_a \sim (\alpha m_e)^{-1} \sim \text{keV}^{-1}$, where r_a is the Bohr radius; hence $m_A \gg \text{keV}$.

In the usual DM-electron scattering case, the momentum transfer is received entirely by the electron. For the Migdal case, the nuclear target of mass m_T receives a momentum transfer $\vec{q}$, such that the velocity of the electrons in the frame of the nucleus is $\vec{q}/m_T$; then the momentum transfer to the electron is just $\vec{q}(m_e/m_T)$. The computation of the ionization form factors for the Migdal effect is straightforward, and it simply entails a replacement of the momentum transfer $q \to q(m_e/m_T)$ in the atomic form factor $f^{(\text{ion})}$ for the DM-electron case [300], *i.e.*

$$f^{(\text{Migdal})}_{nl\to k'}(k', q) = f^{(\text{ion})}_{nl\to k'}(k', q(m_e/m_T)), \tag{4.76}$$

and the computation of the recoil spectrum for Migdal scattering proceeds as in (4.15) with the form factor replaced by $f^{(\text{Migdal})}$. In [270] they tabulated the atomic form factors for xenon only in the range $-1 \leq \ln\left(\frac{q}{\alpha m_e}\right) \leq 4$, *i.e* between 1.37-203.6 keV. The Migdal form factor, on the other hand, requires us to evaluate $f^{(\text{ion})}$ at a momentum q rescaled by $m_e/m_T \sim \mathcal{O}\,(10^{-5})$, and

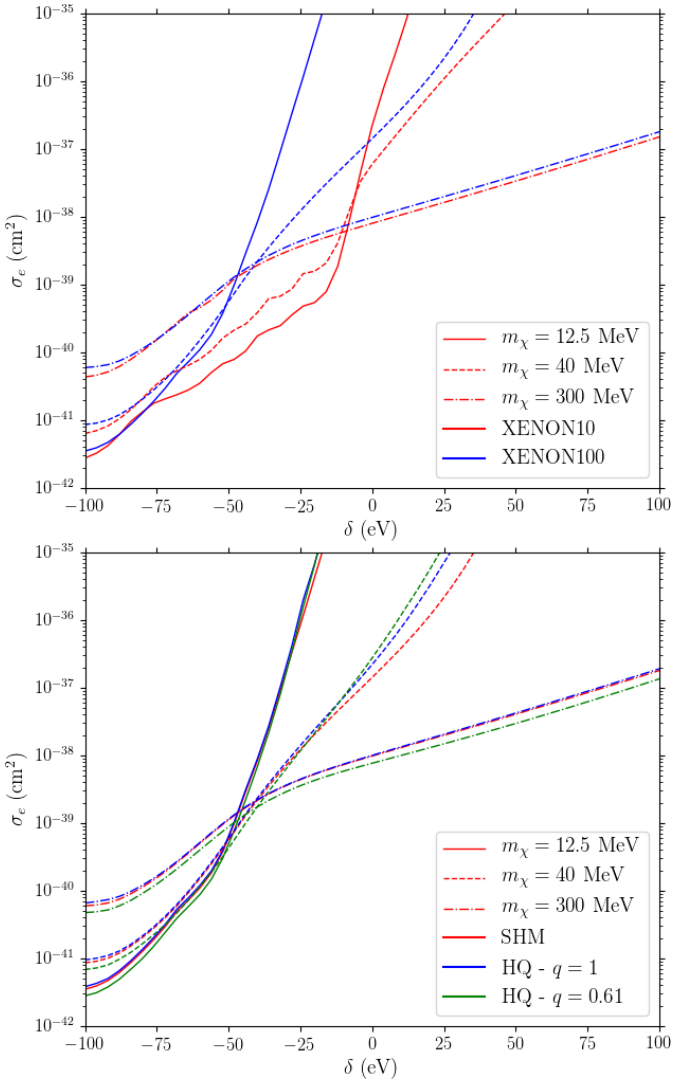

Figure 4.8: Exclusion limits on σ vs the mass splitting δ, for representative values of the DM mass. In the top panel, the SHM is assumed, while, in the bottom panel, we only consider XENON100 data.

we might need form factors outside the range of q where it is tabulated. To extrapolate the form factor for low q, we adopted the so-called dipole approximation as in [300], where the form factor is approximated as a power law. One can justify the use of the dipole approximation by considering the matrix element $\langle\psi_f|e^{i\vec{q}_e\cdot\vec{x}}|\psi_i\rangle$ for Migdal scattering. Taking $q \sim 10^{-3} m_\chi (v/10^{-3})$ and $|\vec{x}| \sim (\alpha m_e)^{-1}$, we have

$$\vec{q}_e \cdot \vec{x} = \frac{m_e}{m_T}\vec{q}\cdot\vec{x} \sim \left(\frac{m_\chi}{200\,\mathrm{GeV}}\right)\left(\frac{100\,\mathrm{GeV}}{m_T}\right), \tag{4.77}$$

so that in the sub-GeV range we are probing, $\vec{q}_e \cdot \vec{x} \ll 1$; of course, this approximation breaks down for larger momentum transfers q.

We show the plot of $\tilde{P}$ in Fig. (4.10), the nonastrophysics part of the integrand needed to compute the recoil spectrum, as a function of v_{min}, comparing the Migdal effect with the

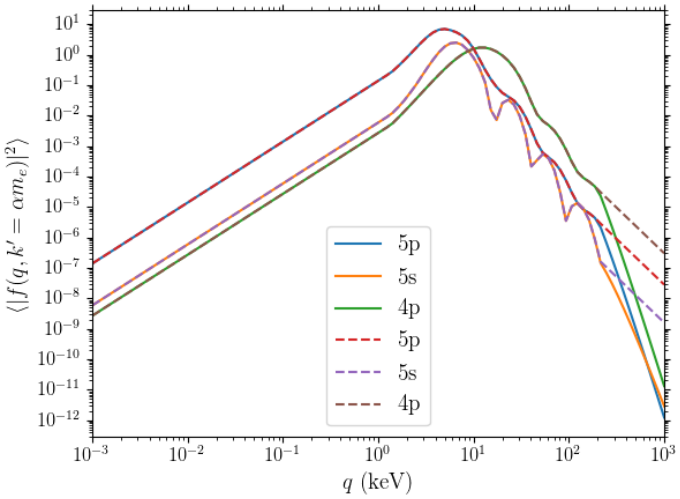

Figure 4.9: Plot of the atomic form factors of xenon, $f^{(\text{ion})}_{nl\to k'}$, for the $4p$, $5s$, and $5p$ orbitals, taken as a function of momentum transfer q. Here the outgoing momentum of the electron is $k' = \alpha m_e$, and the form factors in the range $-1 \leq \ln\left(\frac{q}{\alpha m_e}\right) \leq 4$ is taken from [270]. Outside that range, we assumed power law scaling for low and high q for the dashed line, while, for the solid line, we considered the form factor at low and high q assuming an outgoing plane wave.

benchmark case of pure DM-electron scattering. The thick lines correspond to the pure DM-electron scattering case, while the thin lines refer to the case of Migdal scattering. We can see that $\tilde{P}$ from Migdal scattering becomes dominant than the prediction from DM-electron scattering for a DM mass of 1 GeV, which lies in the high mass tail that DM-electron scattering can probe. In Fig. (4.11), we then overlay the exclusion limits in the m_χ-σ_e plane for the Migdal case, alongside the limits from pure DM-electron scattering. Here we are assuming contact interactions just as reference. As one can see from the exclusion limits, Migdal effect is sensitive to heavy DM within the sub-GeV range. In some sense, one can think of Migdal scattering as an intermediate regime between DM-electron scattering and DM-nucleus scattering.

4.11 Annual modulation

Going back to the case of pure DM-electron scattering, we finally discuss the effects of axisymmetric modelling on annual modulation. As we have mentioned in Sec. (4.6), the Earth's velocity is time dependent since it revolves around the Sun; the VDF becomes time dependent, which makes the rate spectrum vary with time as well. Its effect on the mean inverse velocity can be seen in Fig. (4.12) where we plot $\langle 1/v \rangle$ as a function of v_{min} for different times of the year. The blue curve corresponds to the time at which the Earth's velocity is at its peak; for larger values of the Earth's speed v_E, $\langle 1/v \rangle$ gets flattened to lower values at lower v_{min} since the mean inverse velocity goes like $1/v_E$ for low v_{min}. Following (4.53), the curve corresponding to the largest v_E has the largest cutoff in v_{min}, and this is what we also see in Fig. (4.12). In performing

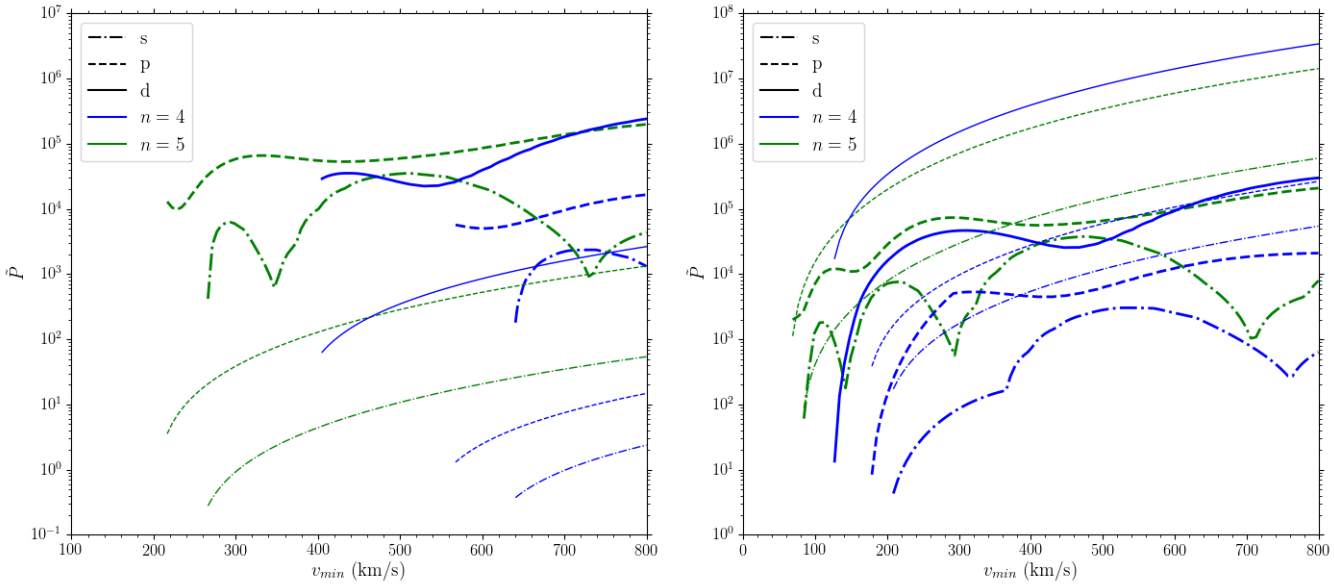

Figure 4.10: Same as in Fig. (4.5) but with the thick lines corresponding to the case of elastic DM-electron scattering, while the thin lines correspond to the prediction from the Migdal effect. The left panel corresponds to a DM mass of 100 MeV, while the right panel corresponds to 1 GeV.

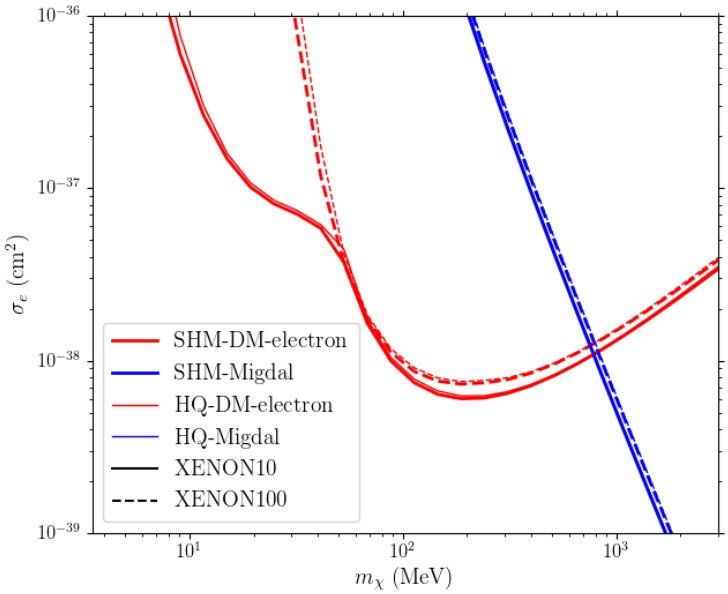

Figure 4.11: Exclusion limits as in Fig. (4.6), but with the Migdal effect incorporated in the computation of the recoil spectrum (blue curves).

the analysis for annual modulation, it is convenient to separate the year into time bin, where each bin corresponds to a monthly interval, and then obtain the time-averaged rate spectrum in each time bin. At first glance, computing the time average appears to be straightforward:

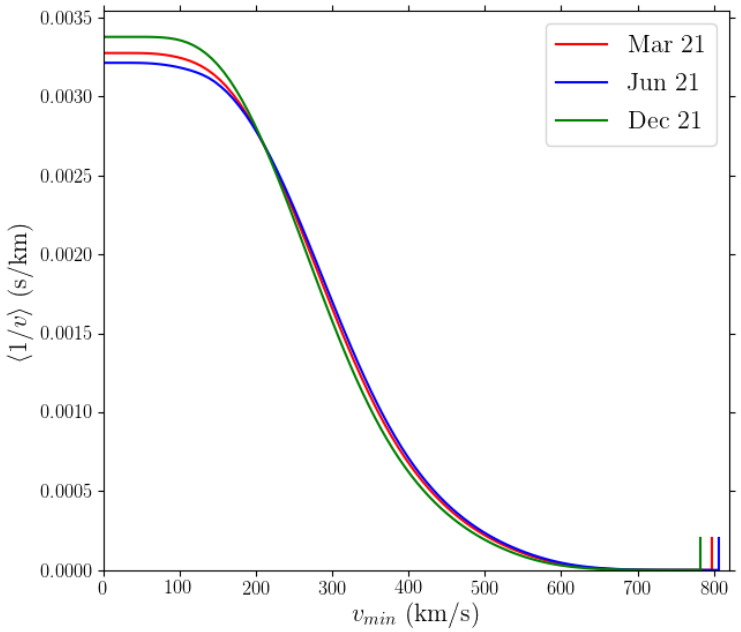

Figure 4.12: Plot of the mean inverse velocity as a function of v_{min} for different times of the year.

one would just replace v_E with $v_E(t)$ in the mean inverse velocity, compute the recoil spectrum, and then compute the time integral. However, in numerically computing the recoil spectrum, we are building tables of the mean inverse velocity as a function of v_{min}, with v_E fixed. From a practical standpoint, what can be done is to build the velocity tables, with values of the mean inverse velocity computed for each node of the time bins, *i.e.* compute the mean inverse velocity for month 1, 2, 3,..., 12. The time average for each bin is computed by taking the simple average of the rates at the nodes that determine that particular bin.

In the top left panel of Fig. (4.13) we then show the spectrum dN/dn_e, the number of events per electron yield n_e for the Nov-Dec bin, for different DM masses and for the case of SHM and HQ. Since the electron yield is correlated with the recoil energy, it is more difficult for low mass DM to produce a higher electron yield. Meanwhile, in order to quantify the effects of annual modulation, we define the modulation fraction f_{mod}, first introduced in [301], as

$$f_{mod} \equiv \frac{(dN/dn_e)_{\max} - (dN/dn_e)_{\min}}{2\mu}, \tag{4.78}$$

where μ is the mean signal across the time bins. Taking f_{mod} as a function of n_e, we see that lighter DM masses tend to be more sensitive to annual modulation, as shown by the three representative DM masses in the electron yield spectrum in the top right panel of Fig. (4.13). Meanwhile, taking f_{mod} as a function of DM mass for fixed $n_e = 1$ and $n_e = 5$, we see the same trend: f_{mod} goes up as we go to lower DM masses. The issue with the modulation fraction overshooting over unity is simply an artifact of having zero average event spectrum in all other time bins except for one time bin. Finally, in Fig. (4.14) we plot the 5-sigma discovery reach

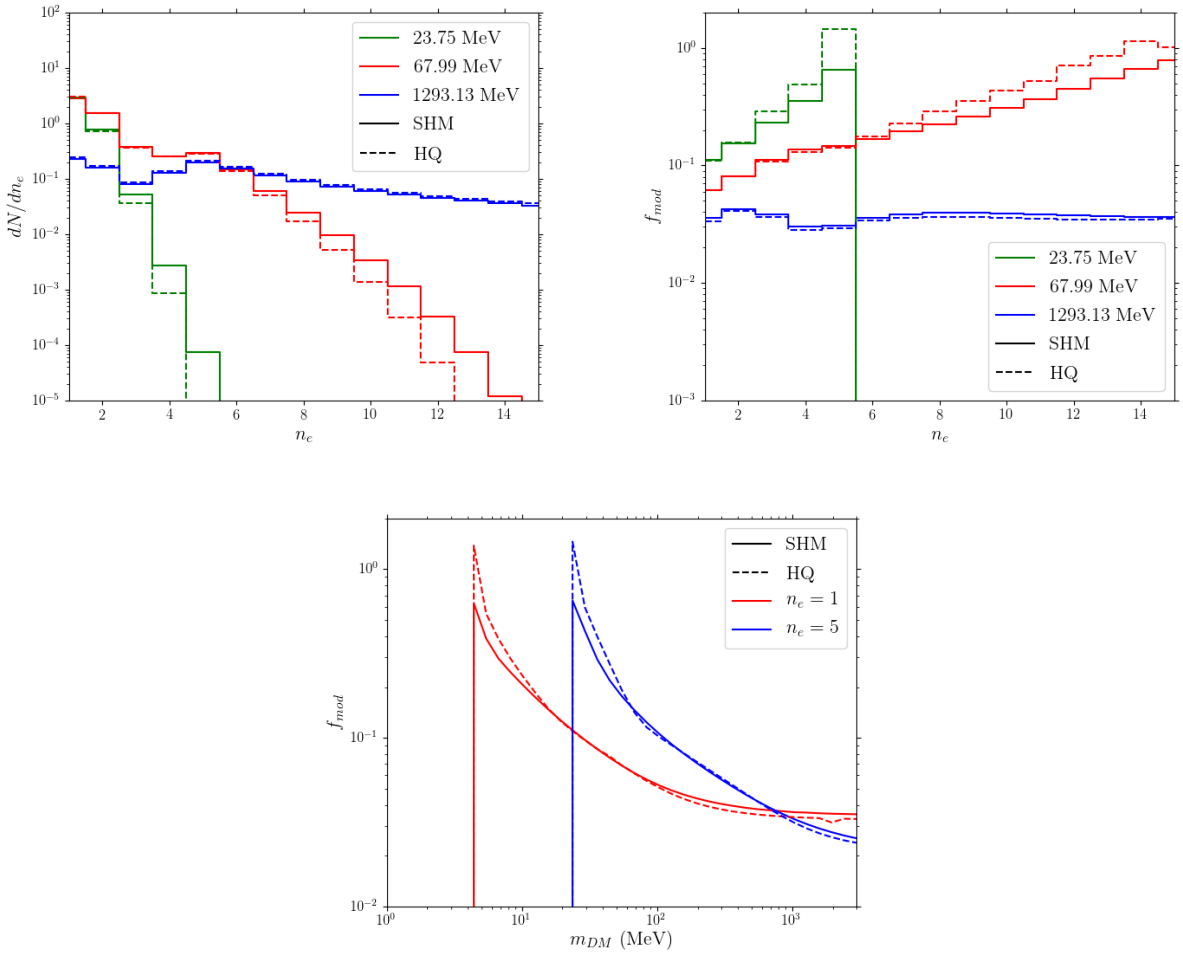

Figure 4.13: (Top left panel) Plot of the event spectrum per electron yield for different DM masses, as a function of electron yield n_e, for low (green), intermediate (red), and heavy (blue) DM masses for the Nov-Dec bin. The solid line assumes the SHM, while the dashed line assumes the axisymmetric halo model. Plot of the modulation fraction f_{mod} as a function of electron yield (top right panel), and as a function of DM mass (bottom panel); see text for the discussion.

for annual modulation for a detector with 1 kg-year exposure with zero background, and for $n_e = 1$ and $n_e = 5$. Following [301], this is obtained by choosing the cross section such that $f_{mod}S/\sqrt{S+B} = 5$ and setting $B = 0$: here S is the total signal rate. As in the usual exclusion limits where annual modulation is not taken into account, the limits are sensitive to the choice of the halo model at low DM masses.

4.12 Summary and conclusions

The proper accounting of astrophysical uncertainties, in the local DM density and the halo velocity distribution, is crucial in interpreting results from direct detection. In reporting DM

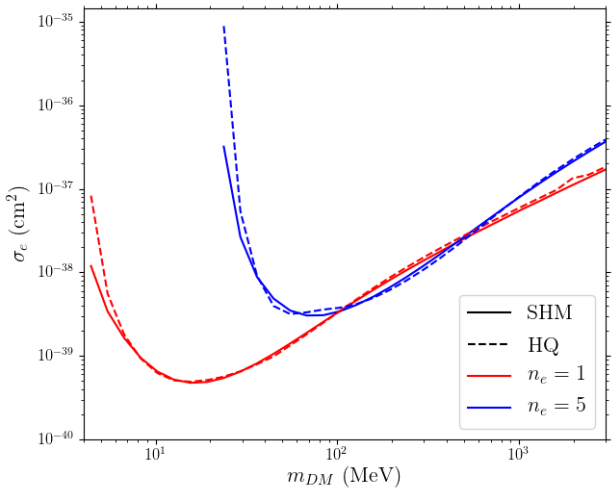

Figure 4.14: Plot of the 5-σ discovery reach in the m_χ-σ_e plane, for electron yields $n_e = 1$ and $n_e = 5$.

direct detection exclusion limits, the SHM is an ansatz often used to describe the VDF; this halo model stems from the assumption of a spherical, isothermal DM halo, which leads to an isotropic velocity distribution. On the other hand, the presence of flattened structures in the Galaxy, such as the disk and bulge, indicates that the VDF may deviate from the SHM. Motivated by the shortcommings of the SHM, we considered axisymmetric halo modelling, where the VDF is obtained by carrying out the Hunter-Qian inversion scheme, given a set of mass models for the Galactic mass components, namely the halo, disk, and bulge. The potentials/mass densities describing these components have been taken such that they reflect the measurements on the kinematics of visible tracers in our Galaxy. Particularly, we have chosen the mass model such that we, at least, reproduce the measured circular velocity at the Solar location. This method of obtaining the VDF has the virtue of being self-consistent. We have applied this axisymmetric halo modelling in the study of DM scattering processes namely: pure DM-electron scattering, inelastic DM-electron scattering, and the Migdal effect, which can induce ionization signals in xenon detectors. The interest in ionization processes is prompted by the reported signal excess in XENON1T at low energy recoils, as well as the prospects of probing the MeV to sub-GeV mass range for DM, given that we are increasingly getting tighter constraints on DM in the GeV-TeV range that is usually probed by DM-nucleus interactions.

The relevant astrophysical quantity that enters in the computation of the predicted recoil spectrum is the mean inverse velocity. From the kinematics of ionization processes, the mean inverse velocity is dependent on v_{min}, the minimum speed required to deposit energy ΔE into the atom and transfer momentum q. Since the choice of the halo model directly influences the mean inverse velocity, we first compared the predictions of the SHM and axisymmetric halo modelling to the mean inverse velocity. Depending on the axisymmetric mass model, the mean inverse velocity deviates from the SHM prediction to within 25% for v_{min} around 500 km/s in the frame of the target, while the cutoff in v_{min} is determined by the local value of the potential. We have seen that the spherical halo reaches a higher cutoff than the SHM and oblate halo.

We have obtained exclusion limits on the DM-electron scattering cross section at some fixed energy scale as a function of the DM mass, using XENON10 and XENON100 as benchmarks for noble gas detectors that seek DM through ionization signals, and also assuming that the elementary DM-electron interaction can either be contact or long-range. We compared the resulting exclusion limits that we have obtained from using three different halo models: (i) the SHM, (ii) axisymmetric modelling with a spherical halo, and (iii) axisymmetric modelling with an oblate halo. In the case of pure DM-electron scattering processes, and focusing on the XENON100 detector and on the case of contact interactions, the resulting exclusion limits marginally deviate from the prediction coming from the SHM in the range $\sim$50 GeV and above. This results from the fact that we are actually integrating over the mean inverse velocity: for the prediction of axisymmetric modelling on the mean inverse velocity, there are intervals in v_{min} where it is above and below the SHM prediction, which could produce a cancellation effect in the total ionization rate upon integration. On the other hand, the reach in DM masses in the low mass region depends on the square of the inverse velocity cutoff, and this velocity cutoff is dependent on the choice of the halo model. While this implies that the resulting exclusion curves at low DM masses is sensitive to the choice of the halo model, the prediction for the local DM density of the different halo models can also affect the discriminating power of the exclusion curves, at low DM masses, on the halo model. For instance, a spherical halo predicts a higher maximum v_{min} ($\sim$ 1.3%) than what one would obtain from the usual choices for the escape speed and the Earth velocity in the SHM, which makes the spherical halo more sensitive to lower DM masses by compared to the SHM. However, a spherical halo predicts a lower local DM density compared to the SHM benchmark by 10.75%; the overall effect is that the case of a spherical halo is less constraining on the DM-electron cross section at $\sim$ 40 MeV.

We have explored other processes that can give rise to ionization signals, such as inelastic DM-electron scattering and the Migdal effect. For the case of inelastic scattering, the exclusion limits on the DM-electron cross section is highly sensitive on the mass splitting δ, of the initial and final DM states: for the exothermic case $\delta < 0$, the cross section is more constrained than in the endothermic case $\delta > 0$. By looking at reference DM masses, we still find marginal deviations between exclusion curves coming from the SHM and axisymmetric halo modelling, except in the intermediate mass range around $\sim$ 40 MeV and $\delta \gtrsim 10$ eV. On the other hand, the Migdal effect, which involves the production of an ionization signal due to DM-nucleus scattering, being more sensitive than pure DM-electron scattering above $\sim$ 700 MeV, is marginally sensitive to the choice of the halo model. Finally, we have looked into annual modulation, and assessed the impact of axisymmetric modelling on the time variation of the ionization signal for the case of pure DM-electron scattering. As in the exclusion limits where annual modulation is not included, the limit curves in the DM mass-cross section plane can discriminate between halo models at low masses.

A natural extension to this work is to account for halo rotation in calculating the PSDF; since at present this cannot be inferred directly from astrophysical observations, an ansatz for halo rotation can be obtained from, *e.g.* N-body simulations that track the evolution history of a Milky Way-like galaxy. Another possibility would be to incorporate the effects of substructure in the PSDF, in which the properties of such unrelaxed systems in the Galaxy can be studied in greater detail from high-quality astrometric data coming from Gaia.

Chapter 5

Conclusions

The existence of DM has been firmly established from the concurrence of completely independent observations, which span a wide range of distance and time scales. Despite all of the compelling results that strengthen the case for DM, its nature is still uncertain. Uncovering the identity of DM is still the subject of active research, from both theoretical and experimental fronts. In this thesis, we have featured research projects that demonstrate a common theme of understanding the nature of DM in the Universe and testing the particle DM paradigm, through the use of a wide variety of analysis tools and theoretical approaches.

Generally, we have to commit to a DM framework in order to extract definite predictions that can be compared with known and measured observables, but at the same time requiring some level of minimality in order to cover a class of specific models. In Chapter 2, we studied a particular realization of a multicomponent dark sector, that is initially motivated by the formulation of a dynamical solution to the flavor puzzle. From the point of view of explaning the cosmic origin of DM, we have pointed out that it is natural to consider multiple stable components to account for the Universe's energy budget for nonbaryonic matter. Whereas the subdominant baryonic component is described by the SM, which has an intricate gauge and flavor structure, it is simply natural to consider the scenario in which the dominant nonbaryonic component is described by a framework that is as complex, or even more elaborate, than the SM. This model of the dark sector contains stable dark fermions that are charged under an unbroken dark U(1) gauge interaction, that is mediated by a massless dark photon mediator. The dark photon in this setup has no kinetic mixing with the ordinary photon, and thus the dark fermions do not acquire millicharges. The stability of the dark fermions is ensured by the conservation of the dark U(1) charge. In addition, the presence of scalar messengers open up a portal interaction between dark fermions and SM fermions. The template for such portal interactions is a Yukawa-like interaction, and the form of the interactions allows the classification of the dark fermions and scalar messengers, according to the flavor and chirality of the SM fermion they couple with. A particular realization of this setup can then be specified by providing: (i) the portal and gauge couplings, which we take to be universal for all dark fermions, and (ii) the mass spectrum of the species living in the dark sector. From complementary constraints on this model coming from other probes such as collider physics, stellar cooling, precision physics, and halo structure, we have a reference framework for the mass hierarchy of particles in the dark sector. Specifically, we demand that: the heaviest species in the model are the scalar messengers sitting at $\sim 10\,\text{TeV}$; the lepton-like dark fermion, the dominant DM component, must be at the TeV scale; and the

quark-like dark fermions must live around the GeV scale.

The primary goal of this project is to complete the "viability tests" for DM on this framework, by obtaining the plausible regions in the parameter space of the theory that are consistent with measured values of the cosmological observables, namely the observed matter relic density and the Planck limit on the extra radiation components in the Universe. Determining the viable parameter region requires us to write down a set of coupled Boltzmann equations for this setup. However, we have emphasized one peculiar feature of this scenario, which gives rise to rich and interesting dynamics for such a minimal setup: the presence of distinct thermal baths, namely the visible sector and dark sector reservoirs. In principle, there is no reason to believe that the visible and dark sector plasmas have the same temperatures, and a temperature mismatch at the CMB epoch is actually favored by the Planck constraints on the amount of extra radiation component in the Universe. Then, one must keep track not only the number densities of the stable species, but also the temperatures of the two sectors.

The relic densities of the stable species are determined by annihilation processes to dark photons and SM fermions, and their production mainly proceeds through thermal frezze-out. However, we have found that, if the portal coupling is small, such that the production is FIMP-like, chemical decoupling occurs mainly with the dark photon bath; for large portal couplings close to the perturbative limit, the dominant lepton-like dark fermion chemically decouples from the SM heat bath, as in the case of thermal WIMPs. Meanwhile, we highlight the result that the bounds on N_{eff}, *i.e.* the effective number of relativistic degrees of freedom at the CMB epoch, imposes lower limits on the masses of the lighter dark quarks, in the case of a single family of dark quarks. On the other hand, increasing the mass of the light dark quarks changes the dominant annihilation channel from final state dark photons to final state SM fermions, which have different mass scalings for the annihilation cross section (m^{-2} and m^2/m_ϕ^4, respectively, where m is the mass of the stable species while m_ϕ is the mass of the scalar mediator). Imposing that dark quarks still have subdominant relic densities with respect to the dark fermion, this implies upper limits on the dark quark mass. Hence, we have quoted a window of allowed dark quark masses.

Finally, we looked at direct detection constraints on our framework, noting that the main driver for direct detection are processes involving the exchange of massless mediators between DM (in this case, the dominant, heavy dark lepton) and nuclei, namely the SM photon and the dark photon. Since dark leptons/nuclei do not directly couple with the SM/dark photon, such scattering processes occur, to leading order, at 1-loop level. From an EFT perspective, these are described by dimension 5 dipole and dimension 6 charge radius operators. We note that while the SM and dark photons give rise to long range interactions, the recoil spectra for these cases are qualitatively different. In the SM photon-mediated case, we are mainly sensitive to the vector current of the quarks in the nucleus, giving rise to coherent, long-range interactions; on the other hand, the dark-photon mediated case is sensitive to the spin of the SM quarks, hence giving rise to incoherent DM-nucleon interactions that can be subdominant with respect to contact charge radius interactions that are coherent. We have found that the constraints on the Wilson coefficients for the dipole and charge radius operators, coming from null results in XENON1T and future projections from DARWIN, lead to limits that are competitive with respect to complementary limits from stellar cooling and precision physics of the lepton magnetic dipole moment.

In Chapter 3, still in line with the study of minimal frameworks to address the DM problem, we considered a new physics model which addresses the recently reported muon $g-2$ anomaly. This minimal setup involves: a bino-like Majorana fermion; scalar partners, which are sleptons in the MSSM, of the left handed muon SU(2) doublet and the right handed muon; and mixing between the scalar species. Meanwhile, the bino and the sleptons interact with the muon via gaugino-like interactions, where the couplings can be taken to be the one from the MSSM: such interactions give rise to new physics contributions to the muon $g-2$ at loop level. A specific realization of this setup is achieved by providing: (i) the mass of the bino M_B, (ii) the masses of the physical slepton states m_1 and m_2, and (iii) the mixing angle θ. In addition, we consider the case of a lone Higgs doublet, in contrast with the MSSM, but still including D-terms in the potential. Then, in order to ameliorate the tension in the $g-2$ anomaly, we have demonstrated that the typical mixing angles are those that are slightly below zero, corresponding to the left handed branch, or slightly above $-\pi/2$, *i.e.* the right handed branch. Meanwhile, taking the bino as the DM, its stability is guaranteed by a $\mathbb{Z}_2$ symmetry analogous to R-parity in the MSSM, and we require that the bino is the lightest species among the non-SM particles in the minimal framework. In order to reproduce the observed relic density of DM, we noted that the pair annihilation cross section of the bino to muons leads to overproduction of DM, if we also require to satisfy $g-2$. Instead, we found that coannihilations involving the sleptons would instead lead to an effective cross section at the picobarn level, that is sufficient to produce the right amount of DM. In achieving the desired DM relic density while simultaneously saturating the required contribution to address the $g-2$ anomaly, we land on two qualitatively different coannihilation scenarios from the left handed and right handed branches. In the left handed branch, the bino and the lighter smuon are both nearly degenerate with the sneutrino, while, in the right handed branch, the sneutrino instead resides at a higher scale, being nearly degenerate with the heavier smuon. We have also looked into the direct detection limits for the bino; we have shown that in the relevant parameter space for saturating $g-2$ and the relic density, the dominant scattering process is photon exchange between the bino and nucleons through the bino anapole moment. Note that the Majorana nature of the bino forbids the presence of a dipole moment; this is in contrast with the case in the dark U(1) sector model we have studied, where the dark fermions are charged, Dirac fermions, and thus dipole moments can be present. We have shown that future detectors such as DARWIN can be sensitive to the bino masses at the same level as the ones required for both $g-2$ and the relic density. Finally, we have investigated the theoretical constraints on this minimal model from the point of view of perturbative unitarity and absolute vacuum stability; we have shown that perturbative unitarity is less constraining on the model parameter space than vacuum stability.

In Chapters 2 and 3 where we considered models for particle DM, we have looked into the limits imposed by current and future direct detection experiments. We have pointed out that one should keep in mind the various astrophysical uncertainties, particularly in the local DM density and DM velocity distribution, when interpreting limits from direct detection. Typically, the SHM is the benchmark halo model used in the literature to describe the velocity distribution of DM in the Galactic halo. The SHM requires two inputs, namely the local circular velocity and the local escape velocity. While the SHM has served us well in enabling us to compute recoil spectra in direct detection experiments and to report exclusion limits, the halo in the SHM is assumed to be spherical and isothermal, implying an isotropic velocity distribution. On

the other hand, the presence of disk and bulge stellar components has motivated us in Chapter 4 to advocate instead for axisymmetric phase space distributions (PSDF), from which one can obtain the velocity distribution functions (VDF) required in direct detection analyses. Apart from the fact that an axisymmetric PSDF reflects the observed distributions of tracers in the Galaxy, the procedure in which this PSDF is obtained comes from the Hunter-Qian inversion scheme. This inversion scheme, reminiscent of Eddington inversion for spherically symmetric configurations, requires the potentials and density profiles of the Galactic mass components as input: this clearly shows the self-consistency of this approach. In turn, the total potential must be normalized with respect to the locally measured circular velocity.

Prompted by the observed excess recoil events in XENON1T, attributed to electronic recoils, and the general interest for probing DM candidates in the MeV and sub-GeV mass scales, we mainly considered the impact of axisymmetric halo modelling on the predicted recoil spectra and on the exclusion limits, assuming that direct detection signals are driven by DM-electron interactions. The crucial quantities that enter in these analyses are the velocity moments, and we focused mainly on the mean inverse velocity, which is relevant for velocity-independent interactions. The mean inverse velocity is a quantity that depends on v_{min} — the minimum velocity required to deposit energy ΔE on an electron, and momentum transfer q. Here we have compared the predictions for the mean inverse velocity from our reference axisymmetric models, with the mean inverse velocity from the SHM, and looked at how they affect the exclusion limits. We have found marginal deviations in the exclusion limits when we compared the results of using our reference axisymmetric models with the SHM, and argued that this is a consequence of integrating over the entire range of v_{min}. On the other hand, the reference axisymmetric models predict slightly different escape velocities than the one used in the SHM. This tells us that probing the behavior of the mean inverse velocity at the high velocity tail allows us to discriminate between halo models. Alternatively, being sensitive to variations of the VDF in the high velocity tail means that the exclusion limits wiggle around low DM masses for different choices of the halo model. Apart from DM-electron interactions, we have also studied the impact of halo modelling in the cases of inelastic DM-electron scattering, Migdal scattering, and in probing annual modulation in the context of DM-electron scattering. In such contexts, choosing different halo models has the effect of shifting the minimum mass that can be probed in direct detection experiments, as in the DM-electron scattering case with no annual modulation.

Appendix A

Multicomponent dark sector

A.1 Matrix elements and Sommerfeld enhancement

In writing the collision term in the right-hand side of the Boltzmann equations in section 2.3, we need the amplitude squared of the relevant annihilation and elastic scattering amplitudes. Regarding the annihilation processes, the dark fermions can annihilate to dark photons or SM fermions (see Fig. 2.1). The squared amplitudes in case of χ (the expressions for Q are specular) are given by

$$
\begin{aligned}
|\mathcal{M}|^2_{\chi\bar{\chi}\to 2\gamma_D} &= 32\pi^2\alpha_D^2 Q_\chi^4 \left[\frac{tu - m_\chi^2(3t+u) - m_\chi^4}{(t-m_\chi^2)^2} - \frac{2m_\chi^2(s-4m_\chi^2)}{(t-m_\chi^2)(u-m_\chi^2)} + \frac{tu - m_\chi^2(3u+t) - m_\chi^4}{(u-m_\chi^2)^2}\right], \\
|\mathcal{M}|^2_{\chi\bar{\chi}\to l\bar{l}} &= 4\pi^2\Big[\left(\alpha_L^2+\alpha_R^2\right)(m_\chi^2+m_l^2-t)^2 + 8\alpha_L\alpha_R m_\chi^2 m_l^2\Big]\left(\frac{1}{t-m_{\phi_+}^2}+\frac{1}{t-m_{\phi_-}^2}\right)^2, \\
|\mathcal{M}|^2_{\chi_R\bar{\chi}_R\to l_L\bar{l}_L} &= 16\pi^2\alpha_L^2\frac{(m_\chi^2+m_l^2-t)^2}{(t-m_\phi^2)^2},
\end{aligned}
\tag{A.1}
$$

where s, t and u are the standard Mandelstam variables. When computing the pair annihilation cross section of dark fermions we need to include the Sommerfeld enhancement induced by the long-range attractive force mediated by dark photons [302] (the importance of this non-perturbative effect in the context of dark matter annihilations was first pointed out by [303]); for such Coulomb term, the enhancement can be computed analytically and added as a multiplicative factor to the cross section σ_0 accounting for contact interactions

$$
\sigma = \sigma_0 S(v) \qquad with \qquad S(v) = \frac{\pi\,\alpha_D}{v}\frac{1}{1-e^{-\pi\alpha_D/v}}, \tag{A.2}
$$

where v is the velocity of each annihilating species in the center-of-mass frame. As for the elastic scattering processes, the dark fermions can either undergo Compton-like processes with

dark photons, or scatter on SM fermions (see Fig. 2.3). The squared amplitudes in case of χ are

$$
\begin{aligned}
|\mathcal{M}|^2_{\chi\gamma_D\to\chi\gamma_D} &= -32\pi^2\alpha_D^2 Q_\chi^4 \left[\frac{su-m_\chi^2(3s+u)-m_\chi^4}{(s-m_\chi^2)^2} - \frac{2m_\chi^2(t-4m_\chi^2)}{(s-m_\chi^2)(u-m_\chi^2)} + \frac{su-m_\chi^2(3u+s)-m_\chi^4}{(u-m_\chi^2)^2}\right], \\
|\mathcal{M}|^2_{\chi l\to\chi l} &= 4\pi^2\Big[\left(\alpha_L^2+\alpha_R^2\right)(m_\chi^2+m_l^2-u)^2 + 8\alpha_L\alpha_R m_\chi^2 m_l^2\Big]\left(\frac{1}{u-m_{\phi_+}^2}+\frac{1}{u-m_{\phi_-}^2}\right)^2, \\
|\mathcal{M}|^2_{\chi_R\bar{l}_L\to\chi_R\bar{l}_L} &= 16\pi^2\alpha_L^2\frac{(m_\chi^2+m_l^2-s)^2}{(s-m_\phi^2)^2}\,.
\end{aligned}
\tag{A.3}
$$

A.2 Computation of thermal averages

In the Boltzmann code developed in Section 2.3 there are several quantities involving thermal averages. Starting with pair annihilation cross sections, a method to efficiently compute $\langle\sigma v\rangle(T)$, as defined in Eq. (2.31), was detailed in [214]: Assuming equilibrium distribution functions with occupation numbers approximated by the exponential in (2.27), one can manipulate the numerator by performing a change of integration variables from the two momenta $\vec{p}_1$ and $\vec{p}_2$ to $E_+ \equiv E_1 + E_2$, $E_- \equiv E_1 - E_2$ and s, with the integral in the first two that can be performed analytically, giving

$$
\langle\sigma v\rangle(T) \simeq \frac{1}{8m^4T[K_2(m/T)]^2}\int_{4m^2}^\infty ds\ \sigma(s)\sqrt{s}\left(s-4m^2\right)K_1(\sqrt{s}/T)\,, \tag{A.4}
$$

where $K_1(z)$ and $K_2(z)$ are the modified Bessel functions of order 1 and 2, respectively. The same method can be applied to $\langle\sigma vE\rangle(T)$, see the definition in Eq. (2.42), obtaining

$$
\langle\sigma vE\rangle(T) \simeq \frac{1}{8m^4T[K_2(m/T)]^2}\int_{4m^2}^\infty ds\ \sigma(s)\ s\left(s-4m^2\right)K_2(\sqrt{s}/T)\,. \tag{A.5}
$$

Both these expressions are very convenient when coming to their numerical implementation: for any given particle physics model, one can first tabulate the cross sections σ as a function of s, and then link to such tabulations for a fast computation of thermal averages at any T in the temperature evolution equations.

On the other hand, an analogous shortcut cannot be implemented in thermal averages for momentum transfer rates. Referring generically to the scattering process $i + B \to i + B$, the thermally averaged momentum transfer rate $\langle\gamma_{iB}\rangle(T_i, T_B)$ is a function of the temperature of both the species i and bath particles B, see Eqs. (2.40) and (2.38), and such dependences cannot be simply factorised, making the implementation in the numerical Boltzmann code CPU-demanding. When investigating the kinetic decoupling of massive dark matter particles i from the heat bath, since this typically occurs in the regime at which the temperature T_i is small compared to the particle mass m_i, [217] and [304] noticed that the dependence on the particle momentum p_i in γ_{iB} can be approximately dropped, thereby allowing to replace $\langle\gamma_{iB}\rangle(T_i, T_B)$ with $\gamma_{iB}(E_i = m_i, T_B)$. When the scattering species is relativistic, this is not a fair estimate; on the other hand, we can still use it as a guideline for a better approximation: At $T_i \ll m_i$ the

occupation number in the integrand at the numerator of the l.h.s. of Eq. (2.40) is sharply peaked at the stationary point $E_i = m_i$ and $\gamma_{iB}(E_i, T_B)$ simply picks up the contribution coming from the stationary point. On the other hand, when $T_i \gtrsim m_i$, the occupation number has a relatively longer tail at higher energies. The pre-factor $(E_i^2 - m_i^2)^{3/2}$ in the integral cannot be neglected, and, to extract the peak contribution, one has to search for the stationary point of the function

$$F(E_i) = \frac{E_i}{T_i} - \frac{3}{2} \ln \left(E_i^2 - m_i^2 \right) , \tag{A.6}$$

which is now at

$$E_*(T_i) = \frac{3T_i}{2} + \sqrt{m_i^2 + \frac{9T_i^2}{4}}. \tag{A.7}$$

Note that going back to the limit $T_i \ll m_i$, one correctly retrieves $E_* = m_i + O(T_i)$. The agreement between $\langle\gamma\rangle(T_i, T_B)$ and $\gamma(E_i = E_*(T_i), T_B)$ is very good, as shown in a sample case in Fig. (A.1).

A.3 Loop calculations

We report here a few details regarding the computation of the γ and γ_D vertex functions represented by the loop diagrams in Fig. 2.8. For the γ_D vertex function, involving a SM quark q on the external legs and a quark-like dark fermion Q (with $U(1)_D$ charge Q_Q) and scalar messengers $S_\pm$ in the loop, we have

$$\begin{aligned} \bar{q}(k')\, i\Gamma^\mu_{\gamma_D} q(k) &= g_D Q_Q\, \bar{q}(k') \sum_{\lambda=\pm} \left[\left(\frac{g_L^2 + g_R^2}{2} \right) I^\mu_{a,\gamma_D} \left(m_Q, m_{S_\lambda}, k, q \right) \right. \\ &+ \left. (\lambda)\, g_L g_R m_Q I^\mu_{b,\gamma_D} \left(m_Q, m_{S_\lambda}, k, q \right) \right] q(k) \,, \end{aligned} \tag{A.8}$$

where q^μ is the momentum transfer. For the γ vertex function, with a lepton-like dark fermion χ on the external legs and the corresponding lepton (with $U(1)_{em}$ charge Q_l) and messengers scalars $\phi_\pm$ in the loop, we have

$$\bar{\chi}(k')\, i\Gamma^\mu_\gamma \chi(k) = e Q_l\, \bar{\chi}(k') \sum_{\lambda=\pm} \left[\left(\frac{g_L^2 + g_R^2}{2} \right) I^\mu_{a,\gamma} \left(m_l, m_{\phi_\lambda}, k, q \right) + (\lambda)\, g_L g_R m_l I^\mu_{b,\gamma} \left(m_l, m_{\phi_\lambda}, k, q \right) \right] \chi(k) \,. \tag{A.9}$$

The functions I_a and I_b are loop integrals, defined as

$$\begin{aligned} I^\mu_{a,V} \left(m_f, m_s, k, q \right) &\equiv \int \frac{d^4 l}{(2\pi)^4} \left[\frac{(\not{l} + \not{q}) \gamma^\mu \not{l} + m_f^2 \gamma^\mu}{D(l, m_f)\, D(l+q, m_f)\, D(k-l, m_s)} \right. \\ &+ \left. s_V \frac{(2l+q)^\mu (\not{k} - \not{l})}{D(l, m_s)\, D(l+q, m_s)\, D(k-l, m_f)} \right] , \end{aligned} \tag{A.10}$$

$$\begin{aligned} I^\mu_{b,V} \left(m_f, m_s, k, q \right) &\equiv \int \frac{d^4 l}{(2\pi)^4} \left[\frac{\gamma^\mu \not{l} + (\not{l} + \not{q}) \gamma^\mu}{D(l, m_f)\, D(l+q, m_f)\, D(k-l, m_s)} \right. \\ &+ \left. s_V \frac{(2l+q)^\mu}{D(l, m_s)\, D(l+q, m_s)\, D(k-l, m_f)} \right] , \end{aligned} \tag{A.11}$$

where we introduced the function $D(p,m) \equiv p^2 - m^2$, while $s_\gamma = 1$ and $s_{\gamma_D} = -1$. The s_V sign structure is motivated by the form of the interaction Lagrangian in Eqs. (2.1) and (2.2): a dark fermion and its corresponding messenger scalar must have opposite $U(1)_D$ charges, while a SM fermion and its corresponding messenger scalar must have the same $U(1)_{em}$ charge.

The additional contribution to the magnetic dipole moment of SM leptons predicted in our dark sector framework is computed from the γ vertex function having SM leptons as external legs and a loop with χ and $\phi_\pm$. We find

$$\bar{l}(k')\, i\Gamma^\mu_\gamma l(k) = eQ_l\, \bar{l}(k') \sum_{\lambda=\pm} \left[\left(\frac{g_L^2 + g_R^2}{2} \right) J_a^\mu \left(m_\chi, m_{\phi_\lambda}, k, q \right) + (\lambda)\, g_L g_R m_\chi J_b^\mu \left(m_\chi, m_{\phi_\lambda}, k, q \right) \right] l(k), \tag{A.12}$$

where

$$\begin{aligned} J_a^\mu \left(m_f, m_s, k, q \right) &\equiv \int \frac{d^4 l}{(2\pi)^4} \, \frac{(2l+q)^\mu (\not{k} - \not{l})}{D(l, m_s)\, D(l+q, m_s)\, D(k-l, m_f)} \\ J_b^\mu \left(m_f, m_s, k, q \right) &\equiv \int \frac{d^4 l}{(2\pi)^4} \, \frac{(2l+q)^\mu}{D(l, m_s)\, D(l+q, m_s)\, D(k-l, m_f)}. \end{aligned} \tag{A.13}$$

Notice that only one term appears in these loop factors; this follows from the fact that the messenger scalars have SM quantum numbers, while the dark leptons do not.

Loop factors are computed using the standard Feynman trick to rewrite denominators. A UV cut-off needs to be introduced since I_a, I_b and J_a are logarithmically divergent; as a renormalization condition, the vertex function at zero momentum transfer q^μ is subtracted to each vertex function. Finally, dipole and charge-radius terms are extracted at leading order in a momentum expansion of the vertex functions. The general structure is

$$\bar{f}(k')\, \Gamma_V^\mu f(k) = \frac{d_{M,V}^{(f)}}{\Lambda_{D,V}^{(f)}} \left[\bar{f}(k')\, i\sigma^{\mu\nu} q_\nu\, f(k) \right] + q^2 \frac{c_{CR,V}^{(f)}}{[\Lambda_{CR,V}^{(f)}]^2} \left[\bar{f}(k') \gamma^\mu f(k) \right] . \tag{A.14}$$

Following the notation introduced in Eqs. (2.53) and (2.56), we find

$$\begin{aligned} F_{D,\gamma}^{(\chi)} \left(m_l, m_{\phi_-}, m_{\phi_+} \right) &= -2 \left[I_1 \left(\frac{m_{\phi_+}}{m_{\phi_-}}, \frac{m_l}{m_{\phi_-}} \right) + I_1 \left(1, \frac{m_l}{m_{\phi_-}} \right) \right] \\ F_{CR,\gamma}^{(\chi)} \left(m_l, m_{\phi_-}, m_{\phi_+} \right) &= -\frac{1}{6} \left[I_2 \left(\frac{m_{\phi_+}}{m_{\phi_-}}, \frac{m_l}{m_{\phi_-}} \right) + I_2 \left(1, \frac{m_l}{m_{\phi_-}} \right) \right] \\ F_{D,\gamma_D}^{(q)} \left(m_Q, m_{S_-}, m_{S_+} \right) &= -2 \left[I_3 \left(\frac{m_{S_+}}{m_{S_-}}, \frac{m_Q}{m_{S_-}} \right) - I_3 \left(1, \frac{m_Q}{m_{S_-}} \right) \right] \\ F_{CR,\gamma_D}^{(q)} \left(m_Q, m_{S_-}, m_{S_+} \right) &= \frac{1}{6} \left[I_4 \left(\frac{m_{S_+}}{m_{S_-}}, \frac{m_Q}{m_{S_-}} \right) + I_4 \left(1, \frac{m_Q}{m_{S_-}} \right) \right] \\ F_{D,\gamma}^{(l)} \left(m_\chi, m_{\phi_-}, m_{\phi_+} \right) &= 2 \left[I_1 \left(\frac{m_{\phi_+}}{m_{\phi_-}}, \frac{m_\chi}{m_{\phi_-}} \right) - I_1 \left(1, \frac{m_\chi}{m_{\phi_-}} \right) \right] , \end{aligned} \tag{A.15}$$

where we introduced the following functions

$$
\begin{aligned}
I_1(a,b) &\equiv \frac{1}{2\left(b^2-a^2\right)^3}\left[-2a^2b^2\ln\left(\frac{b^2}{a^2}\right)+b^4-a^4\right] \\
I_2(a,b) &\equiv \frac{1}{2\left(b^2-a^2\right)^4}\left[2\left(b^6-a^6\right)\ln\left(\frac{b^2}{a^2}\right)-3\left(b^2-a^2\right)^2\left(b^2+a^2\right)\right] \\
I_3(a,b) &\equiv \frac{1}{\left(b^2-a^2\right)^3}\left[\left(b^2-a^2\right)^2-a^2\left(b^2-a^2\right)\ln\left(\frac{b^2}{a^2}\right)\right] \\
I_4(a,b) &\equiv \frac{1}{6\left(b^2-a^2\right)^4}\left[6\left(b^6+a^6\right)\ln\left(\frac{b^2}{a^2}\right)-4\left(b^6-a^6\right)-9\left(b^2-a^2\right)^3\right] .
\end{aligned}
\tag{A.16}
$$

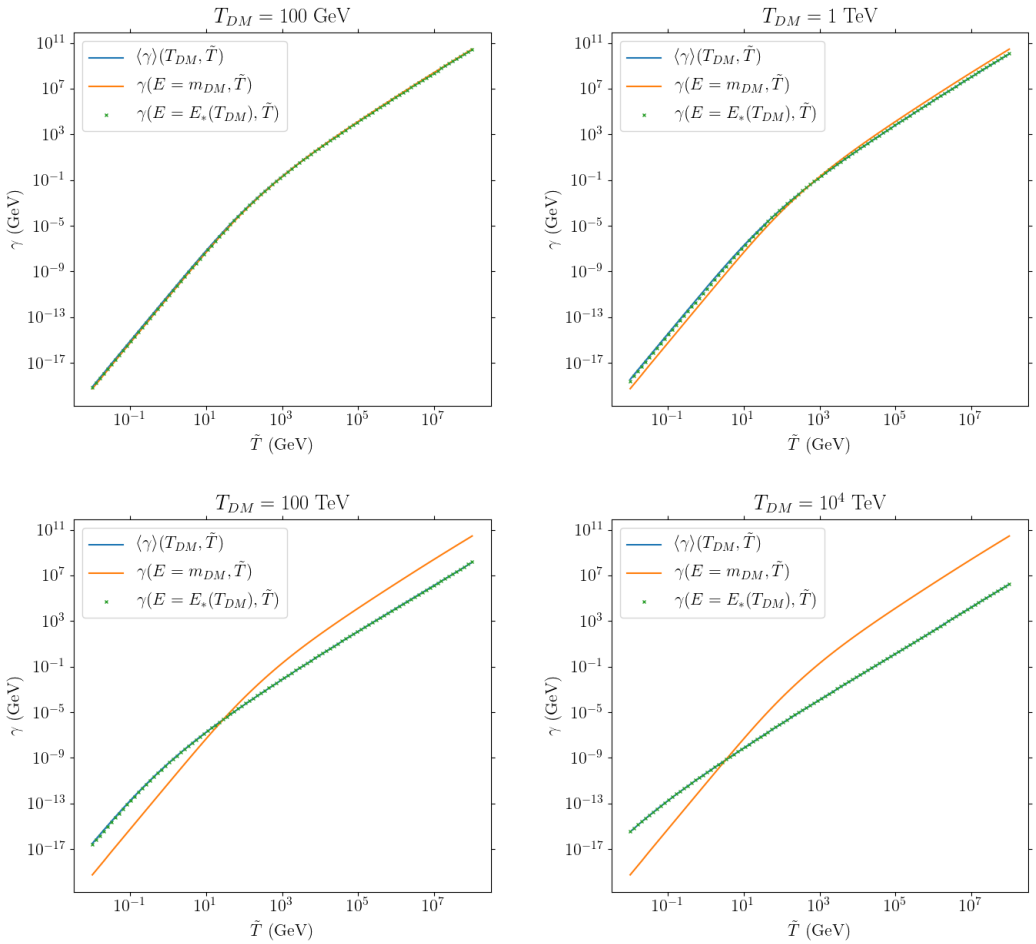

Figure A.1: Plots of the thermal average of the momentum transfer rate, $\langle\gamma\rangle$ (solid blue curve), the momentum transfer rate evaluated at zero momentum (solid orange curve), and the momentum transfer rate evaluated at the stationary point $E = E_*(T_{DM})$ (green crosses), as functions of the bath temperature $\tilde{T}$. The process being considered here is Compton scattering between dark fermions, with mass $m_{DM} = 1\,\text{TeV}$ and temperature T_{DM}, and dark photons which serve as the heat bath. The dark coupling is chosen to be $\alpha_D = 10^{-2}$. Notice the large deviation between the blue and orange curves when $T_{DM} \gg m_{DM}$. On the other hand, there is a good agreement between $\gamma(E = E_*(T_{DM}), \tilde{T})$ and $\langle\gamma\rangle(T_{DM}, \tilde{T})$.

Appendix B

Derivation of the velocity moment for an axisymmetric PSDF

Let us derive (4.44). We start by noting that

$$f(\vec{v}) = \int d\mathcal{E}' dL'_z \; f(\mathcal{E}', L'_z) \; \delta(\mathcal{E}' - \mathcal{E}(\vec{v}))\delta(L'_z - L_z(\vec{v})) \tag{B.1}$$

where

$$\mathcal{E}(\vec{v}) = \psi - \frac{1}{2}|\vec{v} + \vec{v}_E|^2, \quad L_z = R(v + v_E)_\phi. \tag{B.2}$$

This is analogous to inserting a "1" in the Fadeev-Popov method. Now, keeping in mind that $v > v_{min}$,

$$\begin{aligned}
\langle v^{k-1} \rangle &= \int d^3\vec{v} \; v^{k-1} f(\vec{v}) && \text{(B.3)} \\
&= \int d^3\vec{v} \; v^{k-1} \int d\mathcal{E}' dL'_z \; f(\mathcal{E}', L'_z) \; \delta(\mathcal{E}' - \mathcal{E}(\vec{v}))\delta(L'_z - L_z(\vec{v})) && \text{(B.4)} \\
&= \int d\mathcal{E}' dL'_z \; f(\mathcal{E}', L'_z) \; \int d^3\vec{v} \; v^{k-1} \delta(\mathcal{E}' - \mathcal{E}(\vec{v}))\delta(L'_z - L_z(\vec{v})). && \text{(B.5)}
\end{aligned}$$

The last line (B.5) is reminiscent of the calculation of the density of states. In any case, we proceed with the integration over velocity. It is convenient to first integrate over the angular velocity, so we have

$$\begin{aligned}
P_k(\mathcal{E}', L'_z) &\equiv \int d^3\vec{v} \; v^{k-1} \delta(\mathcal{E}' - \mathcal{E}(\vec{v}))\delta(L'_z - L_z(\vec{v})) && \text{(B.6)} \\
&= \frac{1}{R} \int dv_R dv_z \; \left[v_R^2 + v_z^2 + (L_z/R - v_{E\phi})^2 \right]^{(k-1)/2} \; \delta(\mathcal{E}' - \mathcal{E}(\vec{v}))\Big|_{v_\phi = L'_z/R - v_{E\phi}}. && \text{(B.7)}
\end{aligned}$$

Let us define

$$v_\perp \equiv \sqrt{v_R^2 + v_z^2} \tag{B.8}$$

and so

$$\mathcal{E}(\vec{v})\Big|_{v_\phi = L_z/R - v_{E\phi}} = \psi - \frac{L_z^2}{2R^2} + \frac{v_\perp^2 + v_{E\perp}^2}{2} + v_\perp v_{E\perp}\cos\phi, \tag{B.9}$$

and

$$dv_R dv_z = v_\perp dv_\perp d\phi = d\left(\frac{v_\perp^2}{2}\right) d\phi. \tag{B.10}$$

Then

$$\begin{aligned} P_k(\mathcal{E}, L_z) &= \frac{1}{R}\int d\left(\frac{v_\perp^2}{2}\right) d\phi \ \left[v_\perp^2 + (L_z/R - v_{E\phi})^2\right]^{(k-1)/2} \\ &\times \ \delta\left(\mathcal{E} - \psi + \frac{L_z^2}{2R^2} + \frac{v_\perp^2 + v_{E\perp}^2}{2} + v_\perp v_{E\perp}\cos\phi\right). \end{aligned} \tag{B.11}$$

In the last line, we have dropped the prime on the integrals of motion. We then integrate over ϕ, so we need to find ϕ that makes the argument zero. One should note that if ϕ_0 is a root, then so is $2\pi - \phi_0$. Then

$$\int \phi\delta\left(\mathcal{E} - \psi + \frac{L_z^2}{2R^2} + \frac{v_\perp^2 + v_{E\perp}^2}{2} + v_\perp v_{E\perp}\cos\phi\right) = \frac{\delta(\phi - \phi_0)}{v_\perp v_{E\perp}|\sin\phi_0|} + \frac{\delta(\phi - 2\pi + \phi_0)}{v_\perp v_{E\perp}|\sin\phi_0|}, \tag{B.12}$$

and so

$$P_k(\mathcal{E}, L_z) = \frac{2}{R}\int d\left(\frac{v_\perp^2}{2}\right) \ \left[v_\perp^2 + (L_z/R - v_{E\phi})^2\right]^{(k-1)/2} \ \frac{1}{v_\perp v_{E\perp}|\sin\phi_0|}\theta(1 - \cos\phi_0)\theta(\cos\phi_0 + 1). \tag{B.13}$$

One can show that

$$|\sin\phi_0| = \frac{1}{2v_\perp v_{E\perp}}\sqrt{(v_+^2 - v_\perp^2)(v_\perp^2 - v_-^2)} \tag{B.14}$$

$$\theta(\cos\phi_0 + 1)\theta(1 - \cos\phi_0) = \theta(v_+^2 - v_\perp^2)\theta(v_\perp^2 - v_-^2), \tag{B.15}$$

where

$$v_\pm \equiv v_{E\perp} \pm \sqrt{2\left(\psi - \mathcal{E} - \frac{L_z^2}{2R^2}\right)}. \tag{B.16}$$

If we let

$$x = v_\perp^2 - \frac{v_+^2 + v_-^2}{2}, \tag{B.17}$$

then

$$\begin{aligned} P_k(\mathcal{E}, L_z) &= \frac{2}{R}\int_{-(v_+^2 - v_-^2)/2}^{(v_+^2 - v_-^2)/2} \frac{dx}{\sqrt{\left(\frac{v_+^2 - v_-^2}{2}\right)^2 - x^2}} \ \left[x + \left(\frac{v_+^2 + v_-^2}{2}\right) + (L_z/R - v_{E\phi})^2\right]^{(k-1)/2} \\ &\times \ \theta\left(\sqrt{x + \left(\frac{v_+^2 + v_-^2}{2}\right) + (L_z/R - v_{E\phi})^2} - v_{min}\right). \end{aligned} \tag{B.18}$$

By introducing an appropriate trigonometric substitution, we have

$$P_k(\mathcal{E}, L_z) = \frac{2}{R}\int_0^{\pi} d\chi \ \left[v_+^2\cos^2(\chi/2) + v_-^2\sin^2(\chi/2) + (L_z/R - v_{E\phi})^2\right]^{(k-1)/2} \quad \text{(B.19)}$$

$$\times \ \theta\left(\sqrt{v_+^2\cos^2(\chi/2) + v_-^2\sin^2(\chi/2) + (L_z/R - v_{E\phi})^2} - v_{min}\right). \quad \text{(B.20)}$$

Finally we have

$$P_k(\mathcal{E}, L_z) = \frac{4}{R}\left[v_+^2 + (L_z/R - v_{E\phi})^2\right]^{(k-1)/2}\int_0^{\pi/2} d\phi \ \left(1 - \gamma^2\sin^2\phi\right)^{(k-1)/2}$$

$$\times\theta\left(\sqrt{1 - \gamma^2\sin^2\phi} - \beta_{min}\right), \quad \text{(B.21)}$$

where

$$\gamma^2 \equiv \frac{v_+^2 - v_-^2}{v_+^2 + (L_z/R - v_{E\phi})^2}, \quad \beta_{min} \equiv \frac{v_{min}}{\sqrt{v_+^2 + (L_z/R - v_{E\phi})^2}}. \quad \text{(B.22)}$$

Plugging (B.21) to (B.5) yields (4.44).

Appendix C

Speed distributions: SHM vs axisymmetric PSDF

For the SHM, the logarithm of the PSDF can be written as

$$\ln f_{SHM} = -\frac{\vec{v}^2}{2v_0^2} + c \tag{C.1}$$

$$\equiv -\vec{v}^T \frac{M_{SHM}}{2} \vec{v}. \tag{C.2}$$

Since the matrix M_{SHM} is proportional to the identity matrix, the velocity ellipsoid for the SHM is a sphere. In general, the matrix M can be obtained from

$$M = -\frac{1}{f} \left(\partial_{\vec{v}_i} \partial_{\vec{v}_j} f\right) \Big|_{\vec{v}=\vec{v}_*}, \quad \left(\partial_{\vec{v}} f\right) \Big|_{\vec{v}=\vec{v}_*} = \vec{0}. \tag{C.3}$$

In the case of an axisymmetric PSDF, in which the PSDF is written as a function of the isolating integrals $\mathcal{E}$ and L_z given by

$$\mathcal{E} = \psi - \frac{\vec{v}^2}{2} \tag{C.4}$$

$$L_z = R v_\phi, \tag{C.5}$$

we have

$$\partial_{\vec{v}_i} f = \left(-\vec{v}_i \partial_{\mathcal{E}} + R\delta_{i\phi} \partial_{L_z}\right) f \tag{C.6}$$

$$\left(\partial_{\vec{v}_i} \partial_{\vec{v}_j}\right) f = \left(-\delta_{ij} \partial_{\mathcal{E}} - v_i \partial_{\vec{v}_j} \partial_{\mathcal{E}} + R\delta_{i\phi} \partial_{\vec{v}_j} \partial_{\mathcal{E}}\right) f. \tag{C.7}$$

The matrix M is then given by

$$M_{ij} = -\frac{1}{f_*} \left[-\delta_{ij} \left(\partial_{\mathcal{E}} f\right)_* + v_{i*} v_{j*} \left(\partial_{\mathcal{E}}^2 f\right)_* + R^2 \delta_{i\phi} \delta_{j\phi} \left(\partial_{L_z}^2 f\right)_* - R \left(v_{i*} \delta_{j\phi} + v_{j*} \delta_{i\phi}\right) \left(\partial_{\mathcal{E}} \partial_{L_z} f\right)_*\right], \tag{C.8}$$

where

$$-v_{i*} \left(\partial_{\mathcal{E}} f\right)_* + R\delta_{i\phi} \left(\partial_{L_z} f\right)_* = 0. \tag{C.9}$$

The asterisks mean evaluation at $\vec{v} = \vec{v}_*$. Assuming that

$$v_{i*} = \delta_{i\phi} v_{\phi *}, \tag{C.10}$$

the matrix M is diagonal, and one can simply read off the inverse velocity dispersions in v_R, v_z, and v_ϕ. We have

$$\sigma_{v_R}^{-2} = \sigma_{v_z}^{-2} = \left[\left(\partial_\mathcal{E} f \right) / f \right]_* \tag{C.11}$$

$$\sigma_{v_\phi}^{-2} = \left[\left(\partial_\mathcal{E} f \right) / f \right]_* - v_{\phi *}^2 \left[\left(\partial_\mathcal{E}^2 f \right) / f \right]_* - R^2 \left[\left(\partial_{L_z}^2 f \right) / f \right]_* + 2 R v_{\phi *} \left[\left(\partial_\mathcal{E} \partial_{L_z} f \right) / f \right]_* . \tag{C.12}$$

It is then apparent that for an axisymmetric PSDF, the velocity dispersions along the two orthogonal directions in the meridional plane are the same, while the tangential velocity dispersion is different. This will manifest in the one-dimensional speed distribution as a distortion relative to the SHM case, as we can see in Fig. (C.1).

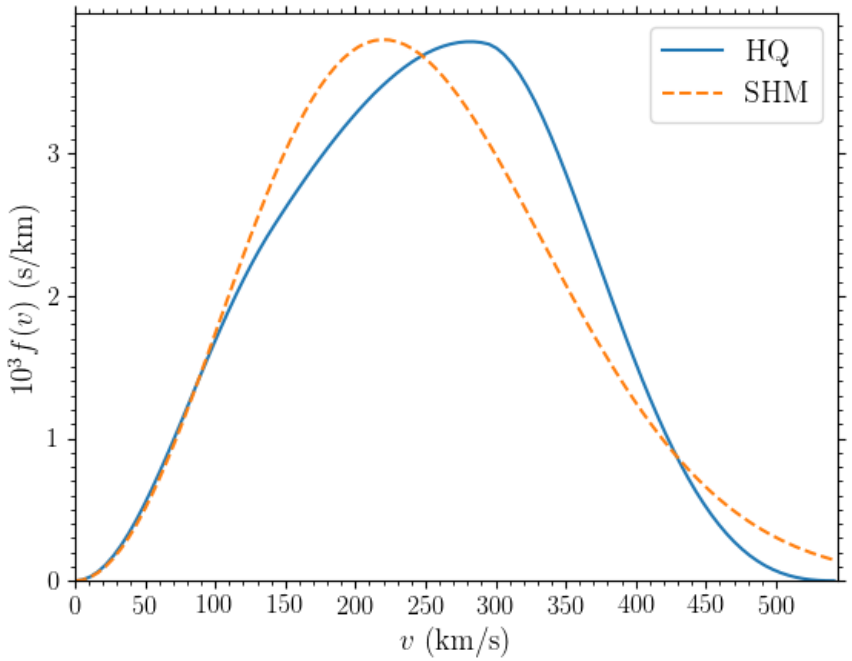

Figure C.1: One-dimensional speed distributions for the SHM (dashed line) and the reference axisymmetric model with a $q = 1$ halo (solid line).

Bibliography

[1] N. Aghanim, Y. Akrami, M. Ashdown, J. Aumont, C. Baccigalupi, M. Ballardini, A. Banday, R. Barreiro, N. Bartolo, S. Basak, *et al.*, Planck 2018 results-VI. Cosmological parameters *Astronomy & Astrophysics* **641** (2020) A6.

[2] J. C. Kapteyn, First Attempt at a Theory of the Arrangement and Motion of the Sidereal System *Astrophys. J.* **55** (1922) 302–328.

[3] J. H. Oort, The force exerted by the stellar system in the direction perpendicular to the galactic plane and some related problems *Bulletin of the Astronomical Institutes of the Netherlands* **6** (1932) 249.

[4] R. Catena and P. Ullio, The local dark matter phase-space density and impact on WIMP direct detection *Journal of Cosmology and Astroparticle Physics* **2012** (2012), no. 05, 005.

[5] J. Buch, S. C. J. Leung, and J. Fan, Using Gaia DR2 to Constrain Local Dark Matter Density and Thin Dark Disk *JCAP* **04** (2019) 026, `arXiv:1808.05603`.

[6] F. Zwicky, Die rotverschiebung von extragalaktischen nebeln *Helvetica physica acta* **6** (1933) 110–127.

[7] F. Zwicky, The redshift of extragalactic nebulae *Helvetica Physica Acta* **6** (1933) 110–127.

[8] F. Zwicky, On the Masses of Nebulae and of Clusters of Nebulae *The Astrophysical Journal* **86** (1937) 217.

[9] **Planck** Collaboration, N. Aghanim *et al.*, Planck 2018 results. VI. Cosmological parameters `arXiv:1807.06209`.

[10] H. W. Babcock, The rotation of the Andromeda Nebula *Lick Observatory Bulletin* **19** (1939) 41–51.

[11] F. Vilardell, I. Ribas, C. Jordi, E. L. Fitzpatrick, and E. F. Guinan, The distance to the Andromeda Galaxy from eclipsing binaries *Astron. Astrophys.* **509** (2010) A70, `arXiv:0911.3391`.

[12] J. H. Oort, Some problems concerning the structure and dynamics of the galactic system and the elliptical nebulae NGC 3115 and 4494 *Astrophysical Journal*, 1940 91–273.

[13] H. I. Ewen and E. M. Purcell, Observation of a Line in the Galactic Radio Spectrum: Radiation from Galactic Hydrogen at 1,420 Mc./sec. *Nature* **168** (1951), no. 4270, 356–356.

[14] M. S. Roberts, A high-resolution 21-CM hydrogen-line survey of the Andromeda nebula *The Astrophysical Journal* **144** (1966) 639.

[15] B. Burke, K. Turner, and M. Tuve, A high-resolution study of the outer parts of the Galaxy in "Symposium-International Astronomical Union", vol. 20, pp. 131–134, Cambridge University Press. 1964.

[16] K. C. Freeman, On the disks of spiral and SO Galaxies *Astrophys. J.* **160** (1970) 811.

[17] V. C. Rubin and W. K. Ford Jr, Rotation of the Andromeda nebula from a spectroscopic survey of emission regions *The Astrophysical Journal* **159** (1970) 379.

[18] D. Rogstad and G. Shostak, Gross properties of five scd galaxies as determined from 21-centimeter observations *The Astrophysical Journal* **176** (1972) 315.

[19] M. Roberts and A. Rots, Comparison of rotation curves of different galaxy types *Astronomy and Astrophysics* **26** (1973) 483–485.

[20] A. Bosma, The distribution and kinematics of neutral hydrogen in spiral galaxies of various morphological types PhD thesis.

[21] A. Bosma, The dark matter problem *Celestial Mechanics and Dynamical Astronomy* **72** (1998), no. 1, 69–90.

[22] V. Rubin, A brief history of dark matter in "The dark universe: matter, energy and gravity", M. Livio, ed., ch. 1, pp. 1–13. Cambridge University Press, 2004.

[23] J. Einasto, A. Kaasik, and E. Saar, Dynamic evidence on massive coronas of galaxies *Nature* **250** (1974), no. 5464, 309–310.

[24] J. P. Ostriker and P. J. Peebles, A numerical study of the stability of flattened galaxies: or, can cold galaxies survive? *The Astrophysical Journal* **186** (1973) 467–480.

[25] S. M. Faber and J. Gallagher, Masses and mass-to-light ratios of galaxies *Annual review of astronomy and astrophysics* **17** (1979), no. 1, 135–187.

[26] W. H. Press and P. Schechter, Formation of galaxies and clusters of galaxies by self-similar gravitational condensation *The Astrophysical Journal* **187** (1974) 425–438.

[27] S. D. White and M. J. Rees, Core condensation in heavy halos: a two-stage theory for galaxy formation and clustering *Monthly Notices of the Royal Astronomical Society* **183** (1978), no. 3, 341–358.

[28] S. J. Aarseth, J. R. Gott III, and E. L. Turner, N-body simulations of galaxy clustering. I-Initial conditions and galaxy collapse times *The Astrophysical Journal* **228** (1979) 664–683.

[29] G. Efstathiou, The clustering of galaxies and its dependence upon Ω *Monthly Notices of the Royal Astronomical Society* **187** (1979), no. 2, 117–127.

[30] J. A. Bond, J. Centrella, A. S. Szalay, and J. R. Wilson, Dark matter and shocked pancakes in "Formation and Evolution of Galaxies and Large Structures in the Universe", J. Audouze and J. Tran Thanh Van, eds., pp. 87–99. D Reidel Publishing Company, 1984.

[31] M. Davis, J. Huchra, D. W. Latham, and J. Tonry, A survey of galaxy redshifts. II-The large scale space distribution *The Astrophysical Journal* **253** (1982) 423–445.

[32] S. D. White, C. S. Frenk, and M. Davis, Clustering in a neutrino-dominated universe *The Astrophysical Journal* **274** (1983) L1–L5.

[33] M. Davis, G. Efstathiou, C. S. Frenk, and S. D. White, The evolution of large-scale structure in a universe dominated by cold dark matter *The Astrophysical Journal* **292** (1985) 371–394.

[34] C. Jones and W. Forman, The structure of clusters of galaxies observed with Einstein *The Astrophysical Journal* **276** (1984) 38–55.

[35] L. Cowie, M. Henriksen, and R. Mushotzky, Are the virial masses of clusters smaller than we think? *The Astrophysical Journal* **317** (1987) 593–600.

[36] J. P. Hughes, The mass of the Coma Cluster-Combined X-ray and optical results *The Astrophysical Journal* **337** (1989) 21–33.

[37] S. D. White, J. F. Navarro, A. E. Evrard, and C. S. Frenk, The baryon content of galaxy clusters: a challenge to cosmological orthodoxy *nature* **366** (1993), no. 6454, 429–433.

[38] F. W. Dyson, A. S. Eddington, and C. Davidson, IX. A determination of the deflection of light by the Sun's gravitational field, from observations made at the total eclipse of May 29, 1919 *Philosophical Transactions of the Royal Society of London. Series A, Containing Papers of a Mathematical or Physical Character* **220** (1920), no. 571-581, 291–333.

[39] D. Walsh, R. F. Carswell, and R. J. Weymann, 0957+ 561 A, B: twin quasistellar objects or gravitational lens? *Nature* **279** (1979), no. 5712, 381–384.

[40] D. Clowe, M. Bradač, A. H. Gonzalez, M. Markevitch, S. W. Randall, C. Jones, and D. Zaritsky, A direct empirical proof of the existence of dark matter *The Astrophysical Journal Letters* **648** (2006), no. 2, L109.

[41] R. A. Alpher and R. C. Herman, Remarks on the evolution of the expanding universe *Physical Review* **75** (1949), no. 7, 1089.

[42] A. G. Doroshkevich and I. D. Novikov, Mean radiation density in Metagalaxy and some problems of relativistic cosmology in "Doklady Akademii Nauk", vol. 154, pp. 809–811, Russian Academy of Sciences. 1964.

[43] A. A. Penzias and R. W. Wilson, A measurement of excess antenna temperature at 4080 Mc/s. *The Astrophysical Journal* **142** (1965) 419–421.

[44] R. H. Dicke, P. J. E. Peebles, P. G. Roll, and D. T. Wilkinson, Cosmic black-body radiation. *The Astrophysical Journal* **142** (1965) 414–419.

[45] J. C. Mather, E. Cheng, D. A. Cottingham, R. Eplee Jr, D. J. Fixsen, T. Hewagama, R. Isaacman, K. Jensen, S. S. Meyer, P. D. Noerdlinger, *et al.*, Measurement of the cosmic microwave background spectrum by the COBE FIRAS instrument *The Astrophysical Journal* **420** (1994) 439–444.

[46] J. Silk, Cosmic black-body radiation and galaxy formation *The Astrophysical Journal* **151** (1968) 459.

[47] R. A. Sunyaev and Y. B. Zeldovich, Small-scale fluctuations of relic radiation *Astrophysics and Space Science* **7** (1970), no. 1, 3–19.

[48] P. J. Peebles and J. Yu, Primeval adiabatic perturbation in an expanding universe *The Astrophysical Journal* **162** (1970) 815.

[49] J. M. Bardeen, P. J. Steinhardt, and M. S. Turner, Spontaneous creation of almost scale-free density perturbations in an inflationary universe *Physical Review D* **28** (1983), no. 4, 679.

[50] C.-p. Ma and E. Bertschinger, Cosmological Perturbation Theory in the Synchronous and Conformal Newtonian Gauges, Astrophys in "J", Citeseer. 1995.

[51] W. Hu and N. Sugiyama, Toward understanding CMB anisotropies and their implications *Physical Review D* **51** (1995), no. 6, 2599.

[52] J. Lesgourgues and S. Pastor, Massive neutrinos and cosmology *Physics Reports* **429** (2006), no. 6, 307–379.

[53] I. Strukov, A. Brukhanov, D. Skulachev, and M. Sazhin, The Relikt-1 experiment–new results *Monthly Notices of the Royal Astronomical Society* **258** (1992), no. 1, 37P–40P.

[54] G. F. Smoot, COBE observations and results in "AIP Conference Proceedings CONF-981098", vol. 476, pp. 1–10, American Institute of Physics. 1999.

[55] P. De Bernardis, P. A. Ade, J. Bock, J. Bond, J. Borrill, A. Boscaleri, K. Coble, B. Crill, G. De Gasperis, G. De Troia, *et al.*, First results from the BOOMERanG experiment in "AIP Conference Proceedings", vol. 555, pp. 85–94, American Institute of Physics. 2001.

[56] C. Bennett *et al.*, First year Wilkinson microwave anisotropy probe (WMAP) observations: Preliminary maps and basic results *Astrophys. J. Suppl* **148** (2003), no. 1,.

[57] R. A. Watson, P. Carreira, K. Cleary, R. D. Davies, R. J. Davis, C. Dickinson, K. Grainge, C. M. Gutierrez, M. P. Hobson, M. E. Jones, *et al.*, First results from the very small arrayi. observational methods *Monthly Notices of the Royal Astronomical Society* **341** (2003), no. 4, 1057–1165.

[58] J. Carlstrom, J. Kovac, E. Leitch, and C. Pryke, Status of CMB polarization measurements from DASI and other experiments *New Astronomy Reviews* **47** (2003), no. 11-12, 953–966.

[59] S. Padin, M. Shepherd, J. Cartwright, R. Keeney, B. Mason, T. Pearson, A. Readhead, W. Schaal, J. Sievers, P. Udomprasert, *et al.*, The cosmic background imager *Publications of the Astronomical Society of the Pacific* **114** (2001), no. 791, 83.

[60] N. Aghanim, Y. Akrami, M. Ashdown, J. Aumont, C. Baccigalupi, M. Ballardini, A. J. Banday, R. Barreiro, N. Bartolo, S. Basak, *et al.*, Planck 2018 results-V. CMB power spectra and likelihoods *Astronomy & Astrophysics* **641** (2020) A5.

[61] W. Hu and S. Dodelson, Cosmic microwave background anisotropies *Annual Review of Astronomy and Astrophysics* **40** (2002), no. 1, 171–216.

[62] S. Dodelson and F. Schmidt, Modern cosmology Academic Press, 2020.

[63] S. Van den Bergh, Collapsed objects in clusters of galaxies *Nature* **224** (1969), no. 5222, 891–891.

[64] J. Tarter and J. Silk, Current constraints on hidden mass in the Coma Cluster *Quarterly Journal of the Royal Astronomical Society* **15** (1974) 122.

[65] K. Griest, The Search for the Dark Matter: WIMPs and MACHOs, in" Texas/Pascos' 92: Relativistic Astrophysics and Particle Cosmology", ed. by CW Akerlof and MA Srednicki *Annals of the New York Academy of Sciences* **688**.

[66] D. J. Hegyi and K. A. Olive, Can galactic halos be made of baryons? *Physics Letters B* **126** (1983), no. 1-2, 28–32.

[67] P. Tisserand, L. Le Guillou, C. Afonso, J. Albert, J. Andersen, R. Ansari, É. Aubourg, P. Bareyre, J. Beaulieu, X. Charlot, *et al.*, Limits on the Macho Content of the Galactic Halo from the EROS-2 Survey of the Magellanic Clouds *Astronomy & Astrophysics* **469** (2007), no. 2, 387–404.

[68] C. Alcock, R. Allsman, D. R. Alves, T. Axelrod, A. C. Becker, D. Bennett, K. H. Cook, N. Dalal, A. J. Drake, K. Freeman, *et al.*, The MACHO project: microlensing results from 5.7 years of Large Magellanic Cloud observations *The Astrophysical Journal* **542** (2000), no. 1, 281.

[69] A. Milsztajn, T. Lasserre, E. collaboration, *et al.*, Not enough stellar mass Machos in the Galactic halo *Nuclear Physics B-Proceedings Supplements* **91** (2001), no. 1-3, 413–419.

[70] B. J. Carr and S. W. Hawking, Black holes in the early Universe *Monthly Notices of the Royal Astronomical Society* **168** (1974), no. 2, 399–415.

[71] B. J. Carr and J. E. Lidsey, Primordial black holes and generalized constraints on chaotic inflation *Physical Review D* **48** (1993), no. 2, 543.

[72] J. S. Bullock and J. R. Primack, Non-Gaussian fluctuations and primordial black holes from inflation *Physical Review D* **55** (1997), no. 12, 7423.

[73] P. Ivanov, Nonlinear metric perturbations and production of primordial black holes *Physical Review D* **57** (1998), no. 12, 7145.

[74] S. Gershtein and Y. Zeldovich, GERSHTEIN 1966 *Pisma Zh. Eksp. Teor. Fiz* **4** (1966) 174.

[75] R. Cowsik and J. McClelland, An upper limit on the neutrino rest mass *Physical Review Letters* **29** (1972), no. 10, 669.

[76] A. Szalay and G. Marx, Neutrino rest mass from cosmology *Astronomy and Astrophysics* **49** (1976) 437–441.

[77] M. Viel, K. Markovič, M. Baldi, and J. Weller, The non-linear matter power spectrum in warm dark matter cosmologies *Monthly Notices of the Royal Astronomical Society* **421** (2012), no. 1, 50–62.

[78] K. Abazajian, Linear cosmological structure limits on warm dark matter *Physical Review D* **73** (2006), no. 6, 063513.

[79] M. R. Lovell, C. S. Frenk, V. R. Eke, A. Jenkins, L. Gao, and T. Theuns, The properties of warm dark matter haloes *Monthly Notices of the Royal Astronomical Society* **439** (2014), no. 1, 300–317.

[80] I. P. Carucci, F. Villaescusa-Navarro, M. Viel, and A. Lapi, Warm dark matter signatures on the 21cm power spectrum: intensity mapping forecasts for SKA *Journal of Cosmology and Astroparticle Physics* **2015** (2015), no. 07, 047.

[81] B. Holdom, Two U(1)'s and Epsilon Charge Shifts *Phys. Lett.* **166B** (1986) 196–198.

[82] M. Fabbrichesi, E. Gabrielli, and G. Lanfranchi, The Physics of the Dark Photon: A Primer Springer, 2021.

[83] H. Vogel and J. Redondo, Dark Radiation constraints on minicharged particles in models with a hidden photon *Journal of Cosmology and Astroparticle Physics* **2014** (2014), no. 02, 029.

[84] V. Poulin, P. D. Serpico, and J. Lesgourgues, A fresh look at linear cosmological constraints on a decaying dark matter component *Journal of Cosmology and Astroparticle Physics* **2016** (2016), no. 08, 036.

[85] T. Bringmann, F. Kahlhoefer, K. Schmidt-Hoberg, and P. Walia, Converting nonrelativistic dark matter to radiation *Physical Review D* **98** (2018), no. 2, 023543.

[86] Y. Fukuda, T. Hayakawa, E. Ichihara, K. Inoue, K. Ishihara, H. Ishino, Y. Itow, T. Kajita, J. Kameda, S. Kasuga, *et al.*, Evidence for oscillation of atmospheric neutrinos *Physical Review Letters* **81** (1998), no. 8, 1562.

[87] Q. Ahmad, R. Allen, T. Andersen, *et al.*, Measurement of the rate of + + + - interactions produced by 8 solar neutrinos at the Sudbury Neutrino Observatory *Phys. Rev. Lett* **87** (2001), no. 7, 071301.

[88] B. Pontecorvo, Neutrino experiments and the problem of conservation of leptonic charge *Sov. Phys. JETP* **26** (1968), no. 984-988, 165.

[89] M. Gell-Mann, P. Ramond, and R. Slansky, Complex spinors and unified theories in "Murray Gell-Mann: Selected Papers", pp. 266–272. World Scientific, 2010.

[90] S. M. Bilenky, J. Hošek, and S. T. Petcov, On the oscillations of neutrinos with Dirac and Majorana masses *Physics Letters B* **94** (1980), no. 4, 495–498.

[91] T. Yanagida, Horizontal symmetry and masses of neutrinos *Progress of Theoretical Physics* **64** (1980), no. 3, 1103–1105.

[92] R. N. Mohapatra and G. Senjanović, Neutrino mass and spontaneous parity nonconservation *Physical Review Letters* **44** (1980), no. 14, 912.

[93] S. Weinberg, Baryon-and lepton-nonconserving processes *Physical Review Letters* **43** (1979), no. 21, 1566.

[94] A. Boyarsky, M. Drewes, T. Lasserre, S. Mertens, and O. Ruchayskiy, Sterile neutrino dark matter *Progress in Particle and Nuclear Physics* **104** (2019) 1–45.

[95] K. A. Olive and M. S. Turner, Cosmological bounds on the masses of stable, right-handed neutrinos *Physical Review D* **25** (1982), no. 1, 213.

[96] S. Dodelson and L. M. Widrow, Sterile neutrinos as dark matter *Physical Review Letters* **72** (1994), no. 1, 17.

[97] K. Fujikawa, Evaluation of the chiral anomaly in gauge theories with γ 5 couplings *Physical Review D* **29** (1984), no. 2, 285.

[98] C. Abel, S. Afach, N. J. Ayres, C. A. Baker, G. Ban, G. Bison, K. Bodek, V. Bondar, M. Burghoff, E. Chanel, *et al.*, Measurement of the permanent electric dipole moment of the neutron *Physical review letters* **124** (2020), no. 8, 081803.

[99] A. Czarnecki and B. Krause, Neutron electric dipole moment in the standard model: complete three-loop calculation of the valence quark contributions *Physical review letters* **78** (1997), no. 23, 4339.

[100] R. Crewther, P. Di Vecchia, G. Veneziano, and E. Witten, Chiral estimate of the electric dipole moment of the neutron in quantum chromodynamics *Physics Letters B* **88** (1979), no. 1-2, 123–127.

[101] R. D. Peccei and H. R. Quinn, CP conservation in the presence of pseudoparticles *Physical Review Letters* **38** (1977), no. 25, 1440.

[102] R. D. Peccei and H. R. Quinn, Constraints imposed by CP conservation in the presence of pseudoparticles *Physical Review D* **16** (1977), no. 6, 1791.

[103] P. Sikivie and Q. Yang, Bose-Einstein condensation of dark matter axions *Physical Review Letters* **103** (2009), no. 11, 111301.

[104] A. H. Guth, M. P. Hertzberg, and C. Prescod-Weinstein, Do dark matter axions form a condensate with long-range correlation? *Physical Review D* **92** (2015), no. 10, 103513.

[105] A. Arvanitaki, S. Dimopoulos, S. Dubovsky, N. Kaloper, and J. March-Russell, String axiverse *Physical Review D* **81** (2010), no. 12, 123530.

[106] A. Ringwald, Axions and axion-like particles *arXiv preprint arXiv:1407.0546*, 2014.

[107] K. Choi, S. H. Im, and C. S. Shin, Recent Progress in the Physics of Axions and Axion-Like Particles *Annual Review of Nuclear and Particle Science* **71** (2021).

[108] P. Tanedo, "Snowmass loi: Defining the wimp". `https://www.snowmass21.org/docs/files/summaries/CF/SNOWMASS21-CF1_CF3-TF9_TF0-056.pdf`.

[109] L. J. Hall, K. Jedamzik, J. March-Russell, and S. M. West, Freeze-In Production of FIMP Dark Matter *JHEP* **03** (2010) 080, `arXiv:0911.1120`.

[110] R. Foot, Mirror dark matter and the new DAMA/LIBRA results: a simple explanation for a beautiful experiment *Physical Review D* **78** (2008), no. 4, 043529.

[111] K. M. Zurek, Multicomponent dark matter *Physical Review D* **79** (2009), no. 11, 115002.

[112] T. Hur, H.-S. Lee, and C. Luhn, Common gauge origin of discrete symmetries in observable sector and hidden sector *Journal of High Energy Physics* **2009** (2009), no. 01, 081.

[113] M. W. Goodman and E. Witten, Detectability of certain dark-matter candidates *Physical Review D* **31** (1985), no. 12, 3059.

[114] I. Wasserman, Possibility of detecting heavy neutral fermions in the Galaxy *Physical Review D* **33** (1986), no. 8, 2071.

[115] A. Drukier and L. Stodolsky, Principles and applications of a neutral-current detector for neutrino physics and astronomy *Physical Review D* **30** (1984), no. 11, 2295.

[116] R. Catena and P. Ullio, A novel determination of the local dark matter density *Journal of Cosmology and Astroparticle Physics* **2010** (2010), no. 08, 004.

[117] J. Bovy and S. Tremaine, On the local dark matter density *The Astrophysical Journal* **756** (2012), no. 1, 89.

[118] J. Billard, M. Boulay, S. Cebrián, L. Covi, G. Fiorillo, A. Green, J. Kopp, B. Majorovits, K. Palladino, F. Petricca, *et al.*, Direct Detection of Dark Matter–APPEC Committee Report *arXiv preprint arXiv:2104.07634*, 2021.

[119] R. Bernabei, P. Belli, F. Cappella, V. Caracciolo, S. Castellano, R. Cerulli, C. Dai, A. dAngelo, S. dAngelo, A. Di Marco, *et al.*, Final model independent result of DAMA/LIBRA–phase1 *The European Physical Journal C* **73** (2013), no. 12, 1–11.

[120] R. Bernabei, P. Belli, A. Bussolotti, F. Cappella, V. Caracciolo, R. Cerulli, C.-J. Dai, A. dAngelo, A. Di Marco, H.-L. He, *et al.*, First model independent results from DAMA/LIBRA–phase2 *Universe* **4** (2018), no. 11, 116.

[121] J. Amaré, S. Cebrián, D. Cintas, I. Coarasa, E. García, M. Martínez, M. Oliván, Y. Ortigoza, A. O. de Solórzano, J. Puimedón, *et al.*, Annual modulation results from three-year exposure of ANAIS-112 *Physical Review D* **103** (2021), no. 10, 102005.

[122] T. Bringmann and C. Weniger, Gamma ray signals from dark matter: Concepts, status and prospects *Physics of the Dark Universe* **1** (2012), no. 1-2, 194–217.

[123] D. Hooper, TASI lectures on indirect searches for dark matter *arXiv preprint arXiv:1812.02029*, 2018.

[124] M. Ackermann, M. Ajello, A. Albert, W. Atwood, L. Baldini, J. Ballet, G. Barbiellini, D. Bastieri, R. Bellazzini, E. Bissaldi, *et al.*, The Fermi galactic center GeV excess and implications for dark matter *The Astrophysical Journal* **840** (2017), no. 1, 43.

[125] H. Collaboration *et al.*, Measurements of the cosmic ray positron fraction from 1-GeV to 50-GeV *Astrophys. J* **482** (1997) L191.

[126] O. Adriani, G. Barbarino, G. Bazilevskaya, R. Bellotti, M. Boezio, E. Bogomolov, L. Bonechi, M. Bongi, V. Bonvicini, S. Borisov, *et al.*, PAMELA results on the cosmic-ray antiproton flux from 60 MeV to 180 GeV in kinetic energy *Physical Review Letters* **105** (2010), no. 12, 121101.

[127] M. Ackermann, M. Ajello, A. Allafort, W. Atwood, L. Baldini, G. Barbiellini, D. Bastieri, K. Bechtol, R. Bellazzini, B. Berenji, *et al.*, Measurement of separate cosmic-ray electron and positron spectra with the Fermi Large Area Telescope *Physical Review Letters* **108** (2012), no. 1, 011103.

[128] M. Aguilar, G. Alberti, B. Alpat, A. Alvino, G. Ambrosi, K. Andeen, H. Anderhub, L. Arruda, P. Azzarello, A. Bachlechner, *et al.*, First result from the Alpha Magnetic Spectrometer on the International Space Station: precision measurement of the positron fraction in primary cosmic rays of 0.5–350 GeV *Physical Review Letters* **110** (2013), no. 14, 141102.

[129] V. Choutko, AMS days at la Palma 2018.

[130] D. Hooper, I. Cholis, T. Linden, and K. Fang, HAWC observations strongly favor pulsar interpretations of the cosmic-ray positron excess *Physical Review D* **96** (2017), no. 10, 103013.

[131] S. Murgia, The Fermi–LAT Galactic Center Excess: Evidence of Annihilating Dark Matter? *Annual Review of Nuclear and Particle Science* **70** (2020) 455–483.

[132] H. Baer and X. Tata, Weak Scale Supersymmetry: From Superfields to Scattering Events Cambridge University Press, 2006.

[133] A. Boveia and C. Doglioni, Dark matter searches at colliders *Annual Review of Nuclear and Particle Science* **68** (2018) 429–459.

[134] D. Abercrombie, N. Akchurin, E. Akilli, J. A. Maestre, B. Allen, B. A. Gonzalez, J. Andrea, A. Arbey, G. Azuelos, P. Azzi, *et al.*, Dark matter benchmark models for early LHC run-2 searches: report of the ATLAS/CMS dark matter forum *Physics of the Dark Universe* **27** (2020) 100371.

[135] J. F. Navarro, C. S. Frenk, and S. D. White, A universal density profile from hierarchical clustering *The Astrophysical Journal* **490** (1997), no. 2, 493.

[136] S. S. McGaugh, V. C. Rubin, and W. De Blok, High-resolution rotation curves of low surface brightness galaxies. I. Data *The Astronomical Journal* **122** (2001), no. 5, 2381.

[137] D. Marchesini, E. DOnghia, G. Chincarini, C. Firmani, P. Conconi, E. Molinari, and A. Zacchei, Hα rotation curves: the soft core question *The Astrophysical Journal* **575** (2002), no. 2, 801.

[138] A. Burkert, The structure of dark matter halos in dwarf galaxies *The Astrophysical Journal Letters* **447** (1995), no. 1, L25.

[139] A. Pontzen and F. Governato, How supernova feedback turns dark matter cusps into cores *Monthly Notices of the Royal Astronomical Society* **421** (2012), no. 4, 3464–3471.

[140] D. N. Spergel and P. J. Steinhardt, Observational evidence for self-interacting cold dark matter *Physical review letters* **84** (2000), no. 17, 3760.

[141] S. Tulin and H.-B. Yu, Dark matter self-interactions and small scale structure *Physics Reports* **730** (2018) 1–57.

[142] A. Brown, A. Vallenari, T. Prusti, J. De Bruijne, C. Babusiaux, C. Bailer-Jones, M. Biermann, D. W. Evans, L. Eyer, F. Jansen, *et al.*, Gaia Data Release 2-Summary of the contents and survey properties *Astronomy & astrophysics* **616** (2018) A1.

[143] M. Buschmann, B. R. Safdi, and K. Schutz, The Galactic potential and dark matter density from angular stellar accelerations *arXiv preprint arXiv:2103.05000*, 2021.

[144] V. Belokurov, D. Erkal, N. Evans, S. Koposov, and A. Deason, Co-formation of the disc and the stellar halo *Monthly Notices of the Royal Astronomical Society* **478** (2018), no. 1, 611–619.

[145] A. Helmi, C. Babusiaux, H. H. Koppelman, D. Massari, J. Veljanoski, and A. G. Brown, The merger that led to the formation of the Milky Ways inner stellar halo and thick disk *Nature* **563** (2018), no. 7729, 85–88.

[146] J. D. Kruijssen, J. L. Pfeffer, M. Reina-Campos, R. A. Crain, and N. Bastian, The formation and assembly history of the Milky Way revealed by its globular cluster population *Monthly Notices of the Royal Astronomical Society* **486** (2019), no. 3, 3180–3202.

[147] A. Helmi, Streams, substructures, and the early history of the Milky Way *Annual Review of Astronomy and Astrophysics* **58** (2020) 205–256.

[148] R. Aaij, C. A. Beteta, T. Ackernley, B. Adeva, M. Adinolfi, H. Afsharnia, C. A. Aidala, S. Aiola, Z. Ajaltouni, S. Akar, *et al.*, Test of lepton universality in beauty-quark decays *arXiv preprint arXiv:2103.11769*, 2021.

[149] **BESIII** Collaboration, M. Ablikim *et al.*, First Measurement of the Absolute Branching Fraction of $\Lambda \to p\mu^-\bar{\nu}_\mu$ `arXiv:2107.06704`.

[150] J. C. Pati and A. Salam, Lepton Number as the Fourth Color *Phys. Rev. D* **10** (1974) 275–289, [Erratum: Phys.Rev.D 11, 703–703 (1975)].

[151] H. Georgi and S. L. Glashow, Unity of all elementary-particle forces *Physical Review Letters* **32** (1974), no. 8, 438.

[152] H. Murayama and T. Yanagida, Viable SU (5) GUT with light leptoquark bosons *Modern Physics Letters A* **7** (1992), no. 02, 147–151.

[153] F. S. Queiroz, K. Sinha, and A. Strumia, Leptoquarks, dark matter, and anomalous LHC events *Physical Review D* **91** (2015), no. 3, 035006.

[154] R. Mandal, Fermionic dark matter in leptoquark portal *The European Physical Journal C* **78** (2018), no. 9, 1–6.

[155] S.-M. Choi, Y.-J. Kang, H. M. Lee, and T.-G. Ro, Lepto-quark portal dark matter *Journal of High Energy Physics* **2018** (2018), no. 10, 1–30.

[156] F. DEramo, N. Košnik, F. Pobbe, A. Smolkovič, and O. Sumensari, Leptoquarks and real singlets: A richer scalar sector behind the origin of dark matter *Physical Review D* **104** (2021), no. 1, 015035.

[157] B. Abi, T. Albahri, S. Al-Kilani, D. Allspach, L. Alonzi, A. Anastasi, A. Anisenkov, F. Azfar, K. Badgley, S. Baeßler, *et al.*, Measurement of the positive muon anomalous magnetic moment to 0.46 ppm *Physical Review Letters* **126** (2021), no. 14, 141801.

[158] H.-S. Lee, Muon g- 2 anomaly and dark leptonic gauge boson *Physical Review D* **90** (2014), no. 9, 091702.

[159] A. Freitas, J. Lykken, S. Kell, and S. Westhoff, Testing the Muon g-2 Anomaly at the LHC *Journal of High Energy Physics* **2014** (2014), no. 5, 1–36.

[160] B. Allanach, F. S. Queiroz, A. Strumia, and S. Sun, Z models for the LHCb and g- 2 muon anomalies *Physical Review D* **93** (2016), no. 5, 055045.

[161] P. Athron, C. Balázs, D. H. Jacob, W. Kotlarski, D. Stöckinger, and H. Stöckinger-Kim, New physics explanations of a_μ in light of the FNAL muon $g-2$ measurement *arXiv preprint arXiv:2104.03691*, 2021.

[162] S. Borsanyi, Z. Fodor, J. Guenther, C. Hoelbling, S. Katz, L. Lellouch, T. Lippert, K. Miura, L. Parato, K. Szabo, *et al.*, Leading hadronic contribution to the muon magnetic moment from lattice QCD *Nature* **593** (2021), no. 7857, 51–55.

[163] E. Aprile, J. Aalbers, F. Agostini, M. Alfonsi, L. Althueser, F. Amaro, V. C. Antochi, E. Angelino, J. Angevaare, F. Arneodo, *et al.*, Excess electronic recoil events in XENON1T *Physical Review D* **102** (2020), no. 7, 072004.

[164] M. A. Deliyergiyev, Recent Progress in Search for Dark Sector Signatures *Open Phys.* **14** (2016), no. 1, 281–303, arXiv:1510.06927.

[165] J. Alexander *et al.*, Dark Sectors 2016 Workshop: Community Report 2016. arXiv:1608.08632.

[166] L. Ackerman, M. R. Buckley, S. M. Carroll, and M. Kamionkowski, Dark Matter and Dark Radiation *Phys. Rev.* **D79** (2009) 023519, arXiv:0810.5126, [,277(2008)].

[167] F.-Y. Cyr-Racine and K. Sigurdson, Cosmology of atomic dark matter *Phys. Rev.* **D87** (2013), no. 10, 103515, arXiv:1209.5752.

[168] P. Agrawal, F.-Y. Cyr-Racine, L. Randall, and J. Scholtz, Make Dark Matter Charged Again *JCAP* **1705** (2017), no. 05, 022, arXiv:1610.04611.

[169] E. Gabrielli and M. Raidal, Exponentially spread dynamical Yukawa couplings from nonperturbative chiral symmetry breaking in the dark sector *Phys. Rev.* **D89** (2014), no. 1, 015008, arXiv:1310.1090.

[170] E. Gabrielli, L. Marzola, and M. Raidal, Radiative Yukawa Couplings in the Simplest Left-Right Symmetric Model *Phys. Rev.* **D95** (2017), no. 3, 035005, arXiv:1611.00009.

[171] F. del Aguila, M. Masip, and M. Perez-Victoria, Physical parameters and renormalization of U(1)-a x U(1)-b models *Nucl. Phys.* **B456** (1995) 531–549, arXiv:hep-ph/9507455.

[172] E. Gabrielli, M. Heikinheimo, B. Mele, and M. Raidal, Dark photons and resonant monophoton signatures in Higgs boson decays at the LHC *Phys. Rev.* **D90** (2014), no. 5, 055032, arXiv:1405.5196.

[173] S. Biswas, E. Gabrielli, M. Heikinheimo, and B. Mele, Higgs-boson production in association with a dark photon in e^+e^- collisions *JHEP* **06** (2015) 102, arXiv:1503.05836.

[174] S. Biswas, E. Gabrielli, M. Heikinheimo, and B. Mele, Dark-photon searches via ZH production at e^+e^- colliders *Phys. Rev.* **D96** (2017), no. 5, 055012, arXiv:1703.00402.

[175] M. Fabbrichesi, E. Gabrielli, and B. Mele, Hunting down massless dark photons in kaon physics *Phys. Rev. Lett.* **119** (2017), no. 3, 031801, arXiv:1705.03470.

[176] M. Fabbrichesi, E. Gabrielli, and B. Mele, Z Boson Decay into Light and Darkness *Phys. Rev. Lett.* **120** (2018), no. 17, 171803, arXiv:1712.05412.

[177] D. Barducci, M. Fabbrichesi, and E. Gabrielli, Neutral Hadrons Disappearing into the Darkness *Phys. Rev.* **D98** (2018), no. 3, 035049, arXiv:1806.05678.

[178] H. Goldberg and L. J. Hall, A New Candidate for Dark Matter *Phys. Lett.* **B174** (1986) 151, [,467(1986)].

[179] B. Holdom, Searching for ϵ Charges and a New U(1) *Phys. Lett.* **B178** (1986) 65–70.

[180] B.-A. Gradwohl and J. A. Frieman, Dark matter, long range forces, and large scale structure *Astrophys. J.* **398** (1992) 407–424.

[181] E. D. Carlson, M. E. Machacek, and L. J. Hall, Self-interacting dark matter *Astrophys. J.* **398** (1992) 43–52.

[182] R. Foot, Mirror matter-type dark matter *Int. J. Mod. Phys.* **D13** (2004) 2161–2192, arXiv:astro-ph/0407623.

[183] J. L. Feng, H. Tu, and H.-B. Yu, Thermal Relics in Hidden Sectors *JCAP* **0810** (2008) 043, arXiv:0808.2318.

[184] J. L. Feng, M. Kaplinghat, H. Tu, and H.-B. Yu, Hidden Charged Dark Matter *JCAP* **0907** (2009) 004, arXiv:0905.3039.

[185] N. Arkani-Hamed, D. P. Finkbeiner, T. R. Slatyer, and N. Weiner, A Theory of Dark Matter *Phys. Rev.* **D79** (2009) 015014, arXiv:0810.0713.

[186] D. E. Kaplan, G. Z. Krnjaic, K. R. Rehermann, and C. M. Wells, Atomic Dark Matter *JCAP* **1005** (2010) 021, arXiv:0909.0753.

[187] M. R. Buckley and P. J. Fox, Dark Matter Self-Interactions and Light Force Carriers *Phys. Rev.* **D81** (2010) 083522, arXiv:0911.3898.

[188] D. Hooper, N. Weiner, and W. Xue, Dark Forces and Light Dark Matter *Phys. Rev.* **D86** (2012) 056009, arXiv:1206.2929.

[189] L. G. van den Aarssen, T. Bringmann, and C. Pfrommer, Is dark matter with long-range interactions a solution to all small-scale problems of Λ CDM cosmology? *Phys. Rev. Lett.* **109** (2012) 231301, arXiv:1205.5809.

[190] J. M. Cline, Z. Liu, and W. Xue, Millicharged Atomic Dark Matter *Phys. Rev.* **D85** (2012) 101302, arXiv:1201.4858.

[191] S. Tulin, H.-B. Yu, and K. M. Zurek, Beyond Collisionless Dark Matter: Particle Physics Dynamics for Dark Matter Halo Structure *Phys. Rev.* **D87** (2013), no. 11, 115007, arXiv:1302.3898.

[192] M. Baldi, Structure formation in Multiple Dark Matter cosmologies with long-range scalar interactions *Mon. Not. Roy. Astron. Soc.* **428** (2013) 2074, arXiv:1206.2348.

[193] J. M. Cline, Z. Liu, G. Moore, and W. Xue, Composite strongly interacting dark matter *Phys. Rev.* **D90** (2014), no. 1, 015023, arXiv:1312.3325.

[194] X. Chu and B. Dasgupta, Dark Radiation Alleviates Problems with Dark Matter Halos *Phys. Rev. Lett.* **113** (2014), no. 16, 161301, arXiv:1404.6127.

[195] K. K. Boddy, J. L. Feng, M. Kaplinghat, and T. M. P. Tait, Self-Interacting Dark Matter from a Non-Abelian Hidden Sector *Phys. Rev.* **D89** (2014), no. 11, 115017, arXiv:1402.3629.

[196] M. A. Buen-Abad, G. Marques-Tavares, and M. Schmaltz, Non-Abelian dark matter and dark radiation *Phys. Rev.* **D92** (2015), no. 2, 023531, arXiv:1505.03542.

[197] D. Hanneke, S. Fogwell, and G. Gabrielse, New Measurement of the Electron Magnetic Moment and the Fine Structure Constant *Phys. Rev. Lett.* **100** (2008) 120801, arXiv:0801.1134.

[198] **Muon g-2** Collaboration, G. W. Bennett *et al.*, Final Report of the Muon E821 Anomalous Magnetic Moment Measurement at BNL *Phys. Rev.* **D73** (2006) 072003, arXiv:hep-ex/0602035.

[199] **ATLAS** Collaboration, M. Aaboud *et al.*, Search for squarks and gluinos in final states with jets and missing transverse momentum using 36 fb^{-1} of $\sqrt{s} = 13$ TeV pp collision data with the ATLAS detector *Phys. Rev.* **D97** (2018), no. 11, 112001, arXiv:1712.02332.

[200] **CMS** Collaboration, A. M. Sirunyan *et al.*, Search for supersymmetric partners of electrons and muons in proton-proton collisions at $\sqrt{s} = 13$ TeV *Phys. Lett.* **B790** (2019) 140–166, arXiv:1806.05264.

[201] S. Hoffmann, Paraphotons and Axions: Similarities in Stellar Emission and Detection *Phys. Lett.* **B193** (1987) 117–122.

[202] B. A. Dobrescu, Massless gauge bosons other than the photon *Phys. Rev. Lett.* **94** (2005) 151802, arXiv:hep-ph/0411004.

[203] M. Giannotti, I. Irastorza, J. Redondo, and A. Ringwald, Cool WISPs for stellar cooling excesses *JCAP* **1605** (2016), no. 05, 057, arXiv:1512.08108.

[204] G. G. Raffelt, Astrophysical methods to constrain axions and other novel particle phenomena *Phys. Rept.* **198** (1990) 1–113.

[205] D. Clowe, M. Bradac, A. H. Gonzalez, M. Markevitch, S. W. Randall, C. Jones, and D. Zaritsky, A direct empirical proof of the existence of dark matter *Astrophys. J.* **648** (2006) L109–L113, arXiv:astro-ph/0608407.

[206] J. L. Feng, M. Kaplinghat, and H.-B. Yu, Halo Shape and Relic Density Exclusions of Sommerfeld-Enhanced Dark Matter Explanations of Cosmic Ray Excesses *Phys. Rev. Lett.* **104** (2010) 151301, arXiv:0911.0422.

[207] T. Lin, H.-B. Yu, and K. M. Zurek, On Symmetric and Asymmetric Light Dark Matter *Phys. Rev.* **D85** (2012) 063503, arXiv:1111.0293.

[208] A. H. G. Peter, M. Rocha, J. S. Bullock, and M. Kaplinghat, Cosmological Simulations with Self-Interacting Dark Matter II: Halo Shapes vs. Observations *Mon. Not. Roy. Astron. Soc.* **430** (2013) 105, arXiv:1208.3026.

[209] P. F. de Salas and S. Pastor, Relic neutrino decoupling with flavour oscillations revisited *JCAP* **1607** (2016), no. 07, 051, arXiv:1606.06986.

[210] H. M. Hodges, Mirror baryons as the dark matter *Phys. Rev.* **D47** (1993) 456–459.

[211] Z. G. Berezhiani, A. D. Dolgov, and R. N. Mohapatra, Asymmetric inflationary reheating and the nature of mirror universe *Phys. Lett.* **B375** (1996) 26–36, arXiv:hep-ph/9511221.

[212] Z. Berezhiani, D. Comelli, and F. L. Villante, The Early mirror universe: Inflation, baryogenesis, nucleosynthesis and dark matter *Phys. Lett.* **B503** (2001) 362–375, arXiv:hep-ph/0008105.

[213] H. Vogel and J. Redondo, Dark Radiation constraints on minicharged particles in models with a hidden photon *JCAP* **1402** (2014) 029, arXiv:1311.2600.

[214] P. Gondolo and G. Gelmini, Cosmic abundances of stable particles: Improved analysis *Nucl. Phys.* **B360** (1991) 145–179.

[215] J. Bernstein, Kinetic Theory in the Expanding Universe Cambridge University Press, 1988.

[216] T. Binder, L. Covi, A. Kamada, H. Murayama, T. Takahashi, and N. Yoshida, Matter power spectrum in hidden neutrino interacting dark matter models: a closer look at the collision term *Journal of Cosmology and Astroparticle Physics* **2016** nov (2016) 043–043.

[217] T. Bringmann and S. Hofmann, Thermal decoupling of WIMPs from first principles *JCAP* **0704** (2007) 016, arXiv:hep-ph/0612238, [Erratum: JCAP1603,no.03,E02(2016)].

[218] R. Foot and S. Vagnozzi, Dissipative hidden sector dark matter *Phys. Rev.* **D91** (2015) 023512, arXiv:1409.7174.

[219] M. Drees, F. Hajkarim, and E. R. Schmitz, The Effects of QCD Equation of State on the Relic Density of WIMP Dark Matter *JCAP* **1506** (2015), no. 06, 025, arXiv:1503.03513.

[220] K. Sigurdson, M. Doran, A. Kurylov, R. R. Caldwell, and M. Kamionkowski, Dark-matter electric and magnetic dipole moments *Phys. Rev.* **D70** (2004) 083501, arXiv:astro-ph/0406355, [Erratum: Phys. Rev.D73,089903(2006)].

[221] T. Banks, J.-F. Fortin, and S. Thomas, Direct Detection of Dark Matter Electromagnetic Dipole Moments arXiv:1007.5515.

[222] V. Barger, W.-Y. Keung, and D. Marfatia, Electromagnetic properties of dark matter: Dipole moments and charge form factor *Phys. Lett.* **B696** (2011) 74–78, arXiv:1007.4345.

[223] J. H. Heo, Minimal Dirac Fermionic Dark Matter with Nonzero Magnetic Dipole Moment *Phys. Lett.* **B693** (2010) 255–258, arXiv:0901.3815.

[224] E. Del Nobile, Direct detection signals of dark matter with magnetic dipole moment *PoS* **EPS-HEP2017** (2017) 626, arXiv:1709.08700.

[225] N. Fornengo, P. Panci, and M. Regis, Long-Range Forces in Direct Dark Matter Searches *Phys. Rev.* **D84** (2011) 115002, arXiv:1108.4661.

[226] A. L. Fitzpatrick, W. Haxton, E. Katz, N. Lubbers, and Y. Xu, The Effective Field Theory of Dark Matter Direct Detection *JCAP* **1302** (2013) 004, arXiv:1203.3542.

[227] N. Anand, A. L. Fitzpatrick, and W. C. Haxton, Model-independent Analyses of Dark-Matter Particle Interactions *Phys. Procedia* **61** (2015) 97–106, arXiv:1405.6690.

[228] **The GAMBIT Dark Matter Workgroup** Collaboration, T. Bringmann *et al.*, DarkBit: A GAMBIT module for computing dark matter observables and likelihoods *Eur. Phys. J.* **C77** (2017), no. 12, 831, arXiv:1705.07920.

[229] **GAMBIT** Collaboration, P. Athron *et al.*, Global analyses of Higgs portal singlet dark matter models using GAMBIT *Eur. Phys. J.* **C79** (2019), no. 1, 38, arXiv:1808.10465.

[230] **XENON** Collaboration, E. Aprile *et al.*, Dark Matter Search Results from a One Ton-Year Exposure of XENON1T *Phys. Rev. Lett.* **121** (2018), no. 11, 111302, arXiv:1805.12562.

[231] M. Schumann, L. Baudis, L. Bütikofer, A. Kish, and M. Selvi, Dark matter sensitivity of multi-ton liquid xenon detectors *Journal of Cosmology and Astroparticle Physics* **2015** oct (2015) 016–016.

[232] F. Bishara, J. Brod, B. Grinstein, and J. Zupan, From quarks to nucleons in dark matter direct detection *JHEP* **11** (2017) 059, arXiv:1707.06998.

[233] E. Del Nobile, Complete Lorentz-to-Galileo dictionary for direct dark matter detection *Phys. Rev. D* **98** (2018), no. 12, 123003, arXiv:1806.01291.

[234] P. Carenza, T. Fischer, M. Giannotti, G. Guo, G. Martínez-Pinedo, and A. Mirizzi, Improved axion emissivity from a supernova via nucleon-nucleon bremsstrahlung *Journal of Cosmology and Astroparticle Physics* **2019** (2019), no. 10, 016–016.

[235] N. Bar, K. Blum, and G. D'amico, Is there a supernova bound on axions? arXiv:1907.05020.

[236] S. Profumo and P. Ullio, SUSY dark matter and quintessence *JCAP* **11** (2003) 006, hep-ph/0309220.

[237] G. Arcadi and P. Ullio, Accurate estimate of the relic density and the kinetic decoupling in non-thermal dark matter models *Phys. Rev. D* **84** (2011) 043520, arXiv:1104.3591.

[238] K. Fukushima, C. Kelso, J. Kumar, P. Sandick, and T. Yamamoto, MSSM dark matter and a light slepton sector: The incredible bulk *Physical Review D* **90** (2014), no. 9, 095007.

[239] K. Griest and D. Seckel, Three exceptions in the calculation of relic abundances *Physical Review D* **43** (1991), no. 10, 3191.

[240] S. Mizuta and M. Yamaguchi, Coannihilation effects and relic abundance of Higgsino-dominant LSPs *Physics Letters B* **298** (1993), no. 1-2, 120–126.

[241] T. Bringmann, J. Edsjö, P. Gondolo, P. Ullio, and L. Bergström, DarkSUSY 6: an advanced tool to compute dark matter properties numerically *Journal of Cosmology and Astroparticle Physics* **2018** (2018), no. 07, 033.

[242] F. Staub, SARAH 4: A tool for (not only SUSY) model builders *Computer Physics Communications* **185** (2014), no. 6, 1773–1790.

[243] G. Bélanger, F. Boudjema, A. Goudelis, A. Pukhov, and B. Zaldivar, micrOMEGAs5. 0: Freeze-in *Computer Physics Communications* **231** (2018) 173–186.

[244] J. Ellis, T. Falk, K. A. Olive, and M. Srednicki, Calculations of neutralino–stau coannihilation channels and the cosmologically relevant region of MSSM parameter space *Astroparticle Physics* **13** (2000), no. 2-3, 181–213.

[245] H. Yamamoto, The International Linear Collider ProjectIts Physics and Status *Symmetry* **13** (2021), no. 4, 674.

[246] K. Griest and M. Kamionkowski, Unitarity Limits on the Mass and Radius of Dark Matter Particles *Phys. Rev. Lett.* **64** (1990) 615.

[247] B. W. Lee, C. Quigg, and H. Thacker, Weak interactions at very high energies: The role of the Higgs-boson mass in "The Standard Model Higgs Boson", M. EINHORN, ed., vol. 8 of *Current PhysicsSources and Comments*, pp. 282–294. Elsevier, 1991.

[248] A. Schuessler and D. Zeppenfeld, Unitarity constraints on MSSM trilinear couplings in "15th International Conference on Supersymmetry and the Unification of Fundamental Interactions (SUSY07)". 10 2007. arXiv:0710.5175.

[249] K. Betre, S. E. Hedri, and D. G. Walker, Perturbative Unitarity Constraints on a Supersymmetric Higgs Portal *arXiv preprint arXiv:1407.0395*, 2014.

[250] W. Porod, SPheno, a program for calculating supersymmetric spectra, SUSY particle decays and SUSY particle production at e+ e- colliders *Computer Physics Communications* **153** (2003), no. 2, 275–315.

[251] W. Porod and F. Staub, SPheno 3.1: Extensions including flavour, CP-phases and models beyond the MSSM *Computer Physics Communications* **183** (2012), no. 11, 2458–2469.

[252] W. G. Hollik, G. Weiglein, and J. Wittbrodt, Impact of vacuum stability constraints on the phenomenology of supersymmetric models *Journal of high energy physics* **2019** (2019), no. 3, 1–37.

[253] G. H. Duan, C. Han, B. Peng, L. Wu, and J. M. Yang, Vacuum stability in stau-neutralino coannihilation in MSSM *Physics Letters B* **788** (2019) 475–479.

[254] W. G. Hollik, A new view on vacuum stability in the MSSM *Journal of High Energy Physics* **2016** (2016), no. 8, 1–27.

[255] T.-L. Lee, T.-Y. Li, and C.-H. Tsai, HOM4PS-2.0: a software package for solving polynomial systems by the polyhedral homotopy continuation method *Computing* **83** (2008) 109–133.

[256] S. Coleman, Fate of the false vacuum: Semiclassical theory *Physical Review D* **15** (1977), no. 10, 2929.

[257] C. G. Callan Jr and S. Coleman, Fate of the false vacuum. II. First quantum corrections *Physical Review D* **16** (1977), no. 6, 1762.

[258] A. Kusenko, P. Langacker, and G. Segre, Phase transitions and vacuum tunneling into charge-and color-breaking minima in the MSSM *Physical Review D* **54** (1996), no. 9, 5824.

[259] I. Dasgupta, Estimating vacuum tunneling rates *Physics Letters B* **394** (1997), no. 1-2, 116–122.

[260] T. Konstandin and S. J. Huber, Numerical approach to multi-dimensional phase transitions *Journal of Cosmology and Astroparticle Physics* **2006** (2006), no. 06, 021.

[261] J.-h. Park, Constrained potential method for false vacuum decays *Journal of Cosmology and Astroparticle Physics* **2011** (2011), no. 02, 023.

[262] F. C. Adams, General solutions for tunneling of scalar fields with quartic potentials *Physical Review D* **48** (1993), no. 6, 2800.

[263] A. Berlin, D. S. Robertson, M. P. Solon, and K. M. Zurek, Bino variations: Effective field theory methods for dark matter direct detection *Phys. Rev. D* **93** May (2016) 095008.

[264] N. W. Evans, C. A. OHare, and C. McCabe, Refinement of the standard halo model for dark matter searches in light of the Gaia Sausage *Physical Review D* **99** (2019), no. 2, 023012.

[265] L. Necib, M. Lisanti, and V. Belokurov, Inferred Evidence for Dark Matter Kinematic Substructure with SDSS–Gaia *The Astrophysical Journal* **874** (2019), no. 1, 3.

[266] C. Hunter and E. Qian, Two-integral distribution functions for axisymmetric galaxies *Monthly Notices of the Royal Astronomical Society* **262** (1993), no. 2, 401–428.

[267] A. Eddington, The distribution of stars in globular clusters *Monthly Notices of the Royal Astronomical Society* **76** (1916) 572–585.

[268] R. Catena, T. Emken, N. A. Spaldin, and W. Tarantino, Atomic responses to general dark matter-electron interactions *Phys. Rev. Res.* **2** (2020), no. 3, 033195, arXiv:1912.08204.

[269] C. F. Bunge, J. A. Barrientos, and A. V. Bunge, Roothaan-Hartree-Fock ground-state atomic wave functions: Slater-type orbital expansions and expectation values for Z= 2-54 *Atomic Data and Nuclear Data Tables* **53** (1993), no. 1, 113–162.

[270] R. Essig, T. Volansky, and T.-T. Yu, New Constraints and Prospects for sub-GeV Dark Matter Scattering off Electrons in Xenon *Phys. Rev. D* **96** (2017), no. 4, 043017, arXiv:1703.00910.

[271] B. M. Roberts, V. A. Dzuba, V. V. Flambaum, M. Pospelov, and Y. V. Stadnik, Dark matter scattering on electrons: Accurate calculations of atomic excitations and implications for the DAMA signal *Phys. Rev. D* **93** Jun (2016) 115037.

[272] M. K. Pandey, L. Singh, C.-P. Wu, J.-W. Chen, H.-C. Chi, C.-C. Hsieh, C.-P. Liu, and H. T. Wong, Constraints on spin-independent dark matter scattering off electrons with germanium and xenon detectors arXiv:1812.11759.

[273] **XENON** Collaboration, E. Aprile *et al.*, Light Dark Matter Search with Ionization Signals in XENON1T *Phys. Rev. Lett.* **123** (2019), no. 25, 251801, arXiv:1907.11485.

[274] C. Savage, K. Freese, and P. Gondolo, Annual Modulation of Dark Matter in the Presence of Streams *Phys. Rev. D* **74** (2006) 043531, astro-ph/0607121.

[275] C. Hunter and E. Qian, Two-integral distribution functions for axisymmetric galaxies *Monthly Notices of the Royal Astronomical Society* **262** 05 (1993) 401–428.

[276] S. G. Johnson, The NLopt nonlinear-optimization package http://github.com/stevengj/nlopt.

[277] W. Dehnen and J. Binney, Mass models of the Milky Way *Monthly Notices of the Royal Astronomical Society* **294** (1998), no. 3, 429–438.

[278] P. J. McMillan, The mass distribution and gravitational potential of the Milky Way *Monthly Notices of the Royal Astronomical Society*, 2016 stw2759.

[279] M. Petač and P. Ullio, Two-integral distribution functions in axisymmetric galaxies: implications for dark matter searches *Phys. Rev. D* **99** (2019), no. 4, 043003, arXiv:1812.01531.

[280] B. Allgood, R. A. Flores, J. R. Primack, A. V. Kravtsov, R. H. Wechsler, A. Faltenbacher, and J. S. Bullock, The shape of dark matter haloes: dependence on mass, redshift, radius and formation *Monthly Notices of the Royal Astronomical Society* **367** (2006), no. 4, 1781–1796.

[281] V. P. Debattista, B. Moore, T. Quinn, S. Kazantzidis, R. Maas, L. Mayer, J. Read, and J. Stadel, The causes of halo shape changes induced by cooling baryons: disks versus substructures *The Astrophysical Journal* **681** (2008), no. 2, 1076.

[282] R. Ibata, G. F. Lewis, M. Irwin, E. Totten, and T. Quinn, Great Circle Tidal Streams: Evidence for a Nearly Spherical Massive Dark Halo around the Milky Way *The Astrophysical Journal* **551** apr (2001) 294–311.

[283] M. Fellhauer, V. Belokurov, N. W. Evans, M. I. Wilkinson, D. B. Zucker, G. Gilmore, M. J. Irwin, D. M. Bramich, S. Vidrih, R. F. G. Wyse, T. C. Beers, and J. Brinkmann, The Origin of the Bifurcation in the Sagittarius Stream *The Astrophysical Journal* **651** nov (2006) 167–173.

[284] D. R. Law, S. R. Majewski, and K. V. Johnston, Evidence for a triaxial Milky Way dark matter halo from the Sagittarius stellar tidal stream *The Astrophysical Journal Letters* **703** (2009), no. 1, L67.

[285] R. Ibata, G. F. Lewis, N. F. Martin, M. Bellazzini, and M. Correnti, DOES THE SAGITTARIUS STREAM CONSTRAIN THE MILKY WAY HALO TO BE TRIAXIAL? *The Astrophysical Journal* **765** feb (2013) L15.

[286] E. Vasiliev, V. Belokurov, and D. Erkal, Tango for three: Sagittarius, LMC, and the Milky Way *Monthly Notices of the Royal Astronomical Society* **501** (2021), no. 2, 2279–2304.

[287] S. Shao, M. Cautun, A. Deason, and C. S. Frenk, The twisted dark matter halo of the Milky Way *Monthly Notices of the Royal Astronomical Society*, 12 2020 staa3883.

[288] R. P. Olling and M. R. Merrifield, Two measures of the shape of the dark halo of the Milky Way *Monthly Notices of the Royal Astronomical Society* **311** 01 (2000) 361–369.

[289] B. Sesar, M. Jurić, and Ž. Ivezić, THE SHAPE AND PROFILE OF THE MILKY WAY HALO AS SEEN BY THE CANADA-FRANCE-HAWAII TELESCOPE LEGACY SURVEY *The Astrophysical Journal* **731** mar (2011) 4.

[290] M. S. Nitschai, M. Cappellari, and N. Neumayer, First Gaia dynamical model of the Milky Way disc with six phase space coordinates: a test for galaxy dynamics *Monthly Notices of the Royal Astronomical Society* **494** 04 (2020) 6001–6011.

[291] M. Cappellari, Measuring the inclination and mass-to-light ratio of axisymmetric galaxies via anisotropic Jeans models of stellar kinematics *MNRAS* **390** (2008) 71–86, `0806.0042`.

[292] M. Petac, Equilibrium axisymmetric halo model for the Milky Way and its implications for direct and indirect DM searches `arXiv:2008.11172`.

[293] D. Lynden-Bell *et al.*, Can spherical clusters rotate? *Monthly Notices of the Royal Astronomical Society* **120** (1960), no. 3, 204–213.

[294] T. Fukushima, Precise and fast computation of a general incomplete elliptic integral of second kind by half and double argument transformations *Journal of Computational and Applied Mathematics* **235** (2011), no. 14, 4140 – 4148.

[295] T. Lacroix, M. Stref, and J. Lavalle, Anatomy of Eddington-like inversion methods in the context of dark matter searches *Journal of Cosmology and Astroparticle Physics* **2018** (2018), no. 09, 040.

[296] C. McCabe, The Earth's velocity for direct detection experiments *Journal of Cosmology and Astroparticle Physics* **2014** feb (2014) 027–027.

[297] I. M. Bloch, A. Caputo, R. Essig, D. Redigolo, M. Sholapurkar, and T. Volansky, Exploring New Physics with O(keV) Electron Recoils in Direct Detection Experiments `arXiv:2006.14521`.

[298] A. Migdal, Ionization of atoms accompanying α-and β-decay *J. Phys. USSR* **4** (1941) 449.

[299] M. Ibe, W. Nakano, Y. Shoji, and K. Suzuki, Migdal effect in dark matter direct detection experiments *arXiv preprint arXiv:1707.07258*, 2017.

[300] R. Essig, J. Pradler, M. Sholapurkar, and T.-T. Yu, Relation between the Migdal effect and dark matter-electron scattering in isolated atoms and semiconductors *Physical review letters* **124** (2020), no. 2, 021801.

[301] R. Essig, M. Fernández-Serra, J. Mardon, A. Soto, T. Volansky, and T.-T. Yu, Direct detection of sub-GeV dark matter with semiconductor targets *Journal of High Energy Physics* **2016** (2016), no. 5, 1–54.

[302] A. Sommerfeld, Über die Beugung und Bremsung der Elektronen *Annalen der Physik* **403** (1931) 257.

[303] J. Hisano, S. Matsumoto, M. M. Nojiri, and O. Saito, Nonperturbative effect on dark matter annihilation and gamma ray signature from the galactic center *Phys. Rev. D* **71** Mar (2005) 063528.

[304] T. Binder, T. Bringmann, M. Gustafsson, and A. Hryczuk, Early kinetic decoupling of dark matter: when the standard way of calculating the thermal relic density fails *Phys. Rev.* **D96** (2017), no. 11, 115010, `arXiv:1706.07433`.